THE UTILIZATION OF TILTING-FILTER PHOTOMETRY IN AIRGLOW AND AURORAL RESEARCH

THESIS
Submitted in fulfilment of the
requirements for the Degree of
MASTER OF SCIENCE
of Rhodes University

by

IAN STUART DORE

Grahamstown
December 1991

TR 92-19

But where, O Nature, is thy law?
From the midnight lands comes up the dawn!
Is it not the sun setting his throne?
Is it not the icy seas that are flashing fire?
Lo, a cold flame has covered us!
Lo, in the night-time day has come upon the earth.

What makes a clear ray tremble in the night?
What strikes a slender flame in to the filament?
Like lightning without storm clouds,
Climbs to the heights from earth?
How can it be that frozen steam
Should midst winter bring forth fire?

Rhetoric (written in 1743)
Lomonosov (1748)

"...We turn to our modern theologians, the physical scientists, for words of comfort. They peer beyond the limits of time and space, wrestle with the inadequacies of language, and at last come forth with the answer: the mystery is even bigger than we thought."

Bruce Catton.

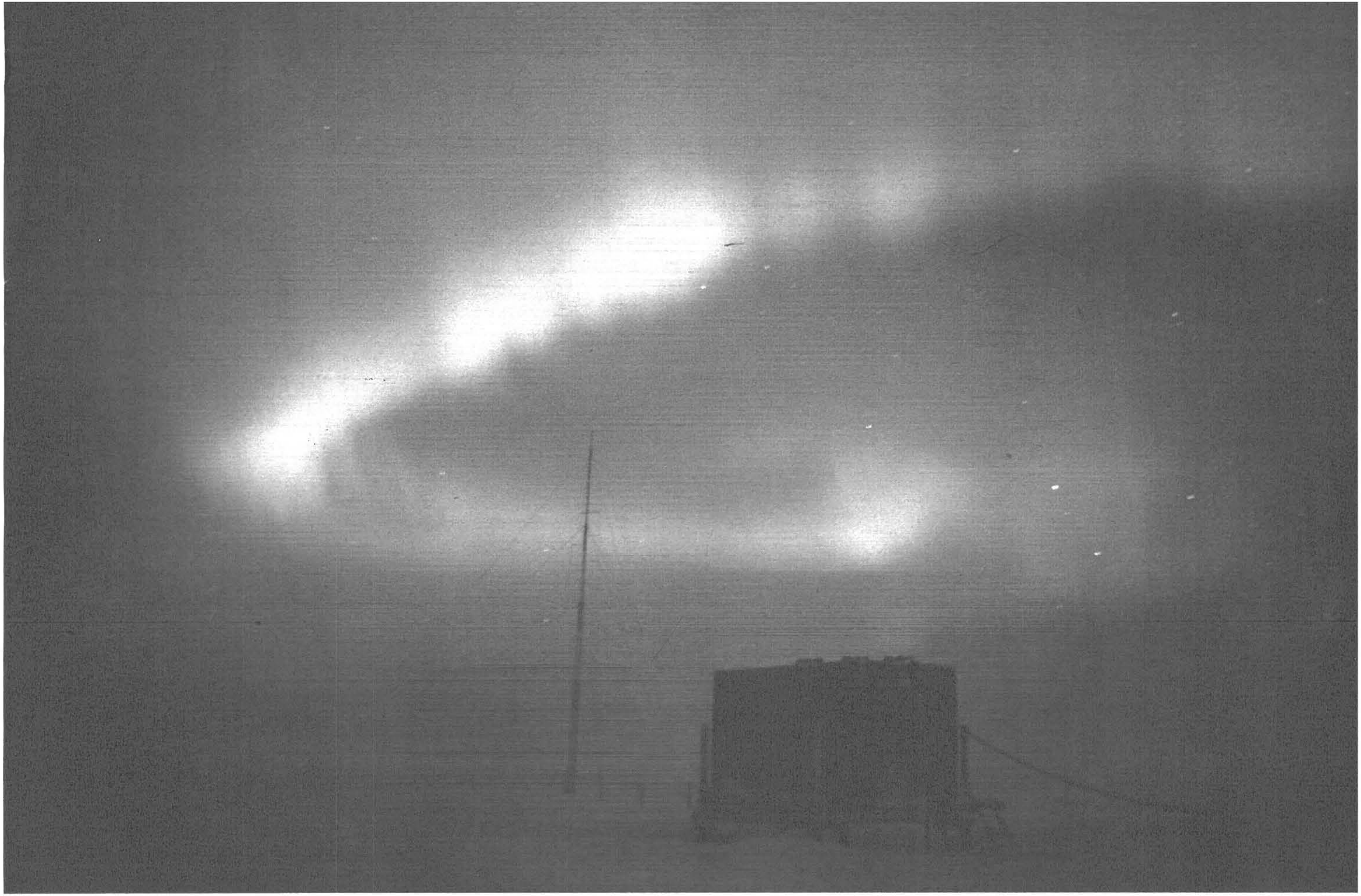

AN AURORA AT SANAE, ANTARCTICA. THE RHODES UNIVERSITY AIRGLOW AND IONOSPHERE HUT IS IN THE FOREGROUND.

TABLE OF CONTENTS

ACKNOWLEDGEMENTS

Many people have contributed to this thesis over the years.

My initial supervisor was the late Professor J.A. Gledhill. His advice, guidance and enthusiastic encouragement were invaluable to the airglow programme, and to this thesis. Without his commitment to Antarctic upper atmosphere research, I would not have had the rare privilege of experiencing the wonders of Antarctica and the aurora.

The groundwork for this thesis was carried out as part of the airglow programme in the Rhodes University Antarctic Research Group. I am grateful to my fellow research officers at that time, Geoff Evans, Ray Haggard and Allon Poole, for the assistance which they readily gave in many ways. My predecessor, Chris Grujon, must be thanked for his sound electronic design of the computer-controlled digital airglow system, upon which I was able to build. Thanks are also due to those who operated the airglow photometers at Sanae. Their comments and suggestions led to many improvements in the instrumentation.

The financial support which the Department of Transport and the Co-operative Scientific Programmes division of the Council for Scientific and Industrial Research provided for the airglow programme is gratefully acknowledged.

The completion of this thesis would not have been possible without the generous period of special study leave granted me by Rhodes University. My sincere thanks to Mike Lawrie, the Director of Computing Services, for suggesting and supporting my application for this leave. Thanks also to the staff of the Computing Centre, especially John Goetsch, for assuming the extra workload created by my absence.

Resumption of work on this thesis after five years was made easier by a number of people. My thanks go to Allon Poole for willingly taking over the supervision of a thesis in a research field about which he claimed to know little. His advice during the write-up period and comments on the draft copy of the thesis are greatly appreciated. Justin Jonas provided computing advice and a contour plotting program which he helped me to adapt to my particular needs. For this I am most grateful. To Paul Nathanson, for several useful discussions on a variety of relevant topics during the year, my thanks.

Thanks are also due to two experts in the field of auroral research, Alister Vallance Jones and Fred Rees, who readily found time in their busy schedules to respond to my questions. The UNINET electronic mail system provided fast and efficient lines of communication with these people in Canada and Alaska. For this I thank the Foundation for Research and Development and the Computing Centre at Rhodes University.

In particular, credit for the excellent Email link to the international academic community must go to Francois Jacot-Guillarmod, Mike Lawrie and Dave Wilson.

The readability of this thesis improved greatly after proof-reading and editing by my wife, Wendy. I hope she learnt as much about photometry and auroral physics as I did about literary style and grammar.

Finally, my sincere thanks to my parents for the sacrifices they made in order to finance my undergraduate studies, and for their support and encouragement over the years. Thanks also to Wendy and our daughters, Dalin and Melissa, for their understanding and the forfeit of many hours of family time for this thesis.

ABSTRACT

This thesis describes the application of tilting-filter photometry to the study of the airglow and aurora. Previous South African photometric research is reviewed.

Optical instrumentation and techniques used in airglow and auroral research are reviewed. The transmission characteristics of narrowband interference filters are discussed. The analogue meridian-scanning tilting-filter photometry system used at Sanae, Antarctica is described. Shortcomings of this system have been identified, and modifications have been made to improve its spatial and temporal resolution. Details are given of the computer-controlled digital photometry system which replaced the analogue system.

Equations are derived for the conversion of raw photometric data (analogue chart deflections or digital photon counts) to absolute emission intensities. The accuracy of the intensities obtained depends on the absolute calibration of the photometer, the transmission characteristics of the filter used to isolate the spectral feature of interest, and the effects of atmospheric extinction and scattering. The influence of these factors on observed emission intensities is discussed. Various models used to determine atmospheric correction factors are reviewed. It is shown that atmospheric correction factors can have a significant effect on both emission intensities and intensity ratios.

The procedure used to determine the transmission characteristics of interference filters is described, as is the procedure used to cross-calibrate secondary light sources. The transmission characteristics of the filters and the brightnesses of the light sources were both found to have changed appreciably with age.

The observation of a magnetospheric substorm at Sanae ($L \approx 4$) is used to illustrate the use of a meridian-scanning tilting-filter photometer system in auroral research. The ratio I(557.7) / I(391.4) observed at Sanae was found to be lower than expected, as were the OI airglow emission intensities.

A prototype digital photometer system was used aboard a ship, to observe the airglow in the region of the South Atlantic Anomaly. Significant N_2^+ 1NG emissions at 391.4 nm were measured, confirming the presence of discernable particle precipitation in the region. The OI 557.7 and 630.0 nm intensities measured from the ship were found to be lower than expected. This, combined with low airglow and auroral intensities measured at Sanae, is a cause for concern. It is recommended that further checks be made regarding the brightness of the calibration sources.

PREFACE

Much of the work for this thesis was completed in the period 1981 to 1985 while the author was employed as Assistant Antarctic Research Officer (Airglow) in the Antarctic Research Group at Rhodes University. Unfortunately, as part of a general cutback in funding for South African Antarctic research, this airglow research post was frozen at the end of 1985. The author then moved to a position in the University's Computing Centre. This thesis was completed during a period of special study leave granted by the University in 1991.

In accordance with South African standards, SI units are used throughout this thesis. Thus, for example, wavelengths are given in nanometres (nm) rather than angstroms (Å), and magnetic flux densities are given in nanoteslas (nT) rather than in gammas (γ). A notable exception is the usage of electron-volts (eV) as a unit of energy in the case of precipitating particles. It is far more convenient to express characteristic energies in terms of eV (or keV) rather than to specify them in terms of Joules. For completeness, Appendix 1 contains a conversion table for commonly-used units.

Declaration of originality

This thesis is the first to be produced at Rhodes University on the subject of airglow photometry, and following those of Robertson (1965) and Steyn (1973) is only the third thesis on this subject produced in South Africa. It is the first South African thesis on tilting-filter photometry, and consequently the author has sought to include material that should provide a solid foundation from which others may work.

The thesis has a number of sections containing review work which are the product of literature surveys conducted by the author. The following review material was compiled by the author:

1/ Previous South African airglow and auroral research (Section 1.2).
2/ Aeronomic background (Chapter 2 and Appendix B).
3/ Optical techniques for observing airglow and aurora (Section 3.2).
4/ The evaluation of the source function (Section 4.3.2).
5/ Some examples of aeronomic applications which use intensity ratios (Section 6.6.1).
6/ Coordinate systems and geomagnetic activity indices (Appendix D).

The review of previous airglow observations in the region of the South Atlantic Anomaly (Section 7.2) was based on the review given by Gledhill (1976).

As regards instrumentation (Chapter 3), the author was responsible for improvements to the analogue airglow system, and for the design and implementation of the digital Mirror Control Unit. The author completed the construction and testing of the digital photometer system, and developed and wrote all the software for the computer-controlling of the digital system.

The 'airglow' equations derived in Section 4.2 represent original work by the author. In addition, the experimental methods (described in Chapter 5) for the measurement of filter transmission characteristics and for the calibration of secondary sources, were devised and conducted by the author.

The raw photometric data used in Chapters 6 and 7 were collected by the author, at Sanae in 1979 and on the ISAAC cruise in 1983. The author also developed the techniques that he used in Chapters 6 and 7 for the processing and presentation of the tilting-filter photometer data.

The above details outline the major sections of original work by the author in this thesis.

I. S. Dore
12 December 1991

CHAPTER 1

INTRODUCTION

1.1 Historical perspective

The visual aurora is one of the most spectacular of the world's natural phenomena. Nevertheless, very few people ever have the opportunity to see this amazing manifestation of the interaction between the sun and the earth. This is because the *aurora borealis* in the northern hemisphere and the *aurora australis* in the southern hemisphere occur mainly in the relatively unpopulated polar regions - usually at magnetic latitudes in excess of 60 degrees. Intense auroras with their dynamic variations in shape and colour are awe-inspiring, and have captured the attention of many people through the ages. Auroras feature prominently in the folklore, art and literature of several sub-arctic countries in the northern hemisphere. Many examples of this are given by Eather (1980) in his book, "Majestic Lights". Although most people are at least aware of the visual phenomenon of the aurora, few are aware of the other form of light also emitted by the upper atmosphere, the sub-visual airglow. Definitions of both phenomena are given in Section 2.2.

The aurora, because of its visibility, first aroused scientific interest several centuries ago. In 1621 Gassendi saw an intense auroral display to the north of France and called it the aurora borealis - the northern dawn. The early history of auroral research is traced by Chapman (1967, 1969) and Eather (1980). Although most of the auroral research has taken place in the northern hemisphere, Gadsden (1962) has concentrated on the history of research into the aurora australis, the southern lights.

Airglow research is a much newer development than auroral research, as this sub-visual phenomenon was only discovered at the turn of this century. Chapman (1967) provides a brief history of airglow research.

Some three decades ago the International Geophysical Year (IGY) came to fruition as the first coordinated research effort, on a global scale, in the area of solar-terrestrial physics. This 'year' was held during the sunspot maximum of 1957/1958, at that stage the largest sunspot maximum of this century. A second period of coordinated research was carried out to coincide with the sunspot minimum of 1964/1965 and was known as the International Years of the Quiet Sun (IQSY). The IGY and the IQSY, together with the then rapid developments in rocket and satellite technology, triggered an intensification in research activity in the fields of upper atmosphere and space physics. This in turn has led to a tremendous enhancement of man's understanding of solar-terrestrial relationships. But despite the considerable progress that has been made due to the continuing efforts of many researchers, there are still some important aeronomic processes that are not fully understood. For example, the predominant excitation mechanisms responsible for the auroral green line emission at 557.7 nm have not been agreed upon (see for example, Paulson *et al.*, 1990; Siskind and Sharp, 1991). Another example is the current uncertainty as to the exact magnetospheric processes which result in the intense auroral activity experienced during magnetospheric substorms (see for example, Kan, 1990; Lui, 1991).

One of the areas of research that featured prominently in the IGY and the IQSY was the optical study of the airglow and auroral emissions from the upper atmosphere. Active research in this field continues strongly to the present day. Results from optical observations have made many valuable contributions to the understanding of the processes responsible for the airglow and aurora. Diverse methods are used to make spectroscopic and morphological measurements of both phenomena (see Section 3.2). One such method is the utilisation of airglow photometers to measure the intensity of light emitted at certain selected wavelengths.

Photometry is well established as an optical tool in many of the countries that are at the forefront of airglow and auroral studies e.g. the U.S.A. and Canada. Consequently, researchers in these countries often have at their disposal previously developed (and hence tried and tested) instrumentation, data recording methods, and data processing methods. Research can proceed from these established foundations, with the development of new recording and processing techniques seldom necessary. By comparison, South African involvement in photometric research of aeronomic processes has been minimal.

1.2 Previous South African airglow and auroral research

South Africa's involvement in utilising photometers for airglow and auroral research first began at the time of the IQSY. Research efforts prior to the start of this thesis (1981) can be divided into three sections:

1/ airglow and auroral research in Antarctica,
2/ airborne airglow research - over the South Atlantic and in equatorial regions, and
3/ ground-based airglow research within South Africa.

1.2.1 South African airglow and auroral research in Antarctica

Stellenbosch University installed an airglow photometer in Antarctica during the fifth South African National Antarctic Expedition (SANAE 5) in 1964. The South African Antarctic base, also called Sanae, is positioned on the ice shelf of Dronning Maud Land and in 1964 had geographic coordinates of 70.30°S; 02.37°W (i.e.

L$\approx$4). The geomagnetist at Sanae, G.T. Robertson, ran a six-colour turret photometer, a 35mm all-sky camera (ASC) and various magnetometers. He was able to observe the airglow and aurora during the entire southern polar winter (late February through to early October). The standard two-colour method (Roach, 1963) was used to process the photometer data, yielding uncalibrated zenith airglow intensities at 427.8 nm (N_2^+ 1NG), 557.7 nm (OI) and 630.0 nm (OI). These data were uncorrected for atmospheric effects (i.e. absorption, scattering etc.), and were prone to contamination from nearby OH and O_2 emissions because of the large bandwidths of the interference filters used. Robertson (1966) has presented these uncalibrated data in an M.Sc. thesis. He recorded zenith starlight intensities under clear sky conditions on six magnetically quiet occasions, and has used these observations to derive a calibration factor for the 557.7 nm emission. This calibration factor has been given as a means of converting the uncalibrated tabulated intensities to absolute intensity values. No mention is made of calibration factors for other wavelengths, and Robertson in fact advocated using the same (557.7 nm) calibration factor at all wavelengths! In addition, a Tritium light source was used to assess the day-to-day variability in the relative sensitivity of the photometer, again apparently only at a single wavelength. The derived sensitivity factors varied from 0.50 to 1.31 during the year, presumably owing to a lack of temperature regulation of the filters and the photomultiplier tube (PMT), and to voltage changes on the PMT. One would expect, however, to find differing sensitivities for the various wavelength channels that are used, as their filter transmission characteristics would not vary with temperature in exactly the same way. It is thus apparent that Robertson's intensity data must be regarded as uncalibrated, and that even if used as relative data, long-term temporal variations in calculated intensities and intensity ratios could well be due to system-induced errors, rather than to variations in the actual intensities of the airglow or aurora. For what it is worth, Robertson has calculated a yearly mean for the emission intensities overhead at Sanae: 48 R at 427.8 nm, 406 R at 557.7 nm, and 118 R at 630.0 nm. These figures are for the combined airglow and aurora, i.e. no attempt was made to differentiate between the two.

Robertson also compared changes in photometric intensities with ASC, magnetic, riometer and ionospheric (sporadic E) observations and noted certain correlations - as would be expected during substorm activity. Mention of these will be made again in Chapter 6.

Torr and Torr (1969) have used Robertson's Sanae ($L=4$) data to show that twilight enhancements of the 630.0 nm emission occur beyond the latitude bounds ($1.1 < L < 3.2$) given by Bennett (1969). These enhancements, of the order of 50 R, occur at the time of conjugate sunrise.

Torr (1971), performing a further analysis using Robertson's data, found that during periods of magnetic activity ($\Sigma Kp > 12$) there were frequently large enhancements in the 630.0 nm emission in the vicinity of local midnight. It was found that these enhancements were usually accompanied by Es (sporadic E) and increases in the 30 MHz riometer absorption. Torr attributed the 630.0 nm enhancement to a low energy component (< 2 keV) of precipitating electrons, and the accompanying ionospheric blackouts to a higher energy component (> 10 kev). Furthermore, it was suggested that the these enhancements are due to the diurnal excursion of the auroral oval towards Sanae (60° invariant latitude). This is consistent with the auroral oval expanding more equatorward during increased magnetic activity.

The 1964 Sanae data were again utilised by Torr and Torr (1971) for an extensive analysis of the general behaviour of the OI emissions at 630.0 and 557.7 nm, as well as the N_2^+ 427.8 nm emission. They review results concerning twilight and midnight enhancements (mentioned above). In addition, it was concluded that apart from the enhancement of emissions in the vicinity of midnight, due to the diurnal equatorward excursion of the auroral oval, there is a prevailing precipitation of soft electrons (< 2 keV) which may be related to the proximity of Sanae to the southern radiation anomaly. This conclusion was drawn from the fact that the 630.0 nm intensities measured by Robertson at Sanae exceeded those measured by Eather (1969) at the same invariant latitude (60°) in the northern hemisphere. The validity of this conclusion is questionable if one recalls the doubts expressed above concerning the usage of Robertson's data as absolute intensity values. Similarly, the accuracy of absolute intensity and intensity ratio values quoted in this paper is debatable. Despite this, conclusions drawn from short-term variations in intensities and in intensity ratios should still be meaningful.

The six-filter turret photometer system installed at Sanae in 1964 was utilised until the end of 1969. In 1970 a new eight-filter turret photometer was installed and operated until the end of 1971. Data bulletins were published for 1967 to 1970 (Zeeman and Hamm, 1967; Zeeman *et al.*, 1968; Zeeman *et al.*, 1969b; Steyn *et al.*, 1973). These tabulate intensities of zenith emissions at 391.4, 427.8, 557.7 and 630.0 nm. The wavelengths of the background filters used in the two-colour data reduction method are not given. The data were calibrated using the premise that the sky continuum in the region of 530 nm has an average intensity of 18 R nm^{-1} (1.8 R $Å^{-1}$) - derived from Krassovsky *et al.* (1962). Adjustments were made for the day-to-day variation in photometer sensitivity (due to PMT temperature fluctuations). This was done by assuming average airglow emissions of 0 R at 391.4 and 427.8 nm, 250 R at 557.7 nm, and 125 R at 630.0 nm, during periods of no magnetic activity (i.e. implying no auroral contribution). Owing to temporal variations in continuum (Gadsden and Marovich (1973) have found considerable diurnal and seasonal variations) and airglow intensities, the accuracy of absolute intensity data derived in this way is highly doubtful. This is borne out by the fact that the tabulated data yields ratios between the (0,0) and (0,1) bands of the first negative N_2^+ system (I(391.4)/I(427.8)) that are highly variable. This is contrary to what is expected, namely a reasonably constant value in the vicinity of 3.28. This value is derived from the Einstein absolute transition probabilities, A, for this band system, obtained using Franck-Condon factors (Shemansky and Broadfoot, 1971). Furthermore, errors in the data might be compounded by contamination effects from other emissions at nearby wavelengths (due to the large filter bandwidths), and by the lack of correction for atmospheric effects.

In 1972 a meridian-scanning filter-wheel photometer (Hamm *et al.*, 1973) was installed at Sanae. This system, which was used until the end of 1975, allowed measurements at zenith angles ranging from 84°N to 84°S (58.1°S to 82.6°S geographic latitude) in 12 degree intervals along the meridian. Instrumentation problems in 1972 prevented the collection of any worthwhile data. Data bulletins of 391.4, 557.7 and 630.0 nm intensities have been published for 1973 and 1974 (de Kock *et al.*, 1975; Hamm *et al.*, 1975). No trace has been found of published data for 1975. The interference filters used in this system had considerably narrower bandwidths than those used in the previous system, thus reducing contamination effects. The two-colour data reduction method was again used to process the data. Calibration factors, obtained using a portable calibration source, were used to yield absolute emission intensities at 557.7 and 630.0 nm. With space for only five filters, no background filter was available for the processing of the 391.4 nm data so that the intensity values reported at this wavelength are not absolute. Corrections were supposedly made to the data for atmospheric extinction, scattering and the van Rhijn effect. No details are given of the exact process used, other than a reference to Ashburn (1954). Extinction coefficients and correction factors were tabulated for the various wavelengths and zenith angles. From the values quoted for the zenith it would appear that corrections have only been made for the extinction of the light originating in the photometer's field of view. The correction factors that are given do not seem to take into account scattered light originating outside of the photometer's field of view, or light reflected off the ground (snow, with albedo $\approx$ 0.8) and then backscattered into the photometer's line of sight (i.e. no account is taken of Ashburn's second and third correction terms).

In 1976 Rhodes University took over the existing airglow research programme at Sanae (Note: at about the same time the Hermanus Magnetic Observatory, who ran the magnetometer and ASC programmes at Sanae, installed a Hβ photometer system in order to study the proton aurora at Sanae). Three meridian-scanning tilting-filter photometers were installed to observe the N_2^+ 1NG band emission at 391.4 nm and the atomic oxygen (OI) emissions at 557.7 and 630.0 nm. This system is described in more detail in Section 3.4, as it was the one in operation at Sanae when this thesis was started. The airglow photometers were run by the ionospheric physicist at Sanae whose primary concern was the running of an ionosonde and the subsequent *in situ* reduction of the ionospheric data. Consequently, lack of time and manpower resulted in none of the tilting-filter system data being processed prior to the start of this thesis. The techniques subsequently developed for processing tilting-filter photometer data form an integral part of this thesis (see Chapter 4).

For completeness, it should be mentioned that besides the above-mentioned airglow photometry systems in operation at Sanae since 1976, additional optical observations of the aurora have been made with an all-sky camera (Hermanus Magnetic Observatory) and a low-light TV imaging system (Natal University).

1.2.2 South African airborne airglow research

A number of airborne airglow expeditions have been mounted from South Africa. Flights to the west and to the south have allowed research in the regions of the South Atlantic Anomaly (in the vicinity of Gough Island) and the Southern Anomaly (positioned to the north of Sanae), respectively. Flights to the northwest of South Africa have been used to investigate the airglow emissions in equatorial regions.

In 1964 and 1966 Stellenbosch University ran two photometers on board a Hercules C130 aircraft of the South African Air Force. This aircraft made a total of eight flights over the South Atlantic, all departing from Cape Town (geographic coordinates: 33.9°S; 18.4°E). The purpose of these flights was to investigate the spatial variation in intensity of certain airglow emissions, and to look for possible enhancement of some airglow intensities in the region of the anomalies. Airglow emissions were monitored at a number of wavelengths, namely 391.4, 418.0, 427.8, 557.7 and 630.0 nm in 1964; and 391.4, 418.0, 557.7, 624.0, 630.0 and 686.1 nm in 1966. Intensity data for these flights are tabulated in two data bulletins (Zeeman *et al.*, 1964, 1966). These bulletins include plots of the 391.4, 557.7 and 630.0 nm intensities versus time and aircraft position. No discernable N_2^+ emissions (diagnostic of particle precipitation) were observed, thus giving no support to Gledhill and van Rooyen's (1963) prediction of enhanced particle precipitation in the region of the South Atlantic Anomaly (SAA) (Robertson, 1966; van der Walt *et al.*, 1966; Gledhill, 1976). The aeronomic effects observed in the region of the SAA are treated in more detail in Chapter 7 of this thesis.

In August 1969 the University of Stellenbosch conducted airglow observations on a series of three flights flown along magnetic meridians. The first flew northwards from Walvis Bay (geographic coordinates: 23.0°S; 14.5°E) to the equator, the second was from Walvis Bay to Cape Town, and the third was southwards from Cape Town to a latitude of 54°S. These flights had the following objectives: the continuation of investigations of the latitudinal variation of airglow intensities and the intensity ratio I(630.0)/I(557.7); the determination of the height at which sodium atoms are excited locally; and the possible observation on the flight south from Cape Town of a 630.0 nm conjugate enhancement. Emission intensities at 557.7 nm, 589.3 nm (NaI), 630.0 nm and 686.1 nm (Meinel OH(7,2)) are tabulated in a data bulletin (Zeeman *et al.*, 1969a). Strong simultaneous enhancements in the atomic oxygen emissions at 557.7 and 630.0 nm were observed near the equator on Flight 1 (Steyn *et al.*, 1971a). The N_2^+ intensities (at 391.4 and 427.8 nm) recorded during the flights are not tabulated, although the data bulletin mentions enhancements in these emissions at the southernmost extent of the flight south (i.e at 54°S), coincident with a visible auroral band to the south.

The two-colour data reduction method was used to process the data collected on all of the airborne airglow expeditions mentioned above (1964, 1966 and 1969). Calibrations were based on the assumption that the continuum emission at 530.0 nm was 18 R nm^{-1}. No correction was made for atmospheric effects, although at an altitude of at least 8000 m these would be minimal for measurements made in the zenith. Owing to the somewhat doubtful calibration method used, the use of the published intensity values as absolute values would again be questionable.

As a result of the enhancements in OI emissions observed near the equator during the 1969 flights, a further airborne expedition was organised in July 1971. This was to continue the investigation into latitudinal variations in emission intensities, and to further the study of tropical airglow phenomena. An improved 5-filter photometer system was used to record the airglow on these flights. Narrowband interference filters (bandwidths of the order of 0.5 nm) were used to measure emissions at 391.4, 557.7 and 630.0 nm, with the additional two filters being used to monitor the background at wavelengths close to the OI wavelengths. The two-colour method was used to obtain background-corrected values for the 557.7 and 630.0 nm emission intensities. A portable light source was used to calibrate the photometer. This source was previously calibrated using a standard light source and a magnesium oxide screen (see Steyn, 1973). A data bulletin for the 1971 flights has been published (Steyn *et al.*, 1971b), containing absolute values of the 557.7 and 630.0 nm emission intensities, and relative values of the 391.4 nm intensities.

Further equatorial airglow data were collected using a special photometer mounted in a commercial aircraft of the South African Airways. This aircraft, a Boeing 707, regularly flew over the equator during August and September of 1971 and recorded OI emissions at 557.7 and 630.0 nm. Steyn (1973) has used all of the collected airborne equatorial data in a Ph.D. thesis that investigates the emission of airglow lines of atomic oxygen in equatorial regions. He finds two phenomena of interest: monochromatic enhancements of the 557.7 nm line, and the existence of structures displaying coincident "pulsations" in the 557.7 and 630.0 nm emissions. The first phenomenon occurs in two belt-like regions extending up to 30° invariant latitude in both hemispheres, but is absent at the geomagnetic equator. The second occurs in a wide invariant latitude range, from about 25°S to 25°N. Steyn describes two models that could explain tropical F-region nightglow enhancements. The airborne observations favour a vertical plasma drift model, without excluding the possible contribution of a model based on neutral atmospheric winds.

Whilst on the subject of airborne airglow observations, it should be mentioned that data collected in this way suffer from a spatial-temporal ambiguity. Variations in measured emission intensities could be due to temporal variations in intensity rather than to latitude/longitude (spatial) effects. This problem is also apparent with satellite and ship-borne observations, and is more pronounced when dealing with the normally more rapid variations of the aurora.

1.2.3 Ground-based photometry in South Africa

As far as the author is aware, the only recent (since 1960) ground-based photometry to have been performed within South Africa was at the site of the South African Astronomy Observatory at Sutherland (geographic coordinates: 32.4°S; 20.8°E). This observatory is well suited to both optical astronomy and airglow photometry because of its geographic remoteness, high altitude (approx. 1800 m) and favourable (arid) climatic conditions. Contamination of data due to man-made light, cloud-cover, dust and aerosols is minimal. Between 1973 and 1977 a meridian-scanning tilting-filter photometer was used to measure the OI emissions at 557.7 and 630.0 nm, and the NI emission at 520.0 nm. These airglow measurements were made under the auspices of the now defunct National Institute of Telecommunications Research (NITR). The little information that the author has been able to find about the Sutherland airglow recordings has been extracted from two papers in the literature (Torr *et al.*, 1976a; Burnside and Tepley, 1990). The photometer was operated on a north-south meridian and made observations at 75°S, 60°S, the zenith, 60°N and 75°N. Each meridian scan took 20 minutes to complete, owing to the long integration times needed to record the low intensity of the NI airglow. The photometer was highly stable, with the filter temperatures being controlled to within 0.5°C. Nevertheless, the photometer was calibrated every 90 minutes at all three wavelengths. A ^{14}C activated phosphor source was used for these calibrations. Its calibration is traceable to the National Bureau of Standards, Boulder, Colorado. In 1976 a recalibration of this source was performed by Torr *et al.* (1977), and showed the calibration to be reliable to within 10%. No mention is made of the data processing techniques used on the Sutherland data, nor is there any mention of atmospheric corrections having been applied to the data.

Torr *et al.* (1976a) have reported measurements of the Sutherland NI 520.0 nm emissions that were made coincident with overhead passes of the AE-C satellite in 1974. The NI emission intensity is very weak, typically 1 or 2 Rayleighs. Mention is made of the problem of contamination of the NI data by the nearby OH (9-2) emission at 518.7 nm. This might cause an over-estimation of the background correction and consequently the 520.0 nm values reported are the lower limits of the actual emission intensity. The ground-based intensity data were combined with satellite observations of neutral and ion densities, temperatures, and the shape of the 520.0 nm emission profile. This yielded values for the rate of quenching of $N(^2D)$ by atomic oxygen and for its production efficiency - values necessary for the understanding of the photochemical processes involving $N(^2D)$ in the F-region of the ionosphere.

Burnside and Tepley (1990) have compared OI emissions at 557.7 and 630.0 nm recorded at Sutherland between 1973 and 1977 with northern hemisphere intensities measured one solar cycle later with a Fabry-Perot interferometer (FPI) located at Arecibo, Puerto Rico (geographic coordinates: 18.3°N; 67.5°W). Average monthly zenith intensities are plotted against local time for both emissions and for both stations. In addition, plots are given for each wavelength of the ratios between the intensities measured to the north and south of each station (using either 60° or 75° zenith angles). The main findings of this analysis were: post-midnight enhancements of the 630.0 nm emission were found at both stations, and were most noticeable in the summer months; the 557.7 nm emissions at both stations peak at the equinoxes; the north/south intensity ratio of the 557.7 nm emission at Sutherland shows an annual variation, peaking in the southern winter. The close proximity in latitude of the Sutherland station to the South Atlantic Anomaly make the Sutherland data useful for comparisons with airglow data recorded in the region of the SAA.

1.3 The scope of this thesis

It is clear from the previous section that a considerable amount of raw photometric data has been collected by South African researchers at a number of places of interest. Some of these data have been processed to yield intensities at a number of wavelengths, mainly those due to emissions of atomic oxygen and molecular nitrogen. Unfortunately, in contrast, little actual aeronomic research has been done with the processed data. The data collection and calibration techniques that have been used in certain cases make the reliability of the resulting intensity data questionable. This is certainly the case with the Sanae data collected before 1972, and the airborne airglow data collected before 1971. Emission intensity data are only usable as absolute values if reliable data collection methods are used, the data are processed correctly (this includes making corrections for atmospheric effects), and the photometers are accurately calibrated at regular intervals with a stable light source of known intensity.

In 1981 the author took over the airglow research post at Rhodes University, having operated the Rhodes ionospheric and airglow programmes at Sanae in 1979. Previous incumbents of this position had concentrated on the development of photometric equipment. There was thus no expertise at Rhodes University in the field of airglow data reduction or calibration techniques when this thesis was commenced. In fact, South African involvement in airglow research at that time consisted solely of the two photometer systems recording data at Sanae (the Rhodes system, and the Hermanus Hβ system). Hermanus first started to use their Sanae Hβ data in 1980 when Lambert (1980) compiled an internal report on the correction of photometric observations for geometric and atmospheric effects. Lambert and Sutcliffe (1981) have reported on the photometric observations of proton aurora at Sanae. This was the first publication of results from either of the meridian-scanning, tilting-filter photometer systems at Sanae.

The author's portfolio as airglow research officer was threefold:

1/ to coordinate the Rhodes airglow programme running at Sanae,

2/ to complete the development of a digital airglow recording system to replace the analogue system that was currently in operation at Sanae, and

3/ to process and analyse some of the Sanae data.

The execution of this third function forms the bulk of this thesis, with a small mention being made of the digital system that was finally installed at Sanae in 1985. The aims of the thesis can be summarised as follows:

1/ To provide the aeronomic background necessary to conduct photometric investigation of the airglow and aurora.

2/ To develop processes which can be used for the accurate reduction of raw tilting-filter photometer data to meaningful absolute emission intensities. This means:

    i/ the derivation of an "airglow equation" which can be used to convert analogue chart deflections, or digital photon counts, to absolute emission intensities in Rayleighs, and

    ii/ the accurate determination of the filter characteristics, atmospheric correction factors, and absolute calibration factors to be used in the above-mentioned equation.

3/ To analyse some airglow and auroral intensity data that have been obtained using the data reduction techniques that have been developed.

4/ To comment on the usability and accuracy of the Rhodes photometric data and techniques, to recommend improvements, and to make suggestions for future photometric research.

The remaining chapters of this thesis can be summarised as follows:

Chapter 2 gives the aeronomic background necessary for this thesis. The phenomena of the airglow and the aurora are defined and discussed. Following this is a section on the chemical processes that lead to the airglow and auroral emissions that are relevant to this thesis. Finally the heights of airglow and auroral emissions are discussed. (Note: Additional aeronomic background to the processes of the aurora is provided in Appendix B. The inter-relationship between the solar wind, the magnetosphere and the ionosphere is described in terms of its relevance to the aurora. Mention is made of the auroral oval and its significance at Sanae. The phenomenon of the magnetospheric substorm is described, with particular reference to its optical signatures).

Chapter 3 deals with instrumentation. By way of introduction, brief mention is made of various optical methods used to observe the airglow and aurora. A tilting-filter photometer is described in terms of its various components and their functions. The characteristics of narrowband interference filters are discussed. A description is given of the analogue photometer system that was in operation at Sanae at the time that this thesis began. The need for an improved digital system is discussed. Functional details are given of the digital photometer system that was developed at Rhodes and installed at Sanae in 1985. Finally, descriptions are given of the two types of low-brightness calibration sources that have been used to calibrate the photometers used at Sanae and on the ISAAC cruise.

Chapter 4 concentrates on data reduction techniques. Equations are derived for converting either photon counts or chart recorder deflections to absolute emission intensities. These equations contain system variables such as filter transmission factors and absolute calibration factors, as well as atmospheric correction factors. The importance of these factors is mentioned as their accuracy directly influences the accuracy of the absolute emission intensities that are obtained. The effects that atmospheric extinction and scattered light have on observed emission intensities are discussed. A range of atmospheric correction factors can be obtained, depending on the extinction coefficients used and on the model used to estimate the contribution made by scattered light. The atmospheric correction factors that are used have a considerable influence on the values that are obtained for emission intensities and the ratios between these intensities. Other factors that influence the accuracy of airglow and auroral intensities are mentioned. These are: possible contamination by other emissions at nearby wavelengths; correction for the proton-induced components of auroral intensities; and correction for the airglow components of auroral intensities.

Chapter 5 describes the methods used to determine the filter transmission factors and the absolute calibration factors that are used in the data reduction equations derived in the previous chapter. The low-light sources used to calibrate the photometers at Sanae and on the ISAAC cruise have been cross-calibrated against two standard lamps. The procedure used for the cross-calibration is described, and the results obtained are compared with the original calibrations of these sources.

Chapter 6 looks at the photometric observation of the airglow and the aurora at Sanae in Antarctica. Methods of presenting the data are discussed, with particular reference to coordinate systems and magnetic-activity indices. It is shown that the best way to present auroral intensity data is in the form of contour plots of emission intensities versus time and invariant latitude. Prior to dealing with the aurora observed at Sanae, typical intensity values for the airglow are given. The main aeronomic research concern at Sanae was the study of the aurora. Consequently, in 1983 a series of workshops was convened amongst the South African upper atmosphere research groups active in Antarctic research to study their combined observations of magnetospheric substorms at Sanae (a sub-auroral station with invariant latitude $\approx 60°$, i.e $L \approx 4$). A substorm on the 27 July 1979 was selected for study. The photometric results of the study are presented in this chapter. These illustrate the need for increased sampling rates, both spatially and temporally. Various uses of auroral intensity ratios are described. Intensity ratios recorded at Sanae during the substorm are presented and compared with ratios obtained by other workers. The ratio of I(557.7) to I(391.4) at Sanae was found to be higher than expected. Possible reasons for this are given.

Chapter 7 looks at aeronomic effects in the region of the South Atlantic Anomaly. During the time of this thesis Rhodes airglow research interests were extended to the SAA with the mounting of Project ISAAC (International South Atlantic Anomaly Campaign). The geophysical significance of the SAA is described. It has been predicted (Torr *et al.*, 1975; Gledhill, 1976) that there should be enhanced particle precipitation in the region of the SAA, to the extent that the emission of the N_2^+ 1NG band at 391.4 nm should be discernable by ground- or sea-based methods. Previous observations made in the region of the SAA are reviewed. Airglow intensities recorded during Project Isaac are presented and discussed.

Chapter 8 is the concluding chapter of this thesis. It summarises the main results of the thesis. The shortcomings of photometric research are discussed, with particular mention being made of those experienced during this study. Recommendations are made as to ways in which the quality of the Rhodes University photometric data can be improved. The continued importance of ground-based photometric research in Antarctic is discussed. Suggestions are made for future South African involvement in photometric research.

CHAPTER 2

AERONOMIC BACKGROUND

2.1 Introduction

This chapter and Appendix B serve to provide the aeronomic background necessary for this thesis. The study of the processes that lead to airglow and auroral emissions is a huge field, consequently the descriptions are necessarily brief. Where possible, the reader is referred to the literature in order to obtain more comprehensive treatments of the subjects under discussion. General usage has been made of a number of texts which have become standards in the field i.e. Akasofu (1968, 1977), Chamberlain (1961), Omholt (1971), Rees (1989a), and Vallance Jones (1974). In addition, review articles have proved most useful in providing references to recent research developments. In particular, the U.S. quadrennial reports to the International Union of Geodesy and Geophysics (IUGG) have provided up-to-date news of both U.S. progress, and any important advances made by non-U.S. workers. Recent examples of these are the reviews for the period 1983-1986 by Gorney (1987), Killeen (1987), and Meier (1987). Reviews of Antarctic upper atmosphere optical research, of specific interest to this study, have been given by Akasofu (1978), Eather (1988), and Rees (1989b).

2.2 The airglow and the aurora

The terms 'airglow' and 'aurora' are both used to describe light that is emitted from an area of the earth's atmosphere loosely termed the 'upper atmosphere'. The earth's atmosphere can be divided altitude-wise into a number of different regions determined by temperature and by the relative ion and neutral densities, as shown in Figure 2.1. Boundaries between the layers are not clearly defined, and the processes that occur in each are to a certain extent coupled with those in adjacent regions. The term 'upper atmosphere' means different things to different people. For instance, a dictionary defines it as a meteorological term used to describe 'that part of the atmosphere above the troposphere'. In aeronomy it is usually taken to mean those regions of the atmosphere from the thermosphere upwards. Between the troposphere and the thermosphere, the stratosphere and mesosphere are taken to constitute the middle atmosphere; they have been the subject of much recent study under the Middle Atmosphere Program (MAP). There is a fair degree of overlap between middle and upper atmosphere research at the border of the two regions, a border usually taken as occurring at altitudes of between 90 and 100 km. The phenomena of airglow and aurora result from the excitation of atoms and molecules to higher energy levels. This occurs

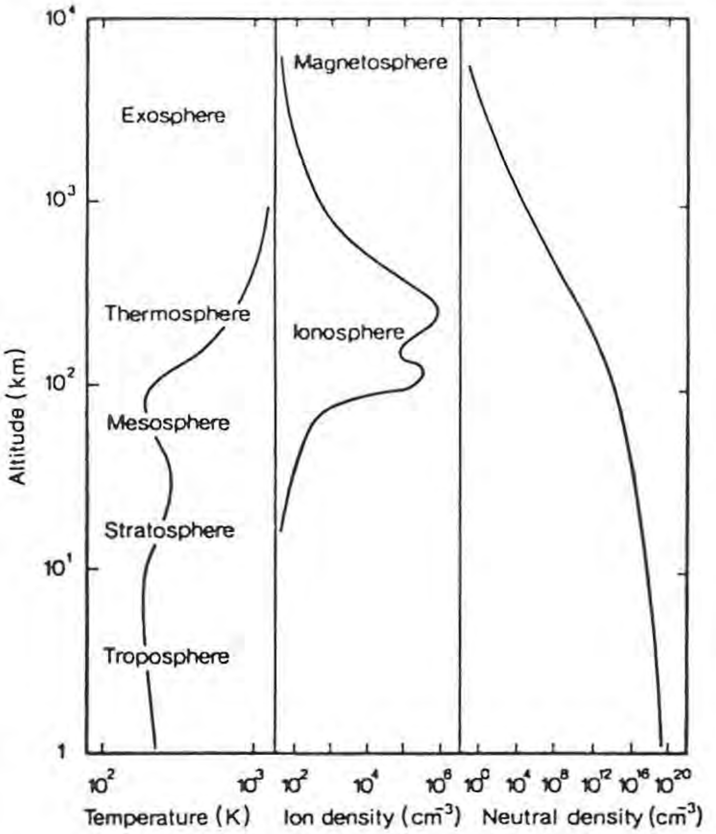

Figure 2.1 Schematic representation of the thermal structure, the ion density and the neutral density of the Earth's atmosphere (after Rees, 1989a).

mostly in the thermosphere, where solar ultraviolet photons are absorbed and energetic particles are stopped. In this region, where the ion density forms a sizeable portion of the (low) total particle density. Emissions do also occur at lower altitudes, in the mesosphere, where radiation is primarily thermal and occurs mostly in infra-red molecular bands (Rees, 1989a). Above the thermosphere, the major particle constituents are hydrogen and helium. Light radiation there takes the form of the geocorona which is caused by the resonant scattering and fluorescence of solar photons (Rees, 1989a).

Airglow and auroral emissions occur when excited atoms or molecules return to their original energy states, giving off the excess energy in the form of light. This normally takes place in a single step, but can be by cascading. The energies of the photons of light that are released are given in terms of the frequency of the emitted light by the well-known equation $E = h\nu$, where h is Planck's Constant. Consequently, the wavelength of the emitted light (given by $\lambda = c\ \nu^{-1}$, where c is the speed of light in free space) characterizes the transition that has taken place. Emissions occur across a wide range of wavelengths, from the ultra-violet (UV) through the visible part of the spectrum to the infra-red (IR). While spectral emissions at visible and near IR wavelengths can be detected on the ground, UV and IR radiation cannot be detected by ground-based observations because of almost total absorption by the atmosphere at these wavelengths (i.e. the atmospheric extinction coefficients ≈ 1). Typical airglow and auroral spectra can be found in Chamberlain (1961), Vallance Jones (1974), Chamberlain and Hunten (1987), and Rees (1989a).

Spectroscopic observation of upper atmosphere emissions can be used to determine the chemical constituents of the region, and the physical processes that occur within it. The intensities of certain auroral emissions, and the ratios between these intensities, can be used to determine the characteristic energy and energy flux of the precipitating electrons that were responsible for the emissions (cf. Rees and Luckey, 1974; Rees *et al.*, 1988). Further examples of the utilization of spectroscopic observations are given in Chapter 3, which includes a section on the different optical instruments used for observation of the airglow and aurora, and their diverse applications.

In the absence of moonlight the airglow and aurora form the major portion of the light emanating from the night sky. Other contributions come from starlight, diffuse galactic light due to unresolved stars, and zodiacal light (sunlight scattered by interplanetary particles). Airglow and aurora also occur in the daytime, when they are swamped, at visible wavelengths, by the scattering of sunlight in the lower atmosphere. Airglow is distinguished from aurora by a number of criteria such as location, occurrence and cause.

Airglow is a global phenomenon that occurs continuously as dayglow, twilight-glow, or nightglow. Being extremely weak and structureless, it is generally subvisual. Airglow is caused by photo-chemical reactions, i.e. by the interaction of normal atmospheric constituents with one another and with sunlight.

In contrast, auroras are normally confined to high geomagnetic latitudes, and are irregular in form and occurrence. They are generally more intense, and are usually visible to the naked eye. Auroras are mainly caused by the precipitation of charged particles into the upper atmosphere. These charged particles, mostly energetic electrons and protons, impact on atmospheric species such as N, N_2, N_2^+, O, O_2, H and OH, directly or indirectly causing excitation. Subsequent radiation is in the form of spectral lines and bands.

Although these descriptions differentiate between the two phenomena, it should be noted both that they contain generalisations, and that exceptions do exist. For example, auroras do not only occur at high latitudes. Mid-latitude auroras, known as Stable Auroral Red (SAR) arcs or M-arcs, occur at geomagnetic latitudes between 41° and 60°. Characteristics of SAR arcs are given by Roach and Smith (1967). The magnetic latitude and height distributions of upper atmosphere emissions are illustrated in Figure 2.2. Emission heights are discussed in more detail at the end of this chapter (see Section 2.4).

It has been mentioned above that airglow is the weak, structureless emission of light that occurs continuously worldwide. Nevertheless, it does display both spatial and temporal variations. Its latitude dependence and diurnal, seasonal and sunspot-cycle variations have been studied extensively (cf. Roach and Smith, 1967; Smith and Steiger, 1968; Silverman, 1970; Fukuyama, 1977; Forsyth and Wraight, 1987). In contrast to the relatively gradual and small-scale variations of the airglow, the spatial and temporal intensity variations shown by the aurora are often far more extreme and dramatic. This is due to the origins of the precipitating

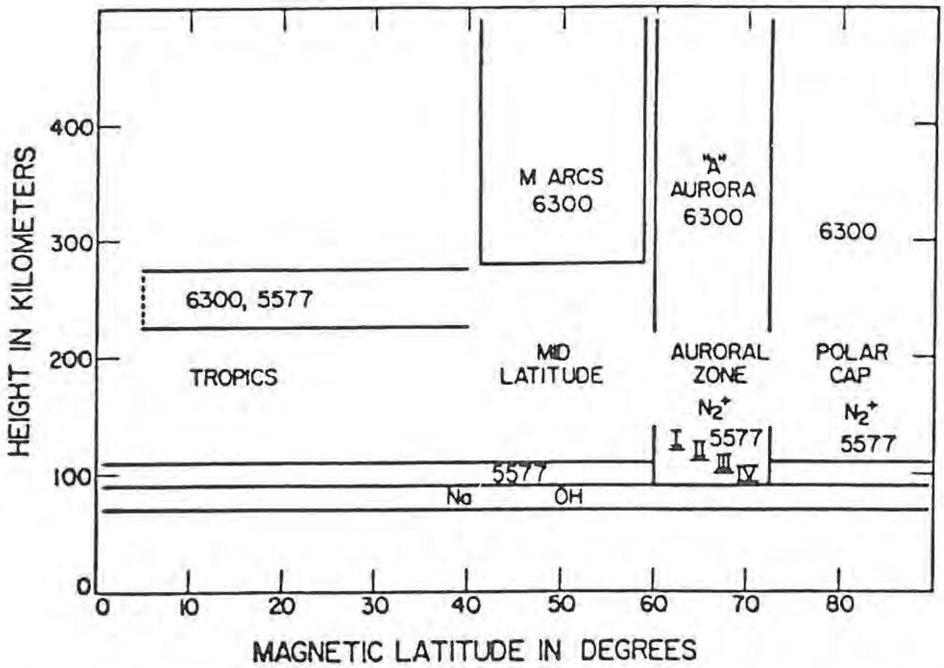

Figure 2.2 Schematic representation of upper atmosphere emissions as a function of height and geomagnetic latitude (after Roach and Smith, 1967).

particles that cause the aurora, which can be traced back to the Sun and the solar wind.

For completeness, details of the interaction between the solar wind, the magnetosphere and the ionosphere, which results in the particle precipitation mentioned above, are given in Appendix B (see Section B.1). Also included in this Appendix are discussions of the auroral oval and auroral morphology (Section B.2), and an outline of the geophysical processes that occur during a magnetospheric substorm (Section B.3).

2.3 Spectroscopic emission lines relevant to this thesis

The airglow and the aurora both consist of large numbers of spectroscopic emissions as shown by the spectra referred to in section 2.2. Atomic emissions cause spectral lines, whereas molecular emissions cause spectral bands. Certain lines and bands have wavelength and brightness characteristics which lend themselves to photometric observation. Furthermore, certain emissions can be used to determine other aeronomic parameters, such as the densities of atmospheric species, thermospheric temperatures and wind velocities, and the energies and fluxes of precipitating particles. Among the most often observed spectroscopic emissions are those of atomic oxygen (OI) at 557.7 and 630.0 nm, and the bands of the N_2^+ First-Negative (1NG) system with bandheads at 391.4 and 427.8 nm. The Rhodes University airglow photometer systems are used to observe emissions at 391.4, 557.7 and 630.0 nm. In addition, the hydrogen Balmer β emission at 486.1 nm is of interest during auroral observations, as it can be used to correct for the proton-induced component of the aurora when studying the electron aurora.

This section describes the energy level transitions that result in the emissions of interest. In addition, their various excitation mechanisms are described. After decades of intensive research into the processes that lead to the atomic oxygen emissions, there is still some uncertainty as to which excitation mechanisms dominate during auroral activity. Photometric observations play an important role in this field of research, as the observed column emission intensities can be used to check the validity of models that incorporate the various excitation mechanisms. It is not within the scope of this thesis to explore too deeply the debate as to which excitation mechanisms are responsible for the various airglow and auroral emissions. Where doubt still exists, known excitation mechanisms are listed and some indication is given as to which of these are currently thought to be the dominant contributors.

2.3.1 The First Negative Nitrogen system

The N_2^+ First-Negative (1NG) band system is excited by electron impact ionization:

$$N_2\ (X^3\Sigma_g^+) + e \rightarrow N_2^+\ (B^2\Sigma_u^+) + 2e \tag{2,1}$$

followed by radiative decay,

$$N_2^+\ (B^2\Sigma_u^+)(\nu') \rightarrow N_2^+\ (X^2\Sigma_g^+)(\nu'') + h\nu \tag{2,2}$$

The light emitted consists of a number of bands which correspond to the different vibrational levels attainable by ionized nitrogen molecules. The relative populations of these levels, and hence the relative band strengths, follow the Einstein transition probability coefficients, A, which are proportional to the Franck-Condon factors. The strongest emissions of the 1NG system occur with $\nu' = 0$, and $\nu'' = 0$, 1 and 2, producing bands at 391.4, 427.8, and 470.9 nm respectively. Figure 2.3 shows the potential energy curve for N_2^+, and it can be seen from this that the threshold energy for ionization of N_2 to the N_2^+ ($B^2\Sigma_u^+$) state is about 19 eV. This precludes any excitation from being caused by chemical processes, although photo-ionization is responsible for 1NG emissions occurring in the dayglow. Thus, in the absence of sunlight, 1NG emissions are diagnostic of particle precipitation, and hence of auroral activity. The majority of the emissions are caused by precipitating electrons, with a small percentage being caused by heavy particle collisional ionization, i.e. protons and fast oxygen atoms (Rees *et al.*, 1988).

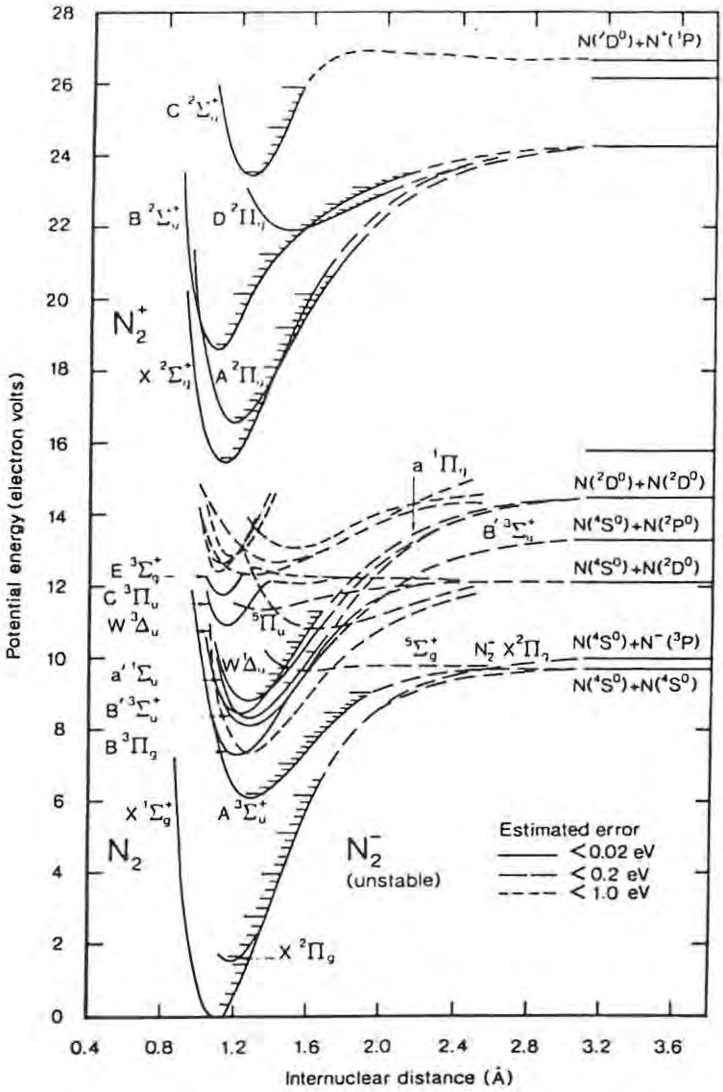

Figure 2.3 Potential energy curves for N_2^+, and other states of molecular nitrogen (After Rees, 1989a).

2.3.2 The atomic oxygen emission at 557.7 nm

The best known airglow and auroral emission is perhaps the so-called 'auroral green line' of atomic oxygen at 557.7 nm which results from the transition O(^{1}D-^{1}S). Unlike the N_2^+ 1NG system, this line, and the 'red doublet' at 630.0 and 636.4 nm due to O(^{3}P-^{1}D), have relatively low excitation thresholds (4.12 and 1.97 eV respectively). This is because they originate from the ground state configuration of atomic oxygen (OI), and result in 'forbidden transitions' (see Figure 2.4). The low excitation thresholds mean that atomic oxygen can be excited by several chemical reactions in addition to excitation by electron impact. Emissions at 557.7 nm can be divided into three categories (Torr and Torr, 1982): lower altitude airglow emissions at E-region heights (90-110 km), higher altitude airglow emissions at F-region heights (250-300 km), and auroral emissions. Each group has different excitation mechanisms.

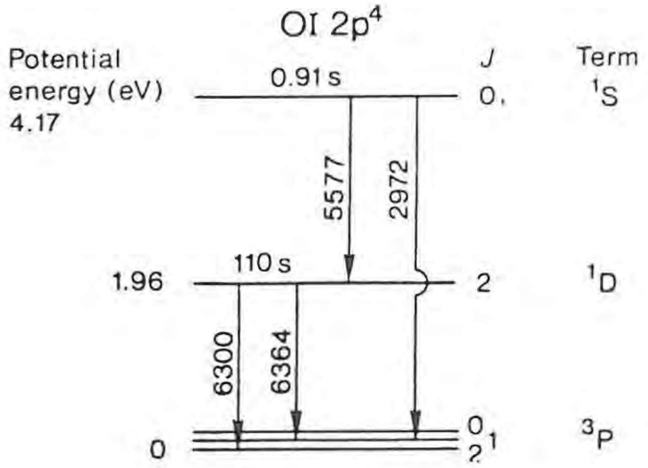

Figure 2.4 Partial energy diagram for atomic oxygen, showing states in the ground configuration of the atom (After Rees, 1989a).

2.3.2.1 Lower altitude O(^{1}S) airglow emissions

Lower altitude 557.7 nm emissions occur in the E-region of the ionosphere at altitudes mostly in the range 95-100 km. For many years the single-step three-body reaction

$$O(^3P) + O(^3P) + O(^3P) \rightarrow O(^1S) + O_2 \tag{2,3}$$

known as the Chapman mechanism was believed to be the source of O(^{1}S) atoms responsible for the 557.7 nm emission in the nightglow. Laboratory data of Barth and Hildebrandt (1961) led Barth (1961, 1964) to formulate a two-step mechanism,

$$O(^3P) + O(^3P) + M \rightarrow O_2^* + M \tag{2,4}$$

where M is an atmospheric species and * denotes an excited species, followed by

$$O_2^* + O(^3P) \rightarrow O_2 + O(^1S) \tag{2,5}$$

which is now known as the Barth mechanism. Although this mechanism is now widely accepted as being the correct one, uncertainty still seems to exist as to the identity of the O_2^* precursor (McDade and Llewellyn, 1986; McDade *et al.*, 1986). Possible states of the molecular oxygen are $A^3\Sigma_u^+$, $c^1\Sigma_u^-$, and $A'^3\Delta_u$ (previously known as $C^3\Delta_u$). Chamberlain and Hunten (1987) give evidence for the precursor being $c^1\Sigma_u^-$, while laboratory studies (Stott and Thrush, 1989) support $A^3\Sigma_u^+$ as the main precursor state.

2.3.2.2 Higher altitude O(^{1}S) airglow emissions

The presence of a higher altitude component of the O(^{1}S) nightglow was first discovered by Wallace and McElroy (1966) as a result of rocket measurements at F-region heights. Ranade *et al.* (1988) have found the intensity of this 557.7 nm emission in the F-region to be about a quarter of the intensity of the O(^{1}D) emission at 630.0 nm. Correction for this F-layer component needs to be made when using ground-based photometric observations to study emissions from the E-region. The major source of the 557.7 nm emission at F-region heights would appear to be dissociative recombination,

$$O_2^+ + e \rightarrow O_2^* \rightarrow O(^1S) + O(^1D) \qquad (2,6)$$

where $O_2^* = O_2(^1\Sigma_u^+)$ i.e. the repulsive state of the neutral molecule (Killeen and Hays, 1983). Zipf (1988) has found a discrepancy between observed intensities and intensities given by a dissociative recombination model, thus there might be the need of an additional process to fully explain the F-region emissions. Torr and Torr (1982) mention other processes that might contribute.

2.3.2.3 Auroral O(^{1}S) emissions

A number of processes are capable of producing the O(^{1}S) atoms that are responsible for the auroral 557.7 nm emissions. These mechanisms have been the subject of intensive and widespread study for the last two decades. At times the issue of their relative importance has been controversial (cf. Rees, 1984a; McDade and Llewellyn, 1984; Rees, 1984b). The following excitation mechanisms have been identified as sources of auroral O(^{1}S):

Electron impact:

$$O(^3P) + e^* \rightarrow O(^1S) + e^{(*)} \qquad (2,7)$$

Dissociative recombination (Donahue *et al.*, 1968):

$$O_2^+ + e \rightarrow O(^1S) + O \qquad (2,8)$$

Energy transfer from excited molecular nitrogen (Parkinson and Zipf, 1970):

$$N_2(A^3\Sigma_u^+) + O(^3P) \rightarrow N_2(X^1\Sigma_g^+) + O(^1S) \qquad (2,9)$$

Electron impact dissociation of O_2:

$$O_2(X^3\Sigma_g^+) + e^* \rightarrow O(^3P) + O(^1S) + e^{(*)} \qquad (2,10)$$

Ion-atom interchange involving nitrogen ions (Rees, 1984a):

$$N^+ + O_2 \rightarrow NO^+ + O(^1S) \qquad (2,11)$$

Ion-atom interchange involving nitrogen atoms:

$$O_2^+ + N \rightarrow NO^+ + O(^1S) \qquad (2,12)$$

Energy transfer from excited oxygen molecules (Solheim and Llewellyn, 1979):

$$O_2^* + O(^3P) \rightarrow O_2 + O(^1S) \qquad (2,13)$$

Recent publications (Gerdjikova and Shepherd, 1987; Srivastava and Singh (1988); Paulson *et al.*, 1990; Steele and McEwen, 1990) all favour excitation by N_2^* energy transfer (Equation 2.9) as the dominant mechanism. Electron impact (Equation 2.7) and dissociative recombination (Equation 2.8) seem to be the next biggest contributors, with other mechanisms usually only playing very minor roles. Rees (1984b) has pointed out that the relative importance of the different mechanisms probably depends on the characteristics of the auroral energetic particle precipitation. Although direct electron impact makes only a small contribution, electron precipitation contributes indirectly to most processes, being the cause of the excited or ionized states involved in these reactions.

2.3.3 The atomic oxygen emission at 630.0 nm

The red doublet at 630.0 and 636.4 nm is produced by the forbidden transition $O(^3P-^1D)$. The lower wavelength emission is brighter than the higher wavelength one by a factor of three, and is the one preferred for photometric research. The $O(^1D)$ state is only 1.97 eV above the atom's ground state and consequently can be excited by a variety of inelastic collisions. However, being highly metastable with a radiative lifetime of 110 s, it suffers severe collisional deactivation (quenching) in the denser atmosphere below the F-region.

2.3.3.1 O(^{1}D) airglow emissions

The nighttime airglow emission at 630.0 nm results primarily from dissociative recombination of molecular oxygen ions in the F-region:

$$O_2^+ + e \rightarrow O(^3P) + O(^1D) \tag{2,14}$$

This process also produces atoms in the O(^{1}S) state (see Equation 2.6 in Section 2.3.2.2) which then form a small source of O(^{1}D) by cascading,

$$O(^1S) \rightarrow O(^1D) + h\nu(557.7\text{nm}) \tag{2,15}$$

Not all of the generated O(^{1}D) atoms produce emissions, as considerable quenching by O_2 and N_2 molecules takes place, especially at lower altitudes.

2.3.3.2 O(^{1}D) auroral emissions

As was the case with the O(^{1}S) auroral emissions, the relative importance of the various mechanisms for auroral O(^{1}D) excitation has not been fully resolved. In addition to dissociative recombination (Equation 2.14) and cascading from O(^{1}S) (Equation 2.15), there are a number of other processes that yield F-region oxygen atoms in the O(^{1}D) state (cf. Rees and Roble, 1986; Solomon *et al.*, 1988):

Electron impact by energetic auroral electrons (low energy secondaries as well as primaries):

$$O(^3P) + e^* \rightarrow O(^1D) + e^{(*)} \tag{2,16}$$

Electron impact by thermal electrons:

$$O(^3P) + e_t \rightarrow O(^1D) + e \tag{2,17}$$

Atom interchange (Rusch *et al.*, 1978):

$$N(^2D) + O_2 \rightarrow NO + O(^1D) \tag{2,18}$$

Electron impact dissociation of O_2:

$$O_2 + e^* \rightarrow O(^3P) + O(^1D) + e^{(*)} \tag{2,19}$$

Ion-atom interchange involving nitrogen ions (Langford *et al.*, 1985):

$$N^+ + O_2 \rightarrow NO^+ + O(^1D) \qquad (2,20)$$

Energy transfer from excited nitrogen atoms (Zipf *et al.*, 1980):

$$N(^2P) + O(^3P) \rightarrow N(^4S) + O(^1D) \qquad (2,21)$$

Energy transfer from excited atomic oxygen ions (Mahadevan and Roach, 1968):

$$O^+(^2D) + O(^3P) \rightarrow O^+(^4S) + O(^1D) \qquad (2,22)$$

It would appear that the major sources of $O(^1D)$ atoms in auroras are one or more of: dissociative recombination (Equation 2.14), energetic electron impact (Equation 2.16), and the reaction of $N(^2D)$ with O_2 (Equation 2.20). Mende *et al.* (1984) list all three processes as major sources, Rees and Roble (1986) advocate the reaction of $N(^2D)$ with O_2 as the only major source, and Solomon *et al.* (1988) favour dissociative recombination and electron impact as major sources (dismissing the ion-atom interchange as a minor source). The only thing that seems to be certain is that, barring these three processes, all of the others listed above appear to make only minimal contributions.

2.3.4 The hydrogen emissions of the proton aurora

Wherever there is electron precipitation there must be proton precipitation in order to maintain charge neutrality, at least on a large scale (Deehr *et al.*, 1981). Although the number fluxes are the same, this is not usually the case with the total energy fluxes of the electron and proton precipitations. Energy deposition by electrons is normally much larger than that by protons, with comparable contributions from the two species only occurring on rare occasions (Rees, 1981). When the precipitating protons reach the atmosphere, a number of collisional processes occur which often lead to auroral emissions (cf. Eather, 1967; Rees, 1981, 1982, 1983, 1989a, 1989b; Vallance Jones, 1974) . Firstly, protons are converted to hydrogen atoms by charge exchange,

$$H^+ + M \rightarrow H^{(*)} + M^{+(*)} \qquad (2,23)$$

where M and M^+ represent any neutral and ionized atmospheric atoms and molecules (e.g. N_2, $N_2{}^+$, O, O^+, etc.), and H can be in a ground state or excited (n = 2,3,4..) state. The excited H atoms return to the ground state by emission of the hydrogen spectrum (Ly_α, H_α, H_β, etc.). The ground state H atoms retain much of the proton energy and are hence a source of collisional excitation,

$$H + M \rightarrow H^{*}(n = 2,3,4...) + M^{(*)} \qquad (2,24)$$

This alternative source of excited H atoms also results in emissions. In addition, the energetic H atoms may cause stripping (which converts H atoms back to protons, thus maintaining a charge equilibrated H^+/H flux),

$$H + M \rightarrow H^{+} + M^{(*)} + e^{*} \qquad (2,25)$$

and ionization,

$$H + M \rightarrow H^{(+)} + M^{+(*)} + (2)e^{*} \qquad (2,26)$$

Both of these reactions are a source of secondary electrons which have energies in excess of the thermal energy of ambient electrons. In turn, these secondary electrons are capable of producing ionization,

$$\begin{aligned} &e^{*} + M \rightarrow e + M^{+(*)} + e \\ \text{e.g.}\quad &e^{*} + N_2 \rightarrow N_2^{+}(B^2\Sigma_u^+) + 2e \end{aligned} \qquad (2,27)$$

and excitation,

$$\begin{aligned} &e^{*} + M \rightarrow e + M^{*} \\ \text{e.g.}\quad &e^{*} + O(^3P) \rightarrow e + O(^1D,^1S) \end{aligned} \qquad (2,28)$$

The examples given with these processes result in the proton-induced components of the auroral 391.4, 557.7 and 630.0 nm emissions. At times the proton-induced components can constitute a significant percentage of the total auroral emission intensities. Consequently, it is necessary to correct for them when investigating only the components of the aurora due to precipitating electrons.

2.4 Emission heights of the airglow and aurora

The heights at which airglow and auroral emissions occur influences photometric measurements of intensities in two ways: Firstly, with a meridian-scanning photometer, the emission heights influence the horizontal extent of the region scanned by the photometer. If the photometer is aligned to scan along a magnetic meridian then the greater the emission height, the greater the range of magnetic latitudes that are observed by the photometer (see e.g. Figure 6.3). Secondly, emission heights influence the determination of atmospheric correction factors (cf. Ashburn, 1954), and, for non-zenith measurements, the van Rhijn factors which are used to correct for the increase in the effective thickness of the emitting layer (and hence increase in intensity) as the zenith angle of the observations increases (see Section 4.3).

In general, emissions of the First-Negative band (391.4, 427.8 nm etc.), hydrogen emissions (e.g. H_β at 486.1 nm), and the major portion of the $O(^1S)$ 557.7 nm emissions occur at E-region heights (90-110 km). The 630.0 nm emission of $O(^1D)$ and a small component of the $O(^1S)$ emission occur at F-region heights (250-300 km). However, rocket measurements have yielded height profiles of emission intensities which show that both the height of the peak emission, and the halfwidth of the emitting layer are very variable. Auroral emission heights depend, to a large extent, on the initial energy of the precipitating particles. The higher the energy of the precipitating particles, the lower they penetrate into the atmosphere, and the lower the height of the peak emission. Figure 2.5 and Table 2.1 show the variability in emission heights that the author has seen reported in the literature.

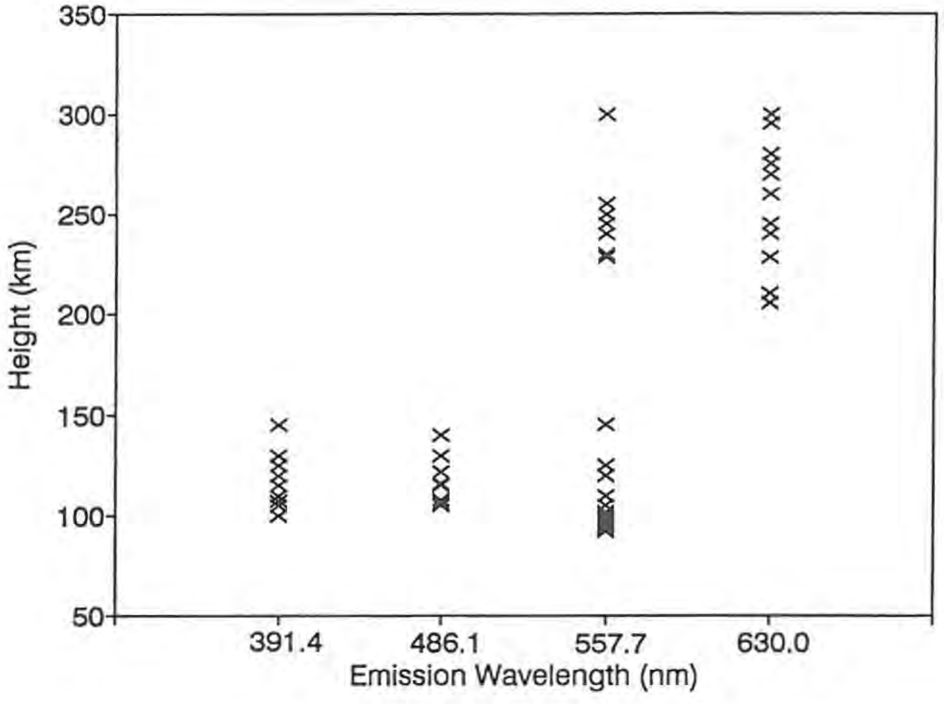

Figure 2.5 The distribution in the emission heights determined by various researchers for N_2^+ 1NG (391.4 and 427.8 nm), H_β 486.1 nm, $O(^1S)$ 557.7 nm, and $O(^1D)$ 630.0 nm emissions.

Table 2.1 Heights of airglow and auroral emissions.

Wavelength (nm) and source	Height (km)				
	Maximum value	Upper Quartile	Median	Lower Quartile	Minimum Value
391.4 / 427.8 N_2^+ 1NG	145	122	115	102	100
486.1 H_β	140	130	115	106	105
557.7 $O(^1S)$ (E-region)	145	100	97	95	88
557.7 $O(^1S)$ (F-region)	300	252	245	235	228
630.0 $O(^1D)$	300	277	275	242	205

Photometric observations can be used in a number of ways to determine the (instantaneous) heights of emission layers:

1/ Triangulation.

This requires the usage of meridian- or almucantar-scanning photometers at two or more separate locations capable of observing the same area of the sky. The zenith angles of discrete features that can be uniquely recognised simultaneously at two or more sites, can be used to determine the heights of the emissions, given that the distance between the sites is known. This technique has been used and discussed by Romick and Belon (1964, 1967). Gattinger *et al.* (1985) have determined emission heights using triangulation methods with low-light TV observations. Owing to the need for features with limited spatial extent, the triangulation method is only applicable to auroral emissions, and even then the method does not appear to be very accurate.

2/ Van Rhijn method.

Owing to the fact that triangulation cannot be used to determine the heights of unstructured airglow emissions, Roach and Meinel (1955) investigated the van Rhijn method as a means of determining these heights. The method uses the fact that photometric observations of a uniform emitting layer yield apparent intensities that increase with increasing zenith angle, due to the van Rhijn effect. Assuming the emissions to be uniform and at a constant height, one can work backwards via the van Rhijn function (given in Section 4.3) to obtain the height of the emitting layer. Non-uniform emissions and heights, as well as complications due to atmospheric extinction, make the method inaccurate. Roach and Meinel state that this method is not valid for individual meridian scans, and can only be used to get average height values over a long period of time.

3/ Rocket measurements.

The advent of rocket-borne photometry improved the accuracy of height determinations. Photometers mounted horizontally in rockets are capable of producing height profiles of emission intensities on both the upward and downward legs of the rocket's flight. This type of measurement yields peak emission heights to an accuracy of 1 or 2 km. Its major drawback is that it yields only instantaneous values for the emission heights.

4/ Satellite measurements.

Satellite-borne photometers have also been used to determine the heights of emission layers. Solomon *et al.* (1984) have developed a tomographic inversion algorithm which can be used to obtain volume emission rate profiles from satellite photometer data. While possibly not as accurate as height determinations by rocket-borne measurements, it does have the advantage of being capable of yielding height values on more than just two occasions! Heights determined when the satellite is passing overhead of ground-based observatories might be very useful during periods of coordinated research.

5/ Emission intensity ratios.

Eather *et al.* (1976) have used the intensity ratio I(630.0)/I(427.8) in order to get an estimate of emission heights. They use the fact that the observed ratio is a function of the energy spectrum of the precipitating particles. This energy determines the extent to which the particles penetrate the atmosphere, and hence the heights of the peak emissions. A table of ratios and heights give ratios from < 0.02 to > 35, with a corresponding height range between < 110 km and 280-360 km. They consider this method to be preferable to assuming the usual arbitrary emission height of 110 km.

It is clear that emission height values are essential to the accurate processing of ground-based photometric data. But, it is difficult to determine these heights with any degree of accuracy if one is only using a single set of ground-based (or ship-borne) photometers .

CHAPTER 3

INSTRUMENTATION

3.1 Introduction

A large variety of optical instruments and techniques are used to observe the structure and dynamics of the upper atmosphere. Optical measurements of airglow and auroral emissions can provide a wealth of information concerning, *inter alia*, the chemical and thermal composition of the upper atmosphere, its spatial and temporal variations, the winds that occur within the region and the flux and energy characteristics of the precipitating particles that cause the aurora. Different instruments have been developed for a diversity of applications. Prior to the IGY, optical observations were restricted to a few relatively elementary ground-based techniques. Since then the scope, sensitivity and accuracy of the instruments used have greatly improved. Aircraft, rockets and satellites have provided alternative platforms from which to observe spectral emissions, and their use has enabled the observable portion of the spectrum to be expanded to include UV and IR emissions. The advent of more sophisticated electronics and computer equipment has also contributed significantly to the development and improvement of useful optical techniques.

This thesis is concerned with the use of tilting-filter photometry as a tool to study the airglow and aurora. Before discussing the tilting-filter photometer in more detail, and describing the analogue and digital systems that have been used, a resumé is given of some of the more important types of optical instruments and techniques that have been utilized for upper atmosphere research.

3.2 Optical techniques for observing airglow and aurora

This section is intended to give a broad overview of optical techniques that have been used in airglow and auroral studies. Descriptions are necessarily brief, and the reader is referred to the literature for more details. A recent general text which provides a good description of many of the optical methods used to observe the aurora, is that of Vallance Jones (1974). Information on newer techniques seems to be confined to journal papers, which usually concentrate on specific instrumentation and techniques.

Optical instrumentation can be divided into a number of broad categories, according to the types of instruments used, or their functions.

3.2.1 Imaging systems

A number of optical systems use cameras to record photographic images of the aurora on film or video tape. The oldest, and possibly most often-used, technique is that of all-sky camera (ASC) photography. This uses a very wide-angle lens with a low f-stop to record images of the aurora on fast 16 or 35 mm film. If a fish-eye lens is used, the resultant image covers a field of view of nearly 180°. ASC data have been used extensively to study the morphology of the auroral ovals and auroral substorms (cf. Akasofu, 1964, 1968; Thuillier *et al.*, 1986). More recently, these studies have been supplemented by the analysis of photographic images taken by satellites (e.g. Akasofu, 1974, 1975a, 1975b, 1976; Pike and Whalen, 1974). Polar orbiting satellites, such as DMSP, have increased the field of view of auroral imaging systems by virtue of their greater distance from the aurora. Any loss in resolution is more than compensated for by the provision of a more global view of the auroras and the auroral oval. One disadvantage of satellite imagery is that it only provides instantaneous 'snapshots' of the aurora. To partially remedy this, some studies have combined the use of ASC photography and satellite images (cf. Akasofu, 1974; Nagata *et al.*, 1976). Recent satellite imagery, i.e. such as was produced by the Ultraviolet Imager (UVI) on the Viking satellite (Anger *et al.*, 1987a), has cut imaging times down to as little as 20 seconds with a spatial resolution of 20-30 km (Anger *et al.*, 1987b). With an apogee of over 2 R_e the Viking satellite is able to keep the polar region in view for extended periods of time (of the order of an hour), thus allowing the continuous study of short duration substorms etc. Satellite imagery data can be combined well with ground-based observations e.g. Viking UV images can be compared with data from the CANOPUS array of meridian-scanning photometers (Vallance Jones *et al.*, 1987a).

Another imaging technique is the use of television systems for auroral cinematography (cf. Davis, 1966, 1969; Scourfield and Parsons, 1969, 1971). These systems provide better spatial and temporal resolution than ASC systems. In fact, they can be utilized for real-time monitoring of the development of auroras, and for the study of rapidly varying forms such as pulsating auroras (cf. Scourfield, 1970; Vallance Jones *et al.*, 1980; Vallance Jones and Gattinger, 1981). Multi-channel TV systems that incorporate interference filters can be used to monitor the relative morphologies of different emissions and the associated particle precipitation patterns (see e.g. Mende and Eather, 1976). There is South African interest in the TV imaging of auroras in Antarctica. The Natal University Space Research Group has developed an advanced low-light television system which utilizes an intensified-silicon intensifier-target (ISIT) camera tube. This system allows them to record the temporal and spatial variations of sub-visual auroras (Tibbenham *et al.*, 1984). Their system has been further enhanced by the addition of digital image processing techniques (Clarke, 1985; Comfort, 1986).

3.2.2 Spectroscopic systems

A variety of spectroscopic instruments and techniques have been used to provide spectral information about the airglow and aurora. Possibly the first was the grating spectrograph, which yielded medium resolution spectra of atmospheric emissions, on photographic paper. Subsequently, an instrument called the patrol spectrograph was developed. It allowed for meridian observations of emission spectra at lower resolutions: Intensity variations along the spectral lines correspond to variations in emission intensities along the observed meridian, normally magnetic N-S (see e.g. Sandford 1961, 1964; Wiens and Vallance Jones, 1969). This device was largely superseded in the late sixties by photoelectric systems, such as the meridian-scanning photometer. More recently, Mende *et al.* (1983a, 1983b) have run what is effectively a slitless spectrograph on board the Space Shuttle, to monitor the effects of vehicle glow. This spectrograph has produced the first known photographic spectra of the Earth's limb airglow from space.

Conventional spectrographs have largely been replaced by grating spectrometers, which utilize photoelectric detecting devices, such as photomultiplier tubes (PMTs) to measure spectral emissions. Spectrometers are used extensively to study the spectral characteristics of airglow and auroral emissions. Increased resolution and sensitivity have permitted the identification of some hitherto unresolved spectral emissions. Quantitatively, spectrometers have an advantage over spectrographs in that photoelectric devices have a linear response to incident light, whereas photographic emulsion does not.

The Ebert-Fastie spectrophotometer is a modified grating spectrometer (Fastie, 1967) used to perform high-resolution spectral scans over a limited range of wavelengths. It has been used for a number of applications, including ground-based airglow intensity measurements where there are problems with contamination from nearby spectral emissions, or where there are very low light levels (e.g. Burnside *et al.*, 1977); airborne intensity measurements (e.g. Dick *et al.*, 1970) and the determination of mesospheric temperatures (e.g. Meriwether, 1984). The sensitivity of such a system can be enhanced by controlling its operation with a computer (Meriwether, 1979).

Another popular spectroscopic device is the Fabry-Perot interferometer (FPI). (Note: There seems to be a certain looseness in terminology in the literature - the term 'interferometer' is often replaced by 'spectrometer' or 'spectrophotometer'). The device can scan over a small wavelength range by changing the pressure, and thus the refractive index, of the gas in the etalon chamber. This yields high-resolution scans of spectral features. An FPI transmits a number of passbands, so a narrowband interference filter is often used between the FPI and its photoelectric detecting device (usually a PMT). Although FPIs can be used to measure emission intensities, they are primarily used to measure thermospheric winds and temperatures by observing the Doppler shifting or Doppler broadening of emission lines, respectively (cf.

reviews by Hernandez and Roble, 1979; Meriwether, 1983; Jacka, 1984; Killeen, 1987; Hernandez and Killeen, 1988).

A number of modified FPIs have been developed for particular applications. For example, Hernandez (1981, 1982a, 1982b) has used a twin-etalon scanning spectrometer (TESS) to enhance the sensitivity of the FPI in order to measure thermospheric gravity waves at mid-latitudes. Hernandez and Roble (1984) have used a feedback-stabilized high-resolution FPI, as described in Hernandez and Mills (1973), to measure nighttime F-region winds and temperatures at mid-latitudes. FPIs and other types of spectrometers have been used on board rockets and satellites, e.g. the FPI and the Wind and Temperature Spectrometer (WATS) used on the DE-2 satellite (cf. Hernandez and Killeen, 1988; Smith *et al.*, 1988).

Another spectroscopic device is the Michelson interferometer which incorporates a Fourier spectroscopy technique, and is used for much the same applications as the FPI. A further development, the wide-angle Michelson interferometer (WAMI), has increased responsivity. It has been used to determine upper atmosphere temperatures from the line broadening of OI 557.7 nm airglow and auroral emissions (Hilliard and Shepherd, 1966a, 1966b).

In addition to these functions, Shepherd (1981) has noted some further applications of spectroscopic devices: They can also be used to determine the rotational temperature of a molecular band by observing the shape of the band, or by determining the relative intensities of the rotational lines within the band. A further application is the observation of the relative intensities of vibrational bands, which enables the determination of vibrational temperatures.

3.2.3 Interference filter photometry systems

Although also spectroscopic instruments, photometers have been put to such varied and extensive use in the optical study of the upper atmosphere since the IGY, that they merit individual discussion. Photometers usually incorporate narrowband interference filters to isolate the airglow and/or auroral emission features of interest. Like spectrometers, photometers use mainly photomultiplier tubes as their detection devices. The peak transmission wavelength of an interference filter is dependent on the filter's temperature, tilt angle (with respect to the incident light) and age. In addition, the effective bandwidth of a filter varies with tilt angle. Interference filters are discussed in the next section. Improvements in technology have seen increases in both the speed and sensitivity of photometry systems. Modern interference filters have lower bandwidths (typically less than 1 nm when aligned normal to incident light), PMTs have higher signal to noise ratios, and computer control helps to reduce scanning times.

In their simplest form, photometers are used with filters positioned at a fixed tilt angle, which necessitates separate filters for the recording of emission and background levels (cf. Section 1.2). Sometimes several filters are mounted on a filter wheel and used in a single photometer with a single detecting device. This enables different spectral emission features to be monitored by the same photometer (see e.g. Meriwether *et al.*, 1970). Hunten *et al.* (1963) and Shepherd and Eather (1976) used fixed-filter photometers to measure the rotational temperature of the N_2^+ 1NG band in auroras. This was done by measuring the relative emission intensities within the band (i.e. the intensities of the R and P branches of the band).

The introduction of tilting-filter photometry systems (Eather and Reasoner, 1969) has allowed tremendous advances in airglow and auroral photometry capabilities. By tilting an interference filter, a small wavelength band can be scanned, thus allowing the monitoring of background emissions close to the spectral line of interest. This improves the accuracy of the background (continuum) correction. With the facility for scanning a wavelength band, one can also ensure that intensity measurements are always made at the actual wavelength of the emission. In contrast, over a period of time the passband of a fixed-filter photometer can easily drift away from the wavelength of the emission feature, because of filter ageing or changes in the operating temperature of the filter. A further advantage of tilting-filter photometers is that, besides being used for emission intensity measurements, they can be used to observe Doppler broadening and shifting of emission features. As was previously mentioned these characteristics normally yield thermospheric temperatures and winds respectively. However, in the case of hydrogen emissions (e.g. the H_β line at 486.1 nm) the radiation is caused by precipitating protons, and hence any Doppler shifting or broadening has a different interpretation. The shape of the hydrogen line profiles reflect the energy and pitch-angle distributions of the precipitating protons (Eather, 1967a).

Ground-based photometry systems are more versatile if they can scan an extended area of the sky, rather than always observing a fixed limited area. One disadvantage is that temporal resolution is forfeited for increased spatial coverage. Normally, an electronically-controlled mirror system is used to scan the areas of interest. Different types of scanning have been used: Almucantar scanning, i.e. azimuthal scans at one or more fixed elevation (zenith) angles (Roach *et al.*, 1958; Steiger, 1967); meridian scanning, i.e. scans in zenith angle at fixed azimuthal angles, normally aligned along the magnetic meridian (Duncan and McEwen, 1979; Creutzberg *et al.*, 1981; Lummerzheim *et al.*, 1990) as well as other types of all-sky scanning, e.g. scans that follow a path given by an Archimedean spiral (Sawchuk and Anger, 1972; Sawchuk, 1973).

In addition to ground-based applications, photometers have been employed on a number of moving platforms, such as ships, aircraft, rockets and satellites. Ship-borne photometers extend the observation of airglow emissions to the ocean regions. A prime example of this is airglow research in the region of the South Atlantic Anomaly (see Chapter 7, and references therein). As ships move relatively slowly, and even have the ability to remain essentially stationary at a fixed geographic point, they can monitor emissions in the same geographic area for a number of hours, thereby minimizing the usual temporal-spatial ambiguity that arises with non-stationary observations.

Airborne photometry allows access to otherwise remote locations. In addition, airborne observations are less affected by atmospheric extinction, as they are usually made with only about 20% of the atmospheric air mass above the aircraft. Aircraft can be flown so that they remain at approximately the same magnetic local time for an extended period of time, which is beneficial when studying auroral morphology (Pike *et al.*, 1977). Possibly the most widely documented utilization of airborne photometry has been the NASA Auroral Airborne Expedition which took place in 1969. A number of flights were conducted, mainly in the polar regions of the northern hemisphere, and a number of different optical instruments were used to observe the aurora and airglow (cf. Dick *et al.*, 1970; Eather and Mende, 1971a, 1971b, 1972; Gattinger and Vallance Jones, 1972; Rees *et al.*, 1976; Rees and Lummerzheim, 1989).

Rocket-borne photometers have been used to obtain altitude profiles of spectroscopic emissions. Furthermore, the optical data from rockets can be combined with a number of other data sets that the rocket measures as it flies through the emitting layer, e.g. electron densities, ionization rates, particle energy fluxes, energy spectra, pitch angle distributions, magnetic and electric fields, currents and atmospheric compositions (Anger, 1967). This is useful when modelling atmospheric processes.

A number of Earth-orbiting satellites have airglow photometers mounted in them. Examples are: OGO-II (Reed and Blamont, 1966); ISIS-II (Shepherd *et al.*, 1973; Anger *et al.*, 1973); AE-C (Hays *et al.*, 1977); and DE-1 (Frank *et al.*, 1981). Both the ISIS (International Satellites for Ionospheric Studies) and the DE (Dynamics Explorer) satellites utilize scanning photometers to generate images of large areas of the aurora. The scanning techniques make use of the transverse spin of these polar-orbiting satellites to scan along the axis perpendicular to the satellite's line of flight. Scanning along the direction of the satellite's line of flight is achieved by a combination of the forward motion of the satellite, and by changing the photometer's field of view with mirroring systems. Owing to its low orbit, the ISIS-II satellite is only able to provide one two-dimensional image per orbit (i.e. a temporal resolution of about 2 hours!), and thus suffers from the previously mentioned spatial-temporal ambiguity. In contrast, the DE-1 satellite has an apogee altitude of 3.65 R_e and an orbit time of 6.83 hours which allows it to continuously image the whole of a polar region for a considerable length of time (more than three hours). The temporal resolution of DE-1 images is good, with images being produced every 12 minutes. Given the right timing (between satellite orbit and substorm occurrence), this allows imaging of the entire temporal evolution of a substorm, albeit at a lower spatial resolution than would be achieved by a satellite in a closer orbit. An overview of the most significant results of the global imaging achieved by the scanning photometers on DE-1 has been given by Frank and Craven (1988).

The spatial-temporal ambiguities arising in aircraft, rocket and satellite data can be reduced to a certain extent by combining these observations with simultaneous ground-based observations (Johnson *et al.*, 1967; Rees *et al.*, 1980). Despite the initial pessimism shown towards the combining of satellite data with ground-based data sets (O'Brien and Taylor, 1964), improvements in technology have seen a number of successful coordinated studies (e.g. Rees *et al.*, 1980; Rees and Abreu, 1984). Satellite data has also been combined with rocket data (e.g. Rees *et al.*, 1977; Sharp *et al.*, 1979), and with aircraft data (e.g. Deehr *et al.*, 1976; Winningham *et al.*, 1978). Furthermore, McEwen and Duncan (1981, and references therein) describe a coordinated study of pulsating aurora which combines satellite, rocket and ground-based data. Another advantage of coordinated studies of auroral events is that they increase both the amount and the diversity of data that can contribute towards the study, with obvious benefits. In addition, overlapping data sets provide useful cross-checks as to the accuracy of that data. For instance, satellite nadir optical data are prone to backscatter effects, especially when the groundcover is snow (albedo $\approx$ 0.8), necessitating major corrections to the data (Rees *et al.* (1980) estimate that 75% of the total measured intensity is due to backscatter). Simultaneous ground-based observations can be used to verify the suitability of the methods used to correct this type of data (e.g. Rees and Abreu, 1984). Hays and Anger (1978) and Abreu and Hays (1981) discuss the processing of satellite data to compensate for parallax, atmospheric scattering and backscattering.

The primary function of airglow photometers, operating in various modes and on various platforms, is to record airglow and auroral emission intensity data. A variety of other secondary functions have already been mentioned above. In addition to these, photometric data are also used to deduce the neutral composition of the thermosphere (cf. Cogger *et al.*, 1981, Lummerzheim *et al.*, 1990; Siskind and Sharp, 1991), and to derive the characteristic energies of precipitating particles, and their number and energy fluxes (e.g. Rees and Luckey, 1974; Rees *et al.*, 1988). Photometric data have also been used to derive ionospheric conductances (Mende *et al.*, 1984; Lummerzheim *et al.*, 1991).

It is clear from the literature that ground-based airglow photometry, and particularly meridian-scanning tilting-filter photometry, still has a significant role to play in upper atmosphere optical research. These instruments can be used by themselves to provide information on auroral morphology which has high-time resolution but which is limited in spatial extent, or they can be used to complement other observations, such as satellite imagery, and thus give a more complete picture of auroral evolution (Rees *et al.*, 1980). Ground-based optical measurements are particularly useful in regions such as the Antarctic, where airborne and rocket-borne observations are impractical, if not impossible.

3.3 The tilting-filter photometer

Since 1976 Rhodes University has used tilting-filter photometers to monitor the airglow and auroral emissions at Sanae, the South African base in Antarctica. Three separate photometers are used in a meridian-scanning mode to monitor the OI emissions at 557.7 and 630.0 nm, and the N_2^+ 1NG emission at 391.4 nm. Figure 3.1 shows the various optical components that make up one of these photometers. The three photometers are mounted inside the roof of a prefabricated hut, which also houses the ionosonde that is run by the university. Sanae is situated on an iceshelf, so the hut is mounted on stilts to keep it above the snow. The main base is sunk beneath the surface of the ever-accumulating snow. The hut is situated some 400 m east of the base, and care is taken to keep any outside lights well away from the photometers' line of sight.

The photometer mirror housings on the roof of the hut are aligned so that the movable mirrors within them scan the sky along the magnetic meridian. The cylindrical perspex windows of the mirror housings are prevented from icing up externally, or from misting up internally, by a demister system which circulates warm ($\pm$ 20°C) air through the mirror housings. For each photometer, the movable mirror reflects incident light onto the fixed mirror, which in turn directs the light into the photometer. A series of baffles limit the field of view of the photometer to 4°: For emission heights of, say, 100 and 300 km this means that observations made in the zenith view areas of sky with radii of about 3.5 and 10.5 km, respectively.

A 50 mm diameter narrowband interference filter is used to limit the wavelength of the light that is passed through to the photomultiplier tube (PMT) which serves as the photoelectric detector. The filter is tilted to scan the wavelength region in the immediate vicinity of the emission feature of interest. This allows both background (continuum) and line intensities to be measured. The filter tilting is achieved by attaching the filter holder to a cam-follower which rests on an eccentrically-mounted circular cam that is rotated using a 400-step stepper motor. Different diameter cams allow for maximum tilt angles of 10 or 15°.

The temperature dependence of an interference filter's transmission characteristics make the control of its temperature critical. The filter chamber is thus made a closed unit, permitting regulation of the filter's temperature to within half a degree Celsius. In order to control the filter's temperature, the air temperature in the hut is kept below the lowest desired filter temperature. Heating of the filter is achieved with a customized blower unit (one per photometer) that contains a standard hair-dryer heating element. Air hoses with a 25 mm diameter are used to complete the closed loop between the blower/heater and the filter chamber. A temperature sensor is mounted in the filter chamber, close to the filter and to the input air hose. This allows the filter temperature to be effectively regulated, whilst offering the best protection to the filter in the event of the blower motor seizing (as happened while the author was operating the equipment at Sanae in 1979!).

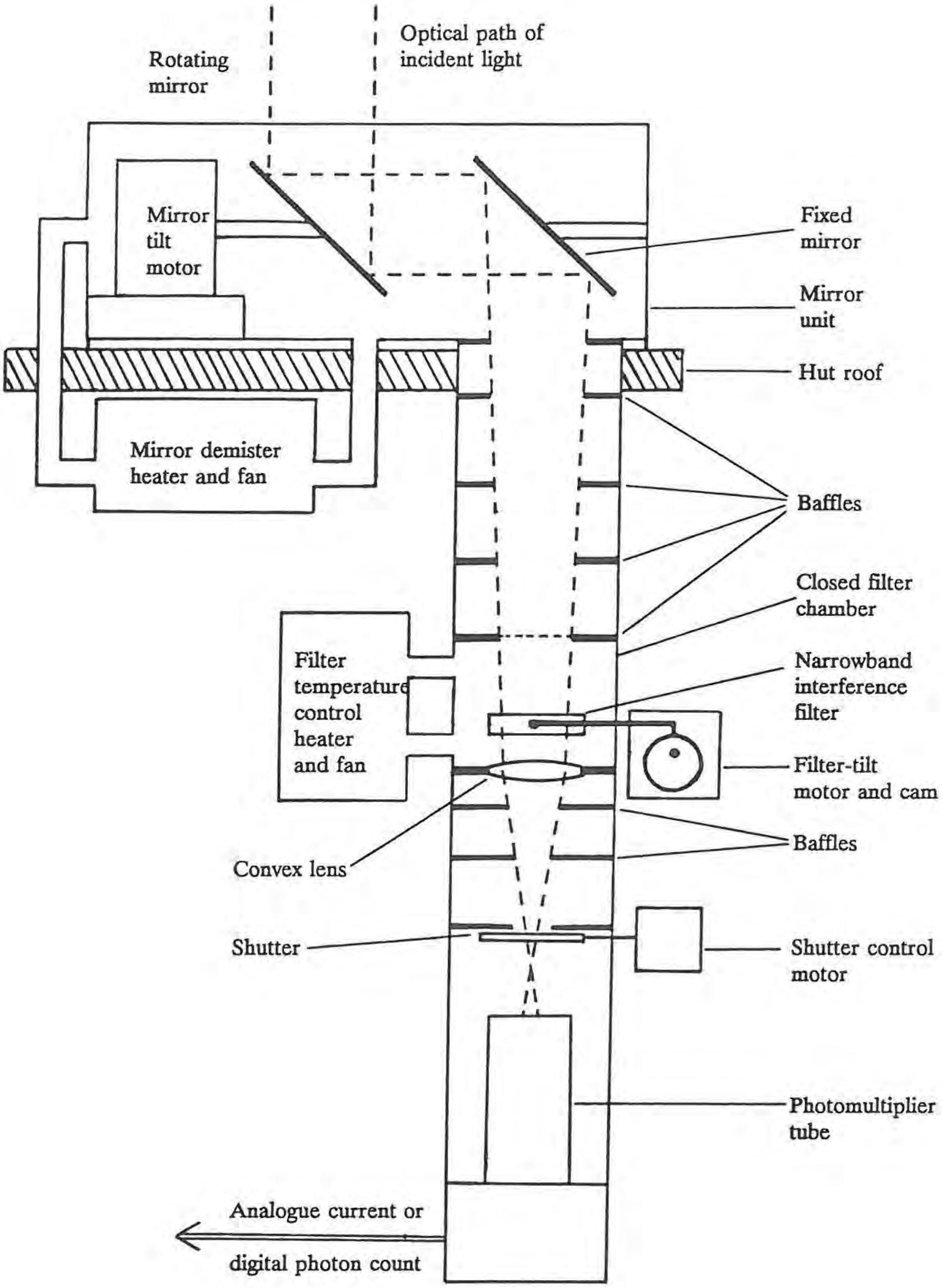

Figure 3.1 Schematic diagram of a meridian-scanning tilting-filter photometer.

Below the filter chamber a convex lens is used to focus the light that is transmitted by the filter, so that it falls within the field of view of the PMT. The vertical position of the lens can be adjusted from outside the photometer, allowing for a limited vertical adjustment in the focusing of the light. A blade shutter is positioned immediately above the PMT. It serves two purposes: It protects the PMT from the possible harmful effects of daylight intensities, and it allows the measurement of PMT dark current levels (with no light incident on a PMT, the PMT still generates a small (dark) current due to thermionic emissions). For correct data reduction, the ambient dark current levels have to be subtracted from the observed line and background intensity levels. Dark current levels become especially significant when observing low-level airglow emissions.

The output of the PMT, either an analogue current which is converted to a voltage and then fed to a chart recorder, or a series of pulses which are counted and stored digitally, is proportional to the intensity of light incident upon it, and can be processed to yield airglow or auroral emission intensities (see Chapter 4).

3.3.1 The narrowband interference filter

The tilting-filter technique makes use of the transmission properties of narrowband interference filters. Before describing the theory of operation of a tilting-filter and the filter's transmission characteristics, it might be appropriate to define a number of the terms that will be used (either in this section or later in the thesis):

Transmittance

The 'transmittance' of a filter is the fraction (or percentage) of the incident light flux that is transmitted by the filter, at a particular wavelength. Transmittance is a dimensionless quantity which varies with wavelength, and is normally represented by the symbol τ.

Peak wavelength

The 'peak wavelength' of a filter is the wavelength at which the filter's transmittance is a maximum.

Peak transmittance

The 'peak transmittance' of a filter is the transmittance of the filter at its peak wavelength.

Bandwidth

The 'bandwidth' or 'half-width' of a filter is the difference between the two wavelengths at which the filter's transmittance is half the value of its peak transmittance.

Passband

The 'passband' of a filter describes the wavelength range in which the filter's transmittance is non-zero. Usually the peak wavelength of a filter coincides with the centre wavelength of its passband.

Transmittance curve

A 'transmittance curve' is a plot of a filter's transmittance versus wavelength, for the wavelength range defined by the passband of the filter.

Transmission factor

A filter's 'transmission factor' is obtained by integrating the area under the filter's transmittance curve. Transmission factors are denoted by the symbol T and have units of wavelength (nm).

Transmission characteristics

The term 'transmission characteristics' is a used to refer globally to the parameter values that define the transmission properties of a filter viz. peak wavelength, transmittance, bandwidth, passband, and transmission factor.

Both the temperature and the tilt angle of a filter influence the peak wavelength of the filter. In an analogue mode the filter is usually tilted from a level position (i.e. normal to incident light) to its maximum tilt angle and then back to a level position. This gives two line readings and either one or two background readings, depending on whether the background readings are obtained with the filter in a position of maximum tilt or in a level position. As a filter is tilted away from being normal to the light incident upon it, its performance deteriorates i.e. its bandwidth increases and its peak transmittance decreases. Consequently, it is best to operate the filter with as little tilt as possible, whilst still being able to observe both the line and background during the tilt cycle. Normally a filter-tilt range of 0°-15° is more than sufficient for this criteria to be met. The range of wavelengths to be scanned by a tilting-filter photometer can be shifted by adjusting the filter's temperature. For a given filter-tilt range, the filter's temperature can be set to ensure that both line and background fall within the wavelengths that are scanned. Furthermore, the filter temperature can be used to get the best wavelength separation between the line and background observations.

Blifford (1966) and Eather and Reasoner (1969) discuss the factors that influence the transmission characteristics of filters. These can be summarized as follows:

1/ Filter tilt angle

As a filter is tilted away from being normal to light incident upon it, its peak wavelength decreases, its peak transmittance decreases, and its bandwidth increases (Figure 3.2). For a given filter tilt angle, θ, the shift in peak wavelength is found to be proportional to θ^2 , and the increase in

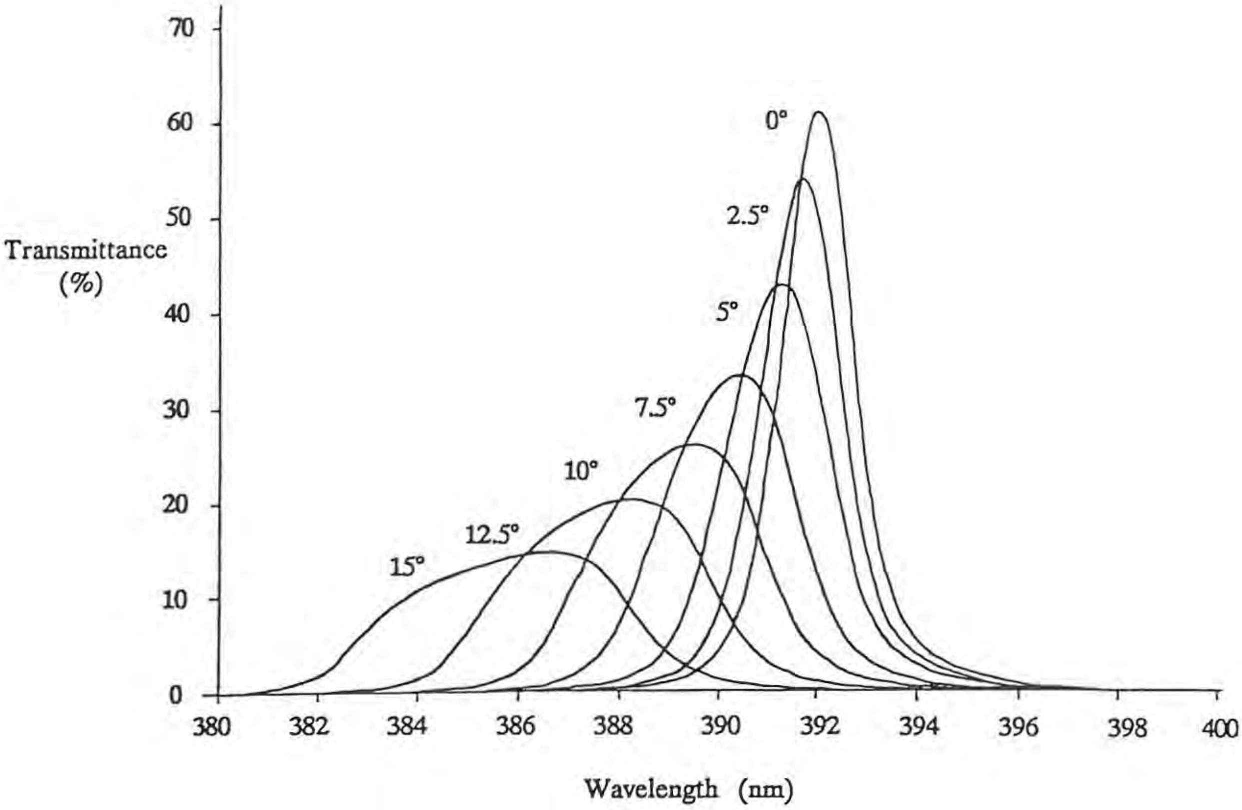

Figure 3.2 The changes in filter transmission characteristics (peak wavelength, peak transmittance, and bandwidth) with filter tilt angle.

bandwidth is almost linear with θ. The variation in peak transmittance cannot be easily described in terms of θ. Blifford found that the changes in bandwidth and transmittance with tilt angle were proportionally larger for filters with narrower passbands.

2/ Temperature

As the temperature of a filter is increased its peak wavelength increases. Blifford (1966) has found the wavelength shift to be between 0.01 and 0.03 nm per °C, depending on the filter. For each filter tested, the change in peak wavelength was found to be essentially linear over the temperature range -20°C to +60°C. Changes in filter temperature seem to have little effect on the bandwidth or the total transmittance of the filter; the area under a filter's transmittance curve does not change significantly with temperature. Anger *et al.* (1973) also reported small increases in peak wavelength with temperature for the filters that they used in the ISIS-II scanning auroral photometer. They reported that the filters showed shifts of between 0.013 and 0.023 nm per °C.

3/ Age stability

It has been found that there is a drift in the passband of most interference filters with age (Eather and Reasoner, 1969). Some researchers have found the drift to be towards higher wavelengths (i.e. a red shift), whilst Eather and Reasoner have found that the ageing of very narrow band filters seem to be characterized by blue shifts. Under normal conditions the shift in passband due to ageing would appear to be slight, and only noticeable over a period of months or even years. Ageing effects can normally be compensated for by adjusting either the filter tilt angles or the operating temperature of the filter.

4/ Uniformity in transmission

Blifford (1966) observed some appreciable variations in transmittance over the surfaces of the filters that he tested. The example that he gives shows a 10% variation in transmission across the surface of the filter. This could affect results if, say, only a small area of the filter were used to determine the transmission characteristics of the filter necessary for data reduction, whilst a larger area of the filter were used during the actual photometric observations.

In Chapter 4, equations are derived which allow absolute emission intensities to be calculated from tilting-filter photometer raw data. These equations include parameters that are associated with the characteristics of the filter used. They are the areas under the filter's transmittance curves corresponding to the tilt angles that are used for line, background and calibration measurements. The measurement of filter transmission characteristics is described in Section 5.2.

3.4 The analogue photometer system

An analogue meridian-scanning tilting-filter photometer system was operated at Sanae during the period 1976-1984. It is called an analogue system because it produces deflections on a chart recorder proportional to the intensity of light received by the PMTs. The system electronically controls the operation of the three photometers, ensuring that they simultaneously observe the same area of the sky. Meridian scans are automatically performed at regular pre-determined intervals. At each mirror position the filter in each photometer is tilted through an entire tilt cycle (level-tilted-level). After observations have been taken at all mirror positions, the EHT power supplied to the PMTs is turned off for a short period (about 10 s) to get a base-line level for the chart recorder deflections. The components of the analogue system can best be described in terms of the photometer functions they control.

3.4.1 Control of the meridian-scanning mirrors

Each photometer has a mirror system which contains both a movable- and a fixed mirror. The movable mirror in each system is attached directly to the shaft of a 400-step stepper motor. Thus each motor step corresponds to a movement in zenith angle of 0.9°. Mirror positions used in a meridian scan must therefore be multiples of 0.9° apart. At the end of each meridian scan a slotted optical switch (an LED/phototransistor pair, hereafter referred to as a photo-sensor) is used to detect a slot on a cam which is also mounted on the stepper motor's axle. This ensures that the mirror has returned correctly to its rest position, and resets a mirror position counter. This check is necessary because spurious noise pulses can cause the mirror's actual position to get out of synchronization with its position counter.

During a meridian scan the mirror steps between mirror positions at a rate of 100 Hz. The mirror is stopped when the value in its position counter coincides with the next pre-programmed mirror position. When the mirror is in position, a logic signal is sent to the filter-tilt control unit, which initiates a filter-tilt cycle. When the filter returns to a level position at the end of a tilt cycle, it causes a logic signal to be sent to the mirror control unit so that the mirror can be moved to its next position. This loop continues until observations have been made at all mirror positions.

The original mirror control unit had 13 mirror positions hard-wired into the control circuitry. When the author analyzed some of the data that he had recorded at Sanae in 1979, it was evident that an increase in both spatial and temporal resolution was required. To take care of the spatial resolution, the mirror control circuitry was redesigned to allow for up to 32 programmable mirror positions. The author then built new mirror control units. These use read-only memory chips (ROMs) to store the desired mirror positions, and make extensive use of TTL logic to generate and handle the many signals needed to coordinate the inter-related movements of the mirrors and filters. The new mirror control system was installed at Sanae at the beginning of 1983, and was configured to use 31 mirror positions, starting at a zenith angle of 81° N and scanning to 81° S with 5.4° (i.e. 6 motor steps) between mirror positions. A hardware switch allows the direction of the scan to be reversed i.e. to run from south to north. Another switch allows the mirrors to be moved directly to the zenith so that each photometer can be calibrated using a mobile low brightness source (LBS) that can be placed above its mirror unit, filling its field of view.

3.4.2 Control of filter tilt angle

It has already been mentioned that each filter is tilted using a stepper motor, an eccentric cam and a cam-follower. One complete revolution of the cam produces a filter-tilt cycle (level-tilted-level). A photo-sensor is used to detect a slot in the cam which marks the filter-level position. A signal from this device serves to stop the filter-tilt at the end of its cycle, and to trigger the advancing of the meridian-scanning mirror to its next meridian position. TTL logic is used to control the stepping of the filter motor. Various filter-tilt speeds are available via a selector switch, which controls the clock rate of the pulses used to drive the motor. Slower filter-tilt speeds can be used to improve the signal-to-noise ratio when observing low light levels (e.g. airglow). The total time taken for a meridian scan is given by the product of the number of mirror positions used in the scan and the duration of each filter-tilt cycle (the filter-tilt time). Consequently, for a given number of mirror positions, the minimum repetition rate that can be used for meridian scanning depends on the filter-tilt speed. Typical filter-tilt times and meridian-scan times, for the 31-position meridian scan, are given in Table 3.1 (Note: The total time taken for a meridian scan includes a 10 s EHT-off period at the end of the scan). In addition, an indication is given of the auroral-activity conditions under which they should be used.

Table 3.1 Filter-tilt times, and meridian-scan times and repetition rates, for auroral observations.

Auroral Activity	Filter-tilt time (s)	Meridian scan	
		Total time (min′ s″)	Repetition rate (min^{-1})
High (substorm)	1.55	58.1″	1
Medium	9.3	4′ 58.5″	5
Low (dull arc)	9.3	4′ 58.5″	10
None (airglow)	18.6	9′ 46.6″	20

3.4.3 Control of filter and demister temperatures

Four identical temperature control circuits are used to control the temperatures of the three filter chambers (one in each photometer), and the temperature of the air used to demist the mirror units. Each filter chamber contains a temperature sensor mounted as close to the filter as possible. As the temperature of the mirror units is not critical, the same heated air is circulated around all three units. A single temperature sensor serves to keep the demister air at a nominal 20°C.

The temperature sensors have a linear output of 10 mV per degree Kelvin. This voltage is used as one of the inputs to a voltage comparator. The other input is a reference voltage, corresponding to the desired temperature and set using an adjustable potentiometer. The output of the comparator is proportional to the difference between the desired- and the actual temperature. The remainder of the temperature control circuitry is designed in such a way that the duty cycle of the heater is proportional to this difference. So the heaters are run in a quasi-continuous mode, operating at low efficiency, rather than being switched between hard-on and hard-off. In addition, the temperature control circuit has a feedback time-constant of 110 s. Both these factors serve to minimize temperature fluctuations, ensuring filter temperature stability to within 0.5°C. Solid-state relays are used to switch the power to the heaters. As a safety precaution the logic signal that switches the relay is routed via the temperature sensor cabling. Thus the heater cannot be turned on unless the temperature sensor is in circuit (i.e. plugged in). The filter and demister temperatures are displayed on analogue meters mounted on the front panel of the photometer controller. This allows the operator to monitor these temperatures in case of heater or temperature controller malfunction.

3.4.4 Shutter control

Originally the photometer shutters were manually operated, using pull-rods mounted on the photometers. Besides being inconvenient, this had the added disadvantage that it was impossible to close all shutters simultaneously. Replacement shutters were built with the pull-rod attached eccentrically to a cam mounted on the axle of a stepper motor. A flange on the circumference of the cam is used in conjunction with two photo sensors, mounted 180° apart, to detect when the shutter is open or closed. The author designed and built a shutter-control box which allows each photometer's shutter to be opened or closed by toggling a switch. This means that dark current levels can be measured more easily, and hence more frequently.

3.4.5 Collection of analogue emission data

When operated in an analogue mode, the current that can be measured at a photomultiplier tube's anode is proportional to the light incident on the tube. The sensitivity of the PMT increases as the high voltage (EHT) supplied to it is increased. Normally EHT voltages of the order of 1 kV are used. The anode current is fed to a current-to-voltage converter with selectable conversion factors of 1, 3, 10, 30, and 100 mV nA^{-1}. The voltage output from this converter is then input to a DC amplifier with selectable gains of 1, 10 and 100. In turn, this amplifier's output is input to one of the three channels of a M.F.E. chart recorder, which in turn has selectable sensitivities, ranging from 10 mV mm^{-1} to 1 V mm^{-1}. The resultant deflections on the chart recorder are directly proportional to the PMT's anode current, and typically have overall scaling factors of the order of nA mm^{-1}. A light source of known intensity is used to obtain calibration factors for each photometer channel. These can be used to convert PMT currents, derived from the chart recorder records, to emission intensities (see Section 4.2).

3.4.6 Limitations of an analogue photometer system

An analogue photometer system, such as the one described above, suffers from a number of shortcomings:

1/ Lack of dynamic recording range

With the data recording method described in Section 3.4.5, the chart recorder deflections vary linearly with input, with a maximum deflection of 100 mm per channel. Assuming a resolution of about 1 mm, this means that the input signal only has to vary by a factor of $< 10^2$, before the deflection either goes off scale, or becomes too small to measure. Whilst variations in airglow emission intensities are usually below this factor, auroral emission intensities can easily vary by a factor of 10^4. This is shown by Table 3.2 which gives the International brightness coefficients (IBCs) corresponding to auroral 557.7 nm emission intensities in the range 0.1 to 1000 kR. Consequently, frequent adjustments to the amplifier gains are necessary in order to obtain usable data when observing auroras. The variations in auroral emission intensities are not only temporal, but spatial as well. As a result, gain adjustments are often needed during the course of a meridian scan, especially when there are isolated discrete arcs occurring in the regions being scanned. This need for constant monitoring and adjusting of the system gains in order to obtain usable data becomes a major problem when one considers that photometric observations at Sanae are possible for up to 16 hours per day in the vicinity of midwinter. A considerable amount of data has been lost because the operator being busy with other duties whilst auroral activity is occurring.

Table 3.2 Classification of auroral intensities

IBC	Intensity at 557.7 nm (Kr)	No. of photons ($cm^{-2}\ s^{-1}$)	Visual appearance
0	0.1	10^8	Subvisual
I	1	10^9	Comparable to Milky Way
II	10	10^{10}	Comparable to thin moonlit cirrus cloud
III	100	10^{11}	Comparable to moonlit cumulus cloud
IV	1000	10^{12}	Sometimes casts easily discernable shadows, equivalent to full moon

2/ Time and labour overheads in the data reduction process

Once the analogue data has been recorded, the reduction of the chart records to yield emission intensities is extremely laborious and time-consuming. This is particularly so when one is dealing with data collected once a minute (or even once every five minutes), for three wavelengths at 31 zenith angles! Clearly there is a need for a more automation in data collection, allowing the data to be directly reduced to emission intensities, without first having to be read from analogue charts.

3/ Expense

The M.F.E. chart recorder used with the analogue system records data on heat sensitive paper. This eliminates the risk of pens running dry etc., but is very expensive. Cost is not a big factor when making airglow observations, as long integration times are normally used, and the chart recorder can be set to run at its slowest speed. Auroral observations, on the other hand, usually necessitate a fast chart speed to handle the large volumes of data that are generated. During auroral activity a roll of chart paper does not last a night.

These problems can be eliminated by a computer-controlled digital photometer system that is capable of handling the large range in intensities, and of writing the observed data onto inexpensive magnetic media (e.g. floppy disks), from whence it can be easily processed.

3.5 The digital photometer system

The author's predecessor in the position of Airglow Research Officer, J.-C. Grujon, was responsible for the initial design of the microcomputer-controlled digital photometer system that was to replace the analogue system at Sanae. The new system was designed to use the photometers and some of the control circuitry of an existing analogue system, nearly identical to the one in use at Sanae. Originally designed for use within South Africa or for ship-borne use, it only differed from the Sanae system in its lack of meridian-scanning ability. The new design incorporates computer control, which allows the photometers' PMTs to be operated in digital (photon-counting) mode. Data can thus be collected on magnetic media e.g. floppy disks. Furthermore, the computer is used to control all other aspects of a photometer's operation, viz. mirror position, filter position, filter temperature and shutter position.

Essentially, the digital photometer system consists of three photometers which are interfaced, together with a number of input/output (I/O) peripheral devices (a VDU, a teletype printer and a disk drive unit), to a South-Western Technical Products (SWTP) 6809 microcomputer. Physically the system can be divided into a number of separate units:

1/ Three separate meridian-scanning tilting-filter photometers, as described in Section 3.3.

2/ A Computer Unit, containing a 6809 Mother Board and an Interface Mother Board (IMB). An interface cable is used to link the 8-bit data-buses and various logic lines of the two mother boards. The interface boards used to control photon-counting, mirror-tilt position, filter-tilt position, filter temperature and shutter position are plugged into the IMB. Each interface board digitally controls a single function on a single photometer. The IMB also holds a clock board which provides time/date information to the computer, for inclusion in the data records that are written to disk. The time/data information is displayed digitally on the front panel of the Computer Unit. The clock board also supplies clock pulses that are used to control the integration times of the photon-counting boards. The Computer Unit also contains interfaces to the various I/O devices mentioned above.

3/ A Photometer Controller Unit, which connects all the computer interface boards (except the mirror-tilt control boards) to the photometer peripherals that they control. This unit, through its front panel switches, allows the operator to choose between automatic (computer-controlled) and manual (purely hardware-controlled) operation of the photometer peripheral devices.

4/ A Mirror Control Unit, which connects the computer's mirror-tilt control boards to the mirror-tilt motors. Mirror positions, corresponding to zenith angles, are displayed on 7-segment LED displays mounted on the front panel. Switches on this panel allow for automatic or manual mirror drive options. This unit also contains the circuitry to control the temperature of the air circulating in the mirror demister system.

5/ An EHT Supply Unit, which contains 4 EHT power supplies (one for each photometer, and one spare). This unit supplies the high voltages needed for the operation of the PMTs.

6/ I/O peripheral devices. There are a number of I/O devices linked to the computer via its I/O ports:

a/ A VDU, used for the general running of the photometer system. The VDU allows the operator to communicate with the computer, using FLEX - the 6809's operating system. The computer program (which controls the operation of the photometers) uses the VDU to interact with the operator, to obtain many of the parameters needed to control the system.

b/ A Disk Drive Unit, which contains two standard (360 kB) floppy disk drives. Drive 0 is used for the System Disk, which contains the system programs and data files of quasi-constant parameters (photometer wavelengths, EHT voltages etc.). Drive 1 is used for data disks; all the output data files are written to disk using this drive. This Unit also contains the power supplies for itself and the Computer Unit.

c/ A Teletype printer (TTY), normally used as a backup output device in case there are problems writing data to floppy disks. In the event of a full data disk, or disk drive errors, the output data files are output to the TTY. The TTY can also be used in place of the VDU to obtain listings of files, or hard copies of the interaction between the operator and the computer during system set-up.

As can be seen from the above description, the computer controls a number of photometer-related functions. Each function is controlled separately, and the operation of the various 'sub-systems' is coordinated under the overall control of a software program. Where possible, the computer control of the photometer functions is backed up either by manual-mode operation (e.g. hardware control of the filter temperatures, and of shutters positions), or by manual-mode testing (e.g. hardware-controlled testing of the mirror- and filter-tilt control circuitry). The computer control of the photometer functions can be described under the same headings that were used to describe the analogue system.

3.5.1 Control of the meridian-scanning mirrors

The control of the meridian-scanning mirrors is achieved in much the same way as it was by the analogue system. However, instead of storing the array of mirror positions in ROMs, they are stored in a data file, which is read by the system program. During a meridian scan, the desired mirror position is fed via the data bus to the appropriate mirror-control interface board, which then moves the mirror until it is in position. This is done by interacting with the mirror drive circuitry in the Mirror Control Unit. Once the mirror is in position, the mirror-tilt interface board sends a signal back to the system program, which then activates a filter scan.

In manual mode, the Mirror Unit has limited control of the mirror movement, independent of the computer control. In this mode, the performance of the mirror drive circuitry can be checked by stepping the mirror motor in both forward and reverse directions. Manual mode is also used to check the correct operation of the mirror photo sensor. Note, however, that one is unable to perform proper meridian scans in manual mode.

3.5.2 Control of filter tilt angle

The digital system controls filter tilt angles in the same way that the mirror positions are controlled: The system program sends the required filter position to the appropriate filter-tilt interface board, which then controls the filter-tilt drive circuitry in the Photometer Controller Unit. The software control of filter tilt angle allows finer control of the filter-tilting operation. Besides being able to perform complete filter-tilt cycles (level-tilted-level), the digital system is capable of moving the filter to specific tilt angles, which correspond to predetermined filter positions for line and background measurements.

With the analogue system, much of a filter-tilt cycle was taken up scanning wavelengths between the emission peak and the background. Unless one wants to look at line profiles, much of this data is superfluous. Computer control of the filter's tilt angle allows one to record data only in the immediate wavelength vicinity of the emission feature, and at a single background position. Some digital systems use only one filter angle for line measurements. This method is prone to errors as Doppler shifting, or shifts in the filter's peak wavelength due to slight variations in its temperature, could mean that the peak wavelength transmitted by the filter does not coincide exactly with the peak wavelength of the emission. For this reason the digital system is set up to take a number of readings (3 or 5) in the vicinity of the emission wavelength.

As with the mirror control circuitry, the filter-tilt circuitry can be operated in manual mode for testing purposes.

3.5.3 Control of filter temperature

The digital system uses the same filter temperature control circuit as that used in the analogue system. However, the addition of a temperature-control interface board allows the filter temperature to be software controlled by the system program. In manual mode, the filter temperatures are controlled in exactly the same way as in the analogue system. In automatic mode, the system program sends a number in the range 0-255, to the temperature-control interface board. This board translates the number, corresponding to a temperature in the range 0-50°C, into a voltage. This is then fed into the voltage comparator of the temperature control circuit, in place of the voltage determined by the potentiometer in the analogue circuit. This means that theoretically the temperature of the filter can be set to within about 0.2°C, although in reality its control is only accurate to within 0.5°C. In addition, the interface board translates the output voltage of the temperature sensor to a digital value (also between 0 and 255), which is relayed back to the computer so that it can be stored on disk. This means that the operating temperature of the filter is stored with the photon-count data.

In the event of problems with the computer control of the filter temperatures, the control can be switched to manual mode, with no appreciable loss in accuracy. Filter temperatures can be monitored using the analogue display on the front panel of the Photometer Control Unit.

3.5.4 Shutter Control

The digital system allows the photometer shutters to be software controlled. This enables dark current counts to be taken automatically at the end of each meridian scan, without operator intervention. In automatic mode, the system program operates the shutters by sending open or shut signals to the shutter-control interface boards. The interface boards then control the shutter motor-drive circuitry in the Photometer Controller Unit.

In the event of problems with the computer control of the shutters, manual mode can be selected. This allows the operator to open and close the shutters using hardware switches.

3.5.5 Collection of digital emission data

In the digital system, the PMTs in the photometers are operated in a photon-counting mode (cf. Morton, 1968; Eather and Reasoner, 1969 for discussions on photon counting). Photon counting is achieved as follows: A negative EHT voltage is applied to the PMT, with its anode held to ground. Photons incident on the PMT cause detectable pulses at its cathode. These pulses, and some non-photon induced 'dark pulses' are fed to the input of an amplifier/discriminator board, positioned immediately below the PMT. This board amplifies the input pulses by a factor of a 100, before filtering out the weaker ones with the discriminator circuitry. The weaker pulses are normally caused by secondary emission within the PMT. The discrimination level can be adjusted using an adjustable potentiometer which is accessible from the outside of the photometer casing. The ECL (emitter-coupled logic) output of this board is then input, via a length of coaxial cable, to a photon-counting interface board in the Computer Unit. Here the pulsed signal is converted from ECL to TTL, before being input into a 24-bit counter made up by cascading three 8-bit counters. The counter has a decimal capacity of 1.678×10^7, which coupled with a range of selectable integration times, gives the photon counters a dynamic range capable of handling both weak airglow emissions and intense auroral emissions.

The system has been designed to allow photon-counting integration times of 1, 2, 4, 8, 16, and 32 seconds. At the end of an integration period, the photometer sends an interrupt signal to the computer. The computer responds to the interrupt by sequentially reading the outputs of the three 8-bit counters via the 8-

bit data bus. The combined 24-bit count is converted to an equivalent decimal count by the system program, and then stored in a buffer. The program then sends a signal to clear the counters on the photon-counting board, before starting the next step in the filter-tilt/meridian-scan process. At the end of a meridian scan, the line, background and dark current count data for all three photometers are written to disk, along with certain system parameters, such as filter tilt angles, temperatures etc. (see Section 3.5.6 below).

3.5.6 Development of the digital system

The overall electronic design of the computer-controlled digital photometer system must be credited to J.-C. Grujon. He designed and built the Computer Unit and most of the interface boards that are used within it. A standard SWTP 6809 microcomputer was dissembled and used in the Computer Unit. In the relatively short time that he worked on this project, Grujon also designed and built the Disk Drive Unit, and designed most of the cabling interconnections between the various control units. He also tested the operation of the photon-counting boards and the interface boards that control filter tilt position, filter temperature and shutter position. He did this using software test routines that he developed in 6809 Assembler.

The author took over the position of Airglow Research Officer while the digitisation project was yet incomplete. He was responsible for the restructuring of the original (analogue) Photometer Controller Unit, so that it allowed for the automatic (computer-controlled) operation of the various photometer functions. The author also designed and built the Mirror Control Unit. Associated with this was the extension of the interface design in the Computer Unit to include another set of interface boards, similar to those used to control filter tilt angle, to control the mirror-tilt circuitry.

The author was responsible for the development of the software used in the digital system. Owing to the high volume of I/O necessary for this computer-controlled system, it was decided to program the software in 6809 Assembler, which allows fast I/O to the various interface boards. The final system program consisted of some 3500 lines of code and comments. Extensive use was made of subroutines and modular programming. The overall program uses a menu which allows the operator to choose one of three sub-programs, or to return to the computer's operating system. The sub-programs allow the system to be run in set-up mode, observation mode, or calibration mode. The operation of these modes can be briefly described as follows:

1/ The set-up program allows the operator to establish which filter tilt angles and filter temperatures are needed in order to observe the emissions of interest. Firstly the mirrors are positioned to observe the zenith. Then the operator is prompted for filter temperatures. Once the filters are at the right temperature, the user is prompted to specify the parameters for a test filter-tilt scan (i.e.

initial filter tilt angle, spacing between filter tilt angles, and the number of angles to be used). This allows the operator to perform a broad wavelength scan in order to determine the filter tilt angles to be used for line and the background measurements. Once the test scan is complete, the operator has the option of performing more test scans (with different filter temperatures, or different filter-tilt parameters). Typically, the operator might use subsequent scans to home in on the filter tilt angles to be used to observe the emission line. Once the operator is happy that he has determined the best filter tilt angles and filter temperatures necessary to make observations of all three emissions (e.g. at 391.4, 557.7 and 630.0 nm), this program is exited.

Once the system has been set up, it is envisaged that this program would only be used occasionally to check that the filter tilt angles are still centred on the emission wavelengths.

2/ The meridian-scanning observation program can be used to perform meridian scans once the system parameters have been determined by the set-up program. Firstly, the operator is asked if any operating parameters are to be changed (the system stores a file containing the parameters last used for meridian scans). Once the system parameters have been set (e.g. filter tilt angles and filter temperatures), the operator is prompted for a repetition rate for the meridian scans, and for the time at which observations are to stop. The program calculates whether there is enough space on the data disk to accommodate the data that are to be recorded. If not, the operator is informed of the time at which the data disk will need changing. The program then loops, performing meridian scans and writing data to disk. If there are problems writing to the data disk, the data are written to the TTY printer. At the end of a scanning period, the program leaves the filters and motors in a rest position, and closes the shutters to prevent possible daylight damage to the PMTs. The program also writes the latest system parameter specifications to a file on the data disk. To save space, this is not done at the end of every meridian scan: A new system parameter data file is only written to disk at the end of an observation session, or prior to the parameters being updated.

The observation program allows the operator to choose between using three or five filter tilt angles for line counts. The filter tilt angles to be used are selected to bracket the emission wavelength. This allows for any movement of the emission wavelength due to Doppler shift. Obviously meridian scans that use five filter tilt angles to observe the emission line at each mirror position, will take longer than scans that only use three filter tilt angles. This must be taken into account when observing the aurora during a substorm, as it decreases the temporal resolution. It is suggested that the five option only be used for airglow observations. During auroral activity, the use of 1 second integration times and three filter tilt angles per mirror position gives the best temporal resolution.

3/ The photometer calibration program allows the operator to calibrate each photometer against a low-brightness source (LBS). The photometers are calibrated with their filters in a level position. The photometer mirrors are moved to a zenith position in order to observe the LBS that is positioned over the mirror housing, filling the photometer's field of view. The LBS has a number of apertures in an attenuation disc which can be selected with an externally mounted rotating wheel. The area of each aperture is double the area of the next smallest aperture. Thus with eight apertures the source brightness can be varied by a factor of 128. This enables the photometers to be calibrated with source brightness roughly equivalent to the brightness of the most recently observed airglow or auroral emissions. The calibration program asks the operator which photometer is to be calibrated, and for the identity of the calibration source. The program records 5 counts for each LBS aperture that is used. At the end of each photometer's calibration, a number of dark current counts are also recorded. Once the photometers have been calibrated, the calibration data are written to the data disk, the mirrors are returned to their rest positions, and the program returns control to the main menu.

More details of the computer-controlled digital photometer system can be found in the digital system documentation, compiled by the author (Dore, 1984).

3.5.7 Utilization of the digital photometer system

The digital photometer system was used in an unfinished form in June-July 1983 for the International South Atlantic Anomaly Campaign (ISAAC) cruise on board the South African Antarctic replenishment vessel, the S.A. Agulhas. The photometers were run in a zenith-observation mode. Owing to the unfinished state of the system, airglow emission data were output in photon-count form to a line printer, and were also converted to an analogue signal that was output to a chart recorder. Long integration times and complete filter-tilt cycles were used to detect the low emission levels experienced during the cruise. More details and results of the ISAAC cruise are given in Section 7.3.

In 1984 the digital photometer system was used to conduct a laboratory cross-calibration of the two low-brightness light sources normally used to calibrate photometers in the field. The sources were calibrated against the brightness of a screen coated with magnesium oxide (MgO), which was illuminated by a standard lamp. Two recently-calibrated standard lamps were used for the cross-calibration. Throughout the cross-calibration the filters used were kept in a level position (normal to incident light), and at a constant temperature of 25°C. Photon-counts for the different light sources were output to a printer. Consequently, calibration of the low brightness sources merely involved multiplying the MgO screen brightness by a count ratio, once the counts had been corrected for dark current. The procedure used, and the results obtained, are given in more detail in Section 5.3.

At the beginning of 1985 the author installed the completed digital photometer system at Sanae. The only parts of the old analogue system not replaced were the mirror systems (housings, mirrors and motors). The reason was that, although two analogue systems were originally built in 1975, only one mirror system was built (i.e. for use at Sanae). Prior to leaving South Africa for Sanae, the operation of the digital system was tested in the laboratory, using a low-brightness source. Operating the photometers individually in a zenith-observation mode allowed the testing of the photon-counting boards, and of the filter tilt angle, filter temperature and shutter control functions. The mirror-tilt control circuitry was tested using a spare (test) stepper-motor.

The shortness of the summer takeover visit to Sanae and the lack of darkness in the polar summer did not permit the *in situ* testing of the digital system before the author returned to South Africa. When auroral observations were started at the beginning of the polar winter, it was found that the meridian-scanning mirrors continually lost synchronization with their intended positions. It is suspected that this was due to interference from the ionosonde operating in the same hut. Despite attempts by the operator to shield the mirror-control circuitry and cabling, no solution was found. This was the only problem encountered with the digital system; the rest of the hardware and software operated as planned. A possible solution would have been to run the system in a zenith-observation mode, to obtain at least some Sanae airglow data for 1985. Unfortunately the system software was written for a meridian-scanning mode only, requiring logic signals from the mirror circuitry (e.g. 'mirror-in-position' and 'mirror-in-rest-position') in order to operate properly. None of the personnel then at Sanae had the expertise to alter the software so that the system could be operated in zenith-observation mode.

With the general reduction in funding for South African Antarctic research at the end of 1985, Rhodes University was forced to freeze the post of Airglow research officer. Consequently, the digital system was returned from Sanae at the end of 1985 and, regrettably, has not been used since.

3.6 Low-brightness light sources for photometer calibration

In order to obtain absolute emission intensities from photometric observation data, it is necessary to calibrate the photometer against a light source of known brightness. It has already been mentioned in Chapter 1 that one way to do this is to observe a star of known brightness. Practical considerations, such as knowing when the star is within the photometer's field of view, make this method unreliable. Furthermore, unless one is monitoring the effects of atmospheric extinction, one is not sure how the intensity of the starlight measured on the ground compares with the actual brightness of the star above the atmosphere. This can introduce considerable errors into the calibration, as the effects of atmospheric extinction have been found to vary by up to 40% from day-to-day (Guttman, 1968). In recent years, a more widely accepted method of calibrating photometers in the field has been to use a portable low-brightness calibration source. Such a 'secondary' source is then cross-calibrated at regular intervals against a 'primary' standard source. Secondary sources have been used at Sanae and on the ISAAC cruise. At Sanae an adjustable-aperture low-brightness source (LBS) incorporating a quartz tungsten-halogen lamp is used. An identical source was used on the ISAAC cruise, along with a radio-active Strontium-90 (^{90}Sr) calibration source. These two types of sources are briefly described below.

3.6.1 The variable-aperture LBS

Two identical variable-aperture low-brightness sources (LBSs) were constructed in 1978. For ease of identification they have been named LBS #1 and LBS #2. LBS #1 was used at Sanae from 1979 until 1984. LBS #2 was kept at Rhodes University and was initially used for the testing of the digital photometer system. In 1983 LBS #2 was used to calibrate the digital photometers when they were used aboard the South African research vessel, the S A Agulhas, during Project Isaac (see Chapter 7). LBS #2 was also used in the cross-calibration of secondary light sources performed in 1984 (see Section 5.3).

The design of the variable-aperture LBS is shown in Figure 3.3. The body of the source is a aluminium cylinder with a 20 cm diameter. With the obvious exception of the diffusing screen at the bottom of the source, all the internal surfaces of the source are coated with matt black paint, to minimize reflections. The lid of the source contains plug sockets for the power leads and voltage sensing leads. A rotating wheel with a sprung locking mechanism is also located on the lid. This wheel is used to select the required aperture in the rotatable attenuation disc situated below the lamp. Each of the 8 apertures in the attenuation disc has an area roughly double the area of the next smallest aperture. (The ratios of the different aperture areas to that of aperture 5 for each LBS are tabulated in Table H.1 of Appendix H). This means that the largest aperture yields a source brightness that is more than 100 times as bright as that given by the smallest aperture. Two baffles are situated between the attenuation disc and the diffusing screen at the bottom of the source. These serve to further minimize any effects from reflected light. The diffusing screen is a disc of translucent white perspex with a thickness of 6 mm. This screen ensures that the light output from the source has a uniform brightness across the surface area of the screen.

The quartz tungsten-halogen lamp used in the source has an advantage over a conventional incandescent lamp in that it does not suffer significantly from light output degradation during its rated lifetime. The light output of a tungsten-halogen lamp stays within 95% of its initial value during its lifetime, whereas the light

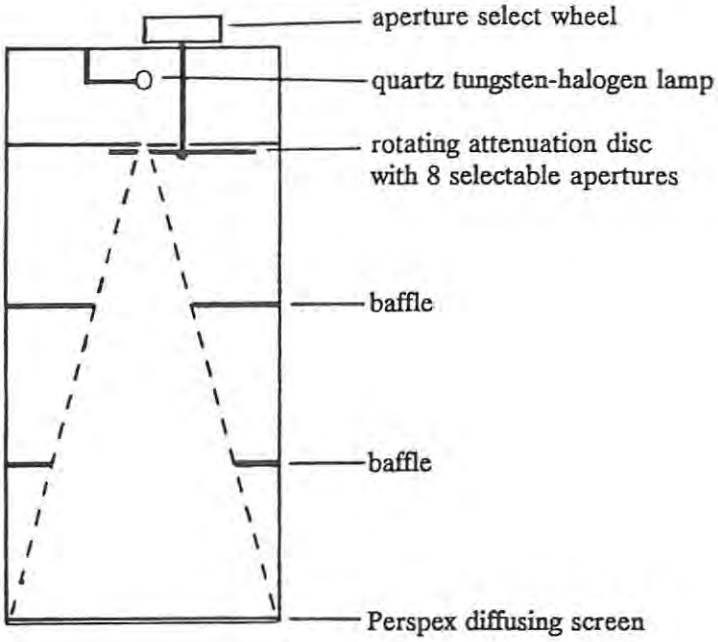

Figure 3.3 Schematic diagram of the variable-aperture low-brightness source constructed for photometer calibration.

output of an incandescent bulb decreases by as much as 30% during its lifetime. A limitation of the quartz tungsten-halogen lamps is that they have shorter life expectancies than incandescent lamps. Their lifetimes are very sensitive to operating voltage.

A precision power supply for the calibration source, which supplies an accurate and constant voltage (12 V) to the lamp, was constructed by the author. The power supply was designed to eliminate any problems that might have been experienced with voltage drops along the long cable (± 8 m) needed to link the power supply in the Sanae hut to the LBS positioned above the photometers on the hut roof. This was achieved using sensor leads in parallel with the supply leads in order to measure the voltage across the lamp. The voltage sensed across the lamp is then used in a feedback circuit which enables accurate control of the lamp voltage. This voltage, and the current flowing through the circuit, are displayed on analogue meters mounted on the front panel of the power supply. The power supply was built in such a way that the voltage across the bulb can be slowly increased, from zero at switch-on, to its operational level. This protects the bulb from surges and extends its lifetime.

3.6.2 The ^{90}Sr-activated phosphor LBS

The radio-active calibration source that was used on the ISAAC cruise was obtained commercially. This source consists of a disk of phosphor that is impregnated with a Strontium isotope, ^{90}Sr. The radio-active decay of this isotope causes excitation of the phosphor which then emits light. The source is laminated between two metal plates. One plate has a number of small holes in it, giving a 'dull' side to the source, whilst the other plate has bigger holes in it, giving a 'bright' side. The plates can be removed from the source, to make it brighter. Even without the plates, the brightness of the source is not the same on both sides i.e. it still has a dull side and a bright side. The diameter of the source is about 10 cm. This adequately fills the field of view of a photometer when it is operated in zenith-observation mode, without a meridian-scanning mirror unit.

CHAPTER 4

DATA REDUCTION

4.1 Introduction

The raw data collected by a tilting-filter photometer system has to be processed in order to produce absolute emission intensities for the spectral features being observed. During airglow and auroral observations, various data are collected which correspond to emission line intensities, background (continuum) intensities, and the dark current levels of the PMTs. In order to obtain absolute (rather than relative) intensities, the photometers are calibrated at regular intervals using a low-brightness source (LBS) to yield calibration factors. The analogue and digital photometer systems described in the previous chapter produce data in the form of chart deflections and photon counts respectively. These data are dependent on the transmission characteristics of the filters used. Clearly any data reduction method that is used has to take into account the filter's transmission characteristics for the various tilt angles that are used to obtain the line, background and calibration data. By combining observational data, calibration factors and filter characteristics, one can obtain intensity values for the observed airglow or auroral emissions.

Emission intensities are given in Rayleighs (R). The Rayleigh is a photometric unit specifically defined for the airglow and aurora by Hunten *et al.* (1956). Derivations of this unit, in terms of photon intensity, are given in a number of standard texts (e.g. Chamberlain, 1961, 1978; Chamberlain and Hunten, 1987). The Rayleigh is a unit of surface brightness, and is defined as follows: If I is the surface brightness of an emitting layer observed in a particular direction (with units of photons $\mathrm{cm^{-2}\,s^{-1}\,sr^{-1}}$), then $4\pi I$ is the total omnidirectional emission from a column of unit cross section along the line of sight. The units of this total column emission are thus photons $\mathrm{cm^{-2}\,s^{-1}}$. A more convenient unit is the Rayleigh (R), where $1\ \mathrm{R} = 10^6$ photons $\mathrm{cm^{-2}\,s^{-1}}$. The Rayleigh is named after Robert John Strutt, Fourth Lord Rayleigh, who performed much pioneering work on the airglow, and who made the first measurement of the absolute intensity of the night airglow in 1930. (He is sometimes called 'the airglow Rayleigh' to distinguish him from his father, the Third Lord Rayleigh, or 'the scattering Rayleigh'.)

The equations used to derive emission intensities from tilting-filter photometer data are derived by the author in Section 4.2. These equations have been extended to include atmospheric correction factors, necessary because intensities observed from the ground are only apparent emission intensities. Actual intensities at the source of the emission, i.e. in the thermosphere, differ from these apparent intensities owing to the effects that the Earth's atmosphere has on light that passes through it. These atmospheric effects are discussed in

Section 4.3. Factors influencing the accuracy of the absolute emission intensities that are obtained using the airglow equations are discussed in Section 4.4. Other factors influencing the accuracy of absolute emission intensity values obtained from tilting-filter photometer data are also discussed.

4.2 The 'airglow' equation

When the author started this thesis there was no local (South African) expertise or documentation available on the processing of raw photometric data to yield emission intensities. A survey of the literature revealed only a reference to Roach (1963), who documents the two-colour method of airglow observation. Early South African airglow research used this method, and some of the data bulletins mentioned in Chapter 1 give details of the equations used in this method (see e.g. Steyn *et al.*, 1971). No documentation has been found for the processing of the raw data provided by tilting-filter photometers. Most of the publications that deal with emission intensities derived from photometric observations give no details of the methods used to process the raw data, and only occasionally mention any corrections used for atmospheric effects.

Owing to the lack of existing data reduction methods, the author has derived, from first principles, equations that can be used to process either analogue or digital tilting-filter photometer data. For the purposes of this thesis it is easiest to present the derivation of the digital airglow equation in full, and then show how this equation is adapted for the analogue case.

4.2.1 The digital airglow equation

In the case of the digital data, an equation is needed that will convert photon-counts, made at different filter tilt angles, to an absolute emission intensity. Such an equation is derived in the following way:

Assume that we have an emission line at λ_1 with an idealized 'flat' background emission on either side, as shown in Figure 4.1. We can define the following filter tilt angles, measured relative to a normal to the light incident on the filter:

θ_1 is the filter tilt angle at which λ_1 is the central transmitted wavelength.

θ_2 is the filter tilt angle at which λ_2 is the central transmitted wavelength, and is such that λ_1 is outside the bandwidth of the filter at λ_2, i.e. no light of wavelength λ_1 is transmitted by the filter when it is tilted to angle θ_2. θ_2 can be greater than or less than θ_1, and correspondingly, λ_2 can be less than or greater than λ_1.

θ_3 is the tilt angle of the filter when it is level, i.e. $\theta_3 = 0°$.

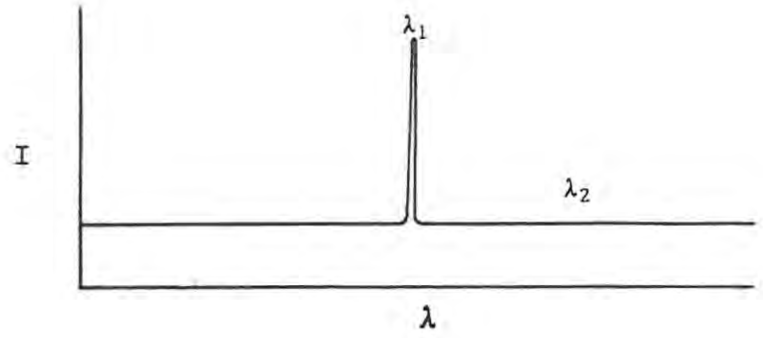

Figure 4.1 An emission line superimposed on a smooth background (continuum) emission.

We can also define the following counts made by counting the pulses given by a photomultiplier tube positioned below the filter:

$n_{1,a}$ are the observed airglow counts with the filter at tilt angle θ_1.

$n_{2,a}$ are the observed airglow counts with the filter at tilt angle θ_2.

$n_{1,c}$ are the counts with the filter at tilt angle θ_1, with a calibration light source above the filter.

$n_{3,c}$ are the counts with the filter level (i.e. at tilt angle θ_3), with a calibration light source above the filter.

$n_{1,l}$ are the number of the observed airglow counts at θ_1 due to the emission line.

$n_{1,b}$ are the number of the observed airglow counts at θ_1 due to the background.

$n_{2,l}$ are the number of the observed airglow counts at θ_2 due to the emission line. However, $n_{2,l} = 0$, as we have already chosen θ_2 such that there is no line contribution at this filter tilt angle.

$n_{2,b}$ are the number of the observed airglow counts at θ_2 due to the background.

Note: The observed counts defined above are assumed to have had the appropriate dark (current) counts subtracted from them.

From these definitions it follows that

$$n_{1,a} = n_{1,l} + n_{1,b} \tag{4.1}$$

and

$$n_{2,a} = n_{2,b} \tag{4.2}$$

These observed counts do not have a one-to-one correspondence with the photons incident on the PMT. This is because the PMT has a sensitivity, S, which varies with wavelength. This sensitivity is dimensionless and has values between 0 and 1. It indicates the fraction of the photons incident on the photocathode that will result in pulses that can be counted at the output of the PMT. For the small range of wavelengths scanned by the tilting filter, S can be assumed to be a constant.

In addition, let k dλ be the number of photons per second in the continuum background between wavelengths λ and $\lambda + d\lambda$, with k independent of λ in the immediate vicinity of the emission line.

The interference filter can be described by transmittance functions $\tau_l(\lambda)$, which peak at wavelengths λ_l, corresponding to tilt angles θ_l. This is shown schematically in figure 4.2.

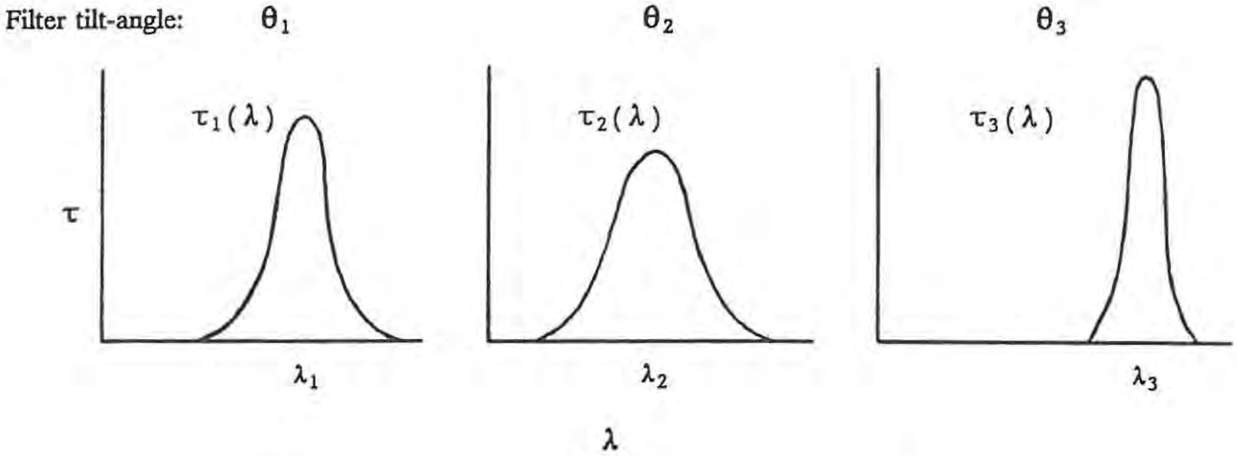

Figure 4.2 . Plots of transmittance (τ) versus wavelength (λ), showing the variation of the filter transmittance function, $\tau_l(\lambda)$, with filter tilt-angle, θ_l.

With the filter at a tilt angle of θ_1, Equation 4.1 becomes:

$$n_{1,a} = n_{1,l} + k\,S \int_0^\infty \tau_1(\lambda)\, d\lambda$$

$$\text{i.e.} \quad n_{1,a} = n_{1,l} + k\,S\,T_1 \tag{4.3}$$

where T_1 is the integrated area under the filter transmittance curve $\tau_1(\lambda)$.

Likewise, with the filter at a tilt angle of θ_2, Equation 4.2 becomes:

$$n_{2,a} = k\,S \int_0^\infty \tau_2(\lambda)\,d\lambda$$

$$\text{i.e.} \qquad n_{2,a} = k\,S\,T_2 \tag{4.4}$$

where T_2 is the integrated area under the filter transmittance curve $\tau_2(\lambda)$.

Eliminating k from Equation 4.3 and 4.4, and re-arranging gives

$$n_{1,l} = n_{1,a} - n_{2,a}\left(\frac{T_1}{T_2}\right) \tag{4.5}$$

This equation gives the photon count due to the emission line, in terms of the observed counts and the (measurable) transmission characteristics of the filter. In order to obtain an emission intensity that corresponds to the line count, we use the photometer calibration. We make the valid assumption that the brightness of the calibration source is essentially constant over the small range of wavelengths that can be scanned by a narrowband interference filter, using a maximum tilt angle range of 15°. If the calibration source has a brightness B (in R nm^{-1}), then with the filter tilted to θ_1 the intensity of the light, $I_{1,c}$, that reaches the PMT is given by:

$$I_{1,c} = B \int_0^\infty \tau_1(\lambda)\,d\lambda$$

$$\text{i.e.} \qquad I_{1,c} = B\,T_1 \quad \text{(in Rayleighs)} \tag{4.6}$$

If this intensity results in a PMT count of $n_{1,c}$, then using the ratio of the line counts to the calibration counts, the apparent intensity of the emission line, I_{app}, measured on the ground is given by

$$I_{app} = \left(\frac{n_{1,l}}{n_{1,c}}\right) B\,T_1 \tag{4.7}$$

However, it is more convenient, from a practical point of view, to calibrate the photometer with the filter level. This yields values of $n_{3,c}$ rather than values of $n_{1,c}$. Consequently we need to establish the relationship between these two parameters. If we define b dλ as the number of photons emitted per second by the calibration source, with wavelengths between λ and dλ, then using the previous assumption of uniform brightness over the range of wavelengths concerned, we have

$$n_{1,c} = b\ S \int_0^\infty \tau_1(\lambda)\ d\lambda$$

$$\text{i.e} \quad n_{1,c} = b\ S\ T_1 \tag{4.8}$$

and

$$n_{3,c} = b\ S \int_0^\infty \tau_3(\lambda)\ d\lambda$$

$$\text{i.e.} \quad n_{3,c} = b\ S\ T_3 \tag{4.9}$$

Combining Equations 4.8 and 4.9 gives

$$n_{1,c} = n_{3,c} \left(\frac{T_1}{T_3}\right) \tag{4.10}$$

Hence, we can rewrite Equation 4.7 as

$$I_{app} = \left(\frac{n_{1,l}}{n_{3,c}}\right) B\ T_3 \tag{4.11}$$

Substituting for $n_{1,l}$ (from Equation 4.5 into Equation 4.11) gives

$$I_{app} = \left(\frac{n_{1,a} - n_{2,a}\left(\frac{T_1}{T_2}\right)}{n_{3,c}}\right) B\ T_3 \tag{4.12}$$

The above equation gives the apparent intensity of the emission feature, as measured on the ground. This apparent brightness, I_{app}, is related to the brightness I_0 at the emitting layer by $I_0 = I_{app} C$, where C is a correction factor for the effects of atmospheric extinction and scattered light (see Section 4.3). Furthermore, the calibration data are usually pre-processed to yield calibration factors B_f equal to B $n_{3,c}^{-1}$ with units R nm^{-1} count^{-1}. Thus Equation 4.12 becomes

$$I_0 = \left(n_{1,a} - n_{2,a}\left(\frac{T_1}{T_2}\right)\right) B_f\, T_3\, C \tag{4.13}$$

Where: $n_{1,a}$ and $n_{2,a}$ are the measured total photon-counts corresponding to the emission line and the background,

T_1, T_2 and T_3 are determined from filter transmittance curves, that can be produced using a spectrophotometer (see Section 5.2),

B_f is determined by combining $n_{3,c}$, the measured counts due to the calibration source, and B, the known calibration source brightness (see Section 5.3), and

C is an atmospheric correction factor that can be estimated (see Section 4.3). C varies with wavelength and zenith angle, and is dependent on such factors as atmospheric extinction coefficients, the scattering model used, the height of the emitting layer, and ground albedo.

4.2.2 The analogue airglow equation

In the case of the analogue data, an equation is needed that will convert chart recorder deflections to absolute emission intensities. These deflections, usually referred to as heights, represent the currents measured at the photomultiplier anode. These analogue currents are directly equivalent to the digital counts, and are given by the chart recorder heights (h_i, in mm) divided by the corresponding chart recorder gains (g_i, in mm nA^{-1}). Thus:

$$\begin{aligned} n_{1,a} &\equiv \left(\frac{h_{1,a}}{g_{1,a}}\right) \\ n_{2,a} &\equiv \left(\frac{h_{2,a}}{g_{2,a}}\right) \\ n_{3,c} &\equiv \left(\frac{h_{3,c}}{g_{3,c}}\right) \end{aligned} \tag{4.14}$$

During airglow observations, $g_{1,a} = g_{2,a}$ i.e. the same gain is used to record both the line and background heights. Substituting currents for photon counts in Equation 4.13 gives

$$I_0 = \left(\frac{\left(\dfrac{h_{1,a} - h_{2,a} \left(\dfrac{T_1}{T_2} \right)}{g_{1,a}} \right)}{\left(\dfrac{h_{3,c}}{g_{3,c}} \right)} \right) B\ T_3\ C \tag{4.15}$$

Again, calibration data are normally pre-processed to yield calibration factors $B_f = B\ g_{3,c}\ h_{3,c}^{-1}$, with units R nm^{-1} nA^{-1}, so that Equation 4.15 simplifies to

$$I_0 = \left(\frac{h_{1,a} - h_{2,a} \left(\dfrac{T_1}{T_2} \right)}{g_{1,a}} \right) B_f\ T_3\ C \tag{4.16}$$

This is an equation that can easily be used to process the raw analogue data, in order to produce absolute emission intensities.

4.3 Corrections for atmospheric effects

The airglow and auroral emission intensities, I_{app}, detected by a ground-based photometer will differ from the true intensities at the emitting layer, I_0, due to a combination of several atmospheric and geometric effects. The derivation of accurate values of I_0, from values of I_{app}, is not a simple problem. Many treatments of this problem can be found in the literature (see e.g. Chandrasekhar, 1950; Ashburn, 1954; Rees, 1958; Chamberlain, 1961; Sawchuk, 1973; Lambert, 1980). This section summarizes the effects that the atmosphere has upon light travelling through it, and discusses the corrections that need to be applied to the apparent intensities, obtained using a meridian-scanning photometer.

4.3.1 The effects of atmospheric extinction and scattered light on observed emission intensities

Firstly, we consider the observation of emitted light in the zenith. Light incident on the atmosphere is subject to absorption and scattering. The light which is absorbed is converted to some other form of energy, and hence will never re-appear in the line of sight. However, light scattered from the line of sight can possibly be scattered back into the line of sight. Furthermore, unless one is observing an isolated point source, there is also the probability of light from other directions being scattered into the line of sight. This is definitely the case when one is observing spatially extended sources, such as those of the airglow and the aurora. If one considers light of frequency ν and intensity I_ν incident on the atmosphere, then after travelling a distance ds, the change in the intensity of the light is given by

$$\frac{1}{\rho}\frac{dI_\nu}{ds} = -(\kappa_\nu + \sigma_\nu)I_\nu + j_\nu \tag{4.17}$$

where ρ is the density of the atmospheric medium,
κ_ν is the mass absorption coefficient,
σ_ν is the mass scattering coefficient, and
j_ν is the emission coefficient, due mainly to scattering.

The combined effect of absorption and scattering is called extinction, so that $(\kappa_\nu + \sigma_\nu)$ is the mass extinction coefficient. We can define the extinction coefficient per unit air mass as $\tau_\nu\,dm = (\kappa_\nu + \sigma_\nu)\,\rho\,ds$, where m is the relative optical air mass. (The relative optical air mass is defined as the ratio of the path length of radiation through the atmosphere at any given angle, $0° \leq \theta \leq 90°$, to the path length of radiation normal to the atmosphere). We can also define a source function, J_ν, as the ratio of the emission coefficient to the extinction coefficient, i.e. $J_\nu = j_\nu\,(\kappa_\nu + \sigma_\nu)^{-1}$.

Consequently, with some rearranging and substitution, Equation 4.17 becomes

$$\frac{1}{\tau_\nu}\frac{dI_\nu}{dm} = -I_\nu + J_\nu \tag{4.18}$$

This is the equation of radiative transfer, which can be solved to give

$$I_{app} = I_0\,e^{-\tau m} + \int_o^m J\,e^{-\tau m}\,\tau\,dm \tag{4.19}$$

where I_{app} is the intensity after traversing a thickness of scattering atmosphere given by optical air mass m, and I_0 is the intensity before entering this atmosphere, i.e. where $m = 0$. The first term on the right of this equation describes the attenuating effects of extinction on the direct radiation (i.e. the light travelling directly between the emitting layer and the observer). The second term describes the indirect light that is scattered into the observer's viewing angle from outside of the field of view. Note that for convenience the author has taken the liberty of dropping the subscript ν from this and subsequent equations, henceforth assuming the frequency dependence of the parameters to be implicit.

There are a number of forms of scattering, which can be distinguished by the spatial distribution of the scattered light relative to the direction of the incident light. Isotropic scattering is scattering in which there is an equal probability of light being scattered in all directions; in most cases of scattering by the atmosphere, this is not the case. The predominant form of scattering in the atmosphere is Rayleigh scattering, in which the light is scattered by particles whose dimensions are small in comparison with the wavelength of the light; there is a higher probability of the light being scattered forward or backward, rather than sideways, relative to the direction of the incident light. For Rayleigh scattering, the probability of the light being scattered at an angle Θ to the direction of the incident light is given by $p(\Theta) = (1 + \cos^2 \Theta)$. This entity is referred to as the Rayleigh phase function. Another form of scattering that takes place in the atmosphere is Mie (or aerosol) scattering, in which the scattering particles have dimensions comparable to the wavelengths of the light that are being scattered; the most probable direction for the scattered light is in a forward direction relative to the direction of the incident light. The distribution of the scattered light relative to the direction of the incident light, for each of these three types of scattering, is illustrated in Figure 3.4 of Sawchuk (1973). It will be shown later that the evaluation of the source function term in the equation of transfer depends on the type of scattering that is assumed.

Above the scattering atmosphere there is a layer of ozone (O_3), which peaks in density at altitudes between 20 and 30 km. This layer also has an attenuating effect on light that passes through it. Consequently, any thermospheric emission incident on the lower atmosphere has already been attenuated by a factor determined by the extinction coefficient for ozone, τ_{ozone}. (Note: The attenuation is due entirely to absorption, rather than scattering; ozone's extinction coefficient is thus the same as its absorption coefficient). So equation 4.19 becomes

$$I_{app} = I_0 \, e^{-(\tau + \tau_{ozone})m} + \int_0^m J \, e^{-\tau m} \, \tau \, dm \qquad (4.20)$$

This equation, as it stands, is only applicable to observations made in the zenith i.e. with a zenith angle, z, equal to zero. As soon as non-zero zenith angles are used for observations, geometric effects must be taken into account: Firstly, for emissions viewed obliquely through the atmosphere, the path-length of the light through the atmosphere (and hence the attenuation due to extinction) increases with z. Secondly, unless an infinitely thin emitting layer is assumed, the effective thickness of the emitting layer (and hence its observed surface brightness) also increases with z. The geometry of both of these effects are shown in Figure 4.3.

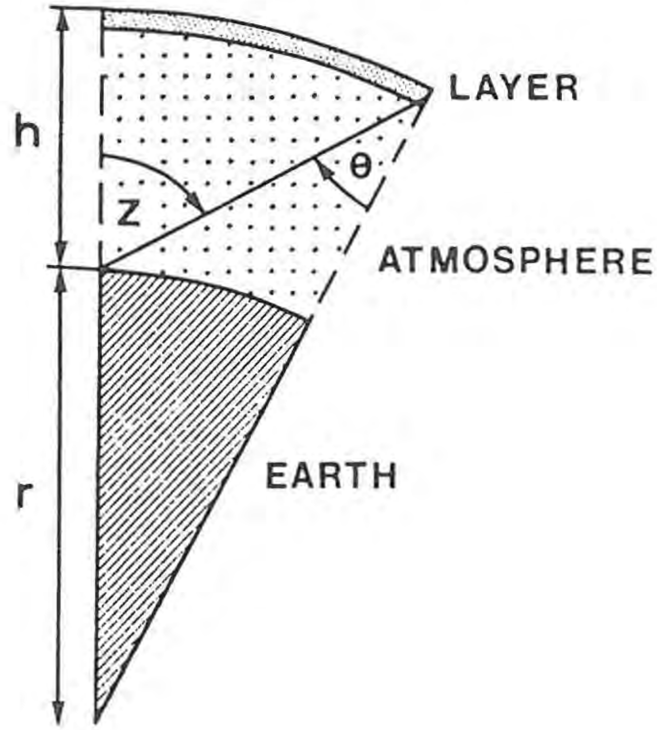

Figure 4.3 The geometry of a radiation path through a spherical atmosphere.

In the case of the path-length through the atmosphere, the associated attenuating effect is actually taken care of by the presence of the air mass, m, in Equation 4.20. The greater the zenith angle of the observation, the greater the air mass that the light has to traverse. As the air mass increases with zenith angle, there is a corresponding increase in the exponential attenuation factor used in the term describing the intensity of the direct light.

The air mass, m, is not the only parameter used to compensate for the variation of the atmosphere's optical depth with zenith angle. Some treatments of the problem of atmospheric extinction assume a plane-parallel atmosphere, which results in sec z being used in place of m. The difference between sec z and m only becomes apparent at large zenith angles. In fact, tabulated values of these two parameters (Allen, 1963, page 120), show differences of less than 1% at z = 70°, and less than 3% at 80°! Thus it would appear that using sec z in place of m for zenith angles up to at least 70° will have a negligible effect on the accuracy of atmospheric correction factors. Values of m for zenith angles between 70 and 90°, with small increments of z, are given by Fen *et al.* (1985). Also, Table 16-2 of Valley (1965) gives values for m for all integer zenith angles between 20 and 89°, inclusive.

Another alternative to using m is to use the Chapman function, Ch(x,z), where $x = (R_e + h_0)\,H^{-1}$, R_e is the radius of the Earth (6370 km), h_0 is the zero reference level (= 0 for ground level) and H is the scale height for the atmosphere. Swider (1964) has found that even for large zenith angles (close to 90°), the Chapman function approximates the optical depth of the atmosphere to within 5%. Tabulated values of the Chapman function are given by Wilkes (1954) and by Smith and Smith (1972). The Chapman Function has in fact been used by Lambert (1980) in her calculations of the atmospheric correction factors to be used with Sanae H_β photometer data.

The second geometric factor influencing the calculation of intensities is the thickness of the emission layer itself. If a thin homogeneous emitting layer is assumed, then the intensity of the light measured at an angle θ from the perpendicular to the layer is proportional to sec θ, and so

$$I(\theta) = I(0)\ V(\theta) \tag{4.21}$$

where: I(θ) is the intensity at angle θ,

I(0) is the intensity from the zenith, and

V(θ) is the van Rhijn function, = sec θ.

Unless one assumes a plane-parallel atmosphere, θ does not have the same value as z, the zenith angle used by the observer. In fact, from Figure 4.3 the Sine law yields

$$\theta = \arcsin\left(\frac{R_e}{(R_e + h)} \sin z\right) \tag{4.22}$$

Furthermore, using $\sec\theta = (\cos\theta)^{-1}$, and $\cos^2\theta = 1 - \sin^2\theta$, we obtain the van Rhijn function, V, in terms of zenith angle and the height of the emitting layer:

$$V = \left(1 - \left(\frac{R_e}{(R_e + h)}\right)^2 \sin^2 z\right)^{-1/2} \tag{4.23}$$

This function is used to convert intensities measured at a zenith angle, z, to the equivalent intensities that would be observed normal to the emitting layer. It can be incorporated into Equation 4.20 to give

$$I_{app} = I_0 V e^{-\tau_{total} m} + \int_0^m J e^{-\tau m} \tau \, dm \qquad (4.24)$$

where we have used τ_{total} in place of $(\tau + \tau_{ozone})$, as the total extinction coefficient.

This equation now relates the apparent intensity measured below the atmosphere to the intensity at the emitting layer, for any zenith angle, $0° \leq z \leq 90°$. The next problem is that in the case of the aurora, which is usually an extended source of non-uniform emission, there is no exact solution to this equation. In particular, it is the source function J, which is difficult to evaluate. In order to obtain values for the source function, judicious approximations have to be made (Rees, 1958).

4.3.2 The evaluation of the source function

Several workers have considered the evaluation of the source function, J, which appears in the equation of transfer. This section summarizes some of the solutions that have been found, and the approximations that were needed to achieve these solutions.

Chandrasekhar (1960; Note: This is the second edition of *Radiative Transfer*, the first edition was published in 1950) has found a solution to the source function by assuming Rayleigh scattering alone, and then considering a plane-parallel atmosphere illuminated by a point source at infinity e.g. a star. Clearly this solution is not applicable to extended sources such as those of the airglow and aurora. However, Ashburn (1954) has used Chandrasekhar's equations and integrated an infinite number of point sources over the night sky hemisphere, to obtain a solution for a uniform source. This solution can be applied to airglow emissions, which can generally be regarded as uniformly illuminating the atmosphere, especially over a limited area such as that observed by a meridian-scanning photometer. Thus, usable solutions for the source function exist for both a point source, and for an extended source that is uniform across the whole sky. Unfortunately auroral emissions fall between these two states, being extended sources of light, but only present over parts of the sky. Furthermore, auroras are normally non-uniform, both spatially and temporally. This means that the source function will have different values across the sky and will vary, probably rapidly, with time. Further approximations are necessary in order to obtain values of the auroral source function which can be applied to observed intensity data.

Rees (1958) makes the assumption that the source function, J, is independent of the air mass, m, so that Equation 4.24 becomes

$$I_{app} = I_0 V e^{-\tau_{total} m} + J (1 - e^{-\tau m}) \tag{4.25}$$

Then, by introducing the Rayleigh phase function, $p(\Theta) = (1 + \cos^2 \Theta)$, he shows that the source function is given by

$$J = \frac{3}{4} \int (1+\cos^2 \Theta) I \frac{d\omega}{4\pi} \tag{4.26}$$

where Θ is taken as the angle between the centre of the auroral luminosity and a position on the meridian plane where direct auroral radiation is absent (i.e. where there are contributions from airglow, scattered airglow, and scattered auroral light only), and $d\omega$ = solid angle ($= \sin\theta \, d\theta \, d\phi$). By considering a uniform average intensity of $\bar{I}$, with half-angle width $\theta_2 - \theta_1$, and with azimuthal extent $\phi_2 - \phi_1$, the following formula is obtained for J:

$$J = \frac{3}{16\pi} \bar{I} (1 + \cos^2\Theta) (\phi_2 - \phi_1) (\cos \theta_1 - \cos \theta_2) \tag{4.27}$$

Rees estimates the spatial extent of the aurora from visual observations, and determines the corresponding value of $\bar{I}$ from the observed intensity measured in a direction where there is assumed to be no auroral component (i.e. at an equatorward zenith angle of 85°). This assumption implies that the observed intensity is due only to airglow and/or scattered auroral light. Thus, Equation 4.25 reduces to $I_{app} = J(1 - e^{-\tau m})$, which yields a value for J (valid for a zenith angle of 85°S) that can be used in Equation 4.27 to determine $\bar{I}$. Values of $\bar{I}$ are then substituted back into Equation 4.27 to yield values for J for the various (auroral) zenith angles of interest. For a particular time or meridian scan, the spatial extent of the aurora is taken as being constant, so that Θ is the only variable in the equation used to determine values for the source function. By definition, Θ is the angle between the direction of the incident light and the direction in which the light is scattered. Rees takes the direction of the incident light to be given by the 'centre of gravity' of the aurora emission, which is usually assumed to be the brightest point in the auroral form. In effect, Θ is the difference between the observation zenith angle and the zenith angle of the brightest point in the aurora, and thus varies with the zenith angle of observation.

The Rees equation for the source function (Equation 4.27) is considered to be a fairly good approximation of the source function for an auroral arc, as long as this is the only auroral form, i.e. the rest of the sky is devoid of auroras (Romick and Belon, 1964; Sawchuk, 1973). Eather (1968) and Harrison (1969) have both applied the Rees equation for the source function to diffuse (uniform) auroral arcs. Furthermore, they have both simplified the process by assuming that $\bar{I} = I_0 / \sqrt{2}$, and $\Theta = \theta_2 - \theta_1$.

Romick and Belon (1964) needed to apply atmospheric corrections to their observations of isolated bright auroral arcs. They were of the opinion that the Rees technique under-estimates the correction needed in the immediate vicinity of the bright auroral forms. Their solution to the problem was to plot a graph of measured (apparent) intensity versus zenith angle for a N-S meridian scan, and then to judiciously draw in the background luminosity beneath the peak corresponding to the auroral arc. Using this technique, the intensity at the emitting layer would be given by

$$I_0 = (I_{app} - I_b)\, e^{\tau_{total} m} \qquad (4.28)$$

where I_b corrects for any extra-terrestrial background, airglow, airglow scatter, and other weaker auroral emissions in the vicinity of the form of interest. Romick and Belon give a sample graph (their Figure 3.1) which shows that their correction in the vicinity of the auroral form would be greater than the correction derived using the Rees technique. This method is acceptable if one is only interested in the intensity of the auroral arcs, but it does not compensate for the effect that light from these bright arcs might have when scattered into adjacent areas of lower intensity. Consequently, this method is not considered applicable to the study of the intensity variations across the entire meridian, necessary when observing the development of an auroral substorm (see Section 6.5).

Sawchuck (1973) has developed an all-sky auroral scanner, which scans the entire night hemisphere in some 2.5 seconds. In this time the scanner measures auroral emission intensities at 3201 positions, using scanning paths that follow the form of an Archimedean spiral. The source function for a particular point in the sky can be established by integrating the contributions of the other 3200 data points. This can be done either by assuming Rayleigh scattering or isotropic scattering. In the case of Rayleigh scattering, Sawchuk has produced an equation for the Rayleigh phase function, $p(\Theta)$, which allows one to calculate the source function, $J(\cos\theta,\phi)$, for an elevation angle $= \theta$, and an azimuth angle $= \phi$, in terms of the intensities measured at all other elevations, θ', and azimuths, ϕ'. Unfortunately, in 1973 the computing power available to Sawchuk meant that determining values for the source function for the 3201 observing positions would take some 50 hours! This was clearly impractical, and so Sawchuk was forced to sacrifice accuracy by reducing the number of observations used to determine each value of the source function. He then considered using an isotropic scattering model, which allowed him to determine the value of the source function by merely taking the average of the 3201 intensities measured in a single scan. This approximation was found to give a value of the source function that was within 15% of the value of the Rayleigh source function, for a number of different auroral configurations. Consequently Sawchuk opted to use the isotropic model for the processing of his scanner data. The important point to come from this is that an isotropic scattering model can be used to estimate the source function, with only small (acceptable) errors in the results. Uncertainties in the values to be used for extinction coefficients (see below), can introduce far greater errors in emission intensities.

Finally, it would appear from the literature that some workers (e.g. Hopgood, 1976; Rees and Lummerzheim, 1989; Lummerzheim *et al.*, 1990) have chosen not to bother to compensate for indirect light scattered into the field of view, and have effectively used a zero source function. This has been concluded from the fact that the correction factors they quote are equal to $e^{\tau m}$, where τ is the extinction coefficient per unit air mass. Essentially, this means that Equation 4.24 has been reduced to

$$I_{app} = I_0 \, V \, e^{-\tau_{total} m} \tag{4.29}$$

where, for the zenith, the van Rhijn factor V is equal to unity. In the case of Rees and Lummerzheim (1989) the measurements were made in the zenith, and from an aircraft (at an altitude equivalent to $m = 0.2$), so that any contribution from scattering would presumably be much less than that experienced on the ground. The measurements of Lummerzheim *et al.* (1990) were also made in the zenith, but were ground-based at Poker Flat in Alaska. Their measurements were made during the northern winter, where one would assume snow cover, and hence a large value for the ground albedo (albedo ≡ spectral reflectance, and is approximately 0.8 for snow at the wavelengths of interest). These would be similar recording conditions to those experienced at Sanae in Antarctica. By ignoring the effects of scattering into the field of view, one will overestimate the intensity of the emission at the emission layer. However, the errors induced by doing this might well be small relative to those due to uncertainties in the value of the extinction coefficient used in the direct light term.

4.3.3 Atmospheric correction methods to be applied in this thesis

Clearly there are a number of methods that can be used to tackle the problem of correcting observed emission intensity data for the effects of atmospheric extinction and scattered light. None of the methods are absolute or error-free, as they all require certain approximations to be made. It now remains to select the correction methods that are most appropriate for use with either the airglow or auroral intensity data provided by the tilting-filter photometers.

In the case of airglow observations, where fairly uniform emissions can be expected across the whole sky, Ashburn's method is probably best. The source function component of the transfer equation is represented by two terms that describe the light scattered into the observer's field of view: Firstly, there is a diffusely scattered component (light scattered directly into the field of view) and secondly, there is a component that describes the light reflected by the ground and then back-scattered into the field of view. Both of these components are proportional to the intensity of the light that is incident on the top of the scattering atmosphere (below the ozone layer). Consequently, for the Ashburn model, Equation 4.24 becomes

$$I_{app} = I_0 \left(V e^{-\tau_{total} m} + e^{-\tau_{ozone}} (D + R) \right) \tag{4.30}$$

where: D is the coefficient for the diffusely transmitted component, and is dependent on the height of the emitting layer (h), the extinction coefficient (τ), and the zenith angle of the observation (z).

R is the coefficient for the ground-reflected and backscattered component, and thus is dependent not only on h, τ, z, but also on the ground albedo (r).

Ashburn has tabulated values for D and R, for various values of h, τ, z, and r (Note: D is taken from those sections of the tables for which the ground albedo is zero). The tables can be used to interpolate values of D and R corresponding to the various values of h, τ, z, and r that are used (or assumed) for the observations. It should be possible to use Equation 4.30 to process airglow data, and even data from observations of diffuse aurora, without incurring large errors due to the effects of scattering.

Let us now consider the correction method(s) that can be used for the processing of intensity data obtained when observing discrete aurora which only cover parts of the sky. It would seem that Sawchuk's method (Sawchuk, 1973) that integrates intensities over the entire night sky to obtain an average value for the intensity of the scattered light, is the best approach providing one has intensity data available for the entire night sky. Unfortunately this is not the case when one uses a meridian-scanning system, which only samples a two-dimensional slice across the sky.

The Rees approach (Rees, 1958), which approximates the spatial extent of the auroral form in order to estimate the source function (Equation 4.27), is fine for the case of an isolated auroral arc. However, during auroral substorms the sky is often filled with multiple auroral forms which exhibit rapid spatial and temporal variations. In these instances application of the Rees equation is impractical, even if there are ASC photographs available to give some idea of the spatial distribution of the auroral forms. The extent of the errors introduced in the determination of the spatial distribution of the auroras and the approximation of a 'centre of mass' do not warrant the time and effort required to determine the scattering correction factors.

The approach of Romick and Belon (1964) is also considered unsuitable for correcting for atmospheric effects on meridian scan data recorded during substorms. The reason for this, already mentioned, is that the method is unlikely to make the right corrections for the regions of diffuse aurora that form the background to the discrete aurora. Also, this method is more suited to treating isolated discrete auroral arcs, rather than the multiple auroral forms that occur during substorms.

We are left with two possible alternatives: Either to use the Ashburn method (Equation 4.30), or to use Equation 4.29 which ignores the contribution from scattered light and only takes into account the effects of extinction. The atmospheric correction factor, C, has been defined such that $I_0 = I_{app}\, C$. Consequently the equations for C for the Ashburn method (which considers extinction and scattering), and the extinction-only model are

$$\text{Extinction and scattering:} \qquad C = \left(V\, e^{-\tau_{total} m} + e^{-\tau_{ozone}} (D + R)\right)^{-1}$$

$$\text{Extinction only:} \qquad C = \left(V\, e^{-\tau_{total} m}\right)^{-1} \qquad (4.31)$$

For convenience, we will call the Ashburn method the A-method, and the method related to the extinction-only model, the E-method. The A-method always gives a value of C which is less than one, so that the calculated intensity at the emitting layer, I_0, is always less than the observed intensity, I_{app}. In contrast, when using the E-method, C is often greater than one, so that I_0 is often greater than I_{app}. These two methods effectively determine the minimum and maximum limits, respectively, of the possible values that can be obtained for I_0, for a given I_{app} and τ. It was decided to use both methods to process auroral data, so that we can get some idea of the variation one might expect at Sanae, both in the values of emission intensities, and the ratios between them. Appendix G describes the procedure used to determine the atmospheric correction factors which were used with the Sanae data.

4.4 The accuracy of calculated absolute emission intensities

There are a number of factors that can influence, to a greater or lesser extent, the accuracy of the absolute emission intensities that are obtained from ground-based photometric observations of the airglow and aurora. Firstly, the equations that were derived in Sections 4.1 and 4.2 use observed data and a number of system parameters in order to calculate emission intensities. Any error in these variables will cause errors in the calculated emission intensities. This is discussed in Section 4.4.1.

Unlike the narrow line emissions of OI at 557.7 and 630.0 nm, the (0,0) emission of the N_2^+ molecule appears as a broad spectral band, with a bandhead at 391.4 nm. When quoting 391.4 nm intensities the total intensity of the band is used. Problems arise when using a narrowband filter in tilting-filter mode to observe the 391.4 nm emission. Often the filter can only scan part of the band. This does not present a problem if the relative intensity distribution of the band is known. However, the spectral distribution of the band varies with the rotational temperature of the molecule. Consequently this can be a source of uncertainty in the intensity of the 391.4 nm band, and also in the calculated intensity ratios involving the 391.4 nm emission. This is discussed in more detail in Section 4.4.2.

Another source of error in the determination of emission intensities is the contamination of line emissions by other nearby emissions. This can cause significant uncertainties in low-level airglow intensities. The possible effects of contamination are discussed in Section 4.4.3.

Finally, if one wants to obtain intensities values for the auroral emissions caused by electron excitation, one has to subtract the contributions due to normal airglow emissions and to proton-induced emissions from the overall calculated emission intensities. Procedures for doing this are discussed in Section 4.4.4.

4.4.1 Factors influencing the accuracy of emission intensities obtained using the airglow equations

Both the digital and analogue airglow equations (Equations 4.13 and 4.16, respectively) yield absolute emission intensities using a combination of observed data, filter transmission factors (T_l), calibration factors (B_f), and atmospheric correction factors (C). By comparison with the equations used to process two-colour photometer data, these equations contain fewer parameters. This is because the tilting-filter photometer uses one filter, one PMT, and a common optical path to measure both line and background data. Furthermore, parameters such as the PMT sensitivity are eliminated from the equations. This is because the wavelengths, at which the line and background observations are made, are sufficiently close together to assume the same PMT sensitivity.

Errors in calculated absolute emission intensities can arise both from errors in the observed data, and from errors introduced by one or more of the parameters (T_l, B_f and C) used in the equations. However, if airglow and auroral observations are made under controlled conditions with good quality equipment, any errors due to the observed data should be minimal. The most probable causes of incorrect intensity values are errors in the values of T_l, B_f or C. Each of these parameters is wavelength dependent i.e. they have different values for the different spectral emissions of interest. Consequently, errors in one or more of these parameters can cause errors not only in emission intensities, but also in the ratios between the emission intensities. It follows that accurate intensity values and intensity ratios are only possible if accurate values are obtained for the above-mentioned T_l, B_f and C parameters. These parameters are now considered in more detail.

4.4.1.1 The filter transmission factors, T_l

The filter transmission factors, T_l, are the areas under a filter's transmittance curves for the filter tilted to angles θ_l. It is possible to obtain accurate transmittance curves for each filter at a number of tilt angles, using a spectrophotometer. The author has done this for the filters used at Sanae and on the ISAAC cruise. The methods used and the results obtained are documented in Section 5.2. From the transmittance curves it is possible to integrate the areas under the curves for each tilt angle, and then produce a plot of T_l versus θ_l. This plot can be used to obtain a value of T_l for any tilt angle that has been used for the airglow observations. Although the method used to obtain the filter transmittance curves is considered to be very accurate, there are still a number of possible sources of error in the values of T_l that are used in the airglow equations:

1/ The accurate determination of the correct values to be used for T_l depends on the accurate determination of the filter tilt angles that were used for the line and background observations. These tilt angles might be subject to errors if the rest position of the filter is not adjusted properly. If the filter is not actually level in its rest position, then all the tilt angles used in a tilt cycle will be offset by an amount equal to the levelling error. Fortunately, each photometer is made up physically of a number of cylindrical brass sections, which screw together. To ensure that the filter is level in its rest position, it is a relatively simple matter to extract the section which houses the filter chamber, position it so that its walls are vertical, and then use a spirit-level to ensure that the filter holder is level within the filter chamber. During a filter tilt cycle a strong retaining spring ensures that the cam-follower follows the cam mounted on the filter-tilt motor. The rest position of the filter, and the mechanics of its tilt mechanism, should be checked at regular intervals (e.g. once a month, typically during the full-moon period), to ensure that the filter is in fact level at the start of a tilt cycle.

The actual tilt angles used for line and background measurements are determined as follows: Tables have been prepared of filter tilt angle versus stepper-motor step number, for both the 10° and 15° maximum-tilt cams. Appendix C shows the geometry of the stepper-motor cam, and derives the equation for the filter tilt angle in terms of the motor step number. In addition, a graph is supplied of filter tilt angle versus filter tilt position (number of motor steps) for both 10° and 15° cams. In the case of the digital system, the tilt angles can then be derived directly from the digital filter tilt positions that are used. The analogue case is slightly more complicated. The stepper motor position has to be determined from the chart records, by obtaining the ratio of the displacement of the line (or the background) from the start of the tilt cycle to the total length of each filter-tilt record. This ratio is then multiplied by 400 (the number of motor steps in a filter-tilt cycle), to give the step position of the line (or the background). The step positions are then used to obtain the corresponding filter tilt angles.

Filter temperature does not seem to have a direct effect on the value of T for a given tilt angle. However, changes to the filter's operating temperature could cause significant changes in the filter tilt angle used for the line. Consequently it is necessary to re-determine the line tilt angle if one changes the operating temperature of the filter. Filter ageing could also cause shifts in the tilt angles used for line measurements. It is recommended that filter tilt angles are determined for each new period of data that is analyzed. Regular use of the digital system's set-up program, to check the filter tilt angles that are to be used for line measurements, should automatically compensate for filter temperature or filter ageing effects.

Any variation in the filter tilt angle used for the line measurement, due to Doppler shifting, is likely to be small and should not affect the value of T_l that is used.

2/ Another possible source of error in the value of T_l is the fact that the transmittance characteristics of filters might not be constant over the surface of the filter (Blifford, 1966). Unfortunately, the author was unaware of this (potential) problem when he measured the transmission characteristics of the filters in 1984, and consequently only made measurements through the centre of the filter. Ideally, one should average the transmission characteristics across the entire surface of the filter. Blifford measured variations in transmittance of up to 10% across the surface of a filter. As a first order approximation, this would be the probable magnitude of the error that one might expect in the values of T_l, due to this problem.

3/ Measurement of the transmission characteristics of the filters used at Sanae from 1976 to 1984 (see Section 5.2) has shown that ageing has not only changed the filters' peak wavelengths, but also their bandwidths and peak transmittances. For the latter parameters, this is contrary to the findings of Eather and Reasoner (1969). Changes in bandwidths and peak transmittances will clearly affect the filters' transmission factors. These effects are discussed in more detail in Section 5.2. It is evident that unless the filters' transmission characteristics are measured regularly, filter ageing can be a significant source of error in the values of the transmission factors.

4.4.1.2 The calibration factors, B_f

The calibration factors, B_f, used in the airglow equations are determined by dividing the brightness of the calibration source used, by the PMT counts or currents that are measured with the calibration source positioned in the photometer's field of view. The most probable source of errors in the values obtained for B_f are errors in the values used for the brightness, B, of the calibration source. To obtain accurate values for B_f, the calibration source itself must be accurately calibrated. This is normally done by cross-calibrating it against a 'standard' calibration source. However, even if a calibration source is accurately cross-calibrated under laboratory conditions, there are still a number of factors that could influence the accuracy of the values of B_f:

1/ For the photometer calibration to be meaningful, the calibration source must fill the field of view of the photometer that is being calibrated. The physical sizes of both the variable-aperture and the ^{90}Sr sources allow this to be done. Use of the same optical path also helps to minimize errors, because the light from the calibration source is subject to the same instrumental optical effects as those experienced by light from the sky.

2/ The photometer must be calibrated using the same system sensitivity that was used to make the airglow or auroral observations. In particular, a change in the EHT voltage supplied to the PMT will change the sensitivity of the photometer. Consequently, it is most important that the photometer is calibrated both before and after any adjustments are made to the EHT voltage supplied to its PMT.

3/ Torr *et al.* (1976b) discuss a possible cause of error in the calibration of photometers when using an extended source. This is the reflection of light by the filter back onto the calibration source screen. The screen will then reflect some of the filter-reflected light back into the photometer. The nett result of these multiple reflections is that the photometer seems more sensitive than it actually is, with the result that emission intensities are underestimated. Torr *et al.* (1976b) have found that this is a significant source of error only if the distance (L) between the filter and the calibration source is less than a factor of five greater than the radius (r) of the filter. In the case of the Rhodes University photometers the values of L and r are 250 mm and 25 mm respectively, giving a ratio $L/r = 10$. Consequently, this should not be a significant source of error in the calibration of the photometers.

4/ A number of factors might affect the actual brightness of a variable-aperture, quartz tungsten-halogen lamp, low-brightness source (i.e. LBS #1 and LBS #2):

The brightness of the source is proportional to the voltage across the lamp. Changes in lamp voltage also change the colour temperature of the lamp, and hence the spectrum of the light emitted by it. This means that changes in lamp voltage can cause not only changes in the brightness of the lamp, but also changes in the relative brightnesses of the lamp at different wavelengths. Consequently, it is important that the same voltage is used across the lamp for photometer calibrations, as was used when the source was calibrated. Extensive testing showed the power supply to be stable to within 1%, over an extended running period. Further tests were conducted during which the calibration source and cabling were placed in a constant environment room and subjected to a range of operating temperatures between -25°C and +25°C. The voltage across the lamp and the current through it were found to be independent of temperature. From this it can be concluded that the power dissipated by the lamp, and hence its brightness, are independent of external temperature. The author is confident that any uncertainty in the brightness of the calibration source due to the power supply is conservatively less than 5%.

The operating mechanism of a quartz tungsten-halogen lamp is such that it keeps the internal surface of the bulb clean. Throughout the lamp's lifetime, the light output of the lamp stays within 5% of its initial value. Consequently, as long as the lamp is replaced well before the end of its rated lifetime, the age of the lamp should have a minimal effect on the brightness of the calibration source. Regular cross-calibration of the source should serve to monitor any ageing effects on the lamp.

The diffusing screen at the base of the LBS is a piece of white translucent perspex 6 mm thick. After consulting with staff of the University's Chemistry Department, it is thought to be improbable that the transmission characteristics of the perspex vary significantly, if at all, in the temperature range -25°C to +25°C. However, any icing of the outside of the diffusing screen might have a significant effect on the photometer calibration. In order to minimize the probability of icing, calibrations of the Sanae photometers were restricted to clear, windless nights on which the temperature was above -25°C. In addition, the LBS was placed outside of the hut some minutes before the commencement of a calibration, in order to achieve temperature stability. Any icing on the perspex screen was removed prior to the source being placed in position above the photometers.

When not in use, the calibration source is stored in a special storage box. This box serves two purposes: Firstly, the perspex diffusing screen is protected from damage, as scratches might alter its transmission characteristics. Secondly, the screen is protected from light, as prolonged exposure to UV light (e.g. sunlight) will cause ageing that will change its transmission characteristics.

5/ In the case of the ^{90}Sr-activated phosphor calibration source that was used on the ISAAC cruise, the brightness of the source varies with the concentration of the radio-active ^{90}Sr in the source. As this substance has a half-life of 28.1 years, the associated change in source brightness over a period of one or two years is small ($\approx$ 5% in two years). Furthermore, it is possible to predict the long-term change in source brightness, using a simple exponential decay formula. Of more concern is the finding of Blacker and Gadsden (1966), that there is considerable temporal variation in the brightnesses of phosphor sources, not related to the half-life of the radioactive material embedded in the phosphor. Furthermore, they found that the relative spectral distribution of the source also varies with time. It is possible that temporal variations in the phosphor source could be as high as 20%, depending on the source.

The brightness of a phosphor source is also dependent on its temperature. Blacker and Gadsden (1966) have measured variations with temperature of between +0.65% per °C and -2.0% per °C, depending on the wavelength at which the measurements were made. Consequently, a difference in source temperature of 10°C from the temperature at which it was calibrated could result in as much as a 20% error in a photometer's calibration factor.

The brightness of a phosphor source is also affected if the source is exposed to light. This causes an increase in the source's brightness. The author has been unable to find any documentation on the magnitude of the effect that light has on a phosphor source, or how long the effect lasts. Presumably the stronger the light that the source is exposed to, the greater the increase in brightness, and the longer the effect will last. When the source is not in use, it is stored in a tightly sealing metal canister, which is in turn enclosed in a light-tight bag similar to those used to hold reels of photographic film. When the source is to be used, care is taken to remove the source from its container only in darkness.

It is evident that photometer calibrations with the radioactive source are unlikely to be as accurate as those with the variable-aperture LBS.

In conclusion, it would appear that as long as the brightness of the primary sources used to calibrate the secondary sources are accurate, then the calibration factors obtained using the variable-aperture source should be accurate to within about 10%. Those obtained using the ^{90}Sr source should be accurate to within about 20%, if the photometer is calibrated at a temperature close to the temperature used to calibrate the ^{90}Sr source. In 1984 both of the above-mentioned sources were cross-calibrated against standard lamps of known brightness. The methods used, and the results of the cross-calibration are described in Section 5.3.

4.4.1.3 The atmospheric correction factors, C

We have seen in Section 4.3 that the atmospheric correction factor, C, used at a particular wavelength, varies with the model that is used to describe the effects of atmospheric scattering, and with the value of the extinction coefficient (τ) that is used. In fact, the greater the value of τ used, the greater are the differences between the minimum and maximum values of the calculated emission intensities I_0, obtained when using different scattering models. To further complicate matters, extinction coefficients vary appreciably with wavelength, peaking at the lower-wavelength end of the visible spectrum. Several workers have cited values of τ (per unit air mass) for various emission wavelengths (e.g. Roach and Meinel, 1955; Chamberlain, 1961; Allen, 1964; Valley, 1965; Guttman, 1968; Hayes and Latham, 1975; Mende *et al.*, 1984; Eather, 1985a; Menzies, 1985). By far the most comprehensive coverage of the variability of extinction coefficients is that given by Guttman (1968), who graphically presents observed and model values of τ for maritime, desert and urban conditions. Guttman has observed day-to-day variations in τ of up to 40%. However, the variations were found to be almost constant over the entire wavelength range of the visible spectrum. The variations in τ are due to changes in the dust, haze, aerosol, and water vapour (or ice crystal) levels in the atmosphere. The presence of clouds will also cause increases in the values of τ at all visible wavelengths.

If all the values of τ that appear in the literature are considered, there is a considerable range in the values for τ at each wavelength. This is shown in Figure 4.4, a graph showing the variation in τ values for the emission wavelengths of interest. At the shorter wavelengths there is a more rapid variation in $d\tau/d\lambda$. It should be noted that in most cases the values of τ given in Figure 4.4 are for overall extinction coefficients, which incorporate the contributions of water vapour, aerosols and ozone. The maximum and minimum values of τ found for the wavelengths 391.4, 557.7, and 630.0 nm are listed in Table 4.1. This table also gives the corresponding correction factors, calculated using both the E-method (extinction-only model) and the A-method (Ashburn's extinction and scattering model). The heights of the emitting layers are presumed to be 100 km for the 391.4 and 557.7 nm emissions, and 300 km for the 630.0 nm emission. From this table it can be seen that, depending on the extinction coefficient and model used, the calculated values for I_0, corresponding to a single value of I_{app}, could differ by the following factors: 2.33 for 391.4 nm, 1.58 for 557.7 nm and 1.45 for 630.0 nm.

Furthermore, the ratios between emission intensities are also affected. It is normal practice to calculate intensity ratios using the intensities measured when looking along a field line. At Sanae the magnetic inclination (dip-angle) is about -62°, which corresponds to an (equatorward) zenith angle of 28°. The nearest zenith angle to this, which is used for observations at Sanae, is 30°. Atmospheric correction factors were calculated for this zenith angle, using both the A-method and the E-method formulae. Factors were determined using both the minimum and maximum values of τ found for each wavelength.
If we define:

$$R_{53} = I_0(557.7) \,/\, I_0(391.4)$$
$$R_{56} = I_0(557.7) \,/\, I_0(630.0)$$
$$R_{63} = I_0(630.0) \,/\, I_0(391.4)$$

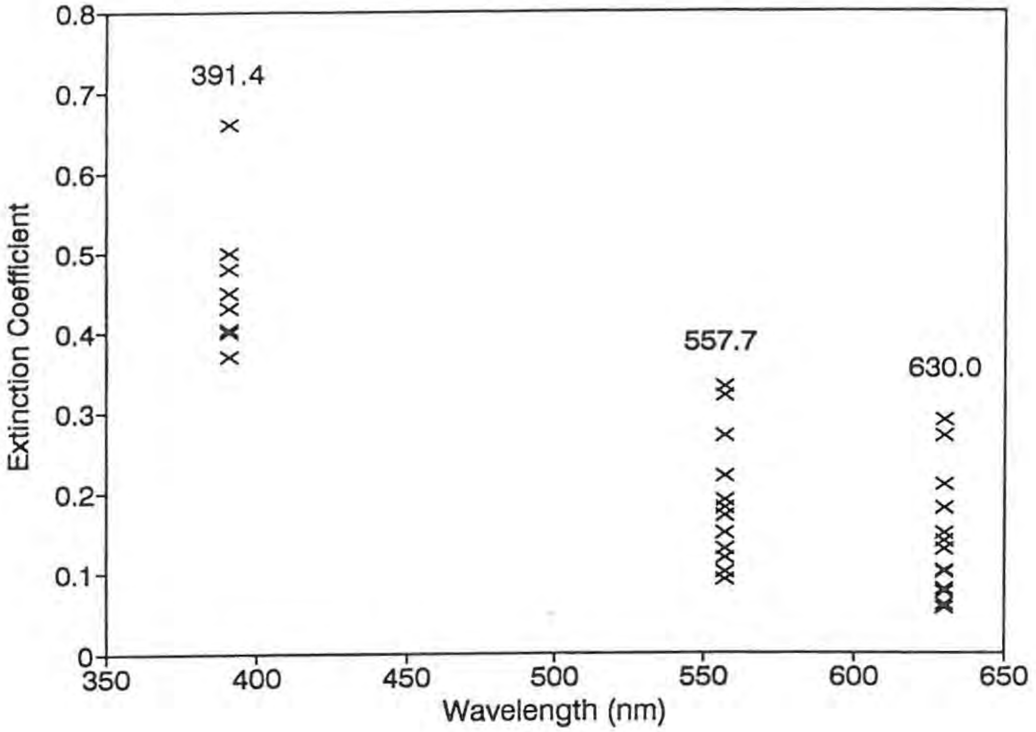

Figure 4.4 Values of τ, the extinction coefficient per unit air mass, that have been measured or used at the emission wavelengths of interest.

Table 4.1 Atmospheric correction factors for different correction models and extinction coefficients.

Emission wavelength (nm)	Height of emitting layer (km)	Extinction Coefficient per unit air mass	Atmospheric Correction Factor	
			E-Method	A-method
391.4	100	0.66	1.93	0.83
		0.37	1.45	0.87
557.7	100	0.33	1.39	0.88
		0.10	1.10	0.94
630.0	300	0.29	1.32	0.92
		0.06	1.06	0.97

then using the minimum value for τ at each wavelength, these ratios vary by factors of 1.52, 1.08 and 1.65 respectively, depending on the atmospheric correction model used. Using the maximum value for τ at each wavelength, the variation in ratios will be 1.54, 1.10 and 1.69 respectively. Although the values of the extinction coefficients can vary appreciably from day to day, the ratio between them for the different wavelengths is unlikely to change much (Guttman, 1968); one would use all high values or all low values of τ, not some high and others low. From the factors given above it is evident that variations in emission ratios depend mostly on the correction model used.

To summarize: Both the calculated values for emission intensities, and the ratios between them, are highly dependent on the model used to determine the corrections for the effects of atmospheric scattering. The emission intensities are also extremely dependent on the values of the extinction coefficients that are used. The uncertainties in the calculated values are of greater magnitude at shorter wavelengths, because Rayleigh scattering varies with λ^{-4}.

Some of the uncertainties in the values of I_0 can be eliminated by using values for the extinction coefficients of the atmosphere that are correct for the time and place of the photometric observations. The only way to ensure this is to make measurements of these coefficients simultaneously with the photometric observations. This is theoretically possible, using a radiometer to measure the changes in apparent brightness of a star with zenith angle, across as wide a range of zenith angles as possible. As the change in air mass with zenith angle is known, the only unknown is the extinction coefficient, which can then be determined. These measurements are only valid if atmospheric conditions do not change during the observation time. Unfortunately, the accurate tracking of a star requires astronomical instrumentation which would be impractical to operate at Sanae.

The author believes that with photometric observations of both airglow and the aurora, the biggest source of errors in the calculated values of emission intensities lies in the estimation of values for the atmospheric correction factors. The next biggest source of errors is probably the calibration factors.

4.4.2 The intensity of the 391.4 nm band

Molecular emissions take the form of spectral bands, rather than spectral lines. The spectral band resulting from the N_2^+ (0,0) 1NG emission has a bandhead at 391.4 nm. Figure 4.5 shows a typical intensity distribution measured for the N_2^+ bands in the vicinity of 391 nm. The P and R branches of the (0,0) band are clearly discernable, with the P branch peaking in intensity at the bandhead wavelength of 391.4 nm.

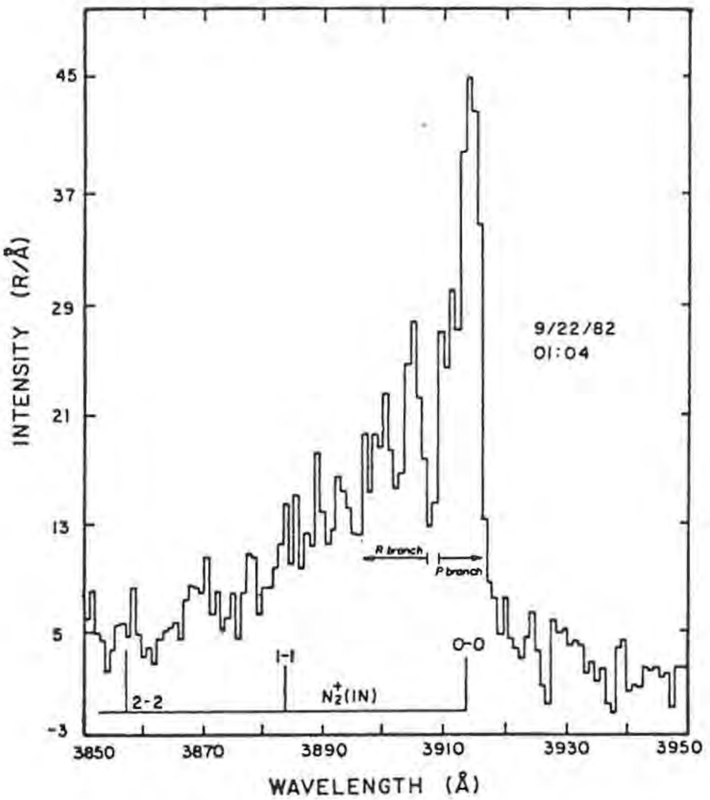

Figure 4.5 A typical measured spectrum of the N_2^+ 1NG (0,0) emission band, showing the P and R branches (after Torr and Torr, 1984). (Note 1 Å = 0.1 nm)

The narrowband interference filter used to measure the 391.4 emissions at Sanae had a peak wavelength considerably greater than 391.4 nm when the filter was in a level position (i.e. normal to incident light). This allowed the background emissions to be sampled at wavelengths above the bandhead. However, when the filter was at its most tilted position, its peak wavelength had only decreased to the wavelength region of the P branch of the band. Consequently, the entire N_2^+ (0,0) band was never fully scanned. The intensity distribution of a molecular band varies with the rotational temperature of the molecule. The inset diagrams in Figure 4.5 are of synthetic spectra which show how the relative intensities of P and R branches of the (0,0) band vary with temperature. The greater the rotational temperature of the molecule, the more spread out the band becomes, and the greater the contribution of the R branch to the total intensity. As a result, the relative contribution of the P branch decreases.

The rotational temperature of a molecular band is dependent on atmospheric temperature, which increases with height. Consequently, the lower the energy of the precipitating particles that cause the N_2^+ emissions, the higher the height of the emission layer, the greater the rotational temperature of the band, and the lower the ratio of the intensity of the P branch to the total intensity of the band. Shepherd and Eather (1976) give ratios of the P branch intensity to that of the whole band, varying between 0.32 and 0.53, which correspond to characteristic energies of <1 keV to 18 keV respectively. Hunten *et al.* (1963) give a diagram which shows the ratio of the P branch intensity of the 391.4 nm band to that of the R branch varying from 0.2 to 1.4. This yields ratios of the P branch intensity to that of the whole band ranging from 0.17 to 0.58.

In order to calculate the total N_2^+ (0,0) band intensity from the measured intensity of the P branch, one has to multiply this intensity by a factor, which is dependent on the (time-varying) intensity distribution of the band. The photometry system used at Sanae does not provide any information as to the intensity distribution of the 391.4 nm band (To do this would require an additional photometer which scans the R branch of the band). As a result, a conversion factor has, somewhat arbitrarily, to be assumed.

Uncertainties regarding the intensity distribution of the band not only affect the determination of the total N_2^+ (0,0) band intensity, but also that of the intensity ratios that use this emission intensity (R_{53} and R_{63}). After communication with Vallance Jones (1991), the author decided that a factor of 2.5 is a reasonable value to use for the conversion of P branch intensities measured at Sanae, to total band intensities. Even taking the (conservative) range of values given by Shepherd and Eather (1976) as limits for the values of the ratio between the P branch intensity and the total intensity, one can expect errors of up to 25% in the values of the N_2^+ (0,0) band intensities that are derived from the Sanae data.

4.4.3 Contamination of OI emissions by nearby OH emissions

The spectral emissions of atomic oxygen at 557.7 and 630.0 nm are prone to contamination by nearby hydroxyl (OH) band emissions. In the vicinity of 630.0 nm, the $P_1(2)$, $P_2(3)$ and $P_1(3)$ rotational components of the OH 9-3 band have bandheads at 628.7, 629.8 and 630.7 nm, with typical intensities of 6 R, 2-4 R and 5-8 R respectively (Hernandez, 1974; Burnside *et al.*, 1977). In the case of the 557.7 nm OI emission, contamination is from the OH 7-2 band at 556.2 nm, which has a typical emission intensity of about 15 R (Davis and Smith, 1965).

The contaminating effects that these emissions have on tilting-filter photometer data differs from the effects that they have on data collected using a fixed filter. With the two-colour fixed-filter method that was popular in the 1960s, the filters used typically had large bandwidths which meant that the OH emissions were measured with the OI line emissions. This resulted in an overestimation of the line emission intensity, due to the contribution of the OH emission. As improvements in technology permitted the production of filters with narrower bandwidths, tilting-filter photometry became possible and background observations could be made at wavelengths in the immediate vicinity of the emission line.

In the case of the tilting-filter photometers used by the author, the background measurements for the OI emissions are made with the filters more tilted than for the line measurements i.e. the backgrounds are recorded at lower wavelengths than those of the lines. For the 557.7 nm observations, this means that the OH 7-2 emission at 556.2 nm will contaminate the background measurements and not the line measurements. Consequently the background will be overestimated, and hence the line emission will be underestimated.

The OH emissions in the vicinity of the 630.0 nm line will have differing effects: Firstly the emission at 628.7 nm will contaminate the background, causing an overestimation of the background. Secondly, the 629.8 nm emission could possibly affect both the line and the background measurements (with more effect on the line measurement). Finally, with a narrowband filter, the 630.7 nm emission is far enough from the line not to have a significant effect on the line measurement. The author is of the opinion that the contaminating effects of the OH emissions in the vicinity of 630.0 nm will probably cancel each other out to a certain degree, resulting in a maximum total contamination effect of less than 5 R.

The $\leq$ 15 R contamination expected at 557.7 nm and the $\leq$ 5 R contamination expected at 630.0 nm will not have significant effects on the emission intensities at these wavelengths during auroral, or even strong airglow, emissions. The effects will only be significant for low level airglow emissions i.e. < 150 R at 557.7, and < 50 R at 630.0 nm.

4.4.4 The airglow and proton-induced components of the aurora

The total emission intensities recorded in the polar regions during auroral activity are made up of a number of components. In the case of the OI emissions at 557.7 and 630.0 nm there is an airglow component due to photo-chemical excitation, a component due to electron excitation, and another due to proton excitation. In the case of the N_2^+ emission at 391.4 nm, the emission is due entirely to particle precipitation; there are electron- and proton-induced components, but no airglow component. To use emission intensities and the ratios between them in order to determine the flux and the energy spectrum of the precipitating electrons, it is necessary to subtract the contributions of the airglow and proton-induced components from the total measured emission intensities.

4.4.4.1 Correction for the airglow component of the aurora

Normally, the airglow contribution to the total emission intensity of the OI lines during auroral activity is negligible. However, for weak auroral emissions (often experienced at Sanae, which is usually outside of the auroral oval) the airglow contribution becomes significant. The airglow components of the total emissions are normally determined by taking the magnitude of the emissions at times when there is either no magnetic activity, or when there is no discernable N_2^+ emission (Eather and Mende, 1972; Gattinger and Vallance Jones, 1972). Both conditions are diagnostic of zero (or minimal) particle precipitation. Airglow emissions normally exhibit slow temporal variations (both diurnally and day-to-day). Consequently, there are two options for estimating the airglow component during auroral activity: For short-duration activity, one can obtain airglow intensity values by interpolating between the airglow values obtained before- and after the auroral activity. For periods of extended activity, one can best estimate the airglow component by using the values for quiet days preceding or following the activity. Either method is more accurate than using arbitrary intensity values for the airglow, such as 250 R at 557.7 nm or 100 R at 630.0 nm. These values are often quoted as typical airglow values, even though airglow intensities show considerable spatial and long-term temporal variations (See Sections 6.4 and 7.3). The variability of the airglow is evidenced by the fact that Gattinger and Vallance Jones (1972) have, during periods of no N_2^+ (427.8 nm) emission, measured large ranges in airglow intensities, viz. 70-300 R at 557.7 nm, and 10-300 R at 630.0 nm. Eather (1968) derived the airglow component of OI emissions by plotting the total measured OI intensities versus the measured H_β intensities for proton-induced auroras. The intercept on the OI intensity axis gives the airglow component. This method yielded airglow emissions of 100-200 R at 557.7 nm and 25-75 R at 630.0 nm. The range in these intensity values were obtained by taking one standard deviation on either side of the mean.

4.4.4.2 Correction for the proton-induced component of the aurora

In Section 2.3.4 it was mentioned that precipitating protons can cause excitation of atoms and molecules that result in auroral emissions. These emissions are called the proton-induced components of the auroral emissions. Eather (1968) has measured the intensities of the N_2^+ 391.4, OI 557.7 and OI 630.0 nm emissions, during proton-excited auroras. The ratios of these emissions to the intensity of the H_β emission were found to have the following ranges (described by one standard deviation from the mean): 10.0 - 17.5, 9.0 - 12.5 and 2.5 - 3.3, respectively. As a result, Eather recommends multiplying the intensities of measured H_β emissions by factors of 17, 10 and 3 respectively, to calculate the proton-induced components of the above-mentioned emissions. These factors were used by Eather and Mende (1972) when they corrected for the proton-excited component of the aurora. Gattinger and Vallance Jones (1972) have used factors of 3, 10 and 3 respectively, for emissions at 427.8, 557.7 and 630.0 nm. The factor of 3 for the 427.8 nm emission would give a factor of about 9.8 for the 391.4 nm emission, using a value of 3.28 for the ratio I(391.4)/I(427.8). Wiens and Vallance Jones (1969) use $I(557.7) = 2.5\,I(H_\alpha)$ as their correction factor for the proton-excited component of the aurora, a figure derived by using Eather's factor of 10 for $I(557.7)/I(H_\beta)$ and a value of 4 for the Balmer decrement $I(H_\alpha)/I(H_\beta)$.

The ratios of the 391.4 and 557.7 nm emissions caused by protons, to the intensity of the H_β emission, are found to increase as the characteristic energy of the precipitating protons increases. This is because protons with higher energies penetrate deeper into the atmosphere, where they encounter higher concentrations of molecular nitrogen ions and oxygen atoms. Edgar *et al.* (1973) predict values of $I(391.4)/I(H_\beta)$ between 0.7 and 10, corresponding to characteristic proton energies of 2 to 100 keV. In contrast, converting the ratios of $I(427.8)/I(H_\beta)$, shown graphically by Rees (1982), to the corresponding values of $I(391.4)/I(H_\beta)$ gives values of 1.6 to 21 for the energy range 2 to 20 keV. Clearly there is a considerable range of ratio values to choose from, both measured and theoretical, when determining the emission intensities of various spectral features due to proton excitation. Consequently, we have another factor that might contribute significantly to the uncertainties in the calculated intensities of the electron-excited component of the aurora.

CHAPTER 5

DETERMINATION OF SYSTEM PARAMETERS

5.1 Introduction

In the previous chapter, equations were derived that can be used to obtain absolute emission intensities from tilting-filter photometer data. These equations contain certain system parameters, namely the transmission factors of the filter (T_l) and the calibration factor of the photometer (B_f). The calibration factor is obtained using the brightness (B) of the light source used to calibrate the photometer. Division of the source brightness by the PMT analogue current or digital counts that it causes, gives calibration factors in units of R nm^{-1} nA^{-1} or R nm^{-1} $count^{-1}$ respectively. Values of T_l and B can be determined in the laboratory prior to (or after) using the photometer in the field. Section 5.2 describes the procedures used to determine the transmission characteristics of the filters that were used at Sanae and on the ISAAC cruise. Section 5.3 describes the cross-calibration of both the quartz tungsten-halogen variable-aperture low brightness source (LBS) and the ^{90}Sr-activated phosphor source.

5.2 The measurement of filter transmission characteristics

The transmission characteristics of narrowband interference filters have already been defined and discussed in Section 3.3.1. Manufacturers of these filters usually supply a typical transmittance curve for the filter, measured with the filter positioned normal to incident light, and at a specific temperature (usually between 20 and 25°C). This makes it possible to determine the peak wavelength, the peak transmittance, the bandwidth and the transmission factor of the filter; but these parameters are only applicable to a newly-purchased filter, when it is used in a level position. Transmission factors are needed for the filters at angles other than normal to incident light. Fortunately, this does not present a problem as the Chemistry Department at Rhodes University has a Beckman spectrophotometer (model UV 5240) which can be used to obtain accurate transmission characteristics for the filters. The spectrophotometer is designed for operation in the UV, visible and near-IR ranges of the spectrum, and so can be operated in the wavelength ranges of the filters in question (380 to 640 nm). The wavelength of the light used by the spectrophotometer to measure a sample's transmittance is accurately controlled and calibrated. Furthermore, it can be swept through a range of wavelengths, to produce a plot of the sample's transmittance versus wavelength. The output plots are produced on a chart recorder built into the spectrophotometer. Chart speeds and gains can be selected to maximize the resolution of the output records.

The sample being tested is placed in a light-tight sample chamber. This chamber contains a set of parallel rails which are normally used to support a standard sample holder (designed to hold small phials of liquid). In order to be able to adjust the tilt angle of the filter relative to the light incident upon it, the author had a special sample holder constructed to replace the standard holder. This holder allows the filter tilt angle to be adjusted to angles between 0 and 25° (relative to the normal to the incident light), in 2.5° steps. The holder fits tightly onto the rails in the sample chamber, thus eliminating any play in the orientation of the holder relative to the spectrophotometer's light beam.

The author made a further modification to the spectrophotometer, to allow accurate control of the temperature in the sample chamber. This was necessary in order to measure the changes in filter transmission characteristics with temperature. Temperature control was achieved in the following way: Firstly the lid of the sample chamber was removed, and replaced with a lid that allows air to be circulated via two 25 mm diameter pipe fittings. Care was taken to ensure that the new lid kept the sample chamber light-tight. The inside of the lid and the floor and walls of the sample chamber were then lined with thin sheets of expanded polystyrene, to provide thermal insulation. These sheets were painted with matt black paint to minimize any reflection of light. The analogue temperature control circuitry which is normally used to control the temperature of the filter chambers in the photometers (see Section 3.4.3), was used to control the temperature in the sample chamber. The temperature sensor was positioned close to the filter, and heated air was circulated via the pipe fittings in the lid of the chamber. Temperature stability was achieved to within 1°C. Unfortunately, the ambient temperature of the room housing the spectrophotometer was only just below 20°C, so that the temperature of the sample chamber could only be regulated at, or above, this temperature.

Prior to measuring the transmission characteristics of the filters, the calibration of the spectrophotometer was checked. The wavelength accuracy was measured using the spectrophotometer's own deuterium ($_1H^2$) lamp, which has spectral lines at 486.2 and 656.3 nm. In each case the wavelength displayed by the instrument was found to deviate from the correct wavelength by 0.1 nm. It was assumed that this error was constant throughout the wavelength range, and consequently a correction of 0.1 nm was applied to all peak wavelength determinations. The 0% and 100% transmittance levels on the chart recorder output were also checked by using a totally opaque sample and no sample, respectively.

The filter characteristics of each filter were measured in the following way: Transmittance curves were obtained at a fixed temperature, for tilt angles between 0° and 15° inclusively, in steps of 2.5°. The fixed temperature used for each filter was set to be the same as that normally used for the filter during photometric observations. Further transmittance curves were recorded with the filter kept in a level position, but with the filter temperature varied in 5°C steps, between 20 and 45°C inclusively. Care was taken to allow the filter temperature to stabilize at each new temperature setting, before recording the transmittance curve.

Finally, for the filters that were used at Sanae, a transmittance curve was obtained with the filter level and at the same temperature as was used by the manufacturer when they produced the filter's transmittance curve. Peak wavelengths, peak transmittances and bandwidths were read directly from the graphs. The values of these parameters for the filters used at Sanae are tabulated for 1975 and 1985 in Table 5.1. All values are for the filters positioned normal to incident light. The 1975 values were determined from the transmittance curves supplied by the filter manufacturers (Thin Film Products) at the time of purchase. The 1985 values are those measured by the author using the spectrophotometer. The latter measurements were taken from the transmittance curves that were recorded with the filters at the same temperatures as those given by the manufacturers for their original measurements. If we assume that both the 1975 and the 1985 measurements are accurate, then from Table 5.1 it is evident that there has been a marked degradation in the performance of all the Sanae filters with age, characterized by decreases in peak transmittance and increases in bandwidth. In the case of peak wavelength, the 391.4 nm filter showed an increase in peak wavelength, whilst the 557.7 and 630.0 nm filters both showed a decrease in peak wavelength. Eather and Reasoner (1969) have attributed the temporal shifts in a filter's peak wavelength to crystallization within the filter. However, they make no mention of changes in peak transmittance or bandwidth. Henriksen (1974), after consultation with Infrared Industries (the parent company of Thin Film Products), says that the principal effect of natural ageing on filters is a wavelength shift of about 0.2 to 0.4 nm towards shorter wavelengths. Apparently there should be no significant change in a filter's peak transmittance or bandwidth with age. In contrast with these reports, the changes in peak wavelength, bandwidth and peak transmittance shown in Table 5.1 are considerable; a disturbing fact, as there is no certainty as to how these parameter values changed in the period between 1975 and 1985. Although the filters were used at Sanae during every

Table 5.1 Transmission characteristics of the Sanae filters measured in 1975 and 1985.

Nominal wavelength of the filter (nm)	Year	Transmission characteristics			
		Peak wavelength (nm)	Half-power bandwidth (nm)	Peak transmittance (%)	Bandwidth x peak transmittance (nm)
391.4	1975	394.1	13.5	19.9	2.69
	1985	396.1	19.0	19.6	3.72
557.7	1975	558.1	0.35	29.0	0.10
	1985	557.6	0.92	14.8	0.14
630.0	1975	630.3	0.35	38.9	0.14
	1985	629.7	0.63	23.7	0.15

winter from 1976 until 1984, it cannot be assumed that the changes in the parameter values were linear with time. In fact, two factors point to the probability that the changes in the filters' characteristics occurred early in their lifetime: Firstly, Henriksen (1974) predicts that the wavelength shift in a filter's peak wavelength should occur during the first two years of the filter's lifetime. Secondly, as early as 1977 (within two years of its purchase) it was necessary to operate the Sanae 630.0 nm filter at a temperature of 45°C in order to get a peak wavelength of above 630.0 nm, even with the filter level. It may be concluded that the major portion of the wavelength shift of this filter had in fact taken place before this time. It seems reasonable to assume that the changes in the filters' peak transmittance and bandwidth probably occurred simultaneously with the wavelength shift.

The transmission characteristics of the filters used on the ISAAC cruise were measured early in 1984. Table 5.2 gives the peak wavelengths, peak transmittances and bandwidths of these filters. Unfortunately there is no evidence of initial (manufacturer's) transmittance curves for these filters, so no assessment could be made of the effects of ageing on these filters. However, in the time between the cruise and the measurement of the filters' transmission characteristics, the filters were not used and were stored in a cool, light-tight environment. Consequently there should have been little change in the filters' characteristics during this time.

Table 5.2 Transmission characteristics of the filters used on the 1983 ISAAC cruise, measured in 1984.

Nominal wavelength of the filter (nm)	Transmission characteristics		
	Peak wavelength (nm)	Half-power bandwidth (nm)	Peak transmittance (%)
391.4	392.1	1.7	30.0
557.7	558.1	0.5	28.0
630.0	630.4	0.8	49.0

Transmission factors for all of the Sanae and ISAAC filters were obtained by manually integrating the areas under their transmittance curves, for the range of tilt angles used. These factors were then plotted against tilt angle, so that values could be interpolated for intermediate tilt angles. Figures 5.1 and 5.2 show the variations in transmission factors with filter tilt angle for the filters used at Sanae from 1976-1984, and for the filters used on the ISAAC cruise during June/July 1983, respectively.

Having seen the effects of ageing on the Sanae filters' other characteristics, it is certain that the transmission factors will also have changed since the filters were manufactured. In most cases a filter's transmission factor (the area under its transmittance curve) is approximately equal to the product of the filter's bandwidth and

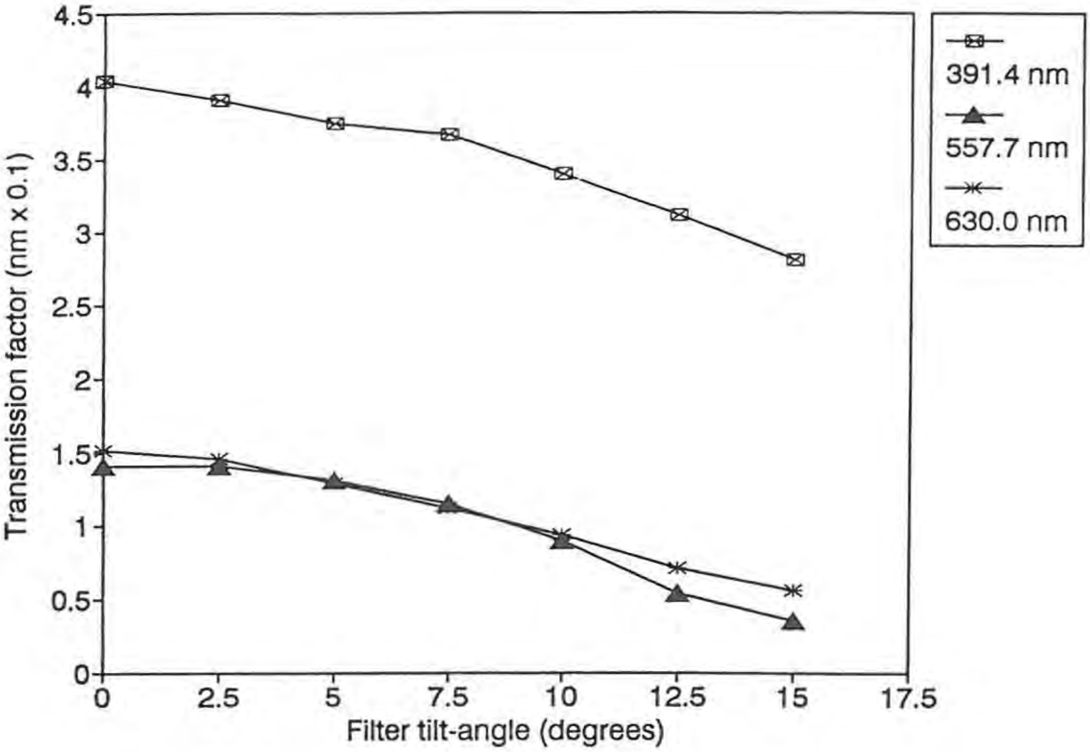

Figure 5.1 The variation in transmission factors with tilt angle for the filters used at Sanae (1976-1984).

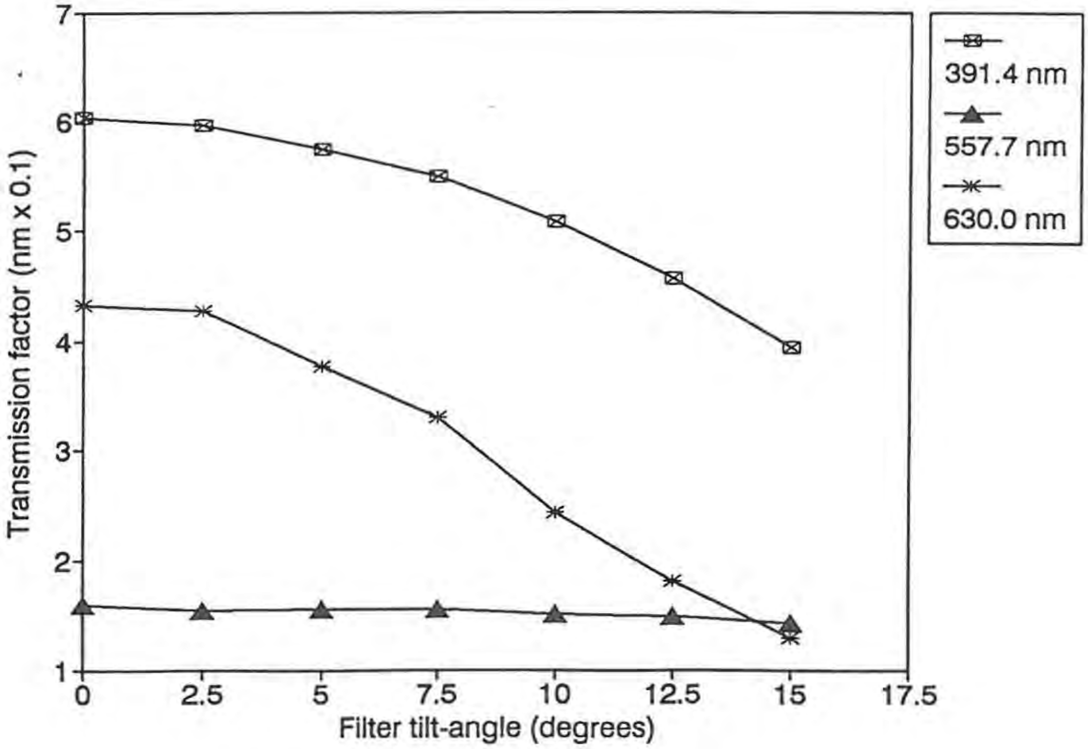

Figure 5.2 The variation in transmission factors with tilt angle for the filters used on the ISAAC cruise in 1983.

peak transmittance. (For a pure Gaussian curve, the area under the curve is a factor of 1.06 greater than the product of the peak height and the bandwidth). Consequently, the decreases in peak transmittance and increases in bandwidth with age will have something of a compensatory effect: The relative changes in the transmission factors of the Sanae filters are unlikely to be as large in magnitude as the changes in their peak transmittance and bandwidth. This is evident if the bandwidth-peak transmittance products for the Sanae filters for 1975 are compared with those for 1985. These products are listed with the filters' transmission characteristics in Table 5.1. The biggest percentage change in the value of the bandwidth-peak transmittance product is 40%. Finally, as we do not know what the Sanae filters' transmission factors were in 1975 for the filters in tilted positions, it was decided to use the 1985 transmission factors for all Sanae data reduction.

With hindsight, it is clear that for accurate results, the transmission characteristics of the filters need to be measured on a regular basis, such as once a year. To do this with the filters that are used in Antarctica would require four filters for each emission feature being observed; at any one time, two filters will be in Antarctica (one filter in use, the other a spare), and two in South Africa (for calibration). The filter sets would then be interchanged at the end of each year, during the summer takeover. This would permit the filters' transmission characteristics to be measured immediately prior to, and immediately after, use in Antarctica.

The measurement of the Sanae filters' transmission characteristics for different filter temperatures yielded results that are in agreement with the findings of Blifford (1966): The only characteristic to show noticeable changes with temperature was the peak wavelength of each filter. No significant changes were evident in bandwidths, peak transmittances or transmission factors. Figure 5.3 illustrates the shift in peak wavelength with temperature for the Sanae filters in a level position. All shifts are measured relative to the peak wavelengths of the filters at 20°C. All three filters show reasonably linear wavelength shifts with temperature. The average changes in wavelength with temperature, over the range 20 to 45°C, are given in Table 5.3. These temperature coefficients are of the same order of magnitude as those measured by Blifford (1966) and Anger *et al.* (1973). A knowledge of the variation of a filter's peak wavelength with temperature allows the determination of the minimum filter temperature that can be used for the filter to scan the spectral emission feature that is to be observed.

5.3 Calibration of the secondary light sources

At Sanae, and on the ISAAC cruise, portable secondary light sources were used to calibrate the photometers in the field. Calibrations with these sources were carried out frequently, in order to monitor the stability of the photometry systems. When calibrating a photometer with a secondary light source, the accuracy of the calibration depends on the stability of the secondary light source, and on its accurate cross-calibration against

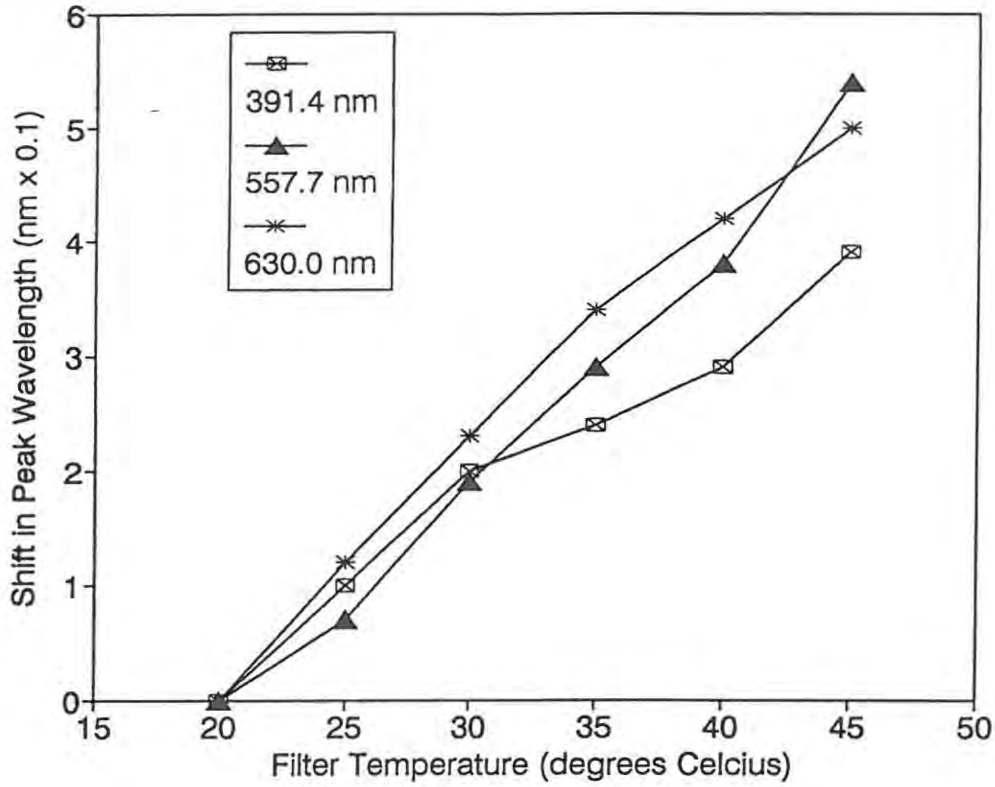

Figure 5.3 The relative shifts in wavelength of the peak wavelengths of the Sanae filters as a function of temperature.

Table 5.3 The average temperature coefficients of the peak wavelength shift of the Sanae filters, measured between 20 and 45°C with the filters at normal incidence.

Nominal wavelength of the filter (nm)	Temperature coefficient of the wavelength shift (nm (°C)$^{-1}$)
391.4	0.016
557.7	0.022
630.0	0.020

a primary light source. In the previous chapter (Section 4.4.1.2, item 4) the stability of the variable-aperture low-brightness sources (used at Sanae and on the ISAAC cruise) was discussed. The brightness of these sources is considered to be stable to within 5%. Thus, the only factor still in doubt is their absolute brightness.

Shortly after their construction at Rhodes University, the two variable-aperture sources (LBS #1 and LBS #2) were cross-calibrated against a ^{14}C-activated phosphor source belonging to the National Institute of Telecommunications Research (NITR). The calibrations were conducted in 1978 at the South African Astronomical Observatory in Sutherland, under the supervision of R. Burnside. The cross-calibrations were performed using the NITR photometer normally used by Burnside to observe the airglow at Sutherland (see e.g. Torr *et al.*, 1976a; Burnside and Tepley, 1990). The ^{14}C source has been calibrated on at least three occasions: Firstly, it was calibrated by M. Gadsden and V. Blacker at the Fritz Peak Observatory in 1970. This calibration is directly traceable to the National Bureau of Standards, Boulder, Colorado (Torr *et al.*, 1976b). Secondly, it was cross-calibrated against the source used to calibrate the photometer on the AE-C satellite (Torr *et al.*, 1977). These two calibrations of the ^{14}C source differ by less than 10%. Finally, after the source became the property of the Magnetic Observatory at Hermanus, it was recalibrated at the IAGA Optical Calibration Workshop held in Aberdeen in August 1981. The transfer source used for this workshop was calibrated by M.R. Torr. The Aberdeen calibration of the ^{14}C source again produced brightnesses that deviated by less than 10% from the source's original calibration in 1970. From the consistency of these results, it can be assumed that the source's calibration is reliable.

At Sutherland the brightnesses of both these Rhodes variable-aperture sources were determined at the following wavelengths: 391.4, 486.1, 557.7 and 630.0 nm. Brightnesses were measured for all eight apertures of each source. Each source was calibrated with its own precision power-supply and cabling. In order to have spare calibrated lamps ready for each source, three tungsten-halogen lamps were calibrated for each source. The relative brightnesses of the six lamps used in the calibration were found to differ by as much as 10%. The brightnesses of LBS #1 and LBS #2, as determined at Sutherland in 1978, are tabulated in Appendix H.

One problem with the cross-calibration was the very low brightness of the ^{14}C source at a wavelength of 391.4 nm (the brightness at this wavelength was only 1 R nm^{-1}, compared with a value of over 90 R nm^{-1} at 630.0 nm). Furthermore, this source was calibrated only once at this wavelength (391.4 nm), at its initial cross-calibration in 1970. Torr (1985) is of the opinion that the brightness of the ^{14}C source at 391.4 is too low to be calibrated accurately. In addition, the intensity of the source varies rapidly with wavelength in this low wavelength region. These two factors together lead to the conclusion that brightness values at this wavelength should be considered unreliable.

Initial processing of Sanae photometer data (see Sections 6.3 and 6.4) yielded airglow and auroral intensities that were lower than might be expected at Sanae. In addition, the ratio of the intensity of the atomic oxygen emission at 557.7 nm to the intensity of the N_2^+ emission at 391.4 nm was found to be higher than the expected value of 2 ± 1. A possible reason for these results might be the calibration of the variable-aperture light source that was used to calibrate the photometers at Sanae. Consequently, it seemed advisable to check the calibration of this secondary source. There are several ways in which this could be done:

Firstly the source could be calibrated against a standard reference light source, e.g. by taking it to the National Bureau of Standards in Boulder, Colorado. Considering the bulk of the source and its power supply, this was not considered a viable option.

Secondly the source could be cross-calibrated against the Rhodes University ^{90}Sr source, which was calibrated at the Calibration Workshops held in Aberdeen (1981) and Lindau (1983). The problem with this option is that the workshops were unable to cross-calibrate light sources at wavelengths as low as 391.4 nm. Consequently this option can only be used for cross-calibrations at 557.7 and 630.0 nm. Another problem with using the ^{90}Sr source is the fact that its Lindau calibration differs significantly from its Aberdeen one. The brightnesses measured at Lindau were found to have decreased by 16% at 557.7 nm and 25% at 630.0 nm, relative to the values obtained at Aberdeen. The reasons for this apparent decrease in the brightness of the ^{90}Sr source are not known. As mentioned in Section 4.4.1.2, the decay of the ^{90}Sr isotope (half-life = 28.1 years) should only cause a decrease in brightness of about 5% over a period of two years. Uncertainties in the absolute brightnesses of the reference (transfer) sources that were used at the workshops might have made some minor contribution, as might the difference between the temperatures at which the cross-calibrations were conducted (26°C at Aberdeen, and 23°C at Lindau).

The third option was to obtain accurately calibrated standard lamps that could be used in conjunction with a white screen, in order to provide a diffuse source of known brightness. Such lamps are supplied locally in South Africa by the National Physical Research Laboratories (NPRL) of the CSIR, so it was decided to pursue this option. Besides cross-calibrating the variable-aperture sources, this method would also supply a means of calibrating the ^{90}Sr source at 391.4 nm. Furthermore, it might also provide useful input to the question of the ^{90}Sr source's differing 557.7 and 630.0 nm brightnesses, obtained at Aberdeen and Lindau.

Two standard lamps were calibrated by the NPRL for use in the Rhodes University cross-calibration. One (#1681) is a squirrel cage filament lamp, the other (#N1) is a automobile tail-light lamp. The bulbs were calibrated by comparison with the known spectral irradiances of standard lamps owned by the NPRL, using a spectroradiometer (Kok, 1984). The spectral irradiances (E_λ, in units of mW m^{-2} nm^{-1}) that were supplied for each lamp, for wavelengths of 391.4, 557.7 and 630.0 nm, are given in Table 5.4. The operating currents and the distances at which the lamps were calibrated are also given. The calibration uncertainties were quoted by the NPRL as ±5% at 391.4 nm, and ±3% at the higher wavelengths. As the spectral irradiances of these lamps are unlikely to be constant in all directions, alignment marks were made on the lamps, to allow the lamps to be orientated in the same way as for their calibration. (The marks must face away from the direction of calibration).

Table 5.4 Spectral irradiances of the standard lamps calibrated by the NPRL.

Lamp identification	Calibration wavelength (nm)	Spectral irradiance (Mw m^{-2} nm^{-1})
#1681 Operating current: 0.2281 A (± 100 V) Calibration distance: 550 mm	391.4	0.0631
	557.7	0.766
	630.0	1.497
#N1 Operating current: 1.000 A (± 12 V) Calibration distance: 350 mm	391.4	0.0943
	557.7	0.814
	630.0	1.486

The theory behind using a standard lamp and a white screen as a means of cross-calibrating a secondary source is as follows: The brightness, B (in R nm^{-1}), of a white screen illuminated by a standard lamp is given (see Appendix D) by

$$B_\lambda = \frac{2.01 \times 10^3 \, E_\lambda \, \rho_\lambda \, \lambda \, d^2}{D^2} \qquad (5.1)$$

where: E_λ is the spectral irradiance of the lamp in mW m^{-2} nm^{-1},

λ is the wavelength in nm,

d is the distance at which the lamp's irradiance was measured,

D is the distance between the lamp and the white screen, and

ρ_λ is the reflectance of the screen (dimensionless, with a value between 0 and 1).

The screen is assumed to be a Lambertian surface, scattering light equally in all directions over the 2π steradians in front of it. If the illuminated screen fills the field of view of a photometer, then the brightness seen by that photometer will be constant, regardless of the distance between the photometer and the screen, and regardless of the angle at which the photometer views the screen. The proof of this statement is included in the derivation of the above equation in Appendix D.

If a photometer is operated in photon-counting mode then the brightness of a secondary source, called the test source, is given in terms of the brightness of the white screen, called the reference source, by

$$B_{\lambda,test} = \left(\frac{n_{test} - n_{dc}}{n_{ref} - n_{dc}} \right) B_{\lambda,ref} \tag{5.2}$$

where: n_{test} is the photometer count when the test source fills the field of view of the photometer,
n_{ref} is the photometer count when the reference source fills the field of view of the photometer, and
n_{dc} is the photometer count with the shutter closed, i.e. the count corresponding to the PMT dark current.

Thus the brightness of a secondary source, at a wavelength determined by the filter used in the photometer, can be determined using the spectral irradiance of a standard lamp.

The accuracy of such a cross-calibration is dependent on the conditions under which it is conducted. The instrumentation for the cross-calibration was set up in a proper light-tight optics laboratory. The configuration used for the measurement of the brightness of the white screen is shown in Figure 5.4. The lamp was positioned on a stand at the same height as the centre of the white screen. Wooden baffles, measuring 1 m by 1 m, were constructed on stands so that they too could be correctly aligned with the lamp and the screen. A square aperture was cut in the centre of each baffle, with dimensions as given in Figure 5.4. The baffles were coated with matt-black paint to minimize reflections. With this configuration, the half-angle of the beam of light illuminating the screen was 1.15°. To test the effectiveness of the baffles, and to check for any contribution of light scattered from sources other than the white screen, the screen was replaced with a matt-black screen and PMT counts were recorded. Although the standard lamp was left burning, no significant counts were recorded above those due to the PMT dark current. As a result, the author is confident that the intensities measured by the photometer are due only to light reflected by the white screen.

The white screen itself was prepared in the following way: A sheet of aluminium of suitable dimensions was selected, which was both flat and relatively unmarked. The sheet was then immersed in a bath containing a strong solution of sodium hydroxide (caustic soda) in order to roughen its surface. Once the surface of the aluminium had been sufficiently etched, it was removed from the bath, washed well and then dried. The surface of the sheet was then coated with magnesium oxide (MgO). This was done by supporting the sheet in a horizontal face-down position and burning pure magnesium ribbon beneath it. Care was taken to ensure that the sheet was evenly coated with a thick deposit of MgO. The coating was done immediately prior to the cross-calibration as the reflectance of MgO decreases with age. The reflectance of a surface newly coated with MgO is virtually a constant 0.98 over the wavelength range 375 to 700 nm (Grum and Luckey, 1968). An alternative to coating the screen with MgO is to coat it with a paint prepared from one part of polyvinyl alcohol and 100 parts of barium sulphate powder. This alternative should be chosen if the screen

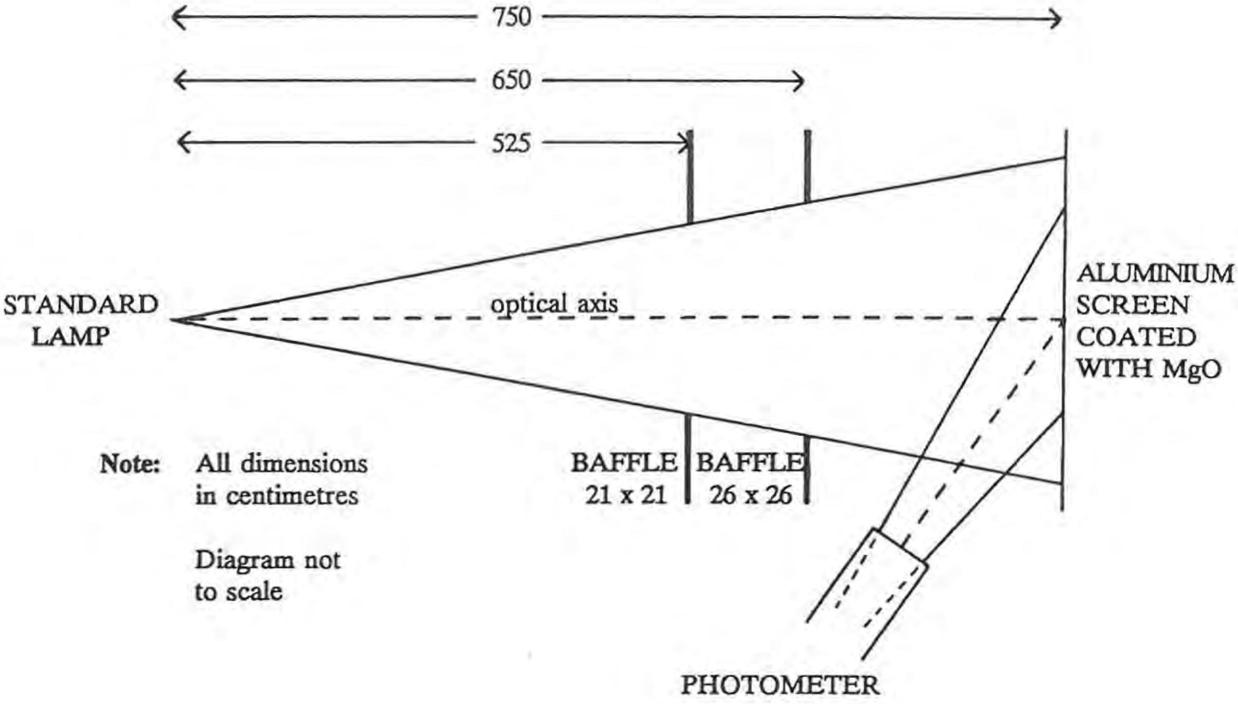

Figure 5.4 The configuration used to measure the brightness of a white screen, illuminated by a standard lamp of known spectral irradiance.

needs to be used over an extended period of time, or if it is to be used in the UV region of the spectrum (Grum and Luckey, 1968).

The photometer configuration for the cross-calibration is shown in Figure 5.5. The measured transmission characteristics of the filters were used to calculate the combinations of filter temperatures and tilt angles necessary to centre the passbands of the filters at the wavelength of the three emission lines of interest (391.4, 557.7, and 630.0 nm). A special computer program was written to control the photometer's operation. This program sets the filter temperatures and tilt angles, and outputs , to a printer or floppy disk, both the source and dark current counts and the difference between them. In order to minimize the chances of introducing uncertainties due to the positioning of the different filters in the photometer, the filters were exchanged as little as possible; when a filter was inserted into the photometer, counts were taken for all four sources (the two standard lamps, the ^{90}Sr source, and the variable-aperture source LBS #2) before changing to the next filter. For each source and wavelength, at least ten sets of source and dark current counts were recorded, all using integration times of 32 seconds. From these data, mean counts and standard deviations were calculated. In all cases the standard deviations were less than 5% of the mean count value.

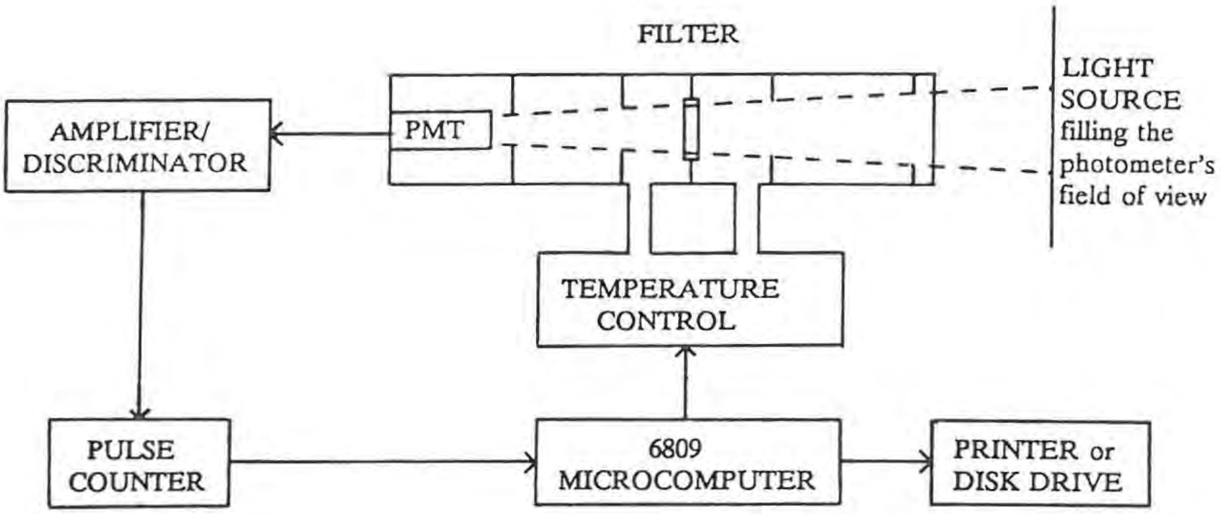

Figure 5.5 A block diagram of the photometer configuration used for the cross-calibration.

The variable-aperture source (LBS #2) calibrated during this cross-calibration was the one used on the ISAAC cruise. The lamp (#6) used in the LBS was also the same as that used on the ISAAC cruise. Only aperture 5 of the LBS was used for the cross-calibration. The brightnesses for other apertures were calculated from the previously-determined ratios between the areas of the apertures (tabulated in Appendix H). Although the variable-aperture LBS used at Sanae (LBS #1) was not cross-calibrated in 1984, it should be possible to relate its brightnesses to the brightnesses of the LBS #2 / lamp #6 combination: One can use the ratios between the brightnesses of the various LBS/lamp combinations measured at Sutherland in 1978 (see Appendix H for the tabulated brightnesses).

The data collected during the cross-calibration were processed in the following way: Equation 5.1 was used to calculate the brightnesses of the MgO screen when illuminated by each of the standard lamps. The distance, D, between the lamp and the screen was fixed at 7.5 m, and a value of 0.98 was used for the reflectance at all wavelengths. Values for E_λ and d were taken from Table 5.4. The resultant brightnesses are given in Table 5.5. Equation 5.2 was then used to calculate the brightnesses of the secondary sources (LBS #2 and the ^{90}Sr source). These are given in Table 5.6, together with the brightnesses previously determined for these sources. (Note: In the case of the Aberdeen and Lindau cross-calibrations of the ^{90}Sr source, two brightnesses are given: The unbracketed values are the brightnesses as determined at the workshops, whilst the values in square brackets [ ] are brightnesses that have been corrected for the reduction in source brightness since the workshops, due to the 28.1 year half-life of ^{90}Sr). Brightness values for the variable-aperture LBS have also been calculated by cross-calibrating it against the half-life corrected brightnesses of the ^{90}Sr source determined from the original Aberdeen and Lindau cross-calibration results. These are also given in Table 5.6. The values given in round brackets ( ) beneath the brightness values in Table 5.6 are the ratios of that brightness to the brightness at 557.7 nm.

Table 5.5 The brightnesses of the MgO screen when illuminated by the standard lamps.

Lamp used to illuminate the MgO screen	Wavelength (nm)	Screen brightness (R nm^{-1})
NPRL #1681	391.4	260.3
	557.7	4154
	630.0	9941
NPRL #N1	391.4	157.5
	557.7	1938
	630.0	3996

Table 5.6 Calibrated brightnesses of the Rhodes secondary light sources. The significance of the bracketed values in the table are explained in the text.

Source calibrated	Location and Date	Reference Source	Source Brightness (R nm^{-1})		
			391.4 nm	557.7 nm	630.0 nm
Variable-aperture LBS #2 Aperture #5 Lamp #6 12 V	Sutherland 09/78	Hermanus ^{14}C (was NITR)	28.9 (0.033)	884 (1.0)	2000 (2.26)
	Rhodes Univ. 06/84	NPRL #1681	23.5 (0.041)	572 (1.0)	1348 (2.36)
	Rhodes Univ. 06/84	NPRL #N1	23.3 (0.037)	624 (1.0)	1426 (2.29)
	Rhodes Univ. 06/84	^{90}Sr phosphor (Aberdeen)	no value	962 (1.0)	1880 (1.96)
	Rhodes Univ. 06/84	^{90}Sr phosphor (Lindau)	no value	847 (1.0)	1490 (1.76)
^{90}Sr activated phosphor bright side plateless	Aberdeen 08/81	The brightnesses of both of the workshop transfer sources are traceable to NBS standards	no value	1467 [1371] (1.0)	212 [198] (0.14)
	Lindau 08/83		no value	1230 [1205] (1.0)	160 [157] (0.13)
	Rhodes Univ. 06/84	NPRL #1681	0.54 (0.0007)	813 (1.0)	141 (0.18)
	Rhodes Univ. 06/84	NPRL #N1	0.53 (0.0006)	888 (1.0)	150 (0.17)

The results of the cross-calibration warrant comment:

Both the LBS #1 and the ^{90}Sr sources show considerable variations in their brightness values obtained from the different cross-calibrations. The decrease in brightness of the variable-aperture source might be due to ageing of the filament of the quartz tungsten-halogen lamp. As mentioned in Chapter 3, this type of lamp is self-cleaning, so there should be minimal deposits on the glass envelope. It is possible that the decrease in source brightness with age observed in the ^{90}Sr-activated phosphor source is due to deterioration of the plastic scintillator containing the phosphor. Although the various cross-calibrations have yielded appreciable ranges in the brightnesses obtained for both sources, for any given source and wavelength all brightnesses are within a factor of two of each other. In fact, the worst range in brightness occurred for the ^{90}Sr source at a wavelength of 557.7 nm, where the ratio of highest to lowest brightness is 1.69. Assuming that the actual brightnesses of the secondary sources are within the ranges defined by the values in Table 5.6, the maximum uncertainty in measured emission intensities, resulting from photometer calibrations that used these secondary sources, should also be under a factor of two.

Another encouraging result is the small variation in the brightness ratios of each secondary source for the different cross-calibrations. The brightness ratios referred to here are the figures in brackets in Table 5.6: B(391.4)/B(557.7) and B(630.0)/B(557.7). The brightness ratios for the variable-aperture source LBS #2, when calibrated against the Hermanus ^{14}C source and the two standard lamps, are consistent to within 20%. This implies that the calibration of the LBS used at Sanae should not be a major source of error in the observed ratios between emission intensities; the high I(557.7)/I(391.4) ratios observed at Sanae definitely cannot be explained solely by uncertainties in the calibration of the photometers.

Returning to the above-mentioned brightness ratios for LBS #2, the only brightness ratio not within 10% of those for the other two cross-calibrations, is that involving the 391.4 nm cross-calibration against the ^{14}C source. This is not unexpected, as it has already been noted that Torr (1985) is of the opinion that the calibration of the ^{14}C source at 391.4 nm is probably unreliable because of its very low brightness at this wavelength. Results of this cross-calibration indicate that the brightness of the ^{14}C at 391.4 nm might be higher than the value obtained for its calibration in 1970.

The cross-calibrations that used the NPRL-calibrated standard lamps as references, yielded brightnesses for the secondary sources that are all lower (by factors in the region of 1.5) than the brightnesses obtained from earlier cross-calibrations of these sources. This prompts one to suspect some sort of systematic error in the cross-calibrations involving the standard lamps. The most logical explanation for the low brightness values obtained for the secondary sources would be that the standard lamps were brighter than their calibrated values. However, the NPRL is confident that the spectral irradiances supplied for the standards lamps are correct to within 5%. During the cross-calibration the currents supplied to the standard lamps were kept within 1% of the values specified by the NPRL. Furthermore, care was taken to ensure that the standard lamps were correctly aligned in the same orientation as was used for the determination of their spectral irradiances. Another factor that might affect the accuracy of the cross-calibration is the determination of the screen's brightness using Equation 5.1. If the spectral irradiances of the standard lamps are assumed to be correct at the distances (d) specified by the NPRL, the only remaining possible sources of error in Equation 5.1 are the parameters λ, D, and r_λ. To consider each of these in turn: The wavelength λ is determined by the tilt angle and temperature of the filter in the photometer. Errors in the wavelengths used for the cross-calibration are probably far less than 1 nm. Variations in the spectral irradiances of the lamps will be insignificant over such a wavelength interval. Secondly, the distance D (= 7.5 m) between the lamp and the reflecting screen was accurately measured. The error in D is much less than 1% (75 mm). Finally, for the screen's reflectance to have any appreciable effect, it would have had to have been significantly lower than 0.98, the value that was used. If this were so, the calculated screen brightness would have been too high, and the calculated brightness of the test source would have been too high, not too low. In view of these considerations, the author is quite unable to find any source of systematic error which could explain the low brightness values obtained in the cross-calibrations of the secondary sources against the standard lamps.

To summarize, the following conclusions can be drawn from the results of the 1984 cross-calibration:

1/ There are still significant uncertainties as to the correct brightnesses of the secondary sources (LBS #1, LBS #2 and the ^{90}Sr-activated phosphor source).

2/ Considering the results of all cross-calibrations, the variable-aperture LBS has more consistent brightnesses and brightness ratios than the ^{90}Sr source. A number of factors point to the LBS being superior to the ^{90}Sr source as a secondary source for the calibration of photometers in the field.

3/ Uncertainties as to the brightness of the variable-aperture sources are unlikely to affect calculated emission intensities by as much as a factor of two.

4/ In view of the consistency in the brightness ratios of the variable-aperture LBS (all brightness ratios are within 20% of each other), the calibration of LBS #1 can be ruled out as a significant contributory factor to the high I(391.4)/I(557.7) intensity ratios observed at Sanae.

5/ For accurate results the secondary calibration sources should be regularly cross-calibrated against reliable primary sources.

CHAPTER 6

PHOTOMETRIC OBSERVATIONS OF THE AIRGLOW AND AURORA AT SANAE, ANTARCTICA

6.1 Introduction

During the period 1976 to 1984, an analogue photometry system consisting of three meridian-scanning tilting-filter photometers was operated by Rhodes University physicists at Sanae, the South African base in Antarctica. The photometers were used to record the intensities of the following airglow and auroral emissions: the OI emission lines at 557.7 and 630.0 nm, and the N_2^+ (0,0) molecular emission with a bandhead at 391.4 nm.

The main function of this chapter is to show how a meridian-scanning photometry system can be used to study the airglow and aurora at Sanae. Clearly the photometric data, collected at Sanae over the nine year period mentioned above, is suitable for the study of the diurnal, seasonal and solar-cycle variations of both the airglow and auroral emission intensities in the vicinity of Sanae. This chapter, however, will concentrate on the application of photometric data to the study of the auroral component of a magnetospheric substorm. The magnetospheric substorm of 27 July 1979 will be used as an example.

Section 6.2 considers the influence that Sanae's geographic and geomagnetic positions have on the photometric observations that can be made there. Section 6.3 discusses the processing and presentation of the intensity data obtained using a meridian-scanning photometry system. Section 6.4 presents some airglow (i.e. non-auroral) observations made at Sanae, immediately prior to the substorm of 27 July 1979. Section 6.5 covers the photometric observations of the aurora during the substorm. Finally, Section 6.6 discusses the intensity ratios during the substorm. The ratios are compared with those obtained by other researchers.

Note: Frequent mention is made in this chapter of various spatial and temporal coordinate systems (e.g. corrected geomagnetic coordinates, invariant latitudes, L-values and magnetic local time), and of magnetic activity indices (e.g. Kp and AE). For the reader's convenience, Appendix E describes many of the coordinate systems and magnetic activity indices that are commonly used in auroral research.

6.2 The effects of Sanae's position on photometric observations

Clearly both the geographic and geomagnetic positions of a station affect the quality, quantity and type of photometric data that can be collected there. Geographic position determines the times at which data can be collected. In polar regions this is particularly relevant because of the considerable variation in nighttime hours at different times of the year; the closer to the geographic poles one gets, the greater the variation. Geographic position also influences the climatic conditions experienced at the station, which in turn can have a significant effect on both the quality and quantity of photometric data that are collected. For example, observatories located in arid desert regions will experience considerably less cloud cover than those in coastal regions.

Geomagnetic position determines whether a station will observe only airglow, or both airglow and auroral emissions. Furthermore, for those stations that are in fact classified as auroral or sub-auroral, their geomagnetic latitude determines the magnetic activity conditions for which they will be within observing range of the auroral oval.

6.2.1 Geographic position

A new Sanae base was erected early in 1979, with geographic coordinates of 70.31°S; 2.40°W. It should be noted that the position of Sanae is not fixed, as it is situated on the Fimbul Ice Shelf, which drifts in a NNW direction at a rate of about 50 m per year. Being so close to the Greenwich meridian, Sanae operates on Universal Time (UT). Strictly speaking, Sanae is 9.6 minutes behind UT; to the nearest minute, its geographic local time is (UT - 00:10). (Note: In this thesis time is given in the format hh:mm , e.g. 01:20 means 1hr 20min).

Each year in the period 1976-1984, photometric data were collected during the months of the southern polar winter (March through September). Owing to Sanae's polar latitude, the daily observation times varied appreciably, depending on the time of the year; during the equinoxes data could only be collected for some eight hours per night (20:00 to 04:00 UT), whereas at midwinter it was possible to observe for some sixteen hours per night (16:00 to 08:00 UT). Photometric observations were only made when the Moon and clouds were well out of the field of view of the photometers. The wind caused an additional restriction on the time available for photometric observations at Sanae, as it often blew strongly enough to lift snow and ice crystals into the photometers' field of view, causing attenuation of the observed emission intensities. There was no way to accurately determine the extent of the attenuation caused by snow and ice particles. Hence, it was only worthwhile making photometric observations when the wind speed was below about 40 knots

(± 70 km h^{-1}). As a result of the frequent presence of either moonlight, cloud or blown snow, it was usually only possible to record 'uncontaminated' data on fewer than ten full nights per month.

6.2.2 Geomagnetic position

In 1979 Sanae had corrected geomagnetic coordinates of -59.91° latitude and 44.13° longitude. This means that Sanae was at an invariant latitude of approximately 60° ($L \approx 4$). The equatorward boundary of the auroral oval is usually well poleward of such a latitude, and thus Sanae is considered to be a sub-auroral station.

During the period 1976 to 1981 the Rhodes University photometers at Sanae were operated using meridian scans which made measurements at 13 mirror positions. In terms of zenith angle, the mirror positions used were: ± 70°, ± 65°, ± 55°, ± 45°, ± 30°, ± 15° and 0°. For this range of zenith angles, the range of invariant latitudes that were scanned was 58.4° to 62.0° for emissions heights of 100 km, and 56.2° to 65.8° for emission heights of 300 km. The method used to determine invariant latitudes and L-values corresponding to the zenith angles used in the Sanae meridian scans, is given in Appendix F.

It is possible to estimate the extent of the magnetic activity required for the equatorward boundary of the diffuse auroral oval to be overhead of a specified invariant latitude at a specified time (see Section B.2 of Appendix B). Both Slater *et al.* (1980) and Gussenhoven *et al.* (1983) have calculated coefficients for the linear equation that gives the invariant latitude of the equatorward boundary of the auroral oval in terms of the Kp magnetic index. Figure 6.1 shows their results; this plot of Kp versus magnetic local time (MLT) gives some indication of the value of Kp necessary for the auroral oval to be overhead of Sanae at a particular MLT (Note: Owing to the variation in solar declination during the year, MLT relative to UT varies with the time of the year; the conversion factor between MLT and UT quoted in Figure 6.1 is applicable at the end of July).

In 1979, when the author was at Sanae, the following general observations, concerning the relationship between Sanae and the auroral oval, were found to hold true:

1/ For quiet magnetic conditions ($Kp \leq 1$), there was little or no variation in actual emission intensities with zenith angle. (The variation in observed intensities with zenith angle is due to the van Rhijn effect). The almost total lack of discernable 391.4 nm emissions shows that the OI emissions were due almost entirely to the airglow, and not to particle precipitation. Under these conditions the auroral oval is still poleward of the photometers' southern-most field of view (when observing at a zenith angle of -70°).

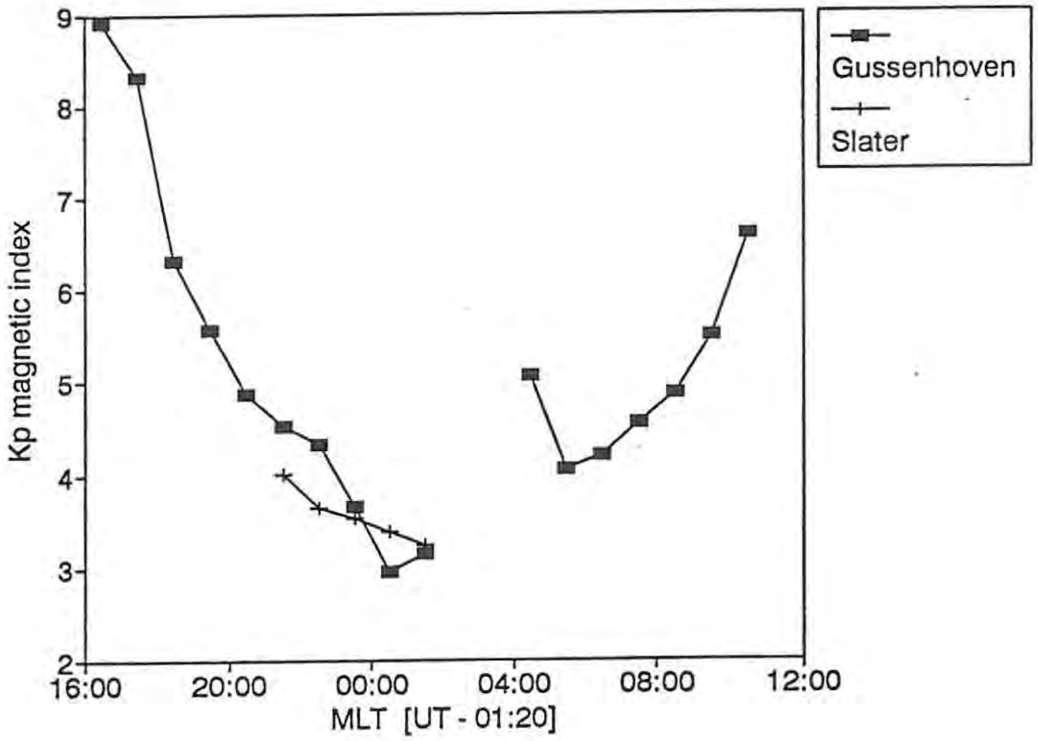

Figure 6.1 A plot of Kp versus MLT, showing the minimum Kp necessary for the auroral oval to be overhead at Sanae (invariant latitude ≈ 60°).

2/ For moderate magnetic conditions (1+ ≤ Kp ≤ 3), enhanced (auroral) emissions were often evident on the chart records, at the poleward-most zenith angles of the meridian scans (-70°, -65° and -55°). The equatorward movement of the auroral oval in the vicinity of local magnetic midnight was often noticeable on the chart records. Frequently during these magnetic conditions a quiet unstructured arc would be visible above the southern horizon. The visibility threshold at 557.7 nm has been quoted between 0.3 kR (Akasofu, 1981c) and 1 kR (Vallance Jones, 1974).

3/ For more disturbed magnetic conditions (Kp ≥ 4-), auroral emissions were evident closer to Sanae. On rare occasions auroral emissions were observed overhead, and even equatorward of Sanae. These occurrences usually coincided with substorm activity, the auroral forms showing rapid spatial and temporal variations (see Section 6.5).

These observations are in general agreement with the models of both Slater *et al.* (1980) and Gussenhoven *et al.* (1983), although the author feels that their Kp values might be a bit low. For example, in the author's experience the minimum value of Kp for the auroral oval to be overhead at Sanae (i.e. at local magnetic midnight) was Kp > 4, rather than Kp = 3. The author's findings are closer to those of Bond and Thomas

(1971), who have used ASC data to plot the equatorward boundary of the auroral oval at geomagnetic midnight versus Kp, for both the southern and northern hemisphere. Their graph shows Kp = 4 for the boundary to be at an invariant latitude of 60°. Sheeham and Carovillano (1978) have used DMSP satellite images to establish the equatorward boundary of the auroral oval in the vicinity of geomagnetic midnight. Extrapolation of their graphical representations of the equatorward boundary indicates a Kp ≈ 6 for the boundary to be overhead at 60° corrected geomagnetic latitude (CGL). They are also of the opinion that the aurora will only extend to 60° CGL (≈ 60° invariant latitude) on exceptional occasions. It should be noted that the equatorward position of the auroral oval shows considerable variance for each Kp value. Instrument sensitivity, and the use of either discrete or diffuse auroral forms to determine the equatorward boundary, will also contribute to the spread in boundary values for a particular Kp.

6.3 The processing and presentation of photometric data

The raw photometric data which were collected using the analogue systems that were at Sanae from 1976 to 1984 are in the form of chart records. Figure 6.2 shows part of a typical analogue chart record, produced by the 557.7 nm photometer . It consists of the filter-tilt cycles performed at the last seven mirror positions of a meridian scan. By using letters to label certain points on the chart record, we can identify various stages of the meridian scan:

Point A marks the beginning of one of the filter-tilt cycles, which starts with the filter in a level position. The filter is tilted to its maximum tilt angle at point B, and then back to a level position at point C. During this cycle the filter sweeps through the emission line twice, at points D and E. The heights of the deflections at these points are averaged to obtain a line reading. Background readings for the 557.7 and 630.0 nm observations at Sanae are taken at point B (i.e. at the filter's most tilted position), so for these emissions there is only one background reading per filter-tilt cycle. For the 391.4 nm observations, the background recordings are made at a wavelength above that of the emission bandhead, so the two filter-level deflections (at points A and C) are averaged to give a background reading. At the end of a filter-tilt cycle (point C) the photometer mirror is moved to its next meridian-scan position. Once the mirror is in position, the filter-tilt cycle for that mirror position is commenced. This process continues until the completion of the filter-tilt cycle at the last mirror position (F-G-H).

When the meridian scan is completed, the high voltage (EHT) supply to the photometer's PMT is switched off; this gives an EHT-off level (between points H and I) which can be used to determine the dark current level for the PMT. With the system at Sanae in 1979, there was no mechanism for the automatic closure of the photometer shutters (to record the PMT dark current levels) at the end of a meridian scan. Dark current recordings (for the various system gains that had been used since the last dark current

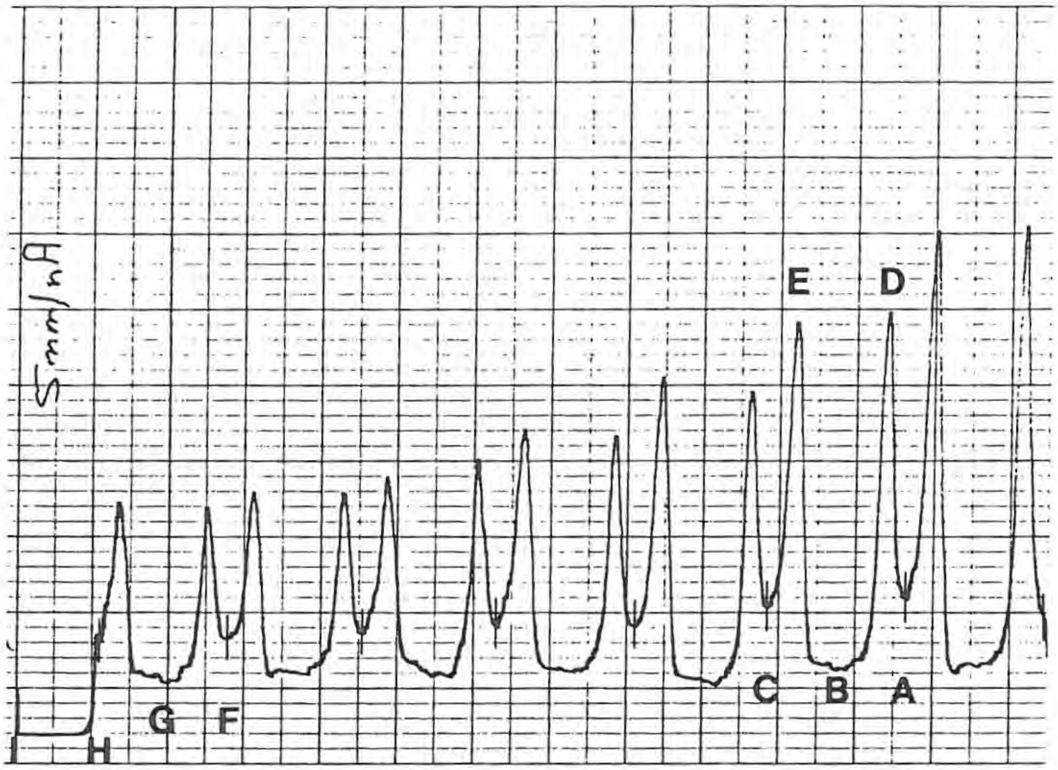

Figure 6.2 · A sample of a typical chart record produced by the analogue 557.7 nm photometer at Sanae. Vertical lines have been used to indicate the start and finish of each of the 7 filter-tilt cycles that are shown.

measurements) were taken manually at regular intervals during each nightly observation period. If the PMT was kept at a stable temperature, the dark current of the tube can be assumed to have remained reasonably constant (within ±5%) for a period of several hours. Dark current levels for the intervals between actual dark current recordings were interpolated by assuming a fixed offset between the EHT-off and dark current levels.

Typically the physical procedure that is used to convert the raw data to meaningful emission intensity data, has a number of steps:

1/ Firstly the heights (h) of the chart recorder deflections corresponding to line, background and dark current levels are read from the chart. The system gains (g) used for the recordings are either taken from the charts, or from the operator's logbook.

2/ Where necessary, values are determined for the filter transmission factors, T_l, the calibration factors, B_f, and the atmospheric correction factors, C, applicable at the time that the photometric data were recorded. In the case of the calibration factors, they are determined from the photometer calibrations that were performed both before and after the time that the observations were made.

3/ Equation 4.16 is then used to process the analogue data, in order to obtain absolute emission intensities.

4/ Finally, the emission intensities are usually presented in some sort of graphical or tabular format.

This procedure raises a number of points that need to be expanded upon.

6.3.1 Parameter values to be used in the processing of intensity data

Before any of the Sanae photometric data can be processed and presented, values have to be assigned to a number of parameters used in the various equations applied in the data reduction process. More specifically, values must be assigned to the emission heights, h, extinction coefficients, τ_{total} and τ_{ozone}, and the ground albedo, r (which are all needed for the calculation of atmospheric correction factors, see Equation 4.30 and Appendix G). Heights of the emission layers are also needed in order to determine the spatial distribution of the intensities resulting from the meridian scans. All of these parameters are wavelength-dependent, and show both temporal and spatial variations. The only way to ensure accurate values for them is to make *in situ* measurements simultaneously with the recording of the photometric data. This was not possible at Sanae, and so approximations are made for these parameter values, based on the findings of other workers.

In the case of the heights for the emission layers, many heights, determined in many different ways, have been published in the literature (see Section 2.4). Auroral emission heights are dependent on the characteristic energies of the precipitating particles that cause the emissions. The more energy a precipitating particle has, the deeper it penetrates into the atmosphere. Thus, the greater the characteristic energy of the particles, the lower the height of the emitting layer. As a result, the heights of auroral emissions are highly variable. The author has assumed, somewhat arbitrarily, heights of 100 km for the 391.4 and 557.7 nm emissions, and 300 km for the 630.0 nm emission. These values are convenient for the determination of atmospheric correction factors, using the tables provided by Ashburn (1954). It is felt that the height chosen for the 391.4 and 557.7 nm emissions might be too low, whereas a height of 300 km for the 630.0 nm emission might be too high. However from Ashburn's tables, it is apparent that an error of 25% in the emission height will only cause a 10% error in the atmospheric correction factor.

As discussed in Section 4.4.1.3, atmospheric extinction coefficients also show appreciable variation (up to 40% from day to day). It was decided, again somewhat arbitrarily, to use the extinction coefficients measured by Guttman (1968) for maritime conditions. His values include the overall effects of the atmosphere, aerosols and ozone, and thus can be used as total extinction coefficients. The values used for τ_{total} are given in Table 6.1.

The extinction caused by ozone is due entirely to absorption. Absorption coefficients for ozone can be found in a number of sources, e.g. Gast (1960), Allen (1963), Valley (1965) and Hayes and Latham (1975). Ozone absorption coefficients are generally quoted in units of cm^{-1} at STP. In order to obtain values for τ_{ozone}, one has to multiply the absorption coefficient by the effective thickness (scale height) of the ozone at STP. Anderson and Muench (1985) give a contour map (their Figure 21-4) of total ozone, in Dobson units (DU), plotted against latitude and month of the year. This diagram yields a value of about 300 Dobson units for the total ozone at Sanae's 70° latitude at the end of July. As $1 \text{ DU} = 10^{-5}$ m, 300 DU correspond to an effective ozone thickness of 0.3 cm at STP. Values of τ_{ozone} for 0.3 cm of ozone were calculated for each of the above sources of absorption coefficient values. For each wavelength of interest, there was less than 10% variation in the values obtained for τ_{ozone}. The average values of τ_{ozone} for each wavelength are given in Table 6.1.

Values of the ground albedo (spectral reflectance) for different ground coverings are given by Condron and Toolin (1960). At Sanae the ground cover is always snow; sometimes fresh snow, but more often a mixture of packed snow and ice. Values of the ground albedo, for the wavelengths of interest, were interpolated from the tables of Condron and Toolin, and are given in Table 6.1. Ashburn (1954) uses 0.8 as one of the ground albedo values in his tables which can be used to determine atmospheric correction factors. It was found that using a value of 0.8 for the ground albedo at all wavelengths does not introduce significant errors in the values of the atmospheric correction factors derived using Ashburn's method.

Table 6.1 Wavelength-dependent parameter values used for the processing of Sanae photometric data.

Emission wavelength (nm)	Emission height (km)	Extinction coefficient		Ground albedo	
		τ_{total}	τ_{ozone}	Fresh snow	Snow/ice
391.4	100	0.48	0.000	0.83	0.72
557.7	100	0.22	0.030	0.77	0.75
630.0	300	0.18	0.029	0.75	0.76

The parameter values in Table 6.1 were used to calculate atmospheric correction factors using both the A-method formula (Ashburn's model of extinction, scattering and ground reflection) and the E-method formula (extinction-only model) as derived in Section 4.3.3. Correction factors were determined for all the zenith angles used in the 1979 meridian scans. Details of how the correction factors were calculated, and their tabulated values, are given in Appendix G. The resultant correction factors are shown graphically in Figure 6.3. With the exception of the 391.4 nm E-method factors, all the correction factors decrease with zenith angle, due to the van Rhijn effect. In the case of the 391.4 nm E-method correction factors, the exponential attenuating effect of the atmosphere dominates the van Rhijn effect at high zenith angles to such an extent that the correction factors start to increase above z = 55°. The greater atmospheric attenuation at lower wavelengths also explains why the 391.4 nm A-method correction factors decrease less rapidly with zenith angle than those for 557.7 and 630.0 nm.

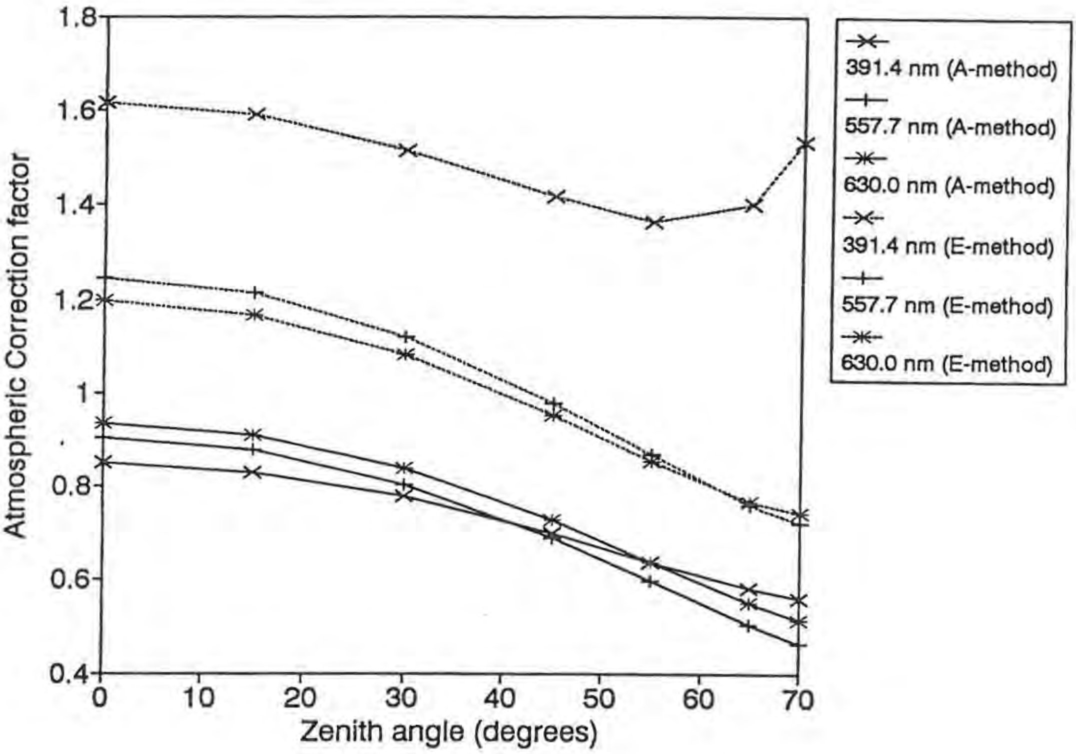

Figure 6.3 The variation of atmospheric correction factors with zenith angle.

6.3.2 Presentation of emission intensity data

Emission intensity data are often made more meaningful when presented graphically, rather than in tabular form. This is especially true for data produced with meridian-scanning techniques. There are a number of graphical formats in which such data can be presented: The simplest method is to plot intensities using conventional (XY) Cartesian axes. This can be done either by plotting emission intensities versus time, for a given zenith angle, or by plotting intensities versus zenith angle (or some equivalent spatial coordinate, such as invariant latitude), for a given meridian scan. These types of graph allow the intensities of different spectral emissions to be plotted on the same axes. This is useful for comparing the relative variations of the different emissions intensities, versus time or zenith angle.

A simple extension of the intensity versus zenith angle format is to stack the plots of several meridian scans, thus creating a two-dimensional representation of emission intensities versus both zenith angle and time. This approach has been used by Vallance Jones *et al.* (1982) to present their meridian-scanning photometer data.

A variation on this type of graph is to generate contour plots of emission intensities versus both time and meridian position (be it zenith angle or geomagnetic latitude). This is the approach taken by the author in presenting auroral substorm intensity data in Section 6.5. The Fortran contour plotting routine used by the author requires the data points to be on an orthogonal and equally-spaced grid. The meridian-scan intensity data satisfy neither of these criteria; the data is not orthogonal because the observations that make up a meridian scan were staggered in time, and the zenith angles at which the observations were made were not evenly spaced. To obtain regularly spaced data points on an orthogonal grid, the author used an IMSL (International Mathematical and Statistical Libraries) Fortran subroutine called IQHSCV. This is a smoothing routine which fits a surface to irregularly distributed data points. The IMSL Edition 9 Reference Manual gives the following brief description of the algorithm used by this routine: 'IQHSCV calculates an interpolating function which is a fifth-degree polynomial in each triangle of a triangulation of the x-y projection of the surface. The interpolating function is continuous and has continuous first-order partial derivatives'. As such, the routine does not change the original data points, but merely interpolates additional points between the existing points. For the 1979 data being studied, the routine was used to generate intensity values at 5-minute time intervals, for zenith angles spaced at 5° intervals between ± 70°.

Yet another way to present this type of data is to generate keograms, which are time-latitude-grey scale plots of emission intensities. (Keograms were first used by Eather *et al.* (1976), who derived the name from 'keoeeit', the Eskimo word for the aurora). Keograms in various forms have been used by a number of workers (e.g. Eather *et al.*, 1976; Eather *et al.*, 1979; Vallance Jones *et al.*, 1982; Eather, 1984; Mende *et al.*, 1984; Eather, 1985b). In a keogram each intensity data point becomes a pixel in a grey-scale map. The greater the spatial and temporal sampling rates of the intensity observations, the better the resolution of the keograms. The same is obviously true for intensity contour plots, although any under-sampling in observations is not as apparent. Keograms would be a good way of presenting the Sanae intensity data that was recorded between 1982 and 1984, because during this period meridian scans using 31 mirror positions were performed either every minute or every five minutes during auroral activity.

So far we have discussed the different types of graphs that can be used to present emission intensity data. A related matter is the choice of coordinate systems to be used with the graphs. Appendix E gives a description of many of the coordinate systems, both spatial and temporal, that are commonly used in airglow and auroral studies.

It is well known that auroral phenomena have a close relationship with the earth's magnetic field. Consequently, it makes sense to use magnetic coordinates, rather than geographic coordinates, when presenting auroral intensity data. Unfortunately, any number of different magnetic coordinate systems have been used by workers in their auroral studies. This makes the comparison of different data sets very difficult (Sandford, 1970). The need to standardize magnetic coordinate systems has more recently seen many workers using either corrected geomagnetic coordinates or invariant latitude in order to specify the location of auroral observations. It would appear to the author that invariant latitude (or its associated L-value) has become the dominant spatial coordinate for the presentation of auroral photometry data. As a result, it was decided to use both zenith angle and invariant latitude as ordinates in intensity contour plots.

The conversion of the zenith angle of an observation to the invariant latitude of the emission depends on the height of the emitting layer. Invariant latitudes can most easily be obtained by assuming the aurora to be a thin horizontal sheet at an assumed height (Vallance Jones *et al.*, 1982). Details of the determination of invariant latitudes and L-values, corresponding to the zenith angles used for observations at Sanae in 1979, are given in Appendix F. The invariant latitudes and L-values corresponding to emission heights of 100 and 300 km are shown, plotted against the zenith angles of the 1979 Sanae observations, in Figures 6.4 and 6.5, respectively. The crossover between the 100 and 300 km lines in each figure occurs at a zenith angle of about 27.6°, corresponding to Sanae's inclination (dip angle) of about 62.4° in 1979. By definition, one is looking directly along a field line at this zenith angle. Consequently, both the invariant latitudes and the L-values should have the same value at 100 and 300 km because, again by definition, they are almost constant for the entire length of a field line.

In addition to using magnetic spatial coordinates, it also makes sense to use a magnetic time coordinate when plotting auroral data. Magnetic local time would appear to be the most widely used magnetic time coordinate, although many workers still use universal time (UT), a geographic time coordinate. As Sanae actually operates on UT, it was decided to use UT as a time coordinate, whilst specifying the relationship between UT and MLT at Sanae on any graphical presentation of auroral data. The author has decided to use the method of Montbriand (1970) in order to calculate corrected geomagnetic midnight (CGM), and hence MLT, for Sanae. Montbriand's formula (see Appendix E, Section E.2) takes into account the variation in solar declination during the year, and thus gives different values of CGM for different times of the year. It yields a CGM of 01:20 UT for Sanae at the end of July. Hence Sanae's MLT at this time is given by (UT - 01:20).

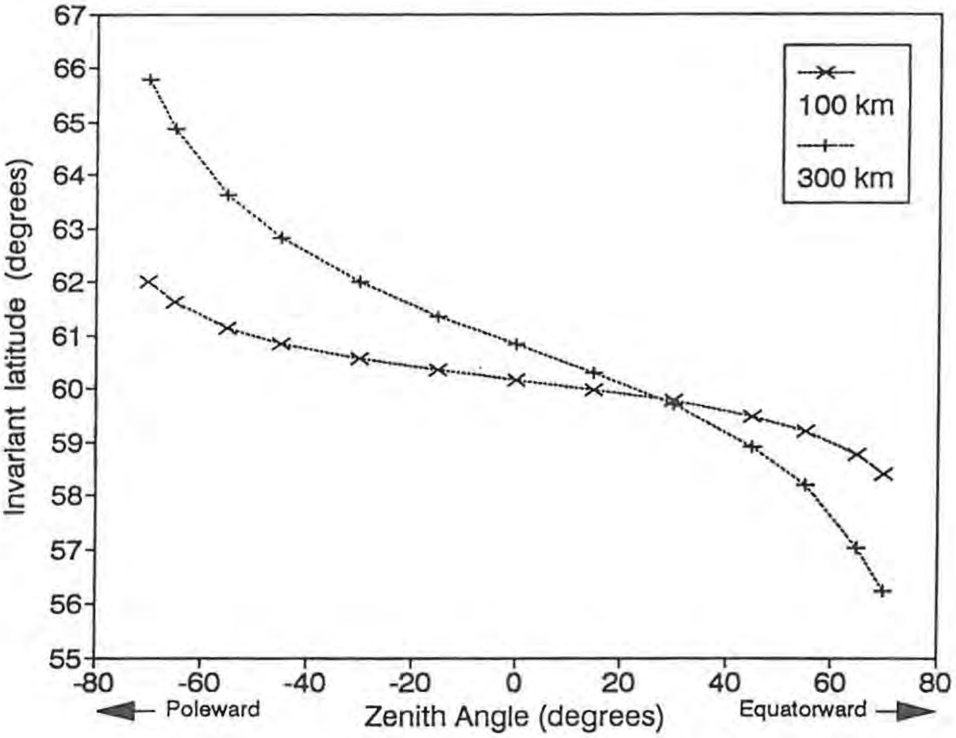

Figure 6.4 Plots of invariant latitude versus zenith angles for Sanae observations, assuming emission heights of 100 and 300 km.

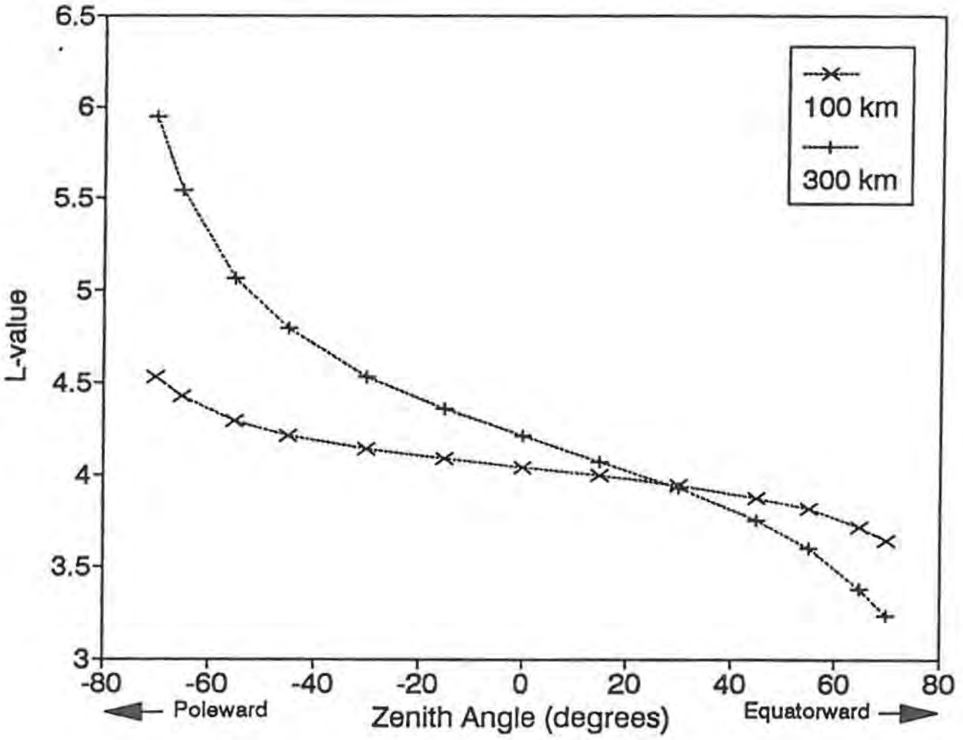

Figure 6.5 Plots of L-value versus zenith angle for Sanae observations, assuming emission heights of 100 and 300 km.

It is also common practice, when presenting the temporal variations of auroral emission intensities, to give some sort of indication of the associated magnetic activity. This is usually done by supplying the values of one or other magnetic activity indices. The indices most often quoted with auroral data are Kp, the planetary K index, and AE, the auroral electrojet index. These and other commonly-used indices of magnetic activity are explained in Section E.3 of Appendix E. While Kp is a three-hourly index, AE is a continuous index, and hence has a better temporal resolution than Kp. The advantage of Kp is that it is more readily available, being published monthly in the Journal of Geophysical Research (JGR). Consequently it was decide to supply Kp values with Sanae emission intensity data. Also quoted are values of the Ks index, which is the K index calculated from magnetograms recorded only in the southern hemisphere. This index is used in the calculation of a new (truly planetary) K index, called Km. Values of Km, Ks and Kn (the northern hemisphere index) are published along with Kp values in JGR. Magnetic activity at Sanae might be better described by Ks, rather than by Kp or Km.

It must be noted that, at best, any global magnetic activity index will only give an approximate indication of the magnetic conditions that prevailed at the time of observation. It is possible that magnetic conditions experienced at a particular station might differ significantly from those indicated by a global index. Furthermore, the use of different indices to characterize magnetic activity also leads to difficulties when comparing the auroral observations of different workers.

In an attempt to find a quantitative relationship between Kp and AE, Rostoker (1991) has found the following (rough) relationship between them:

$$\begin{aligned} Kp < 3o: &\quad \langle AE \rangle = 100Kp + 60 \\ Kp > 3o: &\quad \langle AE \rangle = 200Kp - 250 \end{aligned} \tag{6.1}$$

where $\langle AE \rangle$, in nT, signifies an average value of AE for the three-hourly Kp periods. It should be noted, however, that the variance in AE for a given value of Kp is considerable; Rostoker (1991) has found that a 700 nT envelope was necessary to contain most of the AE values corresponding to a given Kp.

6.4 Airglow emissions observed at Sanae, prior to the substorm of 27 July, 1979.

This section serves two purposes: It gives some indication of the magnitudes of the airglow emission intensities that can be expected at Sanae, and it provides average airglow intensity values which can be subtracted from the total emission intensities recorded during the substorm to give the intensities of the emissions due to particle precipitation. Airglow emissions do not exhibit temporal or spatial variations to the same extent as auroral emissions do, and hence they should not vary significantly across the relatively small latitude range covered by a meridian scan. Consequently, it should be permissible to use intensities measured in the zenith to approximate the airglow at all zenith angles of observation.

The two nights prior to the night of 26/27 July 1979, when the substorm of interest occurred, were magnetically very quiet. In fact, 24 July was classified as the fifth quietest day in July (ΣKp = 11+), and 25 July was the second quietest (ΣKp = 6). Values of the Kp and Ks indices for these two nights and the night of the substorm are given in Table 6.2. In all cases the value of Ks was less than or equal to the value of Kp. Moonlight, cloud and blown snow prevented the collection of photometric data during any magnetically quiet periods in the week following the substorm. As a result, the only options for determining the extent of the airglow contributions during the substorm are to either use the airglow values recorded on the two quiet nights prior to the storm, or to use any true airglow values recorded on the actual night of the substorm. In the latter case, the intensities used are those which were observed during the times when there was no evidence of 391.4 nm emissions (which are diagnostic of particle precipitation).

Table 6.2 Kp and Ks magnetic activity indices for the nights 24/25, 25/26 and 26/27 July 1979.

Date in July 1979	Magnetic activity index	Value of three-hourly magnetic activity index					
		15-18	18-21	21-24	00-03	03-06	06-09
24/25	Kp	1+	1o	2-	1+	1+	1-
	Ks	1-	0+	1-	1+	1+	1-
25/26	Kp	1-	1-	1-	1-	1o	2-
	Ks	0o	0o	0+	0o	1-	2-
26/27	Kp	2-	5-	6-	5+	4+	2-
	Ks	1o	4o	5-	5o	4-	1+

On both quiet nights prior to the substorm, there were no discernable 391.4 nm emissions in the zenith. This means that there was little or no particle precipitation in the zenith, and that the zenith OI emissions were due entirely to airglow. There were, however, small magnitude 391.4 emissions and slightly enhanced OI emissions evident at the poleward-most zenith angles of some of the meridian scans. These low intensity auroral emissions coincided with the equatorward excursion of the auroral oval in the vicinity of local magnetic midnight. The zenith emission intensities for the nights of 24/25 and 25/26 July 1979 are shown in

Figures 6.6 and 6.7 respectively. It was decided in Section 4.3.3 that Ashburn's method (called the A-method) should be used to calculate the atmospheric correction factors to be applied to straight airglow data. This method assumes a uniform source function across the sky; it corrects for extinction of the direct light component, and also for the contributions of scattered and ground-reflected light which originate outside of the field of view of the photometer. In accordance with this decision, the airglow intensities shown in Figures 6.6 and 6.7 were derived using atmospheric correction factors which were generated using the A-method (see Appendix G). To get an idea of the intensities that would be obtained using E-method correction factors, which correct only for the exponential extinction of the direct light component, the 557.7 and 630.0 nm intensities in Figures 6.6 and 6.7 must be multiplied by 1.38 and 1.28, respectively.

The airglow intensities shown in Figures 6.6 and 6.7 warrant some comment:

The intensities show a fair amount of variability during the course of each night. The 630.0 nm intensities on both nights follow the expected trend, steadily decreasing from a twilight maximum to an early morning minimum before increasing again towards dawn. The 630.0 nm enhancement in the vicinity of 03:00 UT on 25 July might be a predawn enhancement due to the effects of conjugate sunrise, as previously found to occur at Sanae (see Torr and Torr, 1969; Torr and Torr, 1971). The 557.7 nm intensities on the night of the 24/25 July are highly variable and show no discernable pattern, whereas the 557.7 nm intensities on the night of 25/26 July show a similar trend to those of the 630.0 emissions.

Possibly the most noteworthy feature of the Sanae airglow intensities is their low values. Average airglow intensities for 557.7 and 630.0 nm OI emissions are often reported in the literature as 250 R and 100 R, respectively. However, it should be mentioned that a survey of the literature has shown a large variance in the 557.7 and 630.0 nm airglow intensity values reported by different workers. The author has found several reports of low emission intensities at geomagnetic latitudes in the vicinity of 60°. For example, Eather (1969a, 1969b) has found a mid-latitude minimum in airglow intensities between invariant latitudes of 45° and 55°; his airglow intensity plots (averaged over 22 flights) show 557.7 and 630.0 nm intensities as low as 55 R and 5 R, respectively. At 60° invariant latitude the graphs indicate average airglow intensities of < 70 R for 557.7 nm and < 15 R for 630.0 nm. Davis and Smith (1965) also give airglow intensity plots versus latitude. At geomagnetic latitudes of 62°, their plots show 557.7 nm intensities between 50 and 140 R, and 630.0 nm intensities between 17 and 50 R. Stegman and Murtagh (1988) have observed the 557.7 nm emissions at Stockholm, Sweden (59°N, 18°E geographic) for some twenty months, and found that 'On some occasions the total green line intensity (including F-layer emission) has been observed to decline to levels of 10-20 R for a period of a few days, whereas it can reach values of more than 300 R on others'. Clearly both the 557.7 and 630.0 nm airglow emission intensities can vary appreciably from their respective generally accepted average values of 250 and 100 R. Besides true variations in the airglow emission intensities, differences in data processing methods (especially the atmospheric correction factors that are used) and uncertainties in

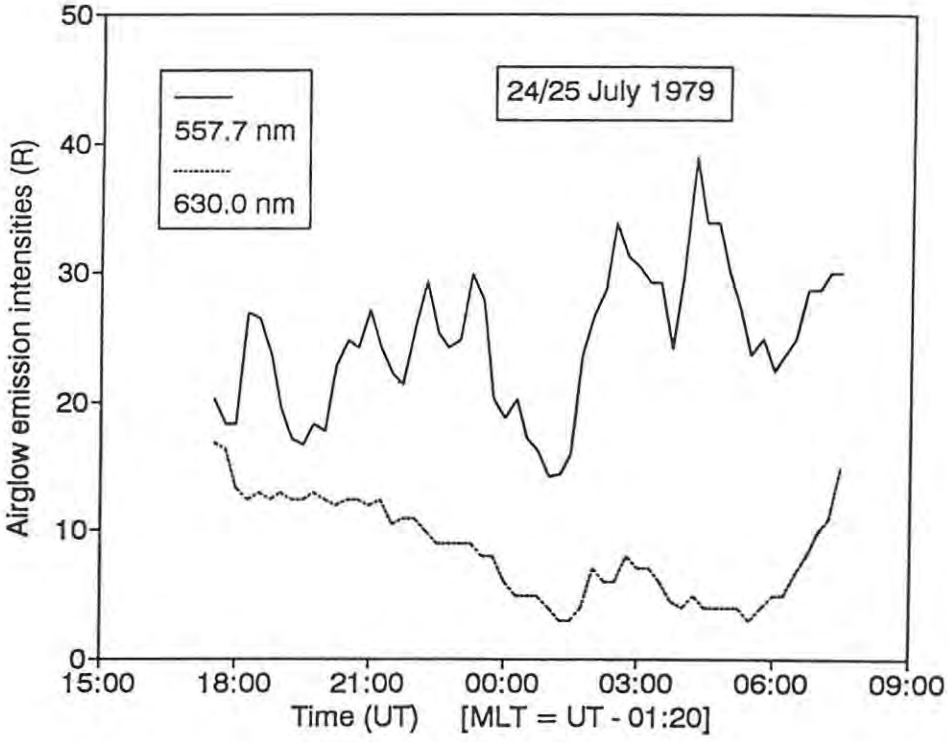

Figure 6.6 557.7 and 630.0 nm OI airglow emission intensities for the zenith above Sanae, on the night of 24/25 July 1979.

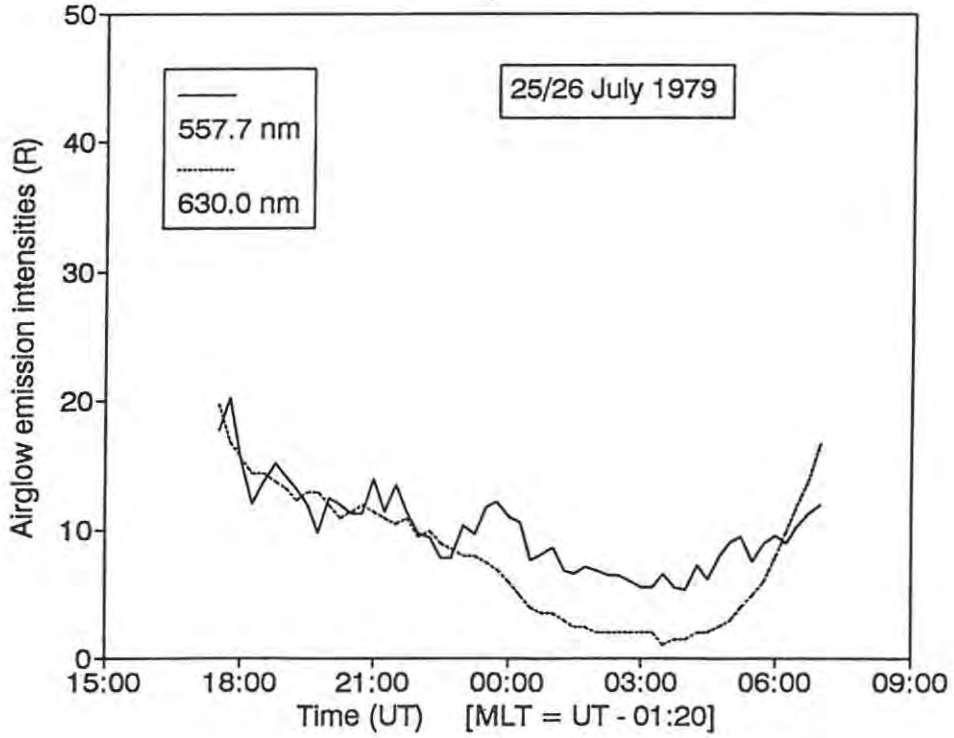

Figure 6.7 557.7 and 630.0 airglow emission intensities for the zenith above Sanae, on the night of 25/26 July 1979.

photometer calibrations, certainly contribute to the large variance in measured airglow emission intensities.

The Sanae airglow emission intensities shown in Figures 6.6 and 6.7 are at least a factor of five lower than the generally accepted (worldwide) average values, and are also lower than the low values of the workers mentioned above. Furthermore, the airglow values observed at Sanae seem to be consistently low; the values observed on the 24/25 and 25/26 July 1979 are typical values, rather than low values for Sanae. It is possible that the minimal sunlight at Sanae during the midwinter months, even at thermospheric heights of 100 and 300 km, might contribute to the low airglow emission intensities. It must be said that the unusually low airglow (and auroral) emission intensities observed at Sanae are one of the reasons why the author has gone to such lengths to check the cross-calibration of the light sources used to calibrate the Sanae photometers.

6.5 Photometric observations of the substorm of 27 July 1979

In 1983 the four South African research groups involved in upper atmosphere and magnetospheric research at Sanae held a number of workshops aimed at the cooperative study of a magnetospheric substorm. At Sanae these groups between them operate magnetometers, photometers, an all-sky camera (ASC), a low light level TV system, an ionosonde and a riometer. In addition to the data recorded at Sanae, magnetometer data from other stations and satellites, and satellite particle data were used. A number of substorms were considered initially, in order to find one in which most of the instrumentation at Sanae was operating reliably, and for which pertinent satellite data were available. Furthermore, for the first attempt at a substorm study, it was decided to choose a substorm whose behaviour was not too complex, so that interpretation would be possible.

The magnetospheric storm that occurred on the night of the 26/27 July 1979 was one of the most active to be observed at Sanae in 1979. Several substorms were discernable within the storm. The substorm of interest commenced at 00:40 UT on 27 July 1979. It met all the above-mentioned criteria for data availability, both in terms of Sanae data and satellite data coverage of the substorm. Although it was one of several substorms to be seen from Sanae that night, it was chosen for study because it was a reasonably simple substorm, being relatively isolated from other substorms that occurred on the same night (i.e. it did not overlap with any other substorms). The results of the substorm workshops were initially published in nine companion papers in the South African Journal of Physics (see Dore, 1984 for the photometric results). A joint paper was then produced (Gledhill *et al.*, 1987), containing all the results of the substorm study.

This section describes the observation of the substorm, using the Rhodes University photometers at Sanae. It serves to illustrate the application of meridian-scanning photometry to the study of auroras, and of substorms in particular. Although we will concentrate mainly on the photometric data recorded between

00:00 and 03:00 UT, zenith intensity data for the entire night are presented to give some idea of emission intensities observed at Sanae during disturbed magnetic conditions. Table 6.2 shows that during the night of 26/27 July 1979 the Kp index reached a maximum value of 6-, with a corresponding value of Ks, the southern hemisphere index, of 5-. Figure 6.8 shows the zenith emission intensities at Sanae for the night of 26/27 July, determined using A-method atmospheric correction factors. Figure 6.9 shows the same emissions, except that their intensities were calculated using E-method correction factors. These graphs effectively give the minimum and maximum limits of the zenith intensities at the emitting layers, which correspond to the observed intensities, I_{app} (see Section 4.3.3). For the 391.4, 557.7 and 630.0 nm zenith emissions, the ratios of the E-method correction factors to the A-method ones are 1.90, 1.38 and 1.28 respectively. The ratios between the intensities shown in Figure 6.8 differ significantly from the ratios between the intensities shown in Figure 6.9. This illustrates a point made in Section 4.4.1.3, namely that different atmospheric correction methods not only affect the magnitudes of the emission intensities, but also the ratios between them.

Horizontal (H) intensity magnetograms from various auroral zone stations show that the magnetospheric storm started at 18:33 UT on the 26 July (Gledhill *et al.*, 1987). However, the H component at Sanae and the zenith emission intensity graphs in Figures 6.8 and 6.9 show that auroral activity was first noticeable at Sanae in the vicinity of 20:30 UT. The delay in the appearance of activity at Sanae is due to Sanae's equatorward position relative to the auroral zone; greater magnetic activity is required before the auroral oval expands equatorward as far as Sanae. The presence of measurable auroral activity overhead at Sanae subsided at about 05:00 UT on the following day. Zenith emission intensities measured before and after this period can be taken as airglow intensities. During the auroral activity, the zenith intensity graphs show good correlations between the temporal variations of the different spectral emissions.

Contour graphs of the 391.4, 557.7 and 630.0 nm emission intensities for the period 00:00 UT to 03:00 UT on 27 July 1979 are given in Figures 6.10 to 6.15. Two graphs were plotted for each wavelength, to show the emission intensities obtained using both A-method and E-method atmospheric correction factors. Figures 6.10 and 6.11 show the 391.4 nm intensities, using A-method and E-method correction factors, respectively. Likewise, Figures 6.12 and 6.13 are for the 557.7 nm emissions, and Figures 6.14 and 6.15 are for the 630.0 nm emissions. The ratio between E-method and A-method correction factors, for a particular wavelength, increases with zenith angle. As a result, the different atmospheric correction methods also influence the variation of each spectral emission's intensities with zenith angle.

Before considering the morphology of the substorm presented in the contour plots, we can make some general comments on the emission intensities shown in the graphs: The considerable differences between the emission intensities derived using A-method and E-method atmospheric correction factors are readily apparent; these differences are most apparent at high zenith angles for the lower wavelength emissions. For example, the 391.4 nm emission during the substorm had a maximum value at 00:45 UT, at a zenith angle

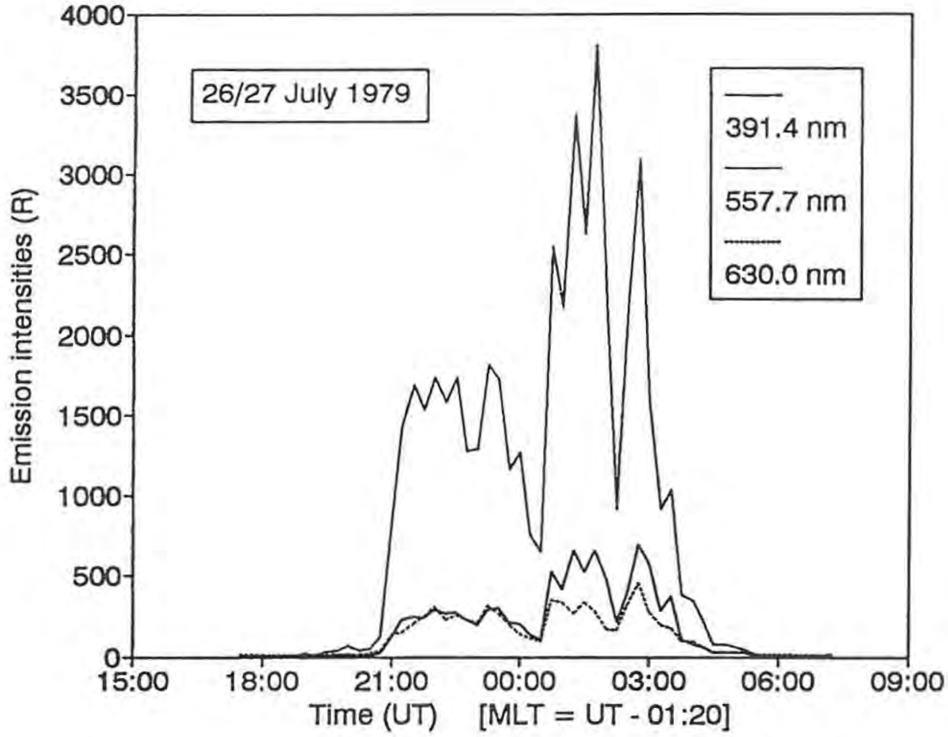

Figure 6.8 Emission intensities for the zenith above Sanae on 26/27 July 1979, determined using A-method atmospheric correction factors.

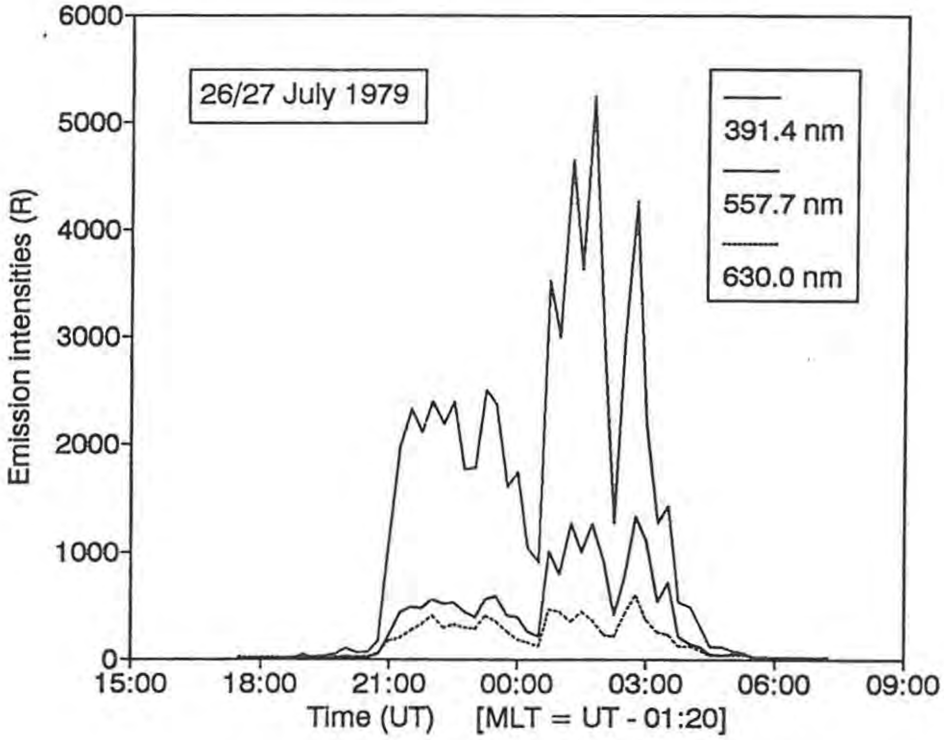

Figure 6.9 Emission intensities for the zenith above Sanae on 26/27 July 1979, determined using E-method atmospheric correction factors.

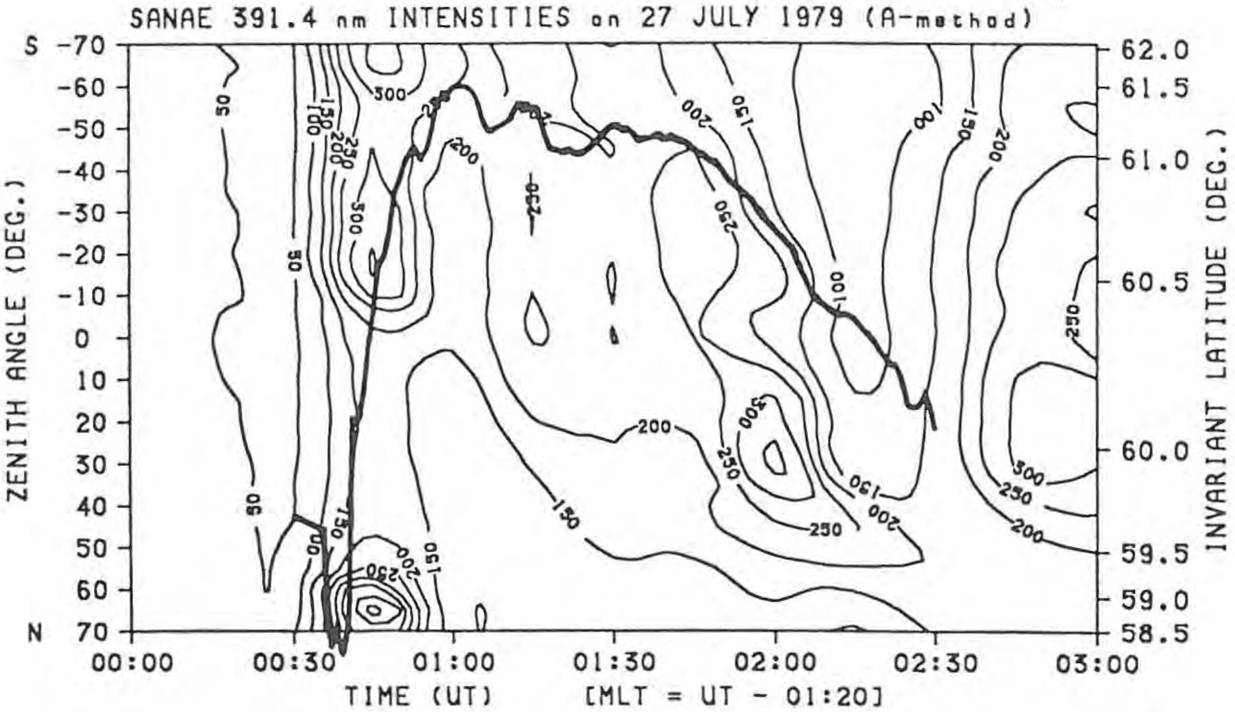

Figure 6.10 Contour plot of 391.4 nm emission intensities recorded at Sanae on 27 July 1979. A-method atmospheric correction factors. Contour interval = 50 R.

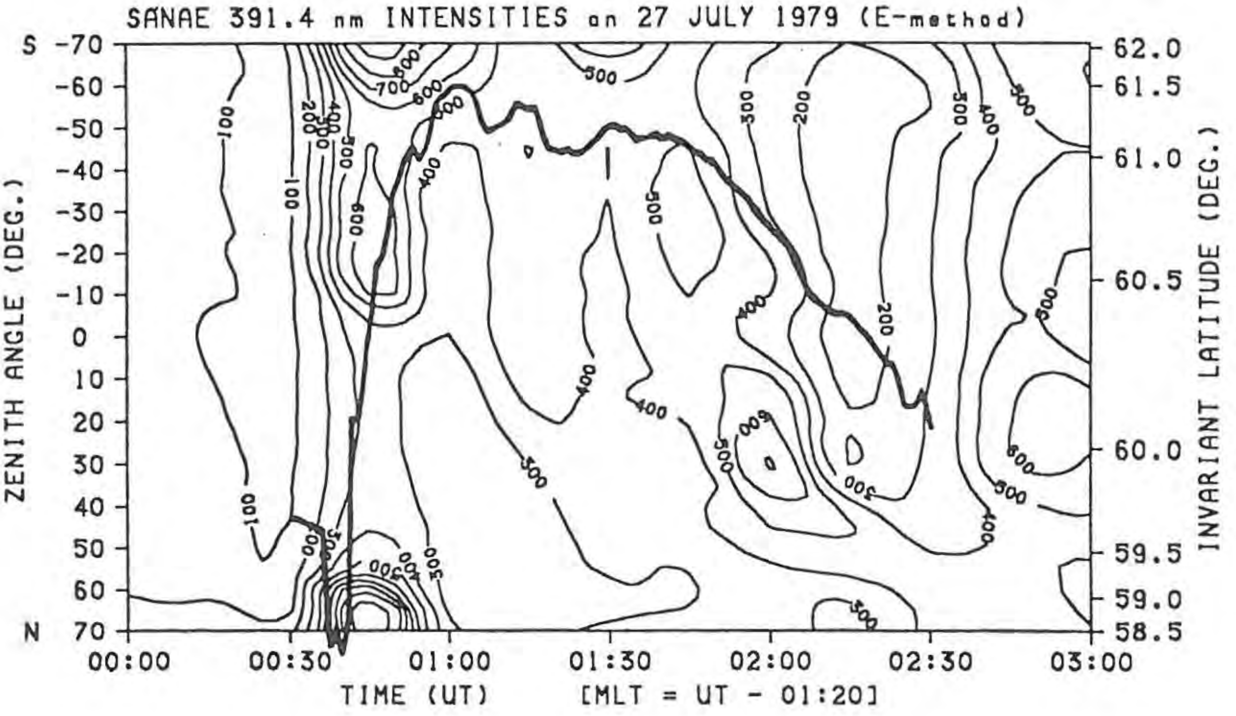

Figure 6.11 Contour plot of 391.4 nm emission intensities recorded at Sanae on 27 July 1979. E-method atmospheric correction factors. Contour interval = 100 R.

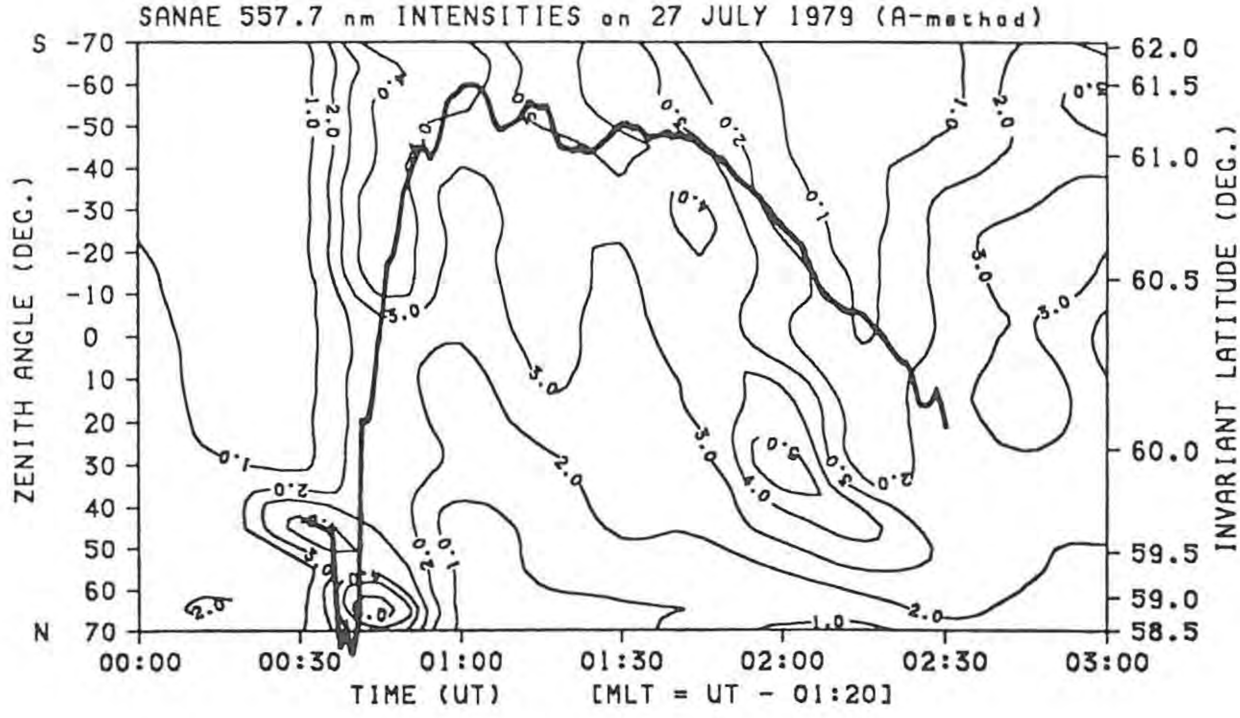

Figure 6.12 Contour plot of 557.7 nm emission intensities recorded at Sanae on 27 July 1979. A-method atmospheric correction factors. Contour interval = 1 kR.

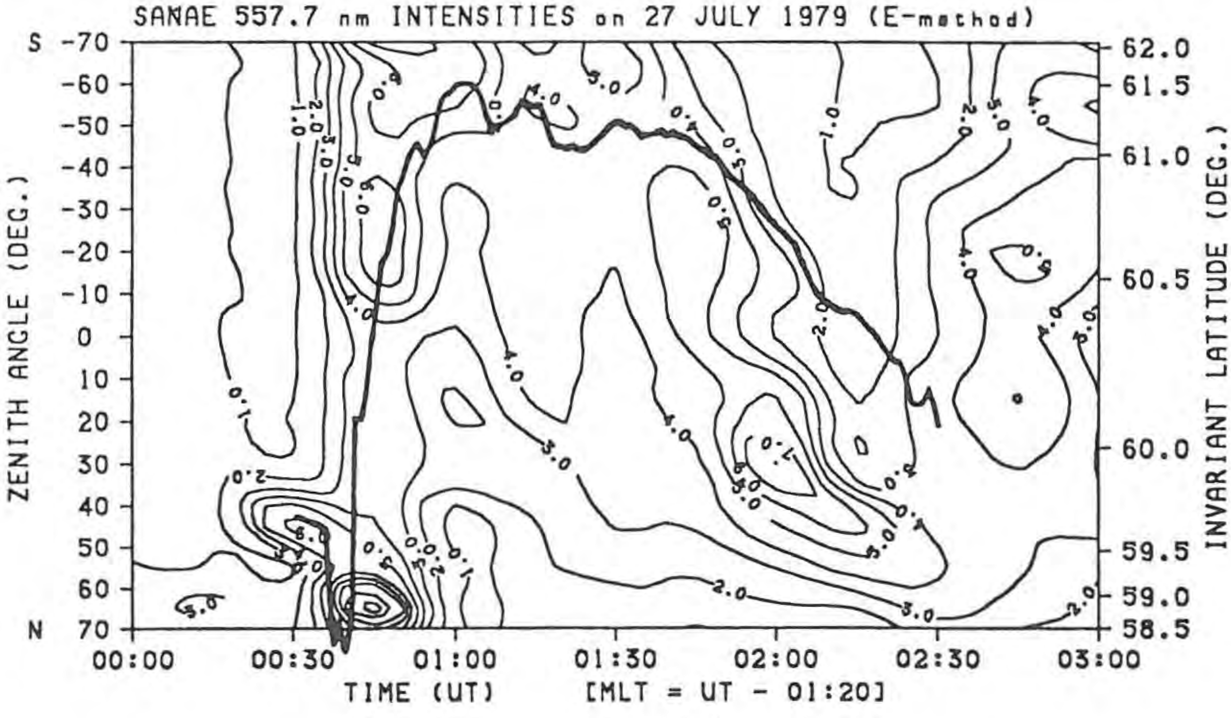

Figure 6.13 Contour plot of 557.7 nm emission intensities recorded at Sanae on 27 July 1979. E-method atmospheric correction factors. Contour interval = 1 kR.

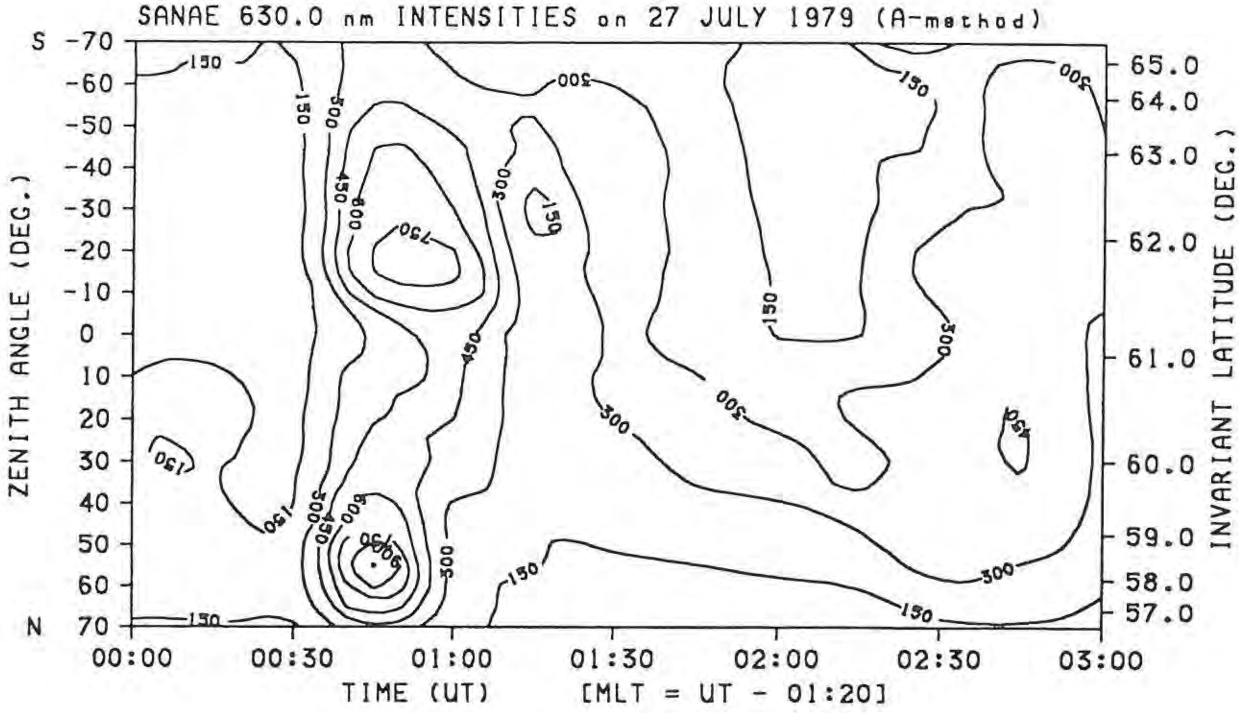

Figure 6.14 Contour plot of 630.0 nm emission intensities recorded at Sanae on 27 July 1979. A-method atmospheric correction factors. Contour interval = 150 R.

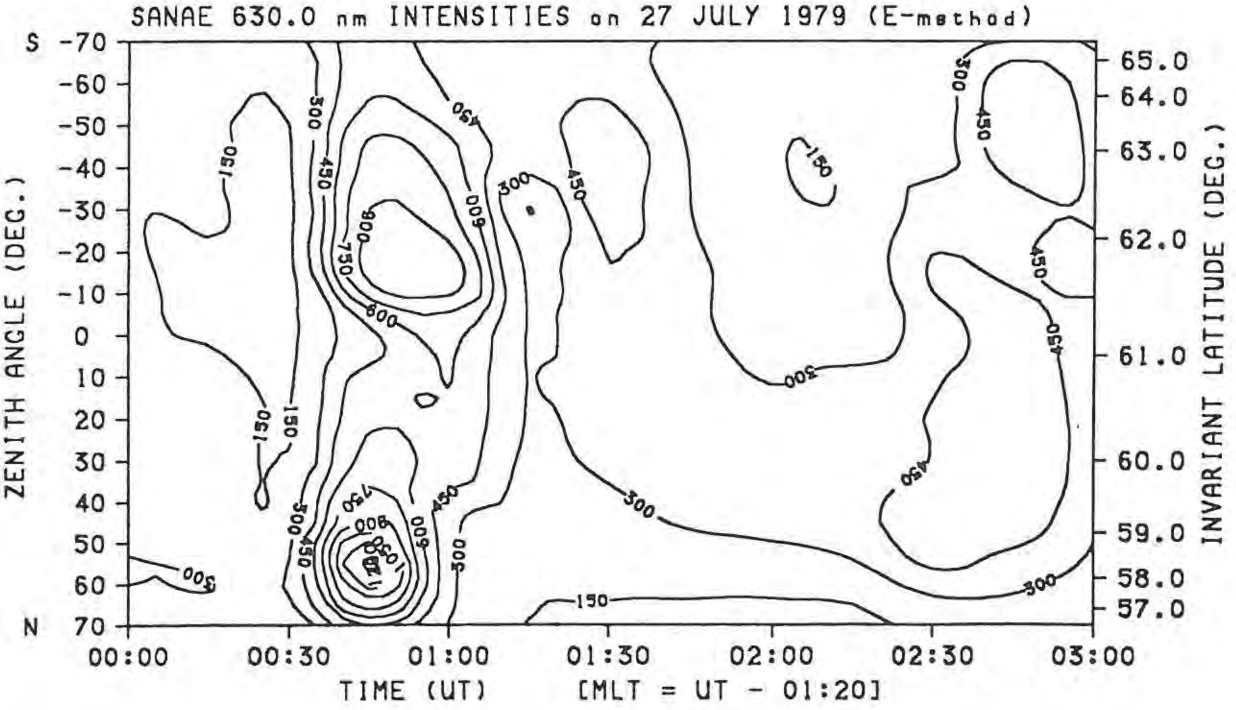

Figure 6.15 Contour plot of 630.0 nm emission intensities recorded at Sanae on 27 July 1979. E-method atmospheric correction factors. Contour interval = 150 R.

of 65°; the E-method gives an intensity of 1156 R, whereas the A-method gives a corresponding intensity of only 480 R!

Regardless of the atmospheric correction method used, the intensities of all emissions appear to be lower than many of the emission intensities reported by other workers, for similar levels of magnetic activity: The Kp value during the duration of the substorm was 5+, whereas the Ks index was 5o. Emission intensities clearly vary from aurora to aurora. However, the emissions seen on the night of the 26/27 July 1979 were overhead, and even equatorward of Sanae, and were some of the brightest seen at Sanae during 1979. This again raises the question of the accuracy of the absolute emission intensities calculated from the photometer records. The only auroral intensities that the author has found for other L = 4 stations, are I(427.8) intensities measured at Siple Station in Antarctica. Helliwell *et al.* (1980) measured intensities of 140 R (→ I(391.4) ≈ 460 R) for Kp values of 5- and 3-. Engebretson *et al.* have reported I(427.8) values of 0.5 kR (→ I(391.4) ≈ 1.64 kR) for Kp = 4-, and 1 kR (→ I(391.4) ≈ 3.28 kR) for Kp = 4. The 391.4 nm intensities equivalent to their 427.8 nm intensities are consistent with the 391.4 nm intensities recorded at Sanae for similar Kp values.

The author's photometer logbook reflects that at 00:45 UT on 27 July (i.e. during the expansive phase immediately after substorm onset), there was a patch of red aurora visible to the naked eye. This patch, along with bright green and yellow auroras, was outside of the photometers' field of view, being about 40-50° to the west of the magnetic meridian through Sanae and at a poleward zenith angle of about 20°. To the naked eye, the auroras on the magnetic meridian through Sanae (those in the photometers' field of view), were less intense and showed no evidence of red colouring. These observations raise two points: Firstly, auroral intensities in the vicinity of Sanae but out of the field of view of the photometers were brighter than those viewed by the photometers. The fact that red aurora were visible to the naked eye implies a minimum 630.0 nm emission intensity of 10 kR, using the visibility threshold for red aurora quoted by Omholt (1971). Secondly, the 630.0 nm intensity measured at this time (at a poleward zenith angle of 15°) was about 1 kR, implying an intensity difference of a factor of 10 between the visible aurora and the emission on the meridian. Assuming an emitting layer at a height of 300 km for the 630.0 nm emission, very rough estimates give the spatial separation of the two areas as about 100 km. This raises the question as to whether such an intensity gradient is probable across an arc, or whether it is partially due to the photometer intensities being too low? It must be noted that the photometer meridian scans were 15 minutes apart, so that it is quite possible that the photometer observations did not coincide temporally with the brightest intensities of the rapidly-varying auroral emissions.

We will now look at the morphology of the auroral substorm from a photometric point of view. It has been determined from Hermanus Pi2 pulsation records that the onset of the substorm was at 00:40 UT. Prior to this time, the contour graphs show low-level emissions across the whole sky, at all three wavelengths. The intensities are slightly higher on the equatorward horizon. Shortly after the substorm onset there was a sharp increase in intensities across the whole sky as the emission regions moved rapidly polewards. This is evident in the contour plots, despite the lack of temporal resolution of the photometers (one meridian scan every 15 minutes). Following the rapid poleward movements, which indicate the expansive phase of the substorm, there were slower equatorward movements of the emitting layers to invariant latitudes of about 59.5°. These latter equatorward movements form the recovery phase of the substorm.

The emissions shown in the contour plots are due mainly to electron precipitation, and are thus termed electron aurora (Note that the plots are of total emission intensities i.e. the airglow and proton-induced components of the emissions have not been subtracted). For comparison, a contour plot of the proton aurora as recorded by the Hermanus group's H_β photometer is given in Figure 6.16. There is a striking resemblance between the movements of the electron aurora, shown in Figures 6.10 to 6.15, and that of the proton aurora shown in Figure 6.16. There seems to be no noticeable separation of the two, even the broadening and slight intensification at about 01:30 UT being common to both. Another interesting observation to arise from the comparison of the electron and proton auroras is that the intensities of the electron auroral emissions increased by at least a factor of three at substorm onset, whereas the H_β intensities only increased by less than a factor of two (from about 40 R to 70 R).

There are definite maxima in the E-region emissions at 391.4 and 557.7 nm at about 02:00 UT, but there is no corresponding increase in the F-region 630.0 nm emission, or in the H_β emission. This would be consistent with a hardening of the precipitating electron energy spectrum at this time, in agreement with the spectra deduced from the Sanae ionograms (Gledhill, 1984; Gledhill *et al.*, 1987).

The position of the westward auroral electrojet, calculated by Sutcliffe and Smits (1984) using Sanae magnetometer data, is superimposed on the 391.4 and 557.7 nm contour plots. Its position was calculated by assuming that the electrojet is an infinitely long line-current flowing at a height of 110 km (see Wu *et al.*, 1991, for a good description of how to calculate the magnetic latitude location of the electrojet, using magnetometer data). The position of the electrojet was not superimposed on the 630.0 nm contour maps because of the ± 200 km difference between the assumed heights of the electrojet and the 630.0 nm emission layer. From the graphs it can be seen that the positions of the 391.4 and 557.7 nm emission maxima and of the electrojet are similar during the substorm expansive phase and during the early part of the recovery phase. However, during the latter part of the recovery phase, i.e. after about 02:00 UT, both the 391.4 and 557.7 nm emission maxima seem to be equatorward of the electrojet. These are identical to the findings of Sutcliffe and Smits (1984), when they compared the relative positions of the westward electrojet and the H_β intensity maxima.

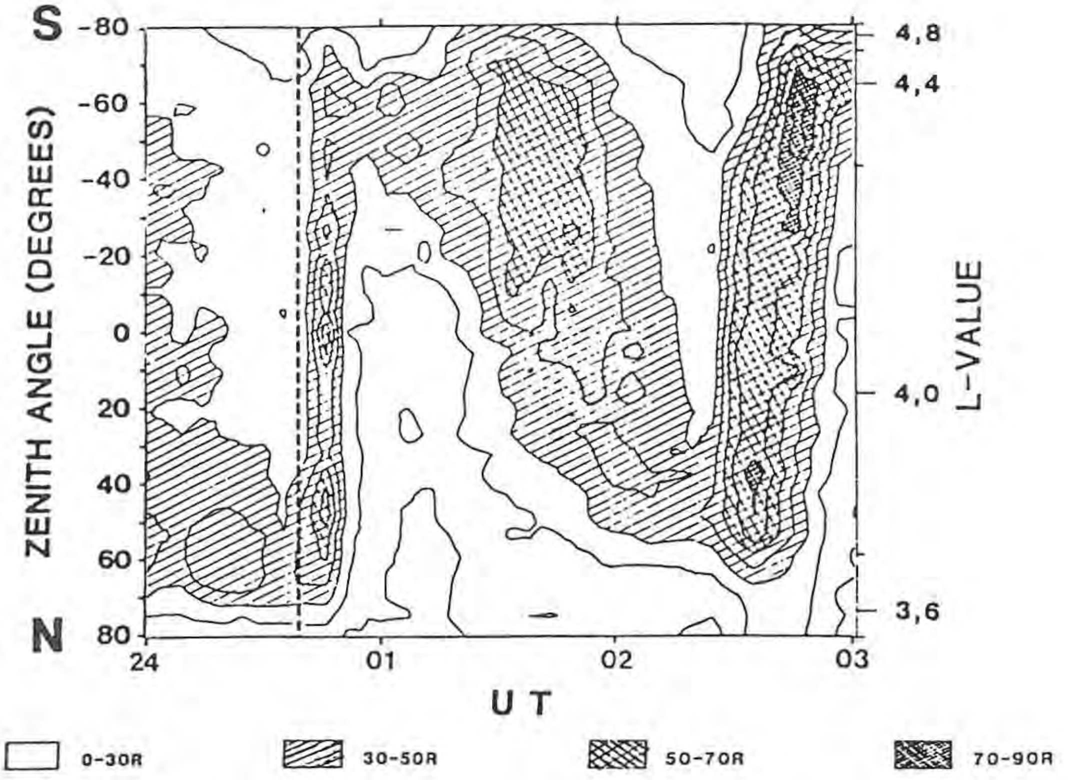

Figure 6.16 Contour plot of proton aurora (H_β) intensity recorded at Sanae on 27 July 1979. Contour interval = 10 R. The vertical dashed line marks the time of the substorm onset. (Adapted from Sutcliffe and Smits, 1984).

Mainly as a result of this substorm study, shortcomings in both the photometer system and its 1979 mode of operation were identified. The spatial variations of aurora are such that the thirteen fixed mirror positions used in the meridian scans are insufficient to give proper spatial resolution of the structure of the aurora. In 1982 the spatial resolution of the meridian scans was improved with the introduction of a meridian-scan consisting of 31 mirror positions (see Section 3.4.1). This improved system allowed meridian scans between zenith angles of ± 81°, in steps of 5.4°. The digital photometer system used in 1985 was a further improvement, allowing the number of mirror positions used in a meridian scan, and their zenith angles, to be software-controlled.

In 1979, as in previous years, the photometer system at Sanae was operated using a meridian-scan repetition rate of 15 minutes, with each scan taking 6.5 minutes to complete. While this sampling rate is suitable for observing the slow temporal variations of the low intensity airglow, it totally lacks the temporal resolution necessary for the study of the rapid variations of the aurora during substorms. This is evident from a comparison of the temporal extent of the higher intensity contours that make up the poleward expansion shown in the contour plots of the electron and proton auroras. The extended period of high intensities shown in the plots of the electron aurora (Figures 6.10 - 6.15) is due to the smoothing of the intensity data collected every 15 minutes, about the peak recorded at 00:45 UT. More frequent sampling, e.g. once every five minutes (as was used to observe the proton aurora), would have shown that the higher intensities of the substorm expansive phase were confined to a far shorter time span, as shown for the proton aurora in Figure 6.16. Obviously, because of the finite time needed per meridian scan, which in turn depends to a large extent on the number of mirror positions used per scan, there is a limit to the minimum time interval that can be used between scans. Until 1982, a meridian scan every five minutes was the fastest repetition rate available using the analogue system at Sanae.

Unfortunately, until the author became Airglow Research Officer at Rhodes University, the Sanae photometers were used very much in a 'synoptic observation' mode, which is suited to airglow rather than auroral research. Previous incumbents of the post were involved almost totally with the development of photometric equipment, and it was 1981 before any photometric data were processed. At this time, the Rhodes University upper atmosphere research group became involved in the cooperative study of magnetospheric substorms. The fact that meridian-scanning rates were not increased during auroral activity prior to 1981, was due to the lack of background in auroral physics given to the photometer operators. The personnel used to operate research equipment at Sanae are normally young and inexperienced; they are often recent graduates, perhaps with electronics qualifications rather than a background in physics. It is thus essential that they be given sufficient aeronomic background as to both the processes of the aurora and its observation, to enable them to make the best use of their equipment and to optimize the quality (and usability) of the data they collect. Prior to 1981, this was not the case with the operators of the Rhodes photometers at Sanae.

From 1981 the operator of the Rhodes University photometers at Sanae was instructed to increase the meridian-scan rate as soon as there was any evidence of auroral activity. Low airglow intensities and economic considerations necessitated a slower scanning speed during non-auroral airglow observations. The new mirror control unit, installed in the Sanae photometer system at the beginning of 1982, not only increased the number of mirror positions used in a meridian scan, but also reduced the lowest meridian scan time to 1 minute. As discussed in Section 3.4.2, this scan speed was designed for substorm observation where emission intensities are high enough to allow 1.55 second integration times at each mirror position. A one minute resolution should be adequate for most auroral studies.

6.6 Intensity ratios during the substorm of 27 July 1979

Auroral spectral intensities, and the ratios between them, have been used extensively as a means of characterizing aurora. Remote sensing methods such as the use of ground-based photometry have allowed workers to evaluate certain parameters associated with the aurora, without having to resort to more expensive data-collection techniques (such as the use of rocket-borne particle detectors etc.). Furthermore, ground-based methods do not suffer from the 'once-off' problem of rockets, or the lack of time resolution of earth-orbiting satellites.

When dealing with intensity ratios it is convenient to define a shorthand notation for some of the intensity ratios that will be mentioned. If R denotes a ratio, and the subscripts 3, 4, 5, and 6 denote the emission wavelengths 391.4, 427.8, 557.7, and 630.0 nm, respectively, then:

R_{34} = I(391.4) / I(427.8)
R_{53} = I(557.7) / I(391.4)
R_{54} = I(557.7) / I(427.8)
R_{56} = I(557.7) / I(630.0)
R_{63} = I(630.0) / I(391.4)
R_{64} = I(630.0) / I(427.8)

Certain intensity ratios, e.g. the ratios of the 557.7 nm OI emission intensity to the intensities of the N_2^+ 1NG band emissions at 391.4 and 427.8 nm (i.e. R_{53} and R_{54}), remain reasonably constant across a wide range of emission intensities and auroral conditions. Consequently, any ratios that are obtained which are beyond the range of normally accepted values might indicate a problem with the absolute calibrations of the photometers that were used to make the intensity measurements (see Section 6.6.3).

Before looking at the intensity ratios measured at Sanae during the substorm of the 27 July 1979, and comparing them with those obtained by other workers at other sites, we look at some examples of the applications to which intensity ratios obtained from ground-based optical measurements can be put.

6.6.1 Some examples of aeronomic applications which use intensity ratios

The ratios between the emission intensities of various spectral features have been used for a number of aeronomic applications. In this section we will look at one or two of the more important uses of intensity ratios that have been measured using ground-based instrumentation. Owing to the effects of atmospheric absorption and scattering, ground-based observations are confined to the spectral range between the near ultraviolet and the near infrared. Observations of spectral features outside of this wavelength range can only be done from rockets and satellites.

Possibly the most important use of intensity ratios is the determination of the characteristics of the precipitating particles that cause the aurora. Although the precipitation of protons and heavier charged particles also contributes to auroral emissions, electrons are by far the biggest carrier of energy into the atmosphere, and are thus the predominant primary cause of auroral emissions. In order to estimate the amount of electron energy entering the atmosphere, it is normal to assume a particular energy spectrum (distribution) for the precipitating electrons. Various workers have established models based on assumed energy distributions, which allow them to relate the energy and flux characteristics of the precipitating electrons to observed emission intensities.

Perhaps the most often-sited work on the relationship between emission intensities and the characteristics of precipitating electrons, is that of Rees and Luckey (1974). For their model computations, they assume that the energy distribution of the precipitating electrons is Maxwellian, i.e. the number of electrons, N, with energy E is given by

$$N(E)\ dE \ = \ N_0\, E\, e^{-(E/\alpha)}\ dE \qquad (6.2)$$

where α is the energy at the peak of the distribution, otherwise known as the electron characteristic energy. (Note: The author has retained the symbols used by Rees and Luckey, although it might be more appropriate to replace N_0 with another symbol, as N and N_0 have different units (number of electrons and energy^{-1} respectively). Rees and Luckey state that this type of distribution is frequently observed for primary electrons that have an energy range of 0.1 keV to several tens of keV. A Maxwellian energy distribution gives a total number flux $F = N_0\alpha^2$, a mean electron energy of 2α, and thus a total energy flux

$$\xi \ = \ 2\alpha F \qquad (6.3)$$

They give diagrams showing the variations of R_{54}, R_{64} and R_{65} versus I(427.8) for various characteristic energies between 0.3 and 10 keV. These curves can be used to determine the characteristic energy, α, corresponding to a measured intensity ratio and 427.8 nm emission intensity. Owing to the uncertainty concerning the processes that cause the auroral 557.7 nm emissions, Rees and Luckey are of the opinion that R_{64} is the best intensity ratio to use in order to determine α. Once a characteristic energy has been obtained, another diagram given by them, showing the variation of I(427.8) with total electron flux F for various values of α, can be used to determine a value for F. Finally, having obtained values for both α and F, Equation 6.3 can be used to determine the total energy flux, ξ. This method can be applied to Sanae emission intensity data, simply by multiplying the measured 391.4 nm intensities by the generally accepted R_{34} value of 3.28 (Vallance Jones, 1974) to get equivalent values for I(427.8).

Many workers have used the preferred R_{64} spectral ratio to infer the characteristic energy α, and hence the mean energy (= 2α) of the precipitating electrons in an aurora (see e.g. Mende and Eather, 1975; Eather *et al.*, 1976; Arnoldy and Lewis, 1977; Vondrak and Sears, 1978; Mende *et al.*, 1984; Christensen *et al.*, 1987; Vallance Jones *et al.*, 1987b; Niciejewski and Forsyth, 1988). In contrast, McEwen *et al.* (1981) have found that R_{54} is a more meaningful measure of the characteristic energy of the precipitating electrons during pulsating auroras. They are of the opinion that R_{84} should only be used for stable auroras, and that a combination of both methods (i.e. using whichever ratio is appropriate) provides a more complete monitoring of the characteristics of precipitating electrons. Niciejewski *et al.* (1989) question the usage of R_{54} because of the uncertainty as to the processes that cause the OI 557.7 nm emission in the aurora (as mentioned above), and because of the lack of variation of R_{54} with electron energy. The only example that the author has found of R_{58} , or rather its inverse R_{85}, being used to determine the characteristic energy of precipitating electrons is that of Deehr *et al.* (1976). They found the characteristic energy derived from R_{85} to be in good agreement with the simultaneous particle energy measurements made from the ISIS-2 satellite.

More recently, Rees and Roble (1986) and Rees *et al.* (1988) have given formulae which give the emission intensities, I, in terms of the characteristic energy of the precipitating electrons, E_0 ($= \alpha$), and the total electron energy flux, ξ. Separate equations are given for each of the spectral emissions: 391.4, 557.7 and 630.0 nm. Careful note should be taken of the units used for the parameters in the equations; sometimes emission intensities are expressed in Rayleighs, and other times in kilo-Rayleighs. The formulae are based on the assumption of a Maxwellian energy distribution for the primary electrons. By substituting for the emission intensities in any two of the equations, two equations in E_0 and ξ are obtained, and can then be solved.

Another intensity ratio has recently been tested as a possible indicator of the characteristic energy of an electron spectrum. This ratio is that between the N_2 2PG (0,0) emission at 337.1 nm and the N_2^+ 1NG (0,1) emission at 427.8 nm. Rees and Lummerzheim (1989) feel that it is a better indicator of electron characteristic energy than the traditional 'red to blue' ratio, R_{84}. This is in contrast with the models of Strickland *et al.* (1989), Solomon (1989) and Richards and Torr (1990), which all predict that for energies above about 1 keV, the ratio I(337.1) / I(427.8) will be constant. Recent experimental results of Gattinger *et al.* (1991) show that this ratio has an energy dependence of less than 15% in the energy range 2 keV to 12 keV. This result raises doubts concerning the validity of using this ratio to determine characteristic energies of precipitating electrons.

Although a Maxwellian energy distribution is frequently used to characterize precipitating electrons, other workers have assumed, or found, that the energy distribution of the precipitating electrons is not as straightforward as a single Maxwellian distribution. For example, the model used by Judge (1972) assumes the electron energy to have a double Maxwellian distribution. Judge uses E_1 and E_2 to denote the characteristic energies of the two distributions, and sets $E_1 = 0.08$ keV. He then presents graphically the variation in the intensity ratios R_{53}, R_{58} and R_{84} versus the characteristic energy E_2. Judge also uses his model to calculate altitude emission profiles for various values of E_2. As expected, the heights of the emission peaks of both the 391.4 and 557.7 nm emissions decrease with increasing characteristic energy. However, the variations in emission height with characteristic energy are not the same for both emissions;

h(557.7) decreases from 200 to 100 km as E_2 is increased from 0.3 and 50 keV, whilst h(391.4) decreases from 175 to 80 km for the same energy range. The heights do not vary linearly with energy; for E_2 = 10 keV, the predicted height of the peak 557.7 nm emission has already dropped to 110 km, whereas that of the 391.4 nm emission is 100 km. In contrast with these emissions, Judge's model shows that the height of maximum 630.0 nm emission does not vary significantly with electron energy, staying in the range 300-320 km for a large range in electron energy.

Eather and Mende (1971) have found that the energy distribution of precipitating particles forms two peaks that indicate two definite particle populations: 'Soft' particles with a spectrum between 0.2 and 0.7 keV, and particles with a harder spectrum between 1 and 10 keV. These findings are in agreement with those of Frank and Ackerson (1971) who made satellite observations of electron fluxes and energies. They found that the electron energy spectra during aurora can best be approximated with a combination of a power law spectrum ($N(E) = E^{-\delta}$; $1.5 < \delta < 2.5$) below 0.2 keV, and a Maxwellian distribution above that.

Mende *et al.* (1984) and Rees *et al.* (1988) have extended the usage of R_{84} and I(427.8) to the determination of the ionospheric Hall and Pedersen conductances, induced by the precipitating electrons. They use the standard techniques described above to determine the characteristic electron energies and the total electron energy fluxes, and then use these to determine the corresponding ionospheric conductances. Mende *et al.* (1984) used ground-based meridian-scanning photometers to record emission intensities, whereas Rees *et al.* (1988) have used intensity data derived from DE-1 satellite images. Mende *et al.* (1984) compare the conductances obtained from the ground-based optical measurements with those obtained from incoherent scatter radar data. Although they find the conductances derived from the photometric data to be less accurate than those yielded by the radar, the optical method provides better time resolution over a larger region of space.

Torr and Sharp (1979) have used R_{53}, measured as a function of altitude, to estimate the atomic oxygen concentration in the thermosphere, between 100 and 160 km. Although these intensity measurements were made with rocket-borne instrumentation, this example does illustrate the continued importance of photometer measurements in the study of the chemistry of the thermosphere. Photometric emission intensity measurements are often used in conjunction with other measurements to check the validity of thermospheric models.

Intensity ratios are also used in the determination of emission heights, as discussed in Section 2.4. Eather *et al.* (1976) use R_{84} to determine the height at which emission intensities peak. They provide a table of emission height ranges corresponding to certain ranges in R_{84}. Ratios of < 0.02 and > 35 yield minimum and maximum emission heights of 80 and 360 km respectively.

Although far from a complete list of the uses that can be made of intensity ratios, the above examples do show that emission intensities and intensity ratios derived from ground-based photometric measurements continue to play an important role in aeronomic research.

6.6.2 Intensity ratios measured at Sanae during the substorm of 27 July 1979

It is possible to calculate intensity ratios for all of the zenith angles used in a meridian scan. However, as emissions of the different spectral features occur at different heights, most of the ratios would be meaningless. The reason for this is simple: Electrons precipitate along field lines, and in most cases the field lines that intersect an observer's line of sight at 300 km are not the same as those that intersect it at 100 km. Consequently, at most zenith angles, the electrons causing the auroral emissions at 300 km are not the same as those causing emissions at 100 km. The only exception to this occurs when the observer looks along a field line, by looking into the magnetic zenith (defined by the station's magnetic inclination, or dip angle). Sanae's inclination in 1979 was -62.4°, which corresponds to an equatorward zenith angle of 27.6°. The closest zenith angle to this in the 1979 meridian scan configuration was 30°. The difference of 2.4° should not have a significant effect. (If field lines are approximated as straight lines below 300 km, then for a zenith angle of observation of 30°, field lines which cross the centre of a photometer's field of view at a height of 300 km would pass some 8 km from the centre of the field of view at a height of 100 km).

The 391.4, 557.7 and 630.0 nm emission intensities for the period 23:00 UT on 26 July to 03:00 UT on 27 July 1979, for a zenith angle of 30°, were extracted from the arrays of intensity data that were used to generate the contour plots of the substorm (shown in Section 6.5). These intensities are total emission intensities which, besides a large electron-induced component, also have smaller airglow and proton-induced components. If the intensity ratios are to be used to determine the characteristics of the precipitating electrons, then the airglow and proton-induced components have to be subtracted from the total emission intensities, before these ratios are calculated.

As the airglow intensities prior to the substorm were so low, it was decided to simplify calculations by assuming constant (non-auroral) airglow emission intensities for the duration of the substorm. The airglow intensity plots in Section 6.4 were used to estimate airglow components of 20 R at 557.7 nm and 10 R at 630.0 nm. These values were then subtracted from the total emission intensities.

In the case of the proton-induced components, H_β intensities were scaled from the contour plots given by Sutcliffe and Smits (1984), as H_β intensities were not readily available from the Magnetic Observatory of the CSIR (who are responsible for the H_β photometer at Sanae). The proton-induced components of the 391.4, 557.7 and 630.0 nm emissions were estimated by multiplying the H_β intensities by factors of 10, 10 and 3 respectively. These factors were taken from Gattinger and Vallance Jones (1972); the factor of 10 for the 391.4 nm emission was estimated by multiplying the factor of 3 used for 427.8 nm emissions by the ratio R_{34}, which was taken as 3.28 (Vallance Jones, 1974). Whilst the factors for the OI emissions are the same as those suggested by Eather (1968), the factor of 10 for the 391.4 nm emission is considerably lower than the factor of 17 given by him. The proton-induced intensities were then subtracted from the total emission intensities.

Prior to the onset of the substorm, the calculated proton-induced components of the 391.4 nm emissions were similar to, and sometimes greater than, the total emission intensities. This resulted in large, and even negative values of the ratios R_{53} and R_{63}. Clearly there is a problem, which could be due to one or more of the following: The total 391.4 nm intensities may be too low, the H_β intensities too high, or the factor of 10 (used to derive the proton-induced component) too large. The factors used to determine proton-induced components from H_β intensities are known to be highly variable (Eather, 1968; Gattinger and Vallance Jones, 1972), but a feasible reduction in the factor used to calculated the proton-induced component of the 391.4 nm emission is unlikely to solve the problem. It seems reasonable to assume that all three possible causes contribute to the high proton-induced components relative to the total 391.4 intensities.

As a result of these problems, the author decided not to apply any correction for proton-induced components of the emission intensities. The emission intensities used to calculate the intensity ratios for the substorm are thus airglow-corrected, but reflect the emissions due to all particle precipitation, not just to precipitating electrons. The highest H_β intensity recorded during the substorm was about 70 R, measured during the expansive phase. From this, we infer a 700 R proton-induced component of the 557.7 nm emission. At the same time, the 557.7 nm total emission intensity was a factor of 10 higher than this. This clearly indicates that the auroral emissions were mainly due to electrons.

To show the effects of atmospheric correction factors on intensity ratios, values of R_{53}, R_{56} and R_{63} were calculated from intensities derived using both A-method and E-method atmospheric correction factors. Figure 6.17 shows the intensity ratios obtained using A-method atmospheric correction factors, whilst Figure 6.18 shows those for E-method correction factors. Table 6.3 gives the mean values of the intensity ratios and their standard deviations. For reference, the mean values of the 391.4 nm emission intensities are included. In all cases the sample number used for the statistical calculations was 14. At all times the values of R_{53} and R_{63} are lower for E-method correction factors than for A-method correction factors. In the case of R_{56} the opposite is true. These results are consistent with the fact that the difference between A-method and E-method atmospheric correction factors, and hence the difference between the intensities that they yield, increases with decreasing wavelength. The intensity ratio values measured during the substorm will be compared with those of other workers, in the next section.

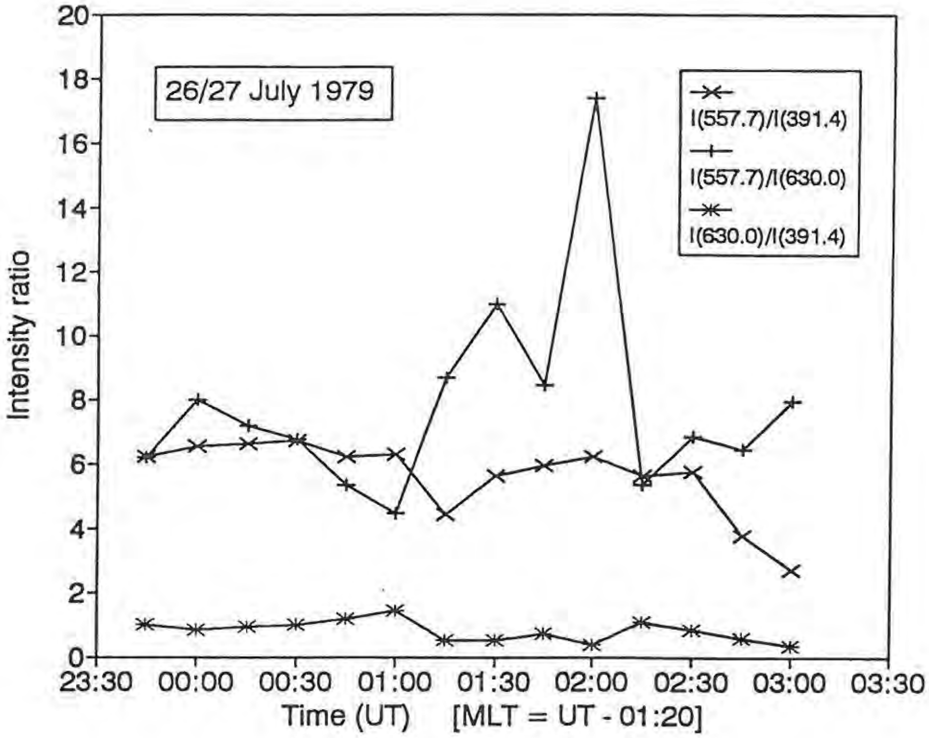

Figure 6.17 Intensity ratios in the magnetic zenith during the substorm of 27 July 1979. Emission intensities were obtained using A-method atmospheric correction factors.

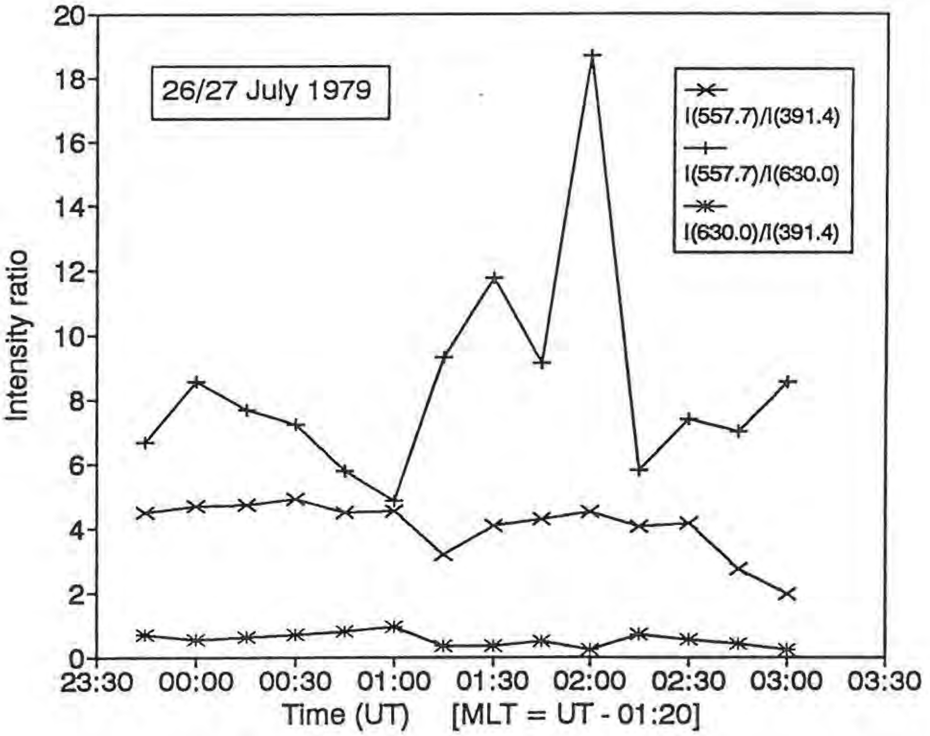

Figure 6.18 Intensity ratios in the magnetic zenith during the substorm of 27 July 1979. Emission intensities were obtained using E-method atmospheric correction factors.

Table 6.3 Intensity ratios measured in the magnetic zenith at Sanae during the substorm of 27 July 1979.

Atmospheric correction method	I(391.4) (R)	$\frac{I(557.7)}{I(391.4)}$	$\frac{I(557.7)}{I(630.0)}$	$\frac{I(630.0)}{I(391.4)}$
A-method	414 ± 249	5.62 ± 1.18	7.85 ± 3.20	0.80 ± 0.31
E-method	808 ± 484	4.04 ± 0.85	8.44 ± 3.43	0.53 ± 0.21

Regardless of the differences in intensity ratios resulting from the two atmospheric correction methods used, the relative temporal variations in the intensity ratios during the substorm are the same for both methods. As would be expected, R_{53} shows the least variation. It is interesting to compare the variations in the values of R_{56} and R_{63} with the variations in the electron energy spectra that Gledhill (1984) derived from N-h profiles, which in turn were derived from the ionograms recorded at Sanae during the substorm (Haggard, 1984). The derived electron energy spectra are shown in Figure 6.19. The solid and dashed energy spectra curves arise from the fact that the sporadic-E traces on the ionograms were very spread. The solid energy spectra curves are a result of N-h profiles generated from the top edge of the sporadic-E traces (i.e. maximum estimates), whilst the dashed energy spectra curves come from N-h profiles generated from the bottom edge of the sporadic-E traces (i.e. minimum estimates). The minimum in R_{56} and the maximum in R_{63} at 01:00 UT coincide with the softest (lowest energy) spectra during the substorm. Furthermore, the higher R_{56} values and lower R_{63} values seen between 01:15 and 02:00 UT coincide with the hardening of the electron energy spectra, which reached a peak at 02:00 UT. Unfortunately, energy spectra were not calculated after 02:00 UT, so no check can be made as to whether there was a subsequent softening of the energy spectra, in line with trends in the ratio values. The increases in R_{56} and the decreases in R_{63}, as the hardness of the electron energy spectra increased, are consistent with the fact that higher energy electrons penetrate deeper into the atmosphere and thus cause increased E-region 391.4 and 557.7 nm emissions relative to the F-region 630.0 nm emissions.

6.6.3 Comparison of Sanae intensity ratios with those determined by other workers at other sites

Since the IGY, intensity ratios have frequently been reported in the literature and have even been the subject of research (e.g. Gattinger and Vallance Jones, 1972; Sawchuk, 1973; Sawchuk and Anger, 1976a, 1976b). A number of different ratios have been reported on, with the various ratios between the emission intensities at 391.4, 427.8, 557.7 and 630.0 nm predominating because of their usefulness in determining electron

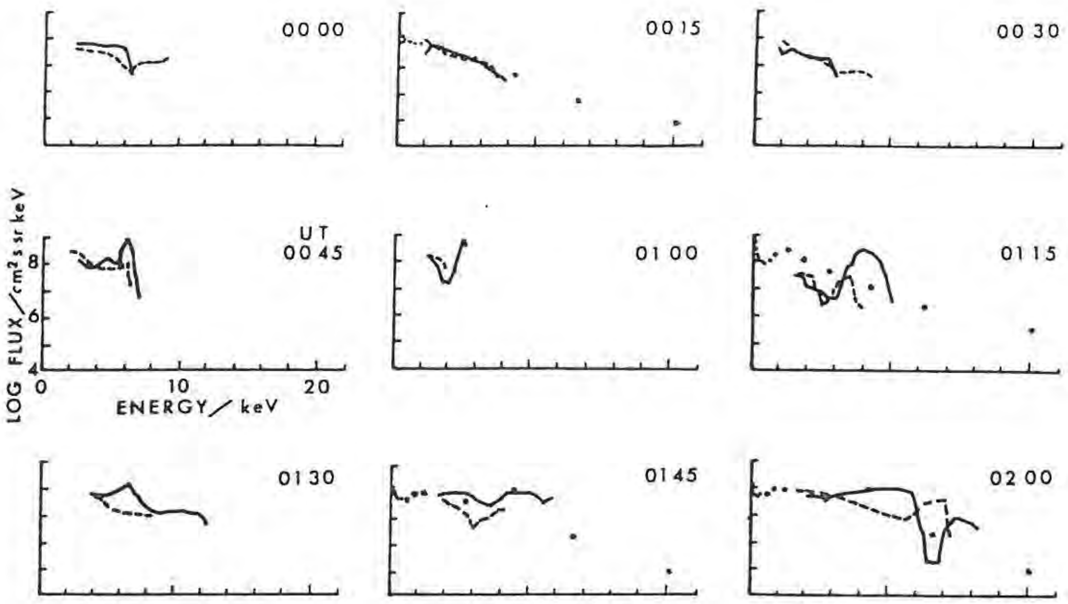

Figure 6.19 Electron energy spectra deduced from Sanae ionograms. Maximum estimates: solid curves; minimum estimates; dashed curves. All scales are as shown for 00:45 UT. (After Gledhill *et al.*, 1987).

energies and fluxes. Values of R_{34}, R_{53}, R_{56} and R_{63} that the author has found reported in the literature, are presented in the form of distribution profiles in Figure 6.20. In addition, values of R_{53} and R_{63}, which have been determined by multiplying the more commonly reported ratios R_{54} and R_{64} by a conversion factor(R_{34}) of 3.28, are also shown. These indirectly determined ratios, labelled R53* and R63* respectively, are not included in the same columns as the directly measured ratios because of the uncertainty in the value of R_{34}. Although most laboratory determinations of R_{34} give values close to 3.28, this is not so for values of R_{34} obtained from simultaneous observations of these two thermospheric emissions. For example, Gattinger *et al.* (1991) show observed ratios ranging from less than 3 to about 4.25. They say that the variability of this measured ratio is due to the effects of atmospheric scattering, which enhance the apparent 391.4 nm intensities to a greater extent than they do the apparent 427.8 nm intensities.

In cases where a range of intensity ratio values was supplied, the author has included both the minimum and maximum ratio values in the distribution profiles. Consequently, while Figure 6.20 reflects the range of values found for each ratio, it does not give any real indication of the frequency distribution of the ratios within each range. Figure 6.20 clearly shows that there is considerable scatter in the values that have been reported for the various ratios. In the case of R_{56} and R_{63}, this is to be expected, as these ratios are dependent on the energy of the precipitating electrons responsible for the aurora. This is not the case with R_{53}, as the

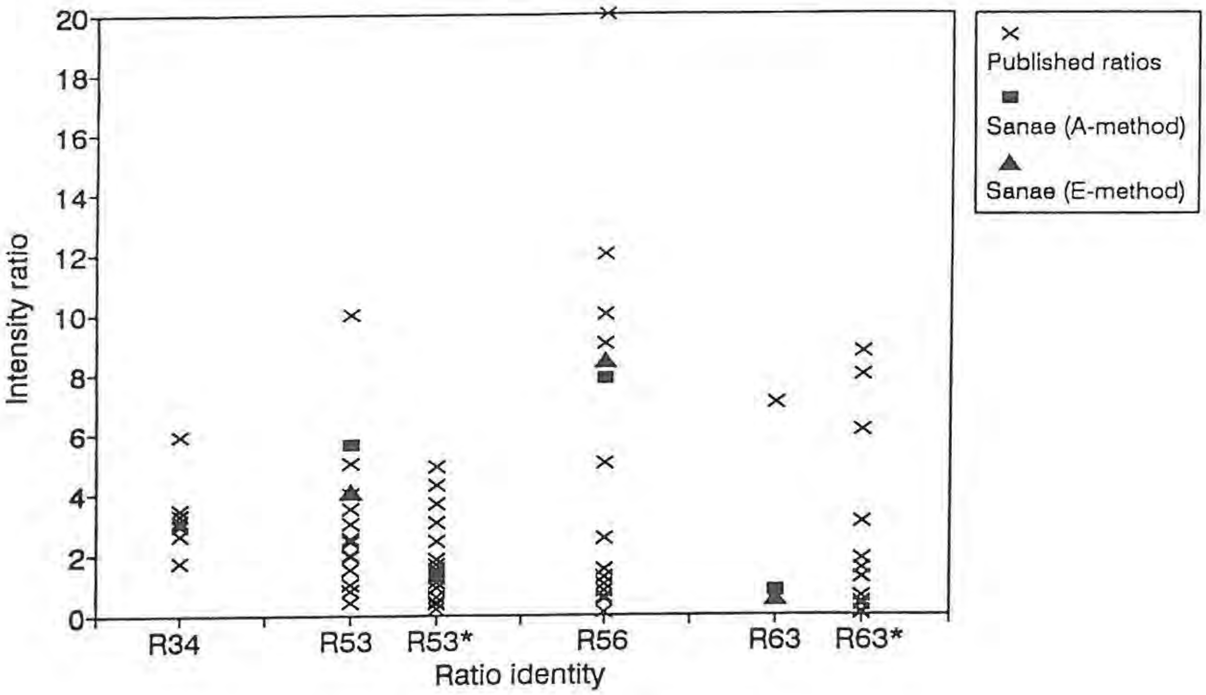

Figure 6.20 Intensity ratios reported in the literature. Note: R53* = 3.28 x R54, and R63* = 3.28 x R64.

391.4 and 557.7 nm emissions occur at approximately the same heights; any intensity changes due to increases in electron energy, or total energy flux, should thus affect both emissions in much the same way. It is generally accepted that R_{53} is reasonably constant (within ± 50%) in ordinary auroras, with a typical value of 2 ± 1 (Omholt, 1971; Vallance Jones, 1971). The spread in observed values of R_{53}, as shown in Figure 6.20, could be due to a number of possible factors:

1/ The intensity ratios have been determined at any number of geomagnetic locations, during various geomagnetic conditions and at various times in the solar cycle. The ratios below 1 are generally those measured for the dayside aurora, where the 391.4 nm enhancements that cause the low ratio values are due in part to the low solar depression angle (see e.g. Cogger *et al.*, 1977; Davydov *et al.*, 1985).

2/ Intensity measurements have been made using a diversity of instrumentation (e.g. spectrographs through to tilting-filter photometers), with a corresponding diversity in sensitivity and accuracy.

3/ Uncertainties in absolute calibration, especially if one considers the low intensities of most calibration sources in the UV (i.e. at 391.4 nm).

4/ The usage of different corrections (if any) for the effects of atmospheric extinction and scattering. The atmospheric correction factors vary with both wavelength and with the zenith angle of the observations. In the wavelength region of 391.4 nm the atmospheric extinction coefficient varies rapidly with wavelength, and thus increases the uncertainty in atmospheric correction factors.

5/ The usage of 'different' emission intensities: Some workers have calculated ratios using total emission intensities, others have only corrected their measured intensities for airglow components, and yet others have (quite rightly) corrected for both airglow and proton-induced components.

6/ The difficulty in estimating the total intensity of an emission band from the measured intensity of only part of the band. This is the case when a narrowband tilting-filter photometer is used to observe the 391.4 nm emission; frequently only the P-branch at the bandhead is measured. Depending on the atmospheric temperature, the factor necessary to convert the measured intensity to a band intensity could be anything between 2 and 4.

To provide a comparison, the mean values of the ratios recorded at Sanae during the substorm of 27 July 1979 have also been shown in Figure 6.20. The ratios resulting from the intensities that were determined using A-method atmospheric correction factors are shown as filled squares, whilst the ratios corresponding to E-method corrections are shown as filled triangles. Regardless of which atmospheric correction method is used, the mean values of R_{56} and R_{63} found at Sanae fall within the generally accepted ranges for these ratios. However, both values for R_{53} (particularly the A-method value) are amongst the highest reported for this ratio. Although these are higher than would be expected, variations in the R_{53} values measured during the substorm do not exceed 50%. This is in agreement with the general limits of R_{53} variability (for observations at a particular station) reported by Omholt (1971).

The question arises as to the feasibility of the high values of R_{53} (> 4) at Sanae. Rees and Luckey's (1974) computations of model spectroscopic ratios indicate that $R_{54} > 12$ (i.e. $R_{53} > 4$) is diagnostic of an electron characteristic energy < 0.3 keV (see their Figure 4). This value does not tie in with the higher energies evident in the electron energy spectra shown in Figure 6.19, which were produced from ground-based ionosonde data and from DMSP satellite particle data. Furthermore, from Rees and Luckey's (1974) Figures 3 and 5, a characteristic energy of < 0.3 keV would be consistent with $R_{64} > 10$ (i.e. $R_{63} > 3$) and $R_{65} > 1$ (i.e. $R_{56} < 1$). These values differ substantially from the average Sanae values obtained for these ratios (see Table 6.3). Unless the physical processes responsible for the aurora at Sanae are different from those that occur elsewhere, the above considerations support the belief that the measured Sanae R_{53} values are too high. Higher 391.4 nm intensities at Sanae (relative to the intensities of the other emissions) would decrease the values of R_{53} and R_{63}, making the three ratios (R_{53}, R_{56} and R_{63}) more consistent with each other in terms of electron characteristic energies. It is probably safe to assume that uncertainties in the 391.4 nm intensities are the major contributor to the high measured values of R_{53} at Sanae.

Several factors could be responsible for the measured 391.4 nm intensities at Sanae being too low: Uncertainty in the 391.4 nm calibration, in the extinction coefficient (and hence in the atmospheric correction factor), and in the factor used to convert the 391.4 nm line intensity to a band intensity (e.g. in the case of the ratios determined from E-method corrected intensities, if a line-to-band conversion factor of 4 was used, instead of 2.5, the mean value of R_{53} would decrease from 4.04 to 2.53). If the N_2^+ (0,1) band at 427.8 nm is observed rather than the (0,0) band at 391.4 nm, advantage can be taken of the higher calibration source brightnesses at the higher wavelength, which should result in lower uncertainties in the absolute calibration. Furthermore, extinction coefficients in the vicinity of 427.8 nm vary less rapidly with wavelength than those at 391.4 nm, and show a smaller range of possible values. This will result in lower uncertainties in the atmospheric correction factors at this wavelength. These improvements would more than compensate for any uncertainties that might result from the lower intensities of the (0,1) band.

In conclusion, with the exception of the R_{53} ratio, the intensity ratios measured at Sanae are within the bounds of acceptable values. The higher-than-expected values of R_{53} would appear to indicate uncertainties in the intensities of the 391.4 nm emission, with the probability that the 391.4 nm intensities are too low. Consequently, there might also be uncertainties in the values of R_{83}. Until the uncertainties in I(391.4) are resolved, using R_{83} and I(391.4) to estimate electron energies and fluxes might prove unreliable.

CHAPTER 7

THE AIRGLOW IN THE REGION OF THE SOUTH ATLANTIC ANOMALY

7.1 Introduction

It is well known that charged particles become 'trapped' in the earth's magnetic field, rapidly spiralling around field lines and bouncing between mirror points on opposite sides of the magnetic equator (see Figure 7.1). In addition to this motion, the particles slowly precess around the earth, electrons moving in an eastward direction and protons in a westward direction. The motions of the particles take place on magnetic shells, which are characterized by a constant value of McIlwain's L parameter. Normally, the mirror points of the low L-value shells occur at high altitudes (in the upper reaches of the thermosphere), where there are negligible densities of atmospheric constituents such as oxygen and nitrogen. However, the asymmetry of the geomagnetic field is such that there is a minimum in the total magnetic field intensity, B, in the vicinity of the South Atlantic. This results in quasi-trapped particles (electrons and ions) penetrating deeper into the atmosphere than they would in other areas with the same L-value. The particles reach lower altitudes in the

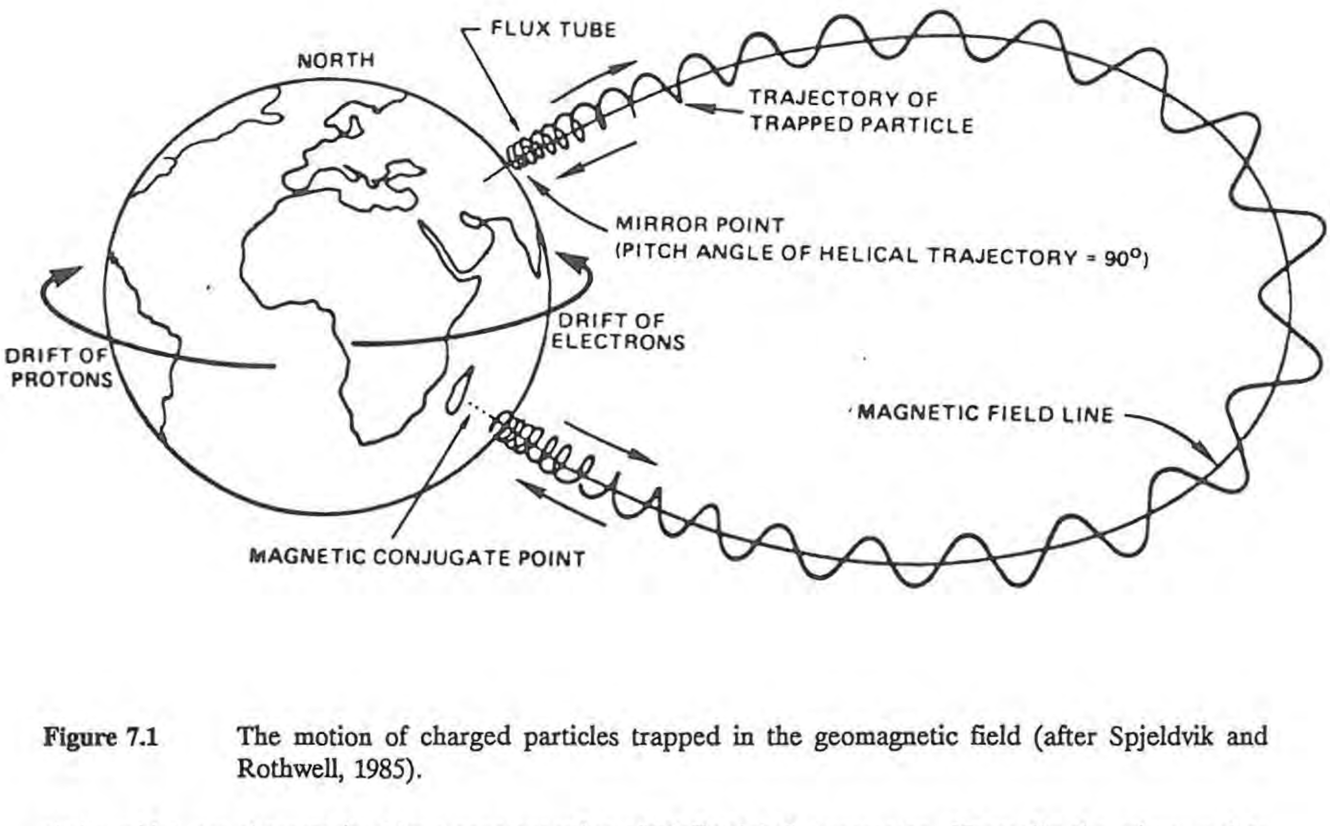

Figure 7.1 The motion of charged particles trapped in the geomagnetic field (after Spjeldvik and Rothwell, 1985).

thermosphere, where there are sufficient densities of atoms and molecules for significant amounts of energy to be lost from the particles through collisions. In addition, some of the particles are scattered into the atmosphere, and are lost from the magnetosphere. These scattered particles cause the production of secondary and tertiary electrons in the atmosphere. In view of the influx of energy into the atmosphere, caused by the precipitation of particles in the 'anomalous' low-B region of the South Atlantic, it is logical to assume that there should be some discernable aeronomic effects in this area.

Experimental proof of the loss of trapped particles into the atmosphere came as early as 1960, shortly after the advent of earth-orbiting satellites (Vernov and Chudakov, 1960; Yoshida *et al.*, 1960). Ginsburg *et al.* (1962) published the first maps of the flux distribution of charged particles entering the ionosphere. Strong maxima were evident off the coast of Brazil (the Brazilian Anomaly) and in that region of the southern Atlantic between South Africa and Antarctica (the Southern Radiation Anomaly). Since then, various anomalous regions have been identified by different workers. The Brazilian Anomaly coincides with the minimum in the magnetic intensity, B. (The 1980 IGRF gives the minimum as about 24000 nT.) The loci of minimum values of B on each L-shell form almost a straight line, which stretches in a south-eastward direction from the coast of Brazil, intersecting the coast of Antarctica at an eastward longitude of about 45°. This, together with the fact that electrons drift eastward under the influence of the geomagnetic field (see Figure 7.1), could explain the presence of anomalies both eastward and southward of the Brazilian Anomaly. Roederer (1972) has shown that anomalies closer to the South African coast can be explained by the higher order terms in a multipole model of the geomagnetic field.

The term 'South Atlantic Anomaly' has been used by various workers to describe a number of anomalous regions in the vicinity of the South Atlantic. To avoid confusion, Gledhill (1976) advocates using this term to describe the total area of the South Atlantic Ocean and the surrounding land masses of South America, South Africa and Antarctica in which anomalous aeronomic phenomena occur.

The aeronomic effects of the South Atlantic Anomaly (SAA) have been reviewed by Gledhill (1976), who gives details of the various particle, airglow, ionospheric and X-ray measurements that had been made in the region of the SAA until 1975. As a result of their analysis of four years worth of nighttime electron flux data, recorded at an altitude of 300 km by the AE-C satellite, Gledhill and Hoffman (1981) concluded that the aeronomic effects of particle precipitation in the region of the SAA should be detectable by ground- or sea-based methods. The flux data that they used was for electrons with energies in the range 0.2 to 26 keV. Electrons with energies in this range will cause ionization in the F- and E-regions of the ionosphere. Consequently, there should be enhancements in the optical emissions from these regions. Relative to their normal airglow levels, enhancements in the OI emissions at 557.7 and 630.0 nm due to particle precipitation in the region of the SAA would be relatively small, and thus difficult to distinguish from the everyday variability that one would expect in these emissions at mid-latitudes. This is not the case with emissions of the N_2^+ 1NG band, which require an excitation energy of 18.75 eV. Energies of this magnitude can only be generated by particle precipitation, and thus any N_2^+ emission is diagnostic of particle precipitation. Other observable effects of particle precipitation in the region of the SAA should be increased E-region ionization (discernable on nighttime ionograms), and increased absorption of radio waves (discernable using a riometer to record the level of absorption of cosmic radio noise at 30 MHz).

The possibility of observing these signatures of particle precipitation in the region of the SAA led to Project ISAAC (the International South Atlantic Anomaly Campaign) which was undertaken in June/July 1983. Before describing the airglow results of Project ISAAC (Section 7.3), we review previous photometric observations made in the region of the SAA.

7.2 Previous airglow observations in the South Atlantic Anomaly

Since 1957 a number of workers have made photometric observations of the airglow either within or close to the region of the South Atlantic Anomaly. Gledhill (1976) gives a comprehensive review of the airglow observations made up until 1975. In view of this, only the more important results of the pre-1976 observations will be given here. In addition, any airglow observations made in the region of the SAA since 1976 will be reviewed.

Airglow observations were made between Cape Town and the Japanese Antarctic base, Syowa, from the Japanese Antarctic research ship, Soya, in the late fifties (Huruhata and Nakamura, 1957; Nakamura, 1958). Enhancements in the OI 557.7 nm emissions were seen in the vicinity of Swoya ($L > 5$), which is at the eastern limit of the anomalous region. However, at an invariant latitude in excess of 63°, it seems most probable that these enhancements were due to subvisual auroral activity, and not to any aeronomic effects of the SAA.

Greenspan and Stone (1964) also used ship-borne photometers to measure N_2^+ 427.8 nm and OI 557.7 and 630.0 nm emissions on a voyage from Cape Town to Gough Island, Bouvet Island, and then back to Cape Town (see Figure 7.2). The only airglow enhancements measured were about midway between Cape Town and Gough Island, in late October 1962. The measured 427.8 nm intensity increased from about 3 to 18 R (and not from 30 to 180 R, as reported by Gledhill, 1976), whilst the 557.7 nm intensity increased from about 200 to 550 R. These enhancements occurred considerably eastward of the eastern limit of the SAA, and no explanation can be found for their occurrence, other than perhaps the existence of a 'South African Anomaly' as predicted by Roederer's (1972) multipole model of the geomagnetic field. Significantly, Greenspan and Stone (1964) observed no evidence of airglow enhancements in the vicinity of Gough Island, which is well within the region of the SAA, even though they were there for some three weeks.

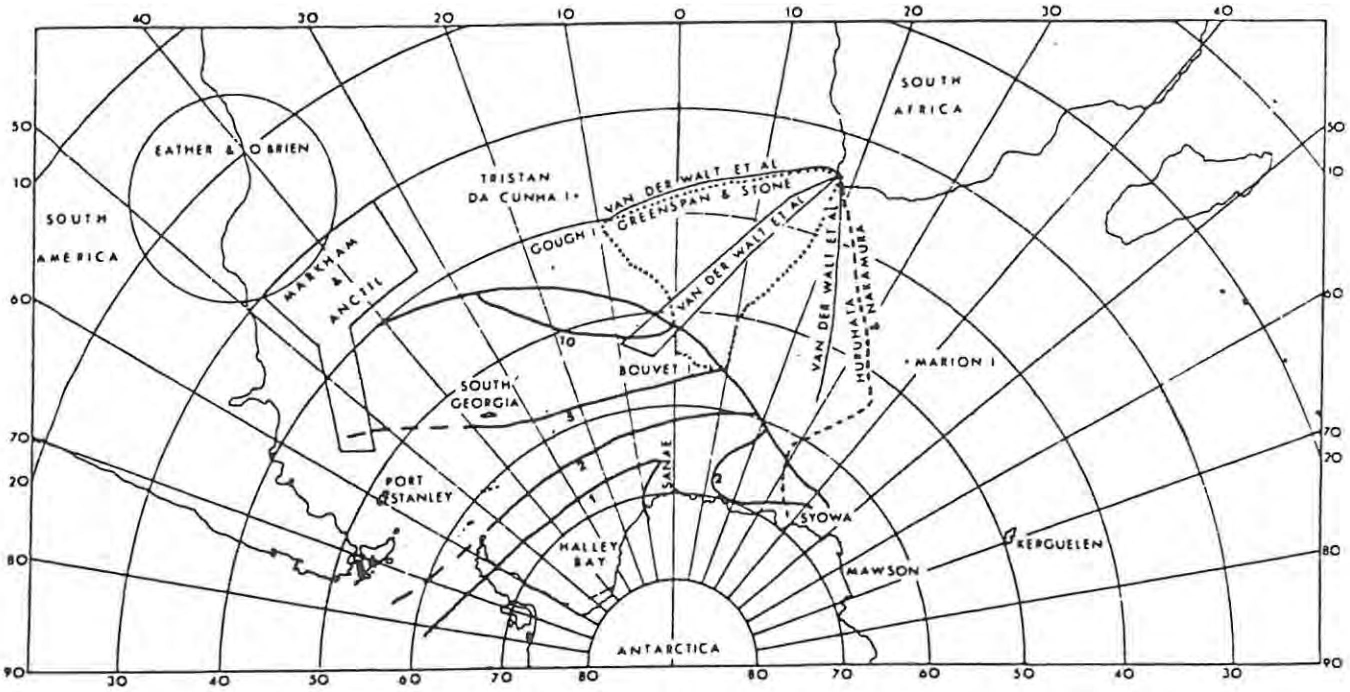

Figure 7.2 Map showing the regions where other workers have made airglow observations. Also shown are predicted 391.4 nm intensity contours (after Gledhill, 1976).

Van der Walt *et al.* (1966) have reported results of airborne measurements of the airglow made whilst following the route taken by Greenspan and Stone (1964) to Gough Island. They found enhancements in the 557.7 nm emission at the same position (midway between Cape Town and Gough Island) as the 557.7 and 391.4 nm maxima found by Greenspan and Stone. However, no significant 391.4 nm emission was observed. On two other flights, one to Bouvet Island and the other in a direction SSE of Cape Town (see Figure 7.2), van der Walt *et al.* (1966) observed 391.4 and 557.7 nm enhancements at the southern-most extent of the flights (at about 55°S). Unfortunately, on both occasions the enhancements coincided with the appearance of the star α Eridani in the photometer's field of view. It is thus improbable that the enhancements are due to aeronomic effects.

As reported in Section 1.2.2, other airborne photometric observations were conducted by Stellenbosch University in 1964, 1966, 1969 and 1971. The results of these flights have only been released in the form of data bulletins (Zeeman *et al.*, 1964; Zeeman *et al.*, 1966; Zeeman *et al.*, 1969a; Steyn *et al.*, 1971b). Some of the flights were into the region of the SAA, but no discernable 391.4 or 427.8 nm emissions were recorded.

Markham and Anctil (1966) also used airborne instrumentation to measure the airglow off the coast of Brazil, in the region of the SAA (see Figure 7.2). They made a number of flights in January and February 1964, using photometers to measure the OI 557.7 and 630.0 nm emissions, and using a 1 metre Ebert scanning spectrometer to monitor 391.4 nm emissions. They found that the OI emissions were typical of the intensities that they had observed in the northern hemisphere. Their graphical representations of the 557.7 and 630.0 nm intensities recorded on two of their flights show that higher intensities were coincident with higher Kp values. The spectrometer used to monitor 391.4 nm emissions had a very low sensitivity; this means that the only conclusion that can be drawn from the fact that they saw no discernable 391.4 nm emissions is that, if present, the intensity of the 391.4 nm emission was less than 200 R. This result is not unexpected, as their observations were conducted to the west of the area of maximum emission intensity predicted by Torr *et al.* (1975), who also predicted a maximum 391.4 nm emission of only about 20 R. Gledhill (1976) has used electron flux contours given by Torr *et al.* (1975) to calculate contours of predicted 391.4 nm emission intensities in the region of the SAA. These contours (shown in Figure 7.2) show that the 391.4 nm intensity in the region of Markham and Anctil's observation should be only 5-10 R.

Eather and O'Brien (1968) have measured various airglow emissions (427.8 nm N_2^+, 486.1 nm H_β, 557.7 nm OI, 5876 nm HeI and 630.0 nm OI) from a ground-based station (22.5°S, 44°W) close to Rio de Janeiro in Brazil. Measurements were made in the zenith, and also in an almucantar-scanning mode at a zenith angle of 70°, using very sensitive tilting-filter photometers. The field of view of the almucantar observations is shown by the circle in Figure 7.2. Eather and O'Brien have only reported the results of two nights' observations, made early in October 1967 during quiet magnetic conditions. They found that the OI emission intensities (75-160 R at 557.7 nm, 25-250 R at 630.0 nm) were consistent with intensities recorded at other mid-latitude stations outside of the influence of the SAA. They were unable to detect significant emissions at 427.8, 486.1 and 587.6 nm and thus put maximum limits on these emissions of < 0.2 R, < 0.7 R and < 1 R respectively.

Since Gledhill's 1976 review of the aeronomic effects of the SAA, the author has found no evidence in the literature of any more recent shipborne, airborne, rocket-borne or satellite-borne airglow observations having been made in the immediate vicinity of the SAA. The closest airglow observations made to the SAA have been ground-based observations at Cachoeira Paulista (geographic coordinates 22.7°S, 45.0°W; geomagnetic latitude -11.9°), which is near Rio de Janeiro. This station is less than 100 km from the site used by Eather and O'Brien (1968). Small 391.4 nm emissions have been observed at Cachoeira Paulista, but only during extremely disturbed magnetic conditions. Emission intensities measured there are summarized in Table 7.1. Rohrbaugh *et al.* (1983) state that they have never detected 391.4 nm emissions at Cachoeira Paulista for $Kp < 5$. Tinsley *et al.* (1982) explain that the N_2^+ emissions are caused by the enhanced ring currents that flow during very disturbed magnetic conditions. Charge exchange of ring current O^+ ions with exospheric neutral constituents produces precipitating O atoms and other ions which cause the N_2^+ emissions. This phenomenon has been observed at other low- and mid-latitude stations, and is not peculiar to the region of the SAA. For example, Chamberlain and Jacka (1979) have reported measuring up to 5 R of 427.8 nm emission ($\equiv$ 16 R of 391.4 nm) at Adelaide in Australia. Meriwether and Walker (1980) and Tinsley and Burnside (1981) have measured up to 2 R of 427.8 nm emission at Arecibo in New Mexico for Kp values of

Table 7.1 N_2^+ emission intensities measured at Cachoeira Paulista in Brazil.

Source of information	Date of observation	I(391.4) (R)	Kp index values
Tinsley et al. (1982)	13 April 1981	1.6	8-
Rohrbaugh et al. (1983)	13/14 July 1982	5-20	8- and 9o
Sahai et al. (1988a)	12/13 June 1983	4	8-
	13/14 June 1983	< 1	4- and 3o
	6/7 August 1983	0	1- to 2-
	7/8 August 1983	4 - 6	6+ to 8-
	28/29 March 1984	0	6- to 6+
	1/2 April 1984	0	3- to 5+

between 6 and 8. In Hawaii, 5-7 R of 391.4 nm emission have been recorded for Kp = 8- and 8 (Tinsley *et al.*, 1982; Rohrbaugh *et al.*, 1983).

At Cachoeira Paulista, OI 630.0 nm emissions are also observed. Sahai *et al.* (1988a) show 630.0 nm intensities on the same graphs as their 391.4 nm intensities (given in Table 7.1). The 630.0 nm plots show a great variation in intensities, from about 600 to 10 R. The predominant trend in all of the 630.0 nm intensity plots is a gradual decrease in intensity during the night, although the decrease is far from smooth. The 630.0 nm emissions at low latitudes also show considerable variations with season and solar cycle, as reported by Sahai *et al.* (1988b). With such diurnal, seasonal and solar cycle variability, any small 630.0 nm intensity enhancements due to effects of the SAA would be impossible to detect.

Gledhill and Hoffman (1981) found that the energy flux of the precipitating electrons in the region of the SAA decreases as Kp increases. This would imply that N_2^+ emissions should be observed during quiet magnetic conditions, and should in fact be more intense than emissions during slightly disturbed conditions. From the above review of airglow emissions in the region of the SAA, it can be seen that there has been no evidence of enhancements in the N_2^+ and OI emissions during magnetically quiet periods.

7.3 The airglow observed during Project ISAAC

Project ISAAC (International South Atlantic Anomaly Campaign) was a South African venture, instigated and coordinated by Prof. J.A. Gledhill for Rhodes University. Although centred around observations made from the South African research vessel S A Agulhas, it included participation from ground-based sites in

Brazil (ionosonde and airglow photometers) and Chile (ionosonde). The S A Agulhas carried a chirp ionosonde, three tilting-filter photometers and a riometer. In addition, fluxgate and micropulsation magnetometers were set up on Gough Island during the campaign. Project ISAAC was conducted in June and July 1983, with the ship leaving Cape Town on 29 June and returning there on 22 July. During the voyage, the ship traversed the region of most intense electron precipitation into the ionosphere. The course followed by the ship is shown in Figure 7.3, which also shows the region of high energy electron precipitation (dashed contour line) observed by Ginsburg *et al.* (1962) and of low energy electron precipitation (solid contour line) determined by Gledhill and Hoffman (1981).

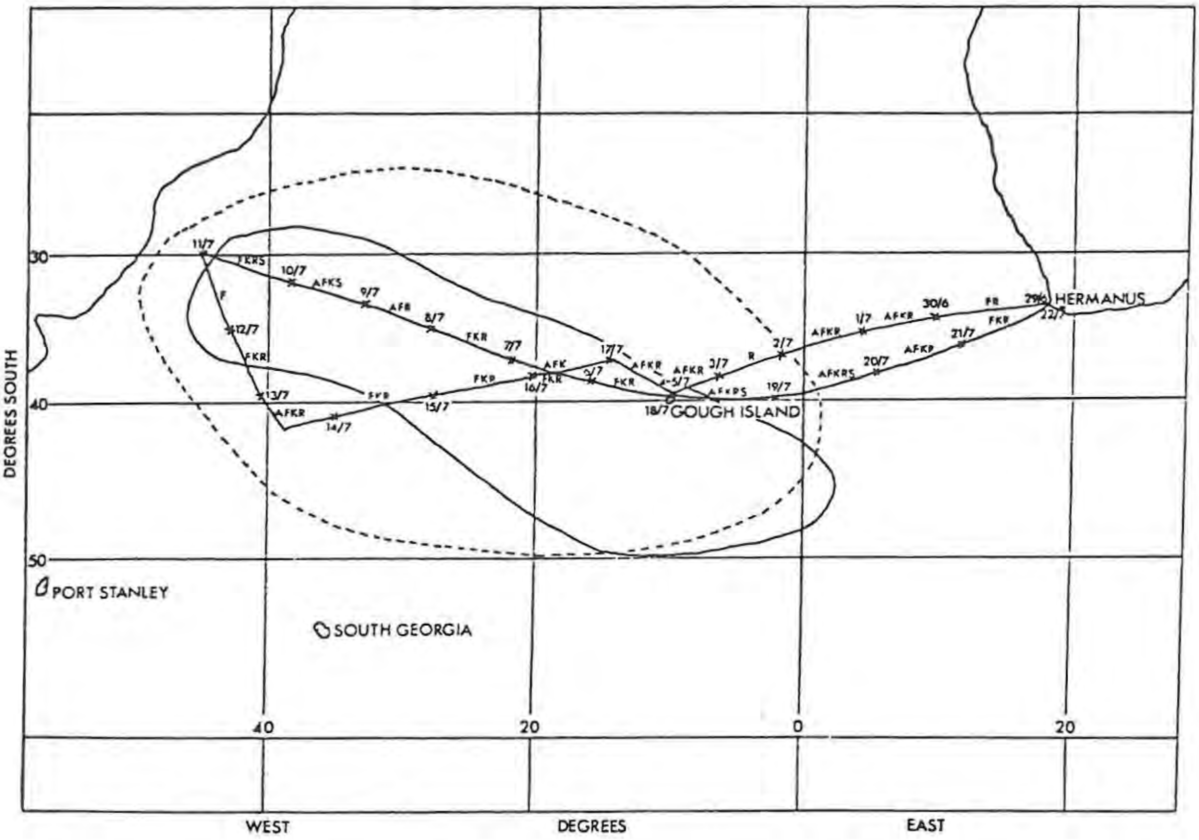

Figure 7.3 The route taken by the S A Agulhas during Project ISAAC. The ship's noon position is indicated for each day of the voyage, as are the sporadic E types observed during the nights.

Preliminary results of Project ISAAC have been reported by Dore *et al.* (1985). A more comprehensive report on the results of Project ISAAC has been prepared (Gledhill *et al.*, 1988), but owing to the untimely death of Prof. Gledhill and to manpower shortages it has not yet been published. We will concentrate on the airglow results of Project ISAAC, and in particular on the results of the airglow observations made from the S A Agulhas.

7.3.1 Instrumentation

The three photometers used on board the S A Agulhas were of the tilting-filter type, as described in Section 3.3. They were mounted in a specially constructed hatch cover positioned in the roof of the ionospheric laboratory, which is on the navigating bridge deck of the ship. Collimator tubes were externally mounted on the hatch, above each photometer. These were used to prevent scattered light from the ship from reaching the photomultiplier tubes. Care was taken to ensure that the collimators did not impinge on the field of view of the photometers, which was about 4°. During airglow observations the ship carried as few navigational running lights as possible. Although nominally directed towards the zenith, the photometers naturally moved with the ship as it pitched and rolled. The S A Agulhas was designed for use in Antarctic conditions, and has a virtually flat bottom to facilitate movement through thin pack-ice. This makes the ship susceptible to rolling, so while most observations were within 10° of the zenith, zenith angles of observation far exceeded this figure at times.

A prototype of the digital photometer system described in Section 3.5 was used during the ISAAC cruise. A microcomputer was used to control the tilting of the filters, the filters' temperatures and the photometers' shutters. The photomultipliers were operated in photon-counting mode. The counts were integrated in a selectable number of bins of filter tilt angle, usually taking 16s at each angle. Long integration times were used because of the low emission intensities being observed (typically less than 30 R); the longer the integration time, the better the signal-to-noise ratio. After each complete run through the filter-tilting cycle, the various line and background counts taken by each photometer were output to a printer. Following this, the photometer shutters were closed and dark current counts were recorded. Immediately after this the next filter-tilt cycle was started. Each cycle took approximately ten minutes to complete. As a backup, the photomultiplier outputs were converted to an analogue form and recorded on a three-channel chart recorder. This form of output also served as a convenient visual monitor of the performance of each photometer, allowing the operator to check the position of the emission lines relative to the filter tilt angles that were used. Filter tilt angles used for background observations were selected to be as far from the emission lines as possible, bearing in mind the variation of filter transmission characteristics with tilt angle.

Two low-brightness light sources were used to calibrate the photometers during the cruise: A variable-aperture source incorporating a quartz tungsten-halogen lamp (LBS #2), and a ^{90}Sr-activated phosphor source. Both sources have been described in Section 3.6. The variable-aperture source was the preferred source, as it allowed calibrations to be performed at a brightness comparable to that of the airglow being measured. The ^{90}Sr source was used primarily as a backup for the other source, and to confirm the absolute brightnesses determined using the variable-aperture source. To ensure that the calibration source filled the field of view of the photometer being calibrated, the external collimator was removed and the source positioned in its place (immediately above the photometer). A thick black cloth was draped over the calibration source, to ensure that no scattered light from the ship entered the photometer during the calibration.

7.3.2 Observations and data processing

Due to cloudiness and moonrise, only five nights of usable data were obtained from the airglow photometers aboard the ship during this campaign. The periods during which usable data were observed are given in Table 7.2. During these times the sky was clear, or there was only thin cloud or haze present overhead. The Kp magnetic indices for these nights are given in Table 7.3. With the exception of the night of the 12/13 July, all usable airglow observations were made under quiet magnetic conditions; that night there was increased magnetic activity, but Kp never exceeded a value of 5.

The raw airglow data (line, background and dark current counts) were processed using the digital airglow equation derived in Section 4.2.1. For convenience, this equation (Equation 4.13) is repeated here:

$$I_0 = \left(n_{1,a} - n_{2,a} \left(\frac{T_1}{T_2} \right) \right) B_f \, T_3 \, C \qquad (7.1)$$

Where: $n_{1,a}$ and $n_{2,a}$ are the counts corresponding to the emission line and the background, after the dark current counts have been subtracted from each.

T_1, T_2 and T_3 are the filter transmission factors corresponding to the filter tilt angles used to record line, background and photometer calibration counts.

B_f is the calibration factor, determined by calibrating the photometer with a calibration source of known brightness, B. Thus, $B_f = B/n_{3,c}$, where $n_{3,c}$ are the total counts taken with the calibration source filling the photometer's field of view, minus the dark current counts taken with the photometer's shutter closed.

C is the atmospheric correction factor.

The transmission characteristics of the filters used on the ISAAC cruise were measured early in 1984, some six months after the cruise. Values for the transmission factors (T_1, T_2 and T_3) for each filter were determined from the measured filter transmission curves (see Section 5.2). As the filters were not used between the time of the cruise and the measurement of their characteristics, it can be assumed that the values obtained for T_i are accurate assessments of the filters' transmission factors at the time of the cruise.

The photometers were calibrated on several occasions during the cruise, using both low-brightness calibration sources mentioned in Section 7.3.1. It was decided to use the calibration factors determined from the

Table 7.2 The times during the 1983 ISAAC cruise when usable airglow data were recorded, using the photometers aboard the S A Agulhas.

Start		Finish		Comments
Date	Time (UT)	Date	Time (UT)	
12 July	00:00	12 July	08:47	Sky clear
12 July	20:58	13 July	08:26	Sky clear 01:11 - 08:26
13 July	22:17	14 July	01:01	Patchy cloud
14 July	20:21	15 July	05:31	Sky clear 03:00 - 05:00
16 July	00:04	16 July	07:19	Thin cloud

Table 7.3 Kp magnetic activity indices for the nights on which usable airglow data were recorded on board the S A Agulhas during the ISAAC cruise.

Date in 1983	Three-hourly Kp magnetic activity index				
	18:00 - 21:00	21:00 - 24:00	00:00 - 03:00	03:00 - 06:00	06:00 - 09:00
11/12 July	1-	2o	2-	1-	1+
12/13 July	5-	4-	5o	4o	4o
13/14 July	1o	2o	1-	2o	2+
14/15 July	2-	1o	1+	2-	1-
15/16 July	2-	2o	3-	3+	2o

calibrations performed with the variable-aperture source (LBS #2). The values of B, the source brightness, that were used to calculate the calibration factors, were the means of the two brightnesses obtained when the source was cross-calibrated against the two NPRL lamps in 1984 (see Section 5.3).

The atmospheric correction factors, C, were determined using Ashburn's method (the A-method), which is applicable to airglow emissions (see Section 4.3.3). Ashburn's method takes into account the exponential attenuation caused by atmospheric extinction (i.e. absorption and scattering of light out of the field of view), and also the effects of light diffusely scattered into the field of view, and light reflected from the ground and backscattered into the photometer's field of view. The airglow observations made from the S A Agulhas were nominally made in the zenith. Although the ship is susceptible to rolling, it is estimated that most of the observations made during the ISAAC cruise were made within 20° of the zenith. At such a zenith angle, both the air mass (m) and the van Rhijn function (V) differ from unity by little more than 5%. Consequently, taking these parameters to be unity for all of the observations would not contribute significantly to uncertainties in the resultant emission intensities. Setting both m and V equal to unity, the A-method formula given in Equation 4.31 simplifies to

$$C = \left(e^{-\tau_{total}} + e^{-\tau_{ozone}}(D + R)\right)^{-1} \qquad (7.2)$$

where D is the coefficient for the diffusely transmitted light component, and R is the coefficient for the ground-reflected and backscattered light component. These coefficients are both dependent on the height of the emitting layer (h), the total extinction coefficient of the atmosphere (τ_{total}), and the zenith angle of the observations (z, = 0°). In addition, R is dependent on the ground albedo (r). The values used for the wavelength-dependent parameters are given in Table 7.4, together with the resultant atmospheric correction factors. The values of τ_{total} are again those measured by Guttmann (1968) for maritime conditions. The values of τ_{ozone} are those calculated in Section 6.3.1 for use at Sanae, which assume an ozone thickness of 0.3 cm at STP. The ground albedo values were obtained by interpolating the tabulated spectral reflectances for water given by Condron and Toolin (1960). The atmospheric correction factors were determined after interpolating values of D and R from the tables given by Ashburn (1954). In the case of R, the ground-reflected coefficient, a two-stage interpolation was needed because neither the extinction coefficients nor the ground albedos coincided with the values used by Ashburn.

Table 7.4 The A-method atmospheric correction factors used to process the airglow data collected on the ISAAC cruise, and the wavelength-dependent parameters used to determine them.

Emission wavelength (nm)	Emission height (km)	Extinction coefficient		Ground albedo of water	Atmospheric correction factor
		τ_{total}	τ_{ozone}		
391.4	100	0.48	0.000	0.17	1.020
557.7	100	0.22	0.030	0.05	1.013
630.0	300	0.18	0.029	0.03	1.032

It can be seen that all three atmospheric correction factors are within 3.5% of unity, and so there will be a negligible difference between the observed and calculated emission intensities. If straightforward exponential correction factors (E-method correction factors) were to be used the resultant 391.4, 557.7 and 630.0 nm emission intensities would be factors of 1.59, 1.23 and 1.16 respectively higher than those calculated using the A-method correction factors.

Once atmospheric correction factors and calibration factors had been determined, Equation 7.1 was used to reduce the raw count data to emission intensities. The 391.4, 557.7 and 630.0 nm emission intensities obtained from the five nights of usable data are shown in Figures 7.4 to 7.8.

7.3.3 The airglow results of Project ISAAC

It is perhaps easiest to consider the N_2^+ and OI emissions separately. In each case the emissions measured aboard the S A Agulhas in the anomaly region will be compared with those measured at Cachoeira Paulista. Where appropriate, reference will also be made to the occurrence of sporadic-E on the ionograms recorded with the ionosonde aboard the ship. Three types of sporadic-E traces are generally accepted as being diagnostic of particle precipitation. These are a-type (auroral-E), r-type (retardation-E) and k-type (particle-E) traces. The types of sporadic-E observed on each night are given in Figure 7.3, between the crosses marking the noon position of the ship. Besides the three types of sporadic-E mentioned above, two other types of sporadic-E were observed on the voyage: f-type (flat) and s-type (slant). The presence of a-, r- and k-type sporadic-E during the cruise is, in itself, good evidence that there are observable effects of particle precipitation in the region of the SAA.

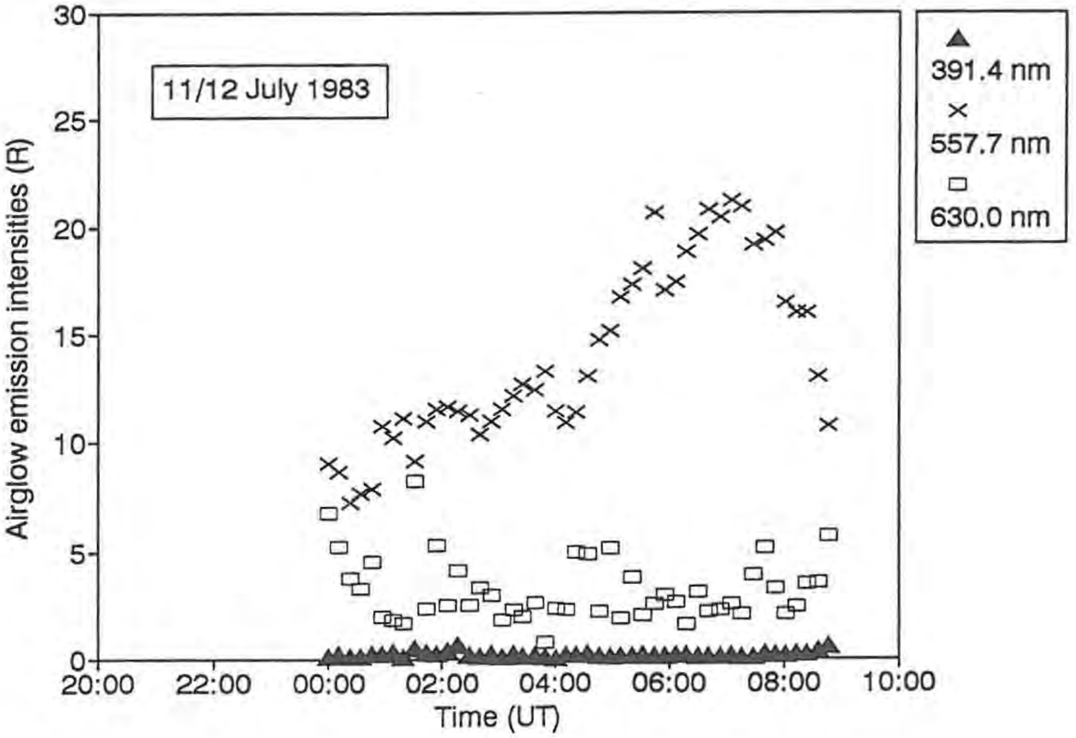

Figure 7.4 Airglow emission intensities measured on the ISAAC cruise during the night of 11/12 July 1983. The ship's midnight position was 32.3°S, 44.5°W.

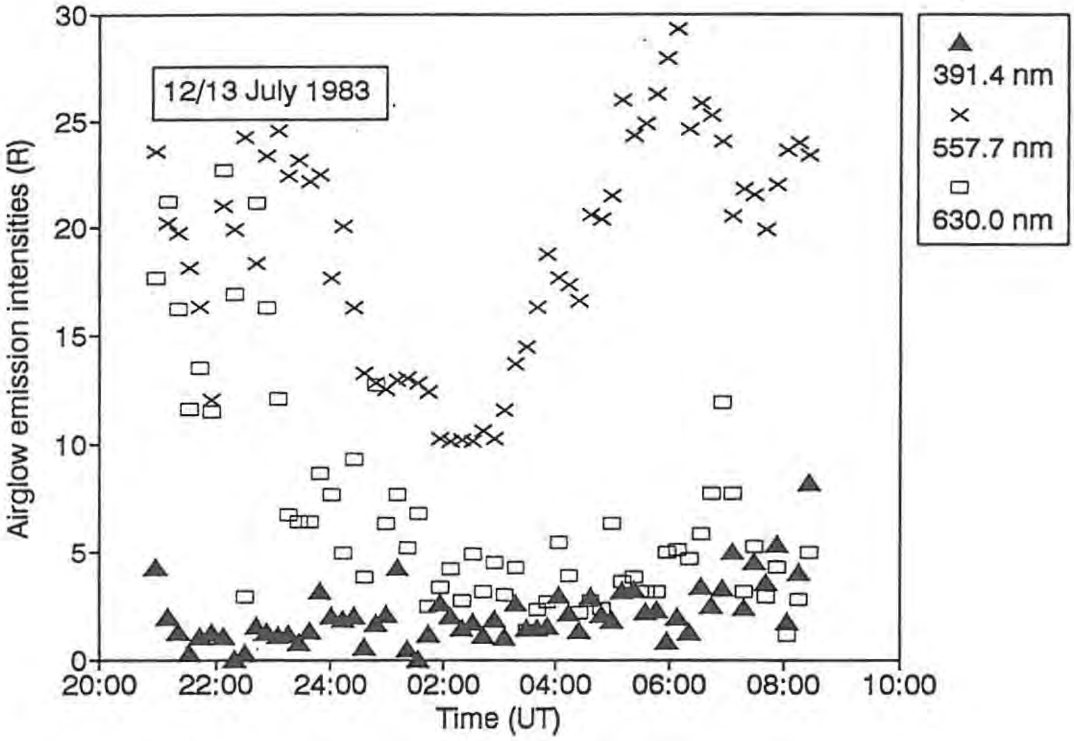

Figure 7.5 Airglow emission intensities measured on the ISAAC cruise, during the night of 12/13 July 1983. The ship's midnight position was 37.2°S, 42.0°W.

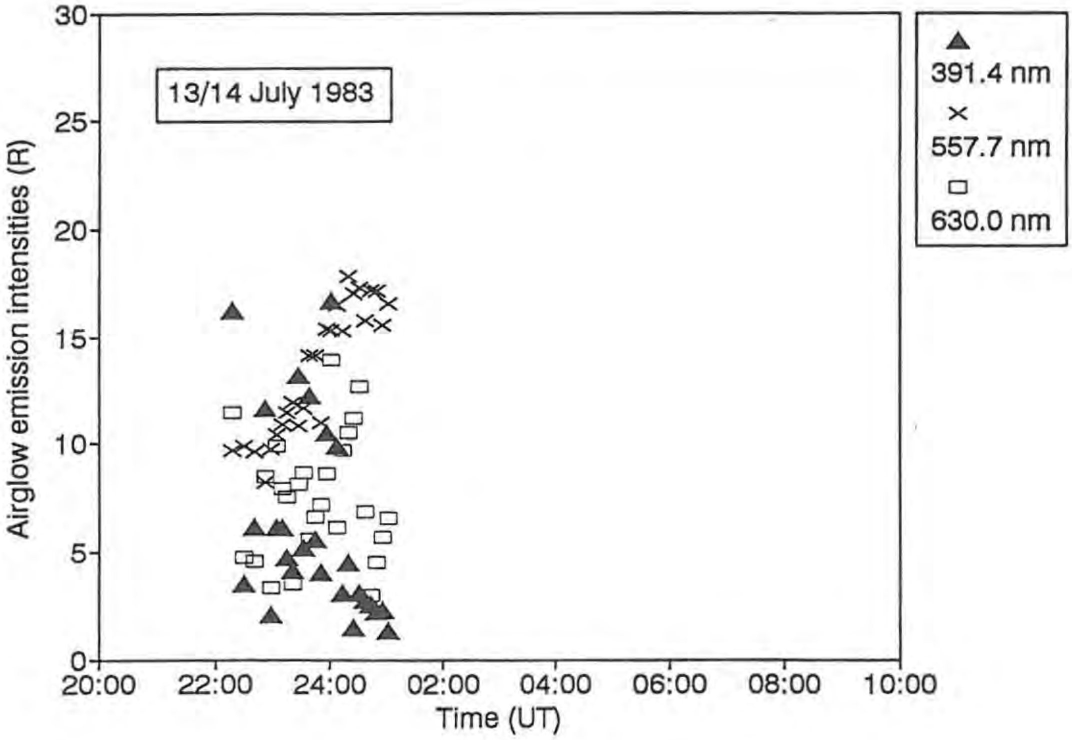

Figure 7.6 Airglow emission intensities measured on the ISAAC cruise, during the night of 13/14 July 1983. The ship's midnight position was 41.6°S, 38.8°W.

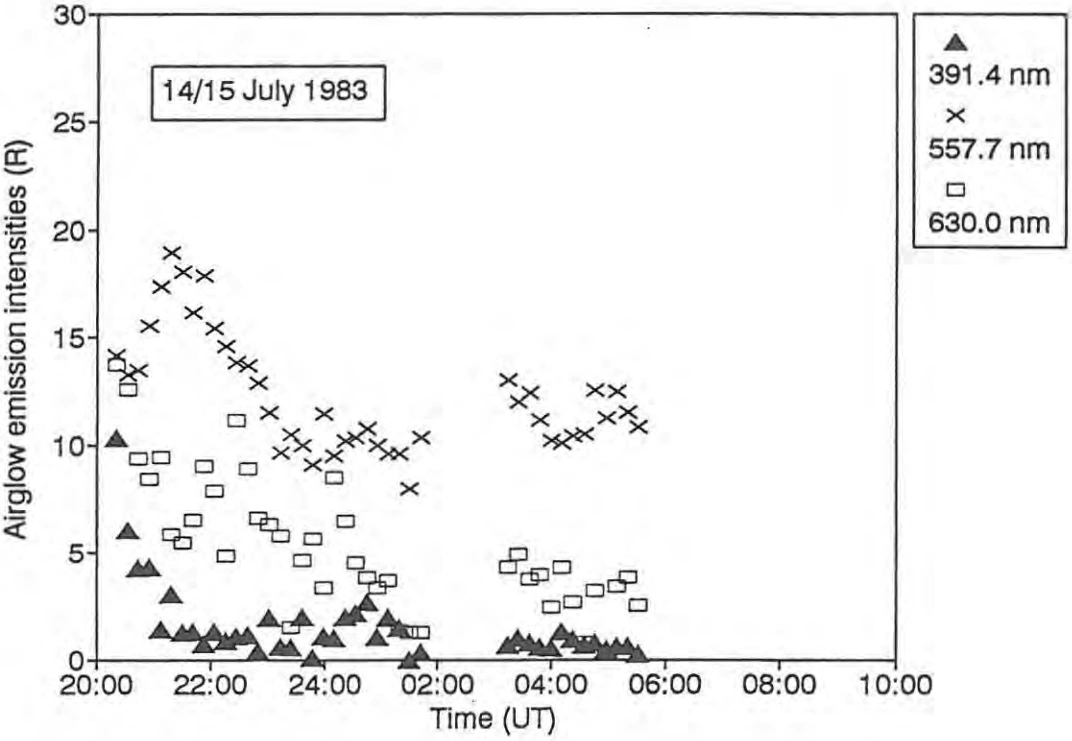

Figure 7.7 Airglow emission intensities measured on the ISAAC cruise, during the night of 14/15 July 1983. The ship's midnight position was 40.2°S, 31.2°W.

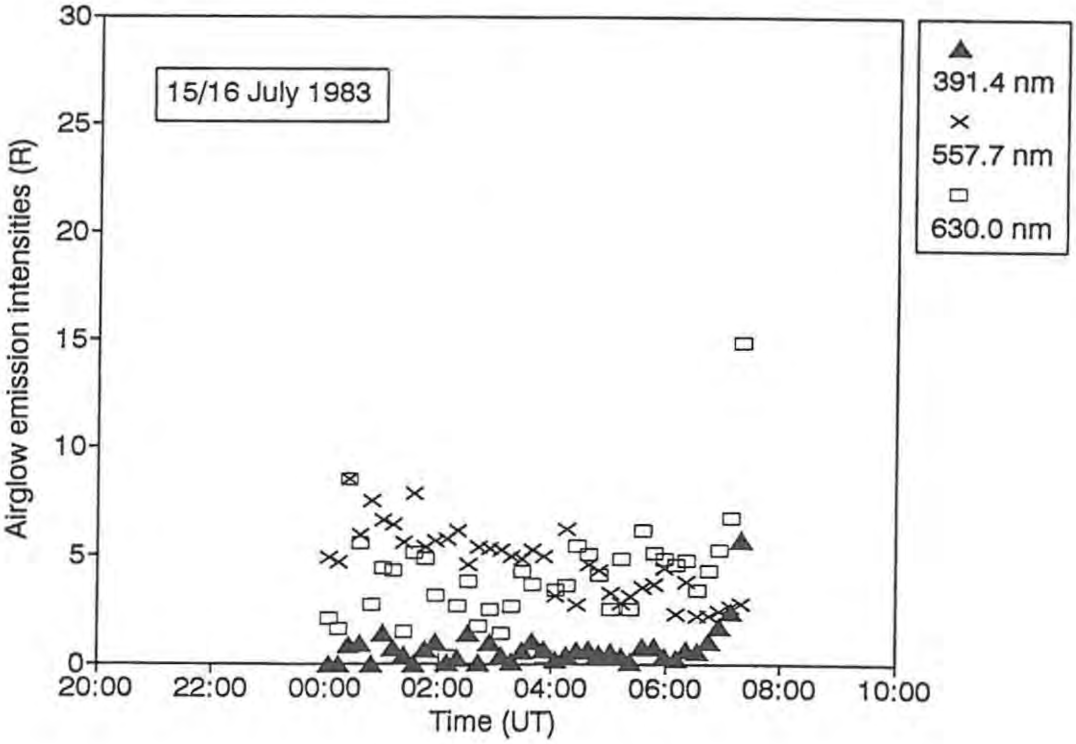

Figure 7.8 Airglow emission intensities measured on the ISAAC cruise, during the night of 15/16 July 1983. The ship's midnight position was 39.0°S, 24.6°W.

7.3.3.1 The N_2^+ 391.4 nm emissions

As N_2^+ emissions are diagnostic of particle precipitation, the 391.4 nm observations are the most important of the three emissions observed from the ship. Non-zero 391.4 nm emissions were seen on four of the five nights during which usable data were collected.

Figure 7.4 shows the airglow intensities observed during the early morning of 12 July, when the ship was at its farthest point west during the voyage, and closest to Cachoeira Paulista (some 700 km away). There was no evidence of 391.4 nm radiation, which is in agreement with the absence of any particle-related sporadic-E ionization during this period (see Figure 7.3). On the night of 12/13 July there was some 391.4 nm activity, with intensities reaching 4 R at times, as shown in Figure 7.5. Contrasted with the 391.4 nm intensities shown in Figure 7.4, this gives confidence that the photometer was actually measuring a variable, low-intensity emission during the night of 12/13 July. Similar, but lower level, emissions were also observed on the nights of 14/15 and 15/16 July, as shown in Figures 7.7 and 7.8 respectively. The occurrence of low-level 391.4 nm intensities on these three nights coincided with the presence of r-type and k-type sporadic-E traces, which are particle-related. However, no a-type sporadic-E was detected on these nights.

On the night of 13/14 July the intensity of the 391.4 nm radiation was never less than 2 R, and twice reached a maximum of 16 R. These higher intensities coincided with the sustained appearance of a-, r- and k-type sporadic-E traces on the ionograms. It is significant that the relatively high 391.4 nm intensities observed on the night of 13/14 July occurred with Kp values of 2 and 1-, whereas the lower intensities observed on the previous night (12/13 July) occurred for Kp values between 4- and 5. This supports the finding of Gledhill and Hoffman (1981) that more intense particle precipitation occurs during magnetically quiet times. The definite presence of 391.4 nm radiation and the presence of particle-related sporadic-E ionization (especially a-type sporadic-E) on the night of 13/14 July are strong evidence of discernable effects of particle precipitation in the region of the SAA.

Kasting and Hays (1977) determined an expression relating the N_2^+ (0,1) emission intensity at 427.8 nm to the energy flux of the precipitating electrons causing the emission. Torr and Torr (1984) modified this expression so that it could be applied to the N_2^+ (0,0) emission at 391.4 nm. (This was done by simply substituting I(391.4)/3.28 for I(427.8) in Kasting and Hays' expression). The resultant equation is

$$\Phi_E = 1.19 \times 10^{-3} I(391.4) \tag{7.3}$$

where Φ_E is the total energy flux of the electrons in mW m^{-2} (= erg cm^{-2} s^{-1}). Most of the 391.4 nm intensities observed on the ISAAC cruise averaged between 2 and 3 R. Using Equation 7.3, these intensities correspond to energy fluxes of 2.4 - 3.6 $\times 10^{-3}$ mW m^{-2}, which compare favourably with the energy fluxes in the area of the ISAAC cruise of about 3 - 3.5 $\times 10^{-3}$ mW m^{-2} found by Gledhill and Hoffman (1981). The

ISAAC 391.4 nm intensities also fall within the maximum emission intensity of 20 R predicted for the region of the SAA by Torr *et al.* (1975). Both of these results serve to confirm that the 391.4 nm intensities observed on the ISAAC cruise are of the right order of magnitude.

In contrast to the shipborne airglow observations, the airglow observed at Cachoeira Paulista on the nights of 11 to 16 July showed no significant evidence of 391.4 nm emissions. A comparison of the times of occurrence of spread Es (particle-related) traces on ionograms recorded aboard the S A Agulhas and at Cachoeira Paulista seems to indicate that intense particle-produced ionization is very variable in both space and time (Gledhill *et al.*, 1988). This factor, and the considerable distance separating Cachoeira Paulista from the high intensity precipitation region of the SAA, might explain the absence of detectable 391.4 nm emission at Cachoeira Paulista when some 16 R were measured from the ship. In fact, the absence of 391.4 nm emissions at Cachoeira Paulista during quiet magnetic conditions (Rohrbaugh *et al.*, 1983; Sahai *et al.*, 1988a), would imply that this station is outside of the area in which the anomaly-related particle precipitation is strong enough to cause 391.4 nm radiation.

7.3.3.2 The OI 557.7 and 630.0 nm emissions

The 557.7 and 630.0 nm airglow intensities measured from the S A Agulhas are characterized by their remarkably low values. Neither emission exceeded an intensity of 30 R during the five nights on which usable data were collected. The very low intensities observed on the night of 15/16 July are almost certainly due to attenuation effects of the cloud cover experienced that night. In fact, thin cloud cover most probably caused varying degrees of attenuation of the observed airglow intensities on most nights.

In contrast to the very low intensities recorded aboard the ship, the 557.7 nm intensities recorded at Cachoeira Paulista during the period 11-16 July averaged about 100 R, whilst the 630.0 nm intensities were usually between 25 and 200 R (decreasing during the course of the night). The question arises as to whether the differences between the Cachoeira Paulista and the shipboard intensities (about a factor of 5) are real, or due to other factors (e.g. data processing methods, photometer calibrations etc.)? A number of points need to be considered:

On each night there was little correlation between the OI intensity variations observed on the ship and those observed at Cachoeira Paulista. The differences between the temporal trends of the shipborne and ground-based observations would support the possibility of different intensities occurring in the two areas, which were a minimum of 700 km apart.

The apparent intensities observed from the ship showed more rapid fluctuations than those measured at Cachoeira Paulista. This phenomenon was probably caused by the rolling and pitching motion of the ship. Significant movement of this type will result in the photometers looking at different areas of the sky during their line and background measurements. This could result in different 'continuum' intensities being measured during these observations, and hence errors in the subtraction of the background. This problem could be especially significant if the ship's motion causes bright stars or the Milky Way to move in and out of the photometers' field of view. Observed intensities will either be too low or too high, depending on whether there was over- or under-compensation for the background. As a result, the rolling and pitching motion of the ship would cause high as well as low intensities to be measured from the ship. The only way to avoid the apparent intensity fluctuations caused by the ship's motion, is to make line and background measurements simultaneously. This would necessitate using double the number of photometers, which besides being expensive, would complicate the data processing techniques that are required, and probably introduce other (smaller) sources of errors in the calculated intensities.

Uncertainties in calculated intensities are probably a major contributing factor to the apparent intensity differences. Absolute calibration of the photometers, filter transmission characteristics, correction methods for the effects of atmospheric extinction and scattering, and data processing methods can all contribute to uncertainties in intensity values. For the shipboard observations, the following estimates can be made of the various contributions to the overall uncertainties in the measured OI emission intensities:

1/ Uncertainties due to the absolute calibration of the photometers.

Uncertainties in the ISAAC emission intensities arise primarily from uncertainties in the brightness of the secondary light source used to calibrate the photometers. The calibration sources used during the ISAAC cruise were cross-calibrated against standard light sources soon after the cruise (see Section 5.3). The shipboard airglow intensities reported in this chapter were calculated using results of the photometer calibrations performed with the LBS #2 variable-aperture source. The brightnesses that were used for the LBS #2 were the average of those brightnesses determined from the cross-calibration of the source against the two NPRL standard lamps. Table 5.6 shows that these brightnesses were the lowest that were obtained from the various cross-calibrations of LBS #2. Using the highest brightnesses given for LBS #2 in Table 5.6 would cause higher intensities by factors of 1.61 at 557.7 nm and 1.44 at 630.0 nm, whilst using the lowest brightnesses (obtained from the cross-calibration against the NPRL lamp #1681) would only decrease the intensities by factors of 0.96 and 0.97 respectively. A further source of uncertainty in the brightnesses of LBS #2 is the possibility of experimental errors in the cross-calibrations (estimated as 10% in Section 4.4.1.2).

2/ Uncertainties due to the filter transmission factors.

The filter transmission factors were determined shortly after the cruise (see Section 5.2). Considering the accuracy of the spectrophotometer that was used to measure the transmission characteristics of the filters, it is conservatively estimated that the maximum experimental error in the determination of these factors was 10%.

3/ Uncertainties due to the atmospheric correction factors.

Measured emission intensities are dependent on the correction factors that are applied for the effects of atmospheric extinction and scattering. Uncertainties in atmospheric correction factors are caused by uncertainties in atmospheric extinction coefficients and by the correction models that are used. If A-method correction factors are used to process the ISAAC data, the uncertainties in the correction factors (due to the atmospheric extinction coefficients that are used) are small: If A-method correction factors are calculated using minimum and maximum extinction coefficients at each wavelength (as given in Table 4.1), then the zenith atmospheric correction factors vary between 0.99 and 1.03 at 557.7 nm, and between 1.01 and 1.05 at 630.0 nm. Consequently, for zenith observations, uncertainties in emission intensities due to uncertainties in A-method correction factors will be negligible. However, if E-method correction factors are used, the range of possible correction factors is 1.10 to 1.39 at 557.7 nm and 1.06 to 1.32 at 630.0 nm. Using A-method correction factors determined for low atmospheric extinction coefficients will yield the lowest intensities, whilst using E-method correction factors determined for high atmospheric extinction factors will yield the highest intensities. It is interesting to note that if Guttman's (1968) maritime atmospheric extinction coefficients are chosen (i.e. 0.22 at 557.7 nm and 0.18 at 630.0 nm), then using E-method rather than A-method correction factors to process the shipboard ISAAC data would result in greater 557.7 and 630.0 nm intensities by factors of 23% and 16% respectively.

4/ Uncertainties due to contamination by OH emissions.

The presence of OH emissions in the vicinity of the OI emissions becomes significant when the OI emission intensities are low (see Section 4.4.3). It was estimated that OH contamination could cause measured 557.7 nm intensities to be too low by as much as 15 R, and 630.0 nm intensities to be too low or too high by as much as 5 R. As the intensities of the OH emissions are independent of the OI intensities, it is not possible to quantify the contaminating effects of the OH emissions in percentage terms.

5/ Uncertainties due to cloud attenuation.

Cloud attenuation is another possible contributor to the low shipboard intensities. Without knowledge of the cloud thickness, it is impossible to estimate the extent of the attenuation that they caused. However, the observations made with clear skies did not result in significantly higher intensity values.

Absolute limits for the uncertainties in the shipboard OI intensities can be estimated by combining the various uncertainty factors listed above. If the 557.7 and 630.0 nm intensities presented in Section 7.3.3 are given by I(557.7) and I(630.0) respectively, then the true emission intensities $I_0(557.7)$ and $I_0(630.0)$ should be within the limits:

$$0.76\ I(557.7) - 0R \ < \ I_0(557.7) \ < \ 2.71\ I(557.7) + 15R$$

and

$$0.77\ I(630.0) - 5R \ < \ I_0(630.0) \ < \ 2.42\ I(630.0) + 5R$$

No indication has been given by the suppliers of the Cachoeira Paulista data, of the uncertainty in their observed intensities. Even assuming that in the worst case the shipboard intensities are too low by the factors given above, the Cachoeira Paulista intensities would still have to be too high by a considerable amount to account for some of the OI intensity differences.

A further consideration is whether or not the low emission intensities measured aboard the ship are realistic. The observations were made at geographic latitudes between 30 and 42°, at an L-value of about 1.5 (invariant latitude $\approx$ 35°). The cruise took place in the southern hemisphere winter of 1983, which was about midway between the solar cycle maximum of 1979 and the minimum of 1986. A survey of low- and mid-latitude OI airglow observations reported in the literature has shown that:

1/ Minima in OI intensities occur in wintertime, and during low solar activity (Sahai *et al.*, 1988b).

2/ OI emissions are latitude-dependent. Eather (1969a, 1969b), reporting the results of northern hemisphere airborne photometric measurements, found a mid-latitude minimum in airglow intensities between 40° and 55° invariant latitude, with 557.7 nm intensities as low as 55 R, and 630.0 nm intensities as low as 5 R. His graphs show average 557.7 and 630.0 nm intensities at an invariant latitude of 35° of < 70 R and < 20 R, respectively. Greenspan (1966) found that 630.0 nm intensities drop rapidly in the geomagnetic latitude interval 15° to 30°, and stay low poleward of 30°. He also observed that intensities were lower in the southern hemisphere than in the northern hemisphere, as did Reed and Chandra (1975).

3/ A number of workers have reported low- or mid-latitude observations of I(557.7) lower than 50 R (e.g. Smith and Steiger, 1968; Kulkarni, 1969; Reed and Chandra, 1975; Lauche, 1977; Burnside and Tepley, 1990).

4/ Values of I(630.0) lower than 25 R have also often been reported in the literature (e.g. Davis and Smith, 1965; Bellew and Silverman, 1966; Peterson and Steiger, 1966; Smith and Steiger, 1968; Eather, 1969a, 1969b; Kulkarni, 1969; Cogger *et al.*, 1974; Wickwar *et al.*, 1974; Cogger and Carlson, 1977; Burnside and Tepley, 1990).

These findings show that the OI intensities observed on the ISAAC cruise are feasible, although a little low. As shown above, uncertainties in the absolute calibration of the photometers, in the filter transmission factors and in the atmospheric correction factors could possibly cause the calculated 557.7 and 630.0 nm emission intensities to be too low by factors of 2.7 and 2.4 respectively. Increasing the ISAAC intensities by such factors and adding an offset to compensate for the contamination effects of nearby OH emissions, would bring them within the bounds of acceptable OI emission intensities, as defined by other workers' observations at low- and mid-latitudes.

CHAPTER 8

CONCLUSIONS

8.1 Summary of results

This thesis was instigated by the lack of South African expertise in the utilization of tilting-filter photometry for airglow and auroral research. A review of previous South African photometric research has shown shortcomings in the methods that were used to obtain emission intensities from raw photometric data. In particular, the absolute calibration of the photometers and the techniques (if any) used to correct for atmospheric extinction and scattering, left a lot to be desired.

The aeronomic background necessary for this thesis has been supplied in Chapter 2. It is apparent that despite intensive research since the IGY, there still remain some important unresolved questions. For example, what are the dominant excitation processes responsible for auroral OI 557.7 nm emissions? Researchers develop models in an attempt to provide answers to this (and other) questions. Observational data are necessary to test the suitability of their models. Photometric observations can provide not only emission intensities, but also densities of atmospheric constituents and particle energies and fluxes which can be used to test the models.

In Chapter 3 the various methods for observing airglow and auroral emissions were reviewed. Tilting-filter photometry systems were found to provide one of the most accurate means of measuring atmospheric emission intensities. Various shortcomings of the original analogue photometry system used by Rhodes University at Sanae were identified. Temporal resolution was increased during auroral observations by increasing the filter tilt speed at each mirror position, thereby increasing the meridian scan repetition rate. A new mirror control system, installed in 1982, improved the spatial resolution of the meridian scans. At best, the improved analogue system could perform a meridian scan of 31 mirror positions once a minute. Further improvements should have been achieved when the analogue system was replaced with a computer-controlled digital photometry system in 1985. The advantages of the digital system are as follows:

1/ Raw digital data (photon counts corresponding to line, background and dark current intensities) are written directly to magnetic disk, thus eliminating the time-consuming process of scaling raw data from analogue charts. Data processing is thus simpler and appreciably faster.

2/ The digital system is capable of handling a greater dynamic range of emission intensities than the analogue system can, without the need for constant monitoring and intervention by the operator. This allows the operator more time for other activities (e.g. running other equipment).

3/ The digital system eliminates the need for complete filter-tilt cycles, as the filter can be moved directly to the tilt angles required for line and background measurements. This decreases the time taken for each meridian scan, thus improving the temporal resolution of the system.

Unfortunately, it seems that the digital system operated at Sanae in 1985 suffered from interference from the RF output of the ionosonde that was being operated in the same room, and thus continually lost mirror-position synchronization. This resulted in no usable photometric data being collected in 1985. This problem will need to be addressed before the digital system can be used successfully in close proximity with an ionosonde.

The computer program developed by the author for the control of the digital photometer system allows the system to be run in three modes:

1/ Set-up mode is used by the operator to determine the optimum combination of filter temperature and filter tilt angles needed for line and background measurements.

2/ Observation mode allows the system to be used in a number of different configurations to observe airglow and auroral emissions.

3/ Calibration mode allows the operator to calibrate each photometer with a low-brightness light source, which is positioned above the photometer, filling its field of view.

In Chapter 4, the author developed equations which can be used to convert analogue and digital photometric data to absolute emission intensities. Besides depending on line, background and dark current measurements (either analogue chart deflections or digital photon counts), the emission intensities depend on the absolute calibration of the photometer, the transmission characteristics of the filter, and the methods that are used to correct for the effects of atmospheric extinction and scattering. Consequently, one can only obtain accurate intensity values if one can accurately determine values for photometer calibration factors, filter transmission factors, and atmospheric correction factors. Various practical considerations which influence the accurate determination of emission intensities have been discussed.

The method used to cross-calibrate the low-brightness light sources, which were used to calibrate the photometers used at Sanae and on the ISAAC cruise, has been described. The cross-calibration showed that the brightness of both the variable-aperture source (which uses a quartz tungsten-halogen lamp) and of the ^{90}Sr activated phosphor source have apparently decreased with age.

The method used to measure the transmission characteristics of the narrowband interference filters which are used in the photometers, has also been described. The transmission characteristics of the filters used at Sanae between 1976 and 1984 were accurately measured in 1985. They were found to have changed appreciably from the characteristics supplied by the manufacturer in 1975. This has resulted in uncertainties in the actual values of the filter transmission factors at any particular time during the period 1975-1985, as we have no knowledge of how the transmission characteristics changed with time.

It is estimated that a combination of the uncertainties in the absolute calibration of the photometers, and in the filter transmission factors, could cause the observed emission intensities to be in error by as much as a factor of two. As a result of the findings regarding the cross-calibration of the light sources, and the measurement of the filter transmission characteristics, it is imperative that both processes be performed at more regular intervals (i.e. at least once a year). This will minimize any uncertainties in the source brightnesses and filter transmission factors due to ageing. If care is taken when performing these measurements, the overall uncertainties in emission intensities should be considerably reduced.

Atmospheric correction factors have been identified as another major source of uncertainty in the emission intensities derived from ground-based photometric observations. These factors depend primarily on which model is used for the atmospheric effects, and on the extinction coefficients that are used. A survey of atmospheric correction methods, and of the extinction coefficients that have been used at the various emission wavelengths, has shown that the resultant large range in atmospheric correction factors can significantly change both the emission intensities and the intensity ratios that are obtained. The effects are more apparent at lower wavelengths. For example, at 391.4 nm the correction factors can vary between 0.83 and 1.93, resulting in calculated intensities that differ by a factor of 2.33. It has been found that some workers (e.g. Hopgood, 1976; Rees and Lummerzheim, 1989; Lummerzheim *et al.*, 1990) use an exponential correction factor which only takes into account the attenuating effects of atmospheric extinction (absorption and scattering of light out of the photometer's field of view). As this method (referred to as the E-method) does not take into account the contribution of light that originates outside of the photometer's line of sight, the resultant intensities are higher than if one uses other correction methods. Straightforward exponential atmospheric correction factors are used by many workers because of the difficulty in evaluating the source function that describes the light contributions of the whole sky.

Photometric data collected by the author at Sanae during the magnetospheric substorm of 27 July 1979 has been used to illustrate the application of meridian-scanning tilting-filter photometer observations in auroral research. Contour plots of emission intensities versus time and invariant latitude were found to be one of the best ways to present the intensity variations along the magnetic meridian during the substorm. A need to increase the temporal and spatial resolution of future substorm observations was identified. This need was partly addressed by improvements to the analogue photometer system (see above). Further enhancements in temporal resolution should be achieved with the digital system (see Section 8.2).

The I(391.4)/I(557.7) ratios observed during the substorm were found to be higher than expected. The most probable cause of this is low 391.4 nm intensities. These could be caused by a number of factors: Uncertainties in the photometer calibration (the source brightness is very low at 391.4 nm), uncertainties in the 391.4 nm line-to-band conversion factor (which is a function of rotational temperature) and uncertainties in the atmospheric correction factors to be used at this wavelength.

Another cause of concern is the low OI airglow intensities observed at Sanae and on the ISAAC cruise. Uncertainties in the photometer calibrations, filter transmission factors and atmospheric correction factors could cause the intensities to be too low by a factor of two. However, even if the measured intensities were doubled, they would still be lower than many of the OI intensities that have been reported in the literature, although the author has in fact found several reports of low intensity values.

The most significant result of the airglow observations made during the ISAAC cruise is the definite detection of non-zero N_2^+ 391.4 nm intensities during four of the five nights on which usable data were collected. These emissions are diagnostic of particle precipitation and, combined with the particle-related sporadic-E traces evident on the shipboard ionograms, are definite proof of the detectability of the effects of particle precipitation in the region of the South Atlantic Anomaly (SAA). The absence of simultaneous N_2^+ emissions at Cachoeira Paulista in Brazil, which is on the edge of the SAA, would imply that these emissions are only detectable in the region of peak particle precipitation. As a result, N_2^+ emissions might only be detectable by ship-borne observations, or possibly by using a meridian-scanning photometer system located on Gough Island, and looking towards the western horizon.

8.2 Suggestions for future work

A number of suggestions can be made for future photometric research, either by using data which have already been collected, or by making new observations.

In view of the doubts caused by the low intensities observed at Sanae, and in the region of the SAA whilst on the ISAAC cruise, it is felt that time could be well spent investigating the possibility of errors in the calibration of the photometers. It is believed that the cross-calibration techniques described in Section 5.3 are sound. If possible, a reliably calibrated light standard (e.g. a standard lamp cross-calibrated by the U.S.

National Bureau of Standards) should be obtained, and used to repeat the cross-calibration. This would serve to check the calibration of the standard lamps supplied by the South African National Physical Research Laboratories. If the brightnesses of these lamps are found to be true, then a cross-calibration of the sources that were cross-calibrated in 1984 should establish any further effects of ageing.

One of the causes of uncertainty in emission intensities is the uncertainty in the values of the extinction coefficients that are used to determine the atmospheric correction factors. It is known that extinction coefficients are highly variable, both spatially and temporally. It is impractical to operate a radiometer in Antarctic conditions in order to monitor the daily change in extinction coefficients. One way to estimate the extinction coefficients that apply to the OI emissions at 557.7 and 630.0 nm, is to assume that airglow (i.e. non-auroral) emissions in very quiet magnetic conditions are uniform across the area of sky covered by the meridian scans. If so, then the intensities measured at the different zenith angles should be the same after they are corrected for atmospheric and van Rhijn effects. Correction factors can be calculated for different extinction coefficients. The correction factors that give the least variation in emission intensity across the meridian, should indicate the correct extinction coefficient. For this method to be reliable, one needs to know the heights of the emitting layers, as they affect the van Rhijn correction factors. Furthermore, if one is using a correction model that compensates for the effect of light reflected from the ground and then back-scattered into the field of view, then the ground albedo will also affect the correction factor that is used. Clearly this method will only give a rough indication of the extinction coefficients and correction factors that are applicable at the time. Ultimately one is forced to accept that there are definite limitations to the accuracy that one can attain with observed emission intensities.

There are some nine years worth of analogue raw data (i.e. chart records) available, which were collected at Sanae during the period 1976 to 1984. There are uncertainties in the absolute intensities that can be obtained from these data, but it should still be possible to use them to determine any diurnal, seasonal and solar cycle effects on the airglow and auroral emissions at Sanae. The biggest deterrent against attempting such a study is the extreme tediousness of converting the analogue chart deflections to emission intensities. This could be alleviated by developing a computer-assisted airglow scaling program which would enable the line, background and dark current data to be reduced from the chart records, using a digitizer. A digitizer system (hardware and software) already exists at Rhodes University, for the scaling of ionograms. New user-interface software would need to be developed, but the same computer, digitizer hardware and digitizer table could be used for the scaling of the analogue airglow records. The raw data would then be available on computer, where a computer program could be used to calculate emission intensities.

Existing analogue data could also be used for further substorm studies. Substorm data recorded after 1982 should be used, to take advantage of the increased temporal and spatial resolution afforded by meridian-scan repetition rates of 1 or 5 minutes, and scans using 31 mirror positions (5.4° apart). It should be possible to compare Sanae intensity data with photometric data collected simultaneously at either Siple Station, Syowa, or South Pole Station. Comparisons with Siple data would be particularly significant, as Siple and Sanae are at almost the same L-value (≈ 4). It might also be possible to compare Sanae data with auroral images recorded by satellites passing overhead.

A number of suggestions can be made for future observations, using the digital photometry system:

Serious consideration should be given to the re-establishment of an airglow programme at Sanae. The digital photometer system should require appreciably less operator time than the analogue system did, and could possibly be run by one of the personnel in an existing scientific post at Sanae. Despite the problems of running optical instrumentation in as remote and inhospitable a location as Antarctica, both Eather (1988) and Rees (1989b) have stressed the continued importance of optical observations in Antarctica. Coordinated observations between the various ground-based observatories in Antarctica and the various polar-orbiting satellites with imaging capabilities could make valuable contributions to ongoing auroral research.

An alternative to restarting photometric observations of the airglow and aurora at Sanae, would be to operate the digital system on Gough Island. This would enable continued observation of the airglow in the region of the SAA. The photometers could be operated in a meridian-scanning mode, but this time in an east-west direction so that one can monitor the variations in emission intensities as one scans towards or away from the region of maximum particle precipitation. Operating the photometers on Gough Island would eliminate the problems experienced on the ISAAC cruise, which occurred as a result of the rolling and pitching motion of the ship. A major problem with running ground-based photometers on Gough Island would be the frequent cloud coverage experienced there (there is cloud cover over Gough Island for more than 60% of the time).

Finally, the following general improvements to the digital photometry system are suggested:

In view of the difficulties involved in making accurate intensity measurements at 391.4 nm, it is recommended that observations of N_2^+ emissions be made using the (0,1) band at 427.8 nm. At this wavelength the brightness of most calibration sources will be greater than at 391.4 nm, and extinction coefficients will vary less rapidly with wavelength and show smaller fluctuations than they do at the lower wavelength. These factors will decrease the uncertainties in the observed N_2^+ emission intensities, which will more than compensate for any difficulties arising from the lower intensities emitted at 427.8 nm (remembering that $I(391.4) \approx 3.28 \times I(427.8)$).

The uncertainties in observed emission intensities would be reduced if the low-brightness light sources, used to calibrate the photometers in the field, were regularly cross-calibrated against reliable light standards.

Further reduction in uncertainties would be achieved by regular measurement of the filters' transmission characteristics. If the photometer system were to be operated at either Sanae or Gough Island, this would necessitate the filters and low-brightness sources being swopped every year for a spare set that has just been calibrated. In this way any changes due to ageing could be more closely monitored.

Another improvement would be to change the way in which meridian scans are performed. Rather than making line and then background measurements at each zenith angle, it would be better to use the meridian scan format used by Lummerzheim *et al.* (1990). They do an entire meridian scan with the filter tilted to the position for line measurements, and then repeat the scan with the filter tilted for background measurements. This eliminates the need to move the filter at each zenith angle, and so considerably reduces the time taken for one complete meridian scan. The time interval between line and background measurements is short enough to safely assume no significant change in background level. The time saved (by not having to move the filter backwards and forwards between line and background positions) could be used to either increase the temporal resolution of the system, the spatial resolution, or a combination of both.

APPENDIX A

Conversion table of commonly used units

Quantity	Units	Relation
Energy	electron-volt (eV)	1 eV = 1.602×10^{-19} J = 1.602×10^{-12} erg
	erg	1 erg = 10^{-7} J = 6.24×10^{11} eV
	Joule (J)	1 J = 6.24×10^{18} eV = 10^{7} erg
Energy flux	mW m^{-2} erg cm^{-2} s^{-1}	1 mW m^{-2} = 1 mJ m^{-2} s^{-1} = 1 erg cm^{-2} s^{-1}
Magnetic flux density	nanotesla (nT)	1 nT = 10^{-5} G = 1 γ
	gamma (γ)	1 γ = 10^{-5} G = 1 nT
	Gauss (G)	1 G = 10^{5} nT = 10^{5} γ
Surface Brightness	Rayleigh (R)	1 R = 10^{10} photons m^{-2} s^{-1} 1 R = 10^{6} photons cm^{-2} s^{-1}
Wavelength	nanometers (nm)	1 nm = 10^{-9} m = 10 Å
	Angstroms (Å)	1 Å = 10^{-10} m = 0.1 nm

APPENDIX B

Aeronomic background to the processes of the aurora

Auroral emissions are the result of complex interactions between the solar wind, magnetosphere and ionosphere. This appendix provides some background to the geophysical processes that result in the aurora. Section B.1 describes the interaction between the Sun, solar wind, magnetosphere and ionosphere which results in the precipitation of energetic particles into the ionosphere, and hence auroral emissions. Section B.2 discusses the concept of the auroral oval and its connection with auroral morphology. Finally Section B.3 outlines the phenomenon of the magnetosphere substorm, with particular reference to its optical signatures.

B.1 The Sun, solar wind, magnetosphere and ionosphere

The Sun is an average star of spectral type G2V, meaning that it has a luminosity of 4 x 10^{26} W, and a surface effective temperature of 5800 K (Venkatesan and Krimigis, 1990). Energy flows from the core of the Sun into the solar corona, which in turn expands and creates a thermally-driven high-speed outflow called the solar wind. Owing to the extremely high temperatures, the particles comprising the solar wind are ionized, forming a plasma. These particles are predominantly protons (H^+) and electrons. The solar wind flows radially outwards from the Sun through the interplanetary medium at supersonic speeds normally ranging from 400 to 600 km s^{-1}. However, during periods of intense solar activity this speed can increase to as much as 2000 km s^{-1}. The solar wind carries the solar magnetic field embedded in its plasma, forming the heliomagnetosphere, or heliosphere. This magnetic field constitutes what is normally known as the interplanetary magnetic field (IMF). The solar wind collides with the earth's magnetic field causing a bow shock, and confines the geomagnetic field to a cavity called the magnetosphere which is bounded by the magnetopause.

The idea of the presence of a magnetosphere was first put forward by Chapman and Ferraro (1931). Their theory, based on the assumption that the solar plasma is diamagnetic, predicted that the earth and its magnetic field would be totally enclosed in a temporary cavity during periods of magnetic storms. The presence of a continuous solar wind, and hence a permanent magnetospheric cavity, was only established later as a result of comet studies. Dungey (1961) was the first to advocate the theory of an open magnetosphere in which the geomagnetic field lines from the polar regions are merged with the IMF lines to form 'open field lines'. This merging allows solar wind plasma to flow across the magnetospheric cavity in the merging area.

During quiet times, i.e. periods of little or no solar activity, the flow of the solar wind is steady, and this leads to a steady state of the magnetosphere, similar to that shown in Figure B.1. The magnetosphere is stretched out on the nightside into a magnetotail which is many tens of earth radii (R_e) in length. The magnetotail is bisected into two lobes by an area called the plasma sheet. Magnetic field lines in the tail lobes are open, being connected at one end to the earth (in the region of the polar cap which is enclosed by the auroral oval), and to the IMF at the other. Field lines in the plasma sheet are closed and connect to the earth in both hemispheres in the nightside section of the auroral oval. The boundary of the plasma sheet, which forms the division between open and closed field lines, contains field lines which pass through a distant neutral line where the magnitude of the magnetic field approaches zero.

On the dayside, the polar cusp defines the boundary between the open field lines that are swept back in the magnetotail, and the closed field lines which join the earth on either side of the equator. At ionospheric heights the polar cusp forms the dayside section of the auroral oval. It funnels some of the solar wind particles (that have entered the front of the dayside magnetosphere) into the dayside atmosphere. Here the particles collide with atmospheric constituents, causing the dayside aurora which extends about 60° on either side of the noon meridian. The precipitating particles in the dayside oval are typically of low energy and thus do not penetrate far into the atmosphere. The resultant spectral radiation is thus dominated by the red (630 nm) emission from atomic oxygen which occurs at F-region heights within the ionosphere (typically 250-300 km).

The magnetosphere has dynamic processes occurring within it, even whilst in a steady or quiet state. A process called magnetospheric convection continually transports plasma, and hence magnetic flux, from the dayside to the tail, and back round the earth to the dayside again. Associated with this motion is an electrostatic field which projects along magnetic field lines into the earth's atmosphere where it forms an ionospheric electric field. This field causes a convection of the charged particles that form the magnetospheric and ionospheric plasma. This results in a system of field-aligned and ionospheric currents. Plasma flows from the magnetosphere into the ionosphere along geomagnetic field lines as field-aligned currents. Such currents are also known as Birkeland currents (Anderson and Vondrak, 1975). In the ionosphere these currents continue, perpendicular to the magnetic field, as horizontal currents. The horizontal currents are made up of Pederson currents parallel to the electric field, and Hall currents perpendicular to the electric field. These currents then link to field-aligned currents flowing back to the magnetosphere.

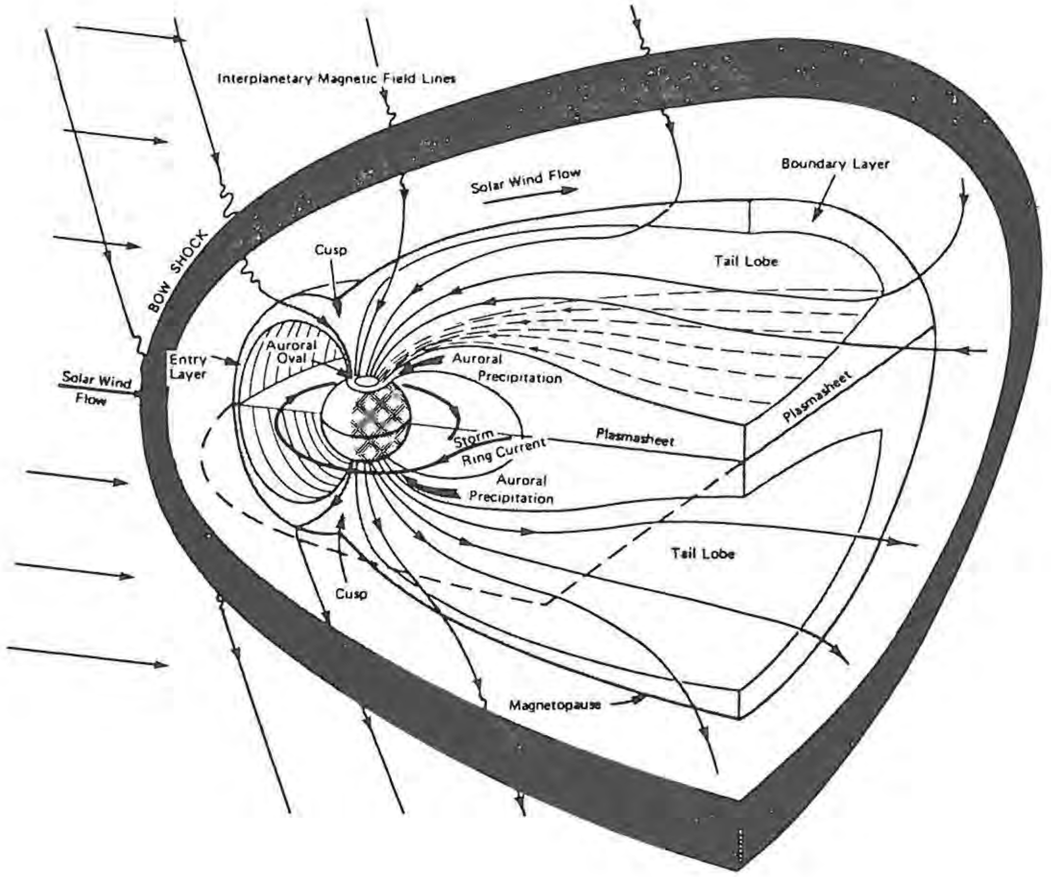

Figure B.1 A schematic diagram of the structures and various regions of the Earth's magnetosphere (after Roederer (1981), p. 29 of *Geophysical Inst. Biennial Report - 1983-84*, Univ. of Alaska, 1984).

This, then, is the mechanism by which energetic particles precipitate into the regions of the auroral ovals, causing auroral emissions. The interaction of the solar wind with the magnetosphere constitutes a gigantic natural magnetohydrodynamic (MHD) dynamo, generating a voltage drop of some 40-50 kV across the magnetosphere. The auroral emissions that result from the action of this dynamo can be thought of as giant electrical discharge processes (Akasofu, 1974, 1977, 1981a). The field-aligned currents which connect the magnetosphere to the ionosphere are always present, and in the absence of solar activity usually have amplitudes of about 1.4×10^6 A. During magnetically disturbed times the amplitudes of these currents double (Stern, 1983). More will be said later in this appendix about ionospheric and field-aligned currents (see Section B.3 on magnetospheric substorms).

The precipitating particles responsible for the auroras in the nightside section of the auroral oval originate mainly from the plasma sheet. Plasma from the solar wind enters the plasma sheet in three ways (Eather, 1980): Firstly, most of the plasma that has entered the magnetosphere from the solar wind streams tailward along the open field lines and forms the so-called plasma mantle. This plasma flow is subject to the electric field generated by the MHD dynamo, and is eventually forced, as part of the cross-tail current loop, to the centre of the tail where it accumulates in the plasma sheet. Secondly, some plasma flows directly into the plasma sheet via the magnetopause of the downstream magnetosphere. Thirdly, some of the particles that become part of the plasma sheet are former ionospheric particles lost along the open field lines that originate from the polar cap regions. Normally there is an equilibrium between the rate at which the plasma sheet loses particles and the rate at which it gains them. There are two loss processes during quiet magnetic times: Firstly the cross-tail currents transport particles back around the boundary layer of the tail lobes where some particles are lost via the magnetopause back into the interplanetary medium. These cross-tail currents flow across the midplane of the plasma sheet in a dawn to dusk direction. Secondly, as mentioned above, a portion of the cross-tail current is deflected to flow along the magnetic field lines into the auroral zone as field-aligned currents. These currents enter the ionosphere in the morning sector, connect horizontally through the ionosphere to the evening sector and then flow back along the magnetic field lines to relink with the cross-tail current. Current systems for the northern hemisphere are shown in Figure B.2. The right hand side of the figure shows the path of the conventional cross-tail current, while the left hand side shows part of the cross-tail current being diverted to the polar ionosphere by means of the field-aligned currents.

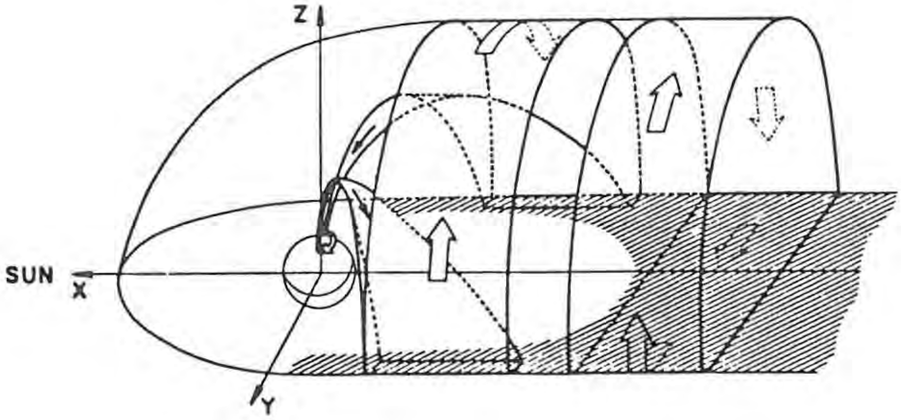

Figure B.2 A schematic representation of part of the current systems that flow in the steady-state magnetosphere (After Eather, 1980). Only the current systems and the tail lobe relevant to the northern hemisphere are shown.

The continual steady-state particle precipitation into the nightside auroral oval usually results in diffuse auroras which are generally sub-visual. Often there is evidence of discreet auroras superimposed upon the diffuse aurora, forming the thin visual section of the ever-present auroral oval. Generally, as magnetic activity increases, the occurrence of discreet aurora increases. Under certain conditions, very bright and highly dynamic auroral displays occur as a result of a phenomenon called the magnetospheric substorm, the optical manifestation of which is known as the auroral substorm (Akasofu, 1968, 1977). Before discussing this phenomenon, it is necessary to examine in more detail the concept of the auroral oval.

B.2 The auroral oval and auroral morphology

The name 'auroral oval' has already been mentioned in connection with the areas of the polar ionosphere in which particle precipitation occurs. If one could view the polar area of the winter hemisphere from several R_e above the geomagnetic pole, one would see a narrow visible ring of auroral emission - the auroral oval. This has in fact been done by polar-orbiting satellites, e.g. Dynamics Explorer 1 (DE-1), and images have been recorded of the entire auroral oval. Excellent examples of such images are shown by Craven and Frank (1985), Frank *et al.* (1985), Craven and Frank (1987), Frank and Craven (1988), and Eather (1988).

Feldstein (1963) first developed the concept of the auroral oval, after examining many all sky camera (ASC) photographs recorded in the polar regions. The term 'auroral oval' is also given a statistical significance as it is generally used to define the region where the percentage probability of an aurora occurring is greater than 75%. Care should be taken not to confuse the auroral oval with the 'auroral zone' which demarcates the geomagnetic latitude at which the occurrence of auroras is most probable at geomagnetic midnight. The auroral zone is taken to be a circle at a geomagnetic latitude of 67°, i.e. at geomagnetic colatitude = 23°. The auroral oval is eccentric with respect to the geomagnetic pole, with its centre lying about 3° towards the dark hemisphere, i.e. it is displaced roughly towards magnetic midnight. This eccentricity is closely related to the day-night asymmetry of the internal structure of the magnetosphere (Akasofu, 1967). The auroral oval is quite dynamic, varying in size with magnetic activity. It expands equatorward with increasing magnetic activity, and contracts poleward as magnetic activity decreases (Feldstein, 1966; Feldstein and Starkov, 1967; Starkov, 1969). This variation in the size of the auroral oval with magnetic activity is shown in Figure B.3. As a first order approximation, the Q index of magnetic activity that is used in the figure can be equated with the same integer value of the Kp index, i.e. $Q = 3$ corresponds to $Kp \approx 3$ (Eather and Mende, 1971a). Holzworth and Meng (1975) have found a strong correlation between the size of the auroral oval and the southward ($-B_z$) component of the IMF. Akasofu *et al.* (1973) and Akasofu (1975a) have made similar findings, i.e. that the size of the auroral oval is controlled by the north-south component of the IMF.

Feldstein's (1963) observations of the auroral oval were based on the presence of discrete aurora in ASC photographs. Subsequent observations with more sensitive equipment revealed the presence of belts of diffuse aurora in addition to the discrete aurora. Lui and Anger (1973), and Lui *et al.* (1973) compared data from the ISIS-II satellite's scanning auroral photometer with ASC pictures and found the presence of diffuse aurora to be generally equatorward of the discrete aurora. The intensity of the diffuse aurora increased as

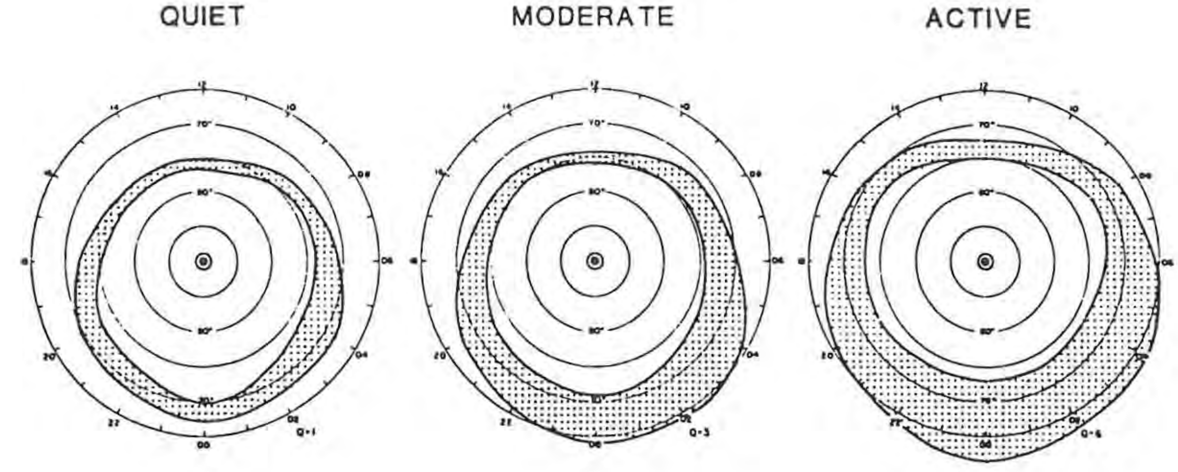
QUIET

MODERATE

ACTIVE

Figure B.3 Variation in the size of the auroral oval with magnetic activity as denoted by the magnetic Q index. Coordinates are corrected geomagnetic latitude and corrected geomagnetic time. (After Whalen, 1985).

the discrete aurora became more active. It was proposed that some of what was previously thought to be proton aurora in ASC pictures could actually be part of the diffuse aurora. In contrast, Nagata *et al.* (1976) thought the discrete and diffuse auroral belts to be synonymous with the electron and proton auroral belts respectively. The proton aurora will be mentioned again later in this section.

Eather and Mende (1971a) advocated that diffuse auroras are due to wide regions of soft precipitation (i.e. particle energies ≤ 1 kev) that extend from the equatorward boundary of the auroral oval to well poleward of normal visible aurora. They found that superimposed upon this soft zone are discrete auroras whose changes in intensity are due to the changes in the average energy of the precipitating electrons rather than changes in the number flux. Deehr *et al.* (1981) found that the soft auroral region which gives rise to the diffuse background radiation is indicated by the extent of the 630.0 nm emission due to particle precipitation (i.e. the extent of the non-airglow component of the 630.0 nm emission). Akasofu (1977) says that the diffuse auroras are due to precipitating particles with energy spectra which consist of a Maxwellian and a power law spectrum. Sometimes a different type of precipitation and intense field-aligned currents develop in thin strips within this diffuse aurora precipitation region, causing the discrete aurora. The energy spectra of the precipitating particles that cause the discrete aurora have a peaked, or 'monoenergetic', component in addition to the usual combination of Maxwellian and power law components. Akasofu tabulates the important features of discrete and diffuse aurora (see Table 2.1, p. 127 of Akasofu, 1977). Meng (1978) outlines the causes of the discrete and diffuse aurora.

Lui *et al.* (1975b) found that a single oval-shaped belt can be defined which contains both the discrete and diffuse aurora. In addition, they found the presence of a second region of diffuse aurora equatorward of the auroral oval, forming a belt almost constant in geomagnetic latitude on the dayside. It was proposed that this corresponds to the mantle aurora and forms the optical component of the hard precipitation zone (see also Lui *et al.* (1973), who made similar findings, and used the name 'drizzle zone precipitation'). Hartz and Brice (1967) give the general positions of these, and other, auroral precipitation zones.

The eccentricity and variability in size of the auroral oval have certain implications as far as ground-based studies of the aurora are concerned. Given that a station conducting optical observations is in fact at an appropriate magnetic latitude to be under the auroral oval, whether or not it actually falls under the auroral oval at a particular instant depends on two factors: the magnetic local time and the extent of the magnetic activity. Many stations only fall under the auroral oval (and thus only have a good probability of seeing auroras) during certain combinations of magnetic local time and magnetic conditions. The more equatorward a station, the more magnetic activity that is required before aurora are likely to be visible in the zenith. Conversely, at more poleward stations the probability of having auroras overhead decreases with increasing magnetic activity. A station such as Sanae (invariant latitude $\approx 60°$) needs at least moderate magnetic activity (i.e. $Kp > 4$) before it will even be beneath the auroral oval just in the vicinity of local magnetic midnight. For Sanae to fall under the auroral oval at other times requires even more disturbed magnetic conditions ($Kp \gg 4$).

Various workers have modelled the shape of the auroral oval. Holzworth and Meng (1975) have fitted a simple seven parameter Fourier series to the shape of Feldstein's auroral oval, with an accuracy of about half a degree of magnetic latitude. Starkov (1969) has derived a formula relating the equatorward boundary of the auroral oval to the magnetic Q index, and to magnetic local time. Slater *et al.* (1980), and Gussenhoven *et al.* (1983) have both tabulated coefficients of a linear relationship between the equatorward boundary of the diffuse auroral oval and the magnetic activity index Kp, for hourly intervals of magnetic local time (MLT). These allow one to determine the minimum magnetic activity necessary for the auroral oval to extend equatorward as far as a specified invariant latitude, at a specified MLT. Bond and Thomas (1971), and Sheehan and Carovillano (1978) have both plotted the equatorward boundaries of the auroral oval at magnetic midnight versus magnetic activity indices.

Bond and Thomas (1971) compared their values for the position of the auroral oval in the southern hemisphere with those given by Feldstein and Starkov (1967) for the northern hemisphere, and found good agreement. For high Kp values they found the broadening of the auroral oval to be more extreme in the southern hemisphere. This is possibly due to the greater sensitivity of the optical instruments used in the southern hemisphere. Feldstein *et al.* (1974) also found a good conjugate relationship between the northern and southern hemisphere auroral ovals. This conjugacy means that any of the above-mentioned formulae or graphs, mostly derived from auroral oval data for the northern hemisphere, can be used to determine when, and under what magnetic conditions, Sanae can be expected to be beneath, or even in line of sight of, the auroral oval (see Section 6.1.2).

For certain applications the auroral oval forms an obvious natural coordinate for studies of the aurora (Akasofu, 1967). Eather and Mende (1972) have devised an 'auroral latitude co-ordinate' by subtracting the invariant latitude of the equatorward oval boundary (as formulated by Starkov, 1969) from the invariant latitude at which observations were made. Similarly, Lui *et al.* (1975a) found the invariant latitude of the equatorward boundary of the diffuse auroral oval at local magnetic midnight to be a useful parameter for characterizing the size of the auroral oval, and auroral activity. However, care should be taken when selecting the auroral oval as a coordinate or parameter. Eather (1973) has questioned the validity of using the auroral oval in some cases, e.g. when using it to characterize particle precipitation or energy disposition.

Further mention needs to be made of the proton aurora, as it affects photometric observations of the electron aurora, and consequently needs to be taken into account when determining auroral emission intensities and emission intensity ratios due to precipitating electrons. The precipitation of energetic protons into the earth's upper atmosphere results in hydrogen emissions which form the proton aurora. Many workers have studied this type of aurora and the existence of an associated proton auroral oval (see, for example, Eather and Sandford, 1966; Eather and Jacka, 1966; Wiens and Vallance Jones, 1969; Montbriand, 1971; Fukunishi, 1975). The hydrogen Balmer β (H_β) line, nominally at 486.1 nm, is perhaps the most frequently investigated proton auroral emission. Auroral intensities of this line are typically between 20 and 50 R, and rarely exceed 100 R, even during intense auroral activity (Eather, 1967a; Omholt, 1971; Vallance Jones, 1974). Proton auroral forms are usually broader and more diffuse than those of electron aurora. There are two reasons for this (Vallance Jones, 1974): Firstly, the radius of gyration of a proton in the earth's magnetic field is large (200 m for 5 keV protons). Secondly, many of the precipitating protons undergo charge exchange with atmospheric constituents, becoming neutral hydrogen atoms that are no longer constrained to follow the magnetic field lines. These hydrogen atoms can then travel in a straight line in a direction determined by the pitch angle, until ionization converts them back to protons that are again forced to spiral around the magnetic field lines (see Figure B.4).

Many observers have found that proton auroras lie slightly (up to 5°) equatorwards of electron auroras in the premidnight sector, and either overlap with or are polewards of the electron auroras in the postmidnight sector (cf. Wiens and Vallance Jones, 1969; Fukunishi, 1975). This apparent crossover of the electron and proton auroras is in agreement with the prediction made by Axford and Hines (1961). There has been some disagreement as to whether the crossover actually occurs (cf. Rees and Benedict, 1970; Eather and Mende, 1971a, 1971b). This uncertainty could, in part, be due to the broadness of the proton aurora. Proton aurora observations and morphology are reviewed by Eather (1967a), and Vallance Jones (1974).

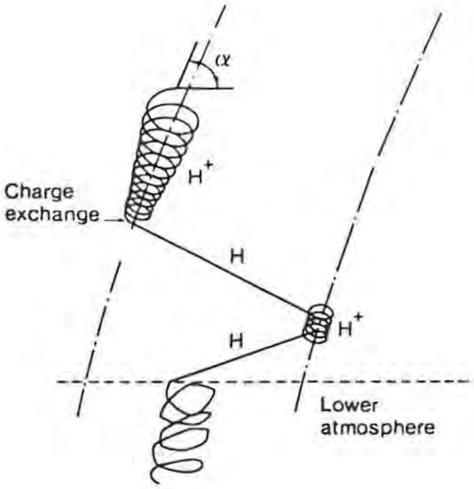

Figure B.4 Schematic representation of the trajectory paths of H^+ and H atoms in the earth's atmosphere (after G.T. Davidson, 1965).

Besides causing the well known H_α and H_β emissions, proton precipitation also causes emissions of the spectral lines and bands that are normally considered to be part of the electron aurora (e.g. the $N_2{}^+$ 1NG band emissions at 391.4 and 427.8 nm, and the OI emissions at 557.7 and 630.0 nm). Consequently, in order to use photometric observations of emissions at these wavelengths to study the electron aurora and the effects of electron precipitation, one has to correct for the contribution made by proton-induced emissions. This can be done if simultaneous measurements are made of one of the hydrogen emissions, as the intensity of this emission can be used to generate the appropriate correction factors (Eather, 1967b, 1968; Gattinger and Vallance Jones, 1972).

B.3 The magnetospheric substorm

This appendix has so far been concerned with the steady-state auroras that are always present somewhere in the polar regions as part of the auroral ovals. They occur when the magnetosphere is in a steady state, with the MHD dynamo operating at minimal efficiency. This is normally a result of the IMF having a large northward component ($B_z \approx 5$ nT) for a period of 6 hours or more (Akasofu, 1977). However, during certain conditions, auroral emissions can intensify greatly and become very dynamic. This usually takes place when the B_z component of the IMF becomes negative (i.e. the IMF turns southward), triggering one or more magnetospheric substorms (Akasofu, 1975b, 1976). Note that because a single southward turning of the IMF can trigger a series of substorms, individual substorms that take place later in the series can actually occur while the IMF is still southward, or even when it has turned northward again (Akasofu, 1975b, 1977; Akasofu and Lepping, 1977; Rostoker *et al.*, 1980).

The concept of the 'auroral substorm' arose after the study of many ASC photographs taken during the IGY (Akasofu, 1964). Akasofu regarded the auroral substorm as having two characteristic phases: an expansive phase and a recovery phase. The substorm itself is preceded by another phase, the quiet phase. Figure B.5 contains six diagrams which illustrate the development of an auroral substorm on the nightside of the northern hemisphere. Diagram A shows the initial quiet condition, in which there are one or two weak arcs aligned along the dark sector of the auroral oval. The onset of the substorm, i.e. the beginning of the expansive phase, is shown in diagram B. This takes the form of a sudden formation of a bright arc, or the brightening of an existing arc in the midnight sector. The arc moves rapidly polewards, forming a bulge, with other auroral forms appearing behind it (diagram C). The bulge continues to expand in all directions to the point that it becomes filled with active bright auroras that become fragmented into curtain-like forms. The large-scale fold in the evening or western side of the bulge is called the westward-travelling surge. This formation propagates rapidly westward at speeds of the order of 1000 m s^{-1}. At the same time, arcs in the morning sector disintegrate into smaller patches that drift eastwards at speeds of the order of hundreds of metres per second. This stage is often referred to as the auroral break-up, and is illustrated in diagram D. When the expanding bulge reaches its most poleward extent the recovery phase of the substorm begins, as shown in diagram E. At this stage the bulge begins to contract. The substorm disturbance dies down with the disintegration of the westward-travelling surge, and the situation returns to its original state (diagram F).

The above description illustrates the optical signatures of a single magnetospheric substorm. Although compiled from studies of ASC pictures that only show the presence of discrete aurora, the description serves to highlight the main optical features of the auroral substorm. Subsequent descriptions of auroral substorms, based on satellite observations, have included the presence of diffuse auroras in auroral substorms. These auroras define the equatorward edge of auroral precipitation during substorms, and form a background to the movements of the discrete auroras (cf. Pike and Whalen, 1974; Lui *et al.*, 1975a). Figure B.6 shows the relative positions of the discrete and diffuse auroras during a substorm; it corresponds to diagram D in Figure B.5. Fukunishi (1975) also included proton auroras in his description of the development of substorms.

The study of auroral substorms is not a simple matter. Although polar-orbiting satellites can image the whole of the auroral oval, they provide only instantaneous pictures and consequently lack temporal resolution, as the period of an orbit is approximately 100 minutes. On the other hand, ground-based observations usually have good temporal resolution, but have restricted spatial coverage. An observer on the ground might only see parts of the evolving substorm. This depends on the size of the substorm, and the observer's position

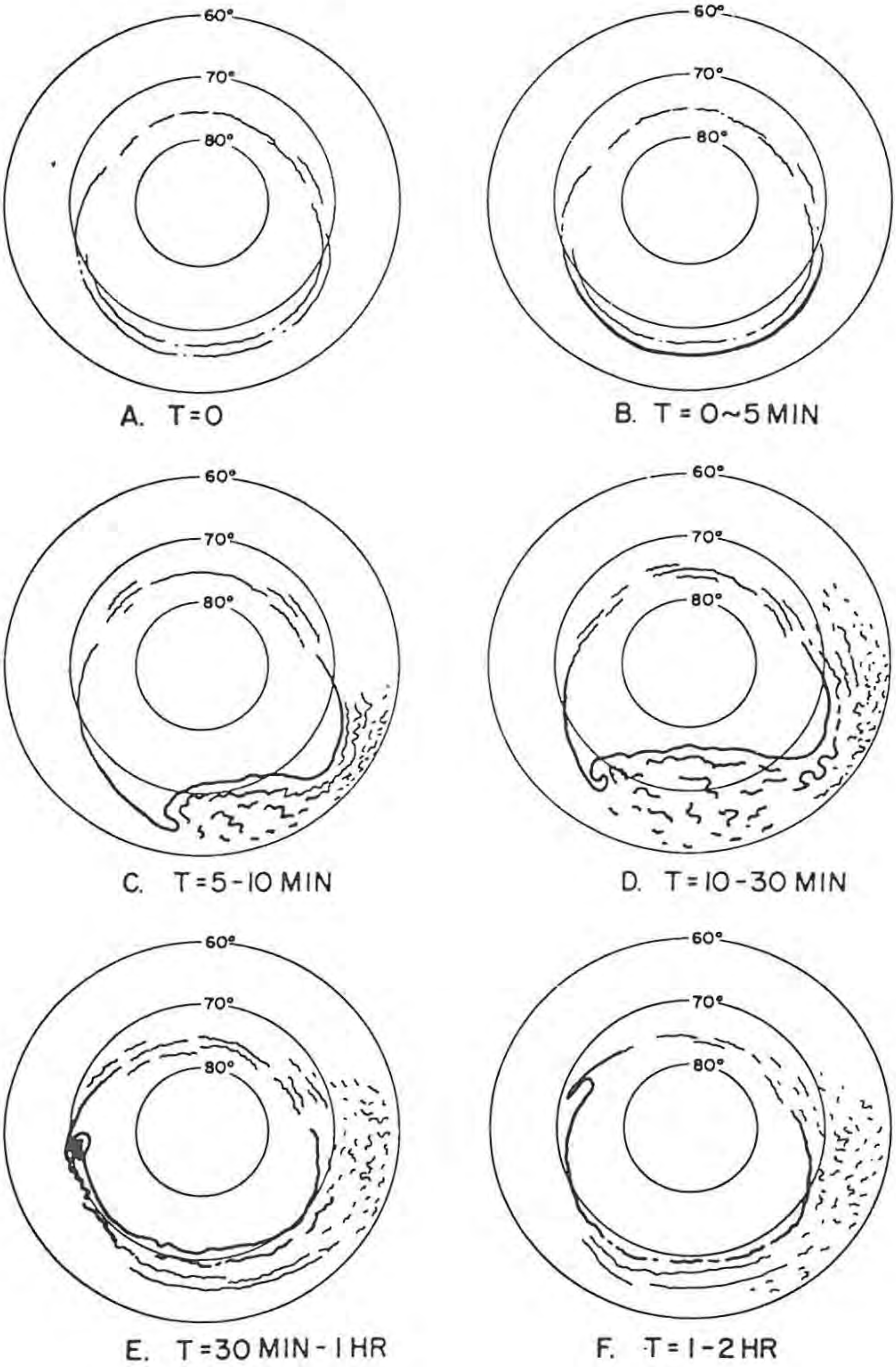

A. T=0

B. T = 0~5 MIN

C. T=5-10 MIN

D. T=10-30 MIN

E. T=30 MIN-1 HR

F. T=1-2 HR

Figure B.5 Schematic diagram showing the main stages in the development of an auroral substorm (After Akasofu, 1968).

relative to it. In addition to these limitations, substorm occurrences are rarely simple isolated events. It is not uncommon to have multiple substorms occurring on one night. To further complicate matters, it is also possible to have multiple substorm onsets that are close enough together to cause the substorms to overlap

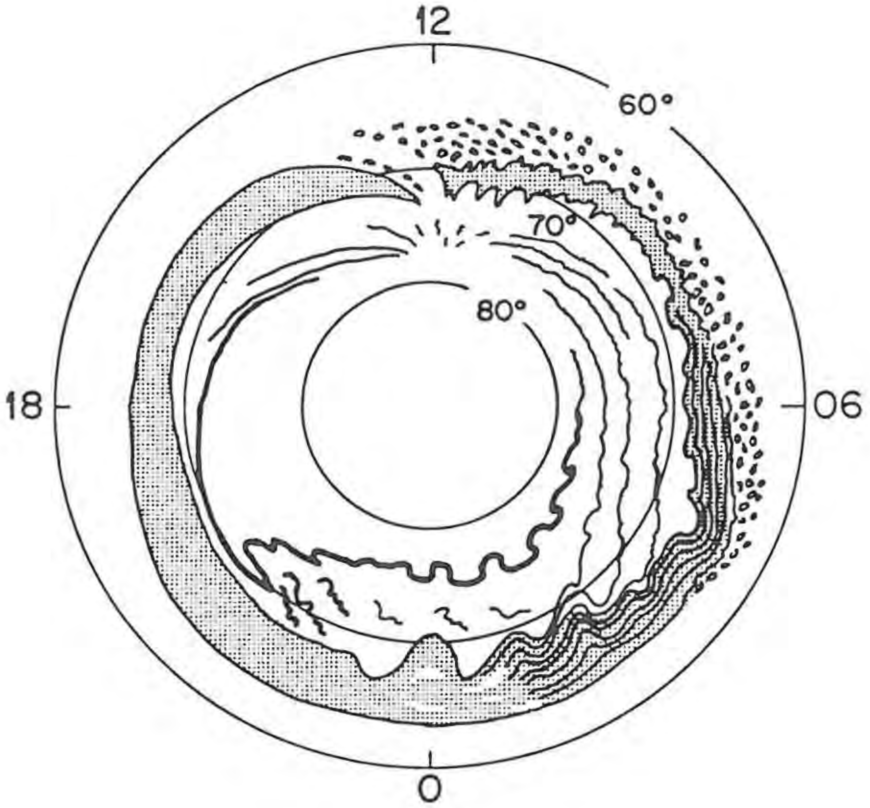

Figure B.6 Schematic diagram showing the relative positions of discrete and diffuse auroras during an auroral substorm. Discrete arcs are shown as lines, and diffuse auroras by shaded areas (after Akasofu, 1976).

in both time and space. Coordinated satellite and ground-based observations of auroral substorms are perhaps the best way to study these phenomena.

The auroral substorm was found to be the optical signature of a much broader phenomenon - the 'magnetospheric substorm' which is manifested in a number of different ways (i.e. as auroral, ionospheric, x-ray, vlf emission, proton aurora, polar magnetic, and micropulsation substorms) (Akasofu, 1968). Magnetosphere substorms are dynamic processes which result from the interaction between the solar wind and the magnetosphere. McPherron (1979) gives the following concise definition of the magnetospheric substorm (as drawn up by a number of leading substorm researchers):

> "A magnetospheric substorm is a transient process initiated on the night side of the earth in which a significant amount of energy derived from the solar wind-magnetosphere interaction is deposited in the auroral ionosphere and magnetosphere."

The energy deposited in the auroral ionosphere is responsible for the displays manifested in the auroral substorm. Rostoker *et al.* (1980) give a lengthier, more operational definition of the magnetospheric substorm in terms of some of the signatures that characterize this phenomenon:

> "The term magnetospheric substorm describes an interval of increased energy dissipation confined, for the most part, to the region of the auroral oval. The onset of this process is signalled by explosive increases in auroral luminosity in the midnight sector, and the entire process encompasses an interval during which the strength of the current in the auroral electrojets increases from and returns to the background level from which the substorm arose. During this interval there may be a sequence of intensifications of the westward electrojet, each associated with a Pi 2 micropulsation burst and a westward-travelling surge. As the substorm develops, the region of discrete auroras in the midnight sector expands poleward and westward (the poleward bulge). Eventually, the region of disturbed aurora reaches a maximum latitude and begins to recover towards its presubstorm location. The interval of time between the first Pi 2 burst and the time the aurora reaches a maximum latitude has been called the expansion phase. The interval during which the aurora in the midnight sector returns to a lower latitude is called the recovery phase."

It is clear from these definitions that the energy which results in the auroral signatures of the magnetospheric substorm, comes from the solar wind via the magnetosphere . Consequently, a complete understanding of the processes that cause the aurora is dependent on a complete understanding of the processes that take place in the magnetosphere. In the last two decades many workers have been striving to reconcile all the constituent signatures of the magnetospheric substorm, and to develop a unified understanding of magnetospheric processes.

Magnetospheric substorm activity is closely related to solar activity. This, in turn, is linked to the sunspot cycle, as the frequency of occurrence of solar activity is proportional to the sunspot number. Note, however, that the magnitude of the solar activity is not correlated with its frequency. Some of the most intense solar activity has coincided with sunspot minima. Solar activity is associated with specific solar eruptions (solar flares) or with solar coronal regions that persist for long periods. During solar activity there is enhanced solar wind flow, with velocities sometimes reaching 2000 m s^{-1}. Energies of the solar wind particles are increased, resulting in enhanced energy transfer from the solar wind to the magnetosphere. Akasofu (1981, 1983a) has found the energy input rate, or input power, to be given by

$$\varepsilon(t) = V\, B^2 \sin^4\left(\frac{\theta}{2}\right) l_0^2 \tag{2.1}$$

where V, B, and θ denote the solar wind speed, the magnitude of the solar wind magnetic field, and the polar angle of the magnetic field vector, respectively, and l_0 is a constant ($\approx 7\ R_e$). It is apparent from this equation that the energy input rate to the magnetosphere is also proportional to the size and direction of the IMF. In fact it can be said that the B_z component of the IMF regulates the efficiency of the MHD dynamo formed by the interaction of the solar wind and the magnetosphere (Kamide and Akasofu, 1974). In general, the power of this dynamo has to exceed 10^{11} W for magnetospheric substorms to occur. When the IMF turns southward, the increased input energy causes enhanced magnetospheric convection, which in turn causes an enhancement in the magnetosphere-ionosphere coupling (Kan *et al.*, 1988). This takes the form of increased field-aligned currents (FACs) and ionospheric currents. During a substorm there are two main types of FACs: region 1 FACs which originate from cross-tail currents, and region 2 FACs which are associated with partial ring currents (Iijima and Potemra, 1976, 1978; Wolf, 1983). The region 2 currents are equatorward of the region 1 currents and flow in the opposite direction i.e. into the ionosphere in the pre-midnight sector, and out it in the post-midnight sector. Stern (1983) identifies an additional two types of FACs which play minor roles during substorm activity. Reviews of ionospheric and magnetospheric currents are given by Kamide (1982, 1988) and Akasofu (1983b). Figure B.7 shows the main magnetospheric, field-aligned, and ionospheric currents systems which flow during a substorm.

As shown in Figure B.7, the main horizontal ionospheric currents that link the field-aligned currents are termed the westward and eastward electrojets. The westward electrojet flows mainly in the dawn to midnight sector, whereas the eastward electrojet flows mainly in the evening sector. However, the front of the westward electrojet, given by the position of the westward-travelling surge, can intrude into the evening sector on the poleward side of the auroral oval (Kan *et al.*, 1984). The intense currents of the electrojets cause deflections in the H component of the magnetic field observed on the ground in the regions adjacent to the electrojet. The westward electrojet shows up as a sharp negative deflection of the H component, and forms one of the most noticeable signatures of the magnetospheric substorm (Kamide and Akasofu, 1975). The poleward or equatorward position of an electrojet relative to a ground-based observatory is shown by positive or negative deflections in the Z component of the magnetic field (a westward electrojet is poleward of a station if the Z deflection is positive, and vice versa for the eastward electrojet). Magnetic variations recorded at Sanae can be used to detect whether Sanae is under the influence of an eastward or a westward electrojet, and whether the electrojet is poleward or equatorward of Sanae (see e.g. Section 6.5). The boundary between the eastward and westward electrojets, where no current flows, is known as the Harang discontinuity (cf. Akasofu, 1977). It corresponds to a narrow region where there are no field-aligned currents. The Harang discontinuity is taken to be overhead of a station during a substorm if there are simultaneous zero deflections in the H and Z components (Sutcliffe *et al.*, 1984).

Perreault and Akasofu (1978), and Akasofu (1980, 1981) have found that the total energy output rate (U_T) of the magnetosphere closely follows the input energy rate (given by Equation B.1.), i.e.

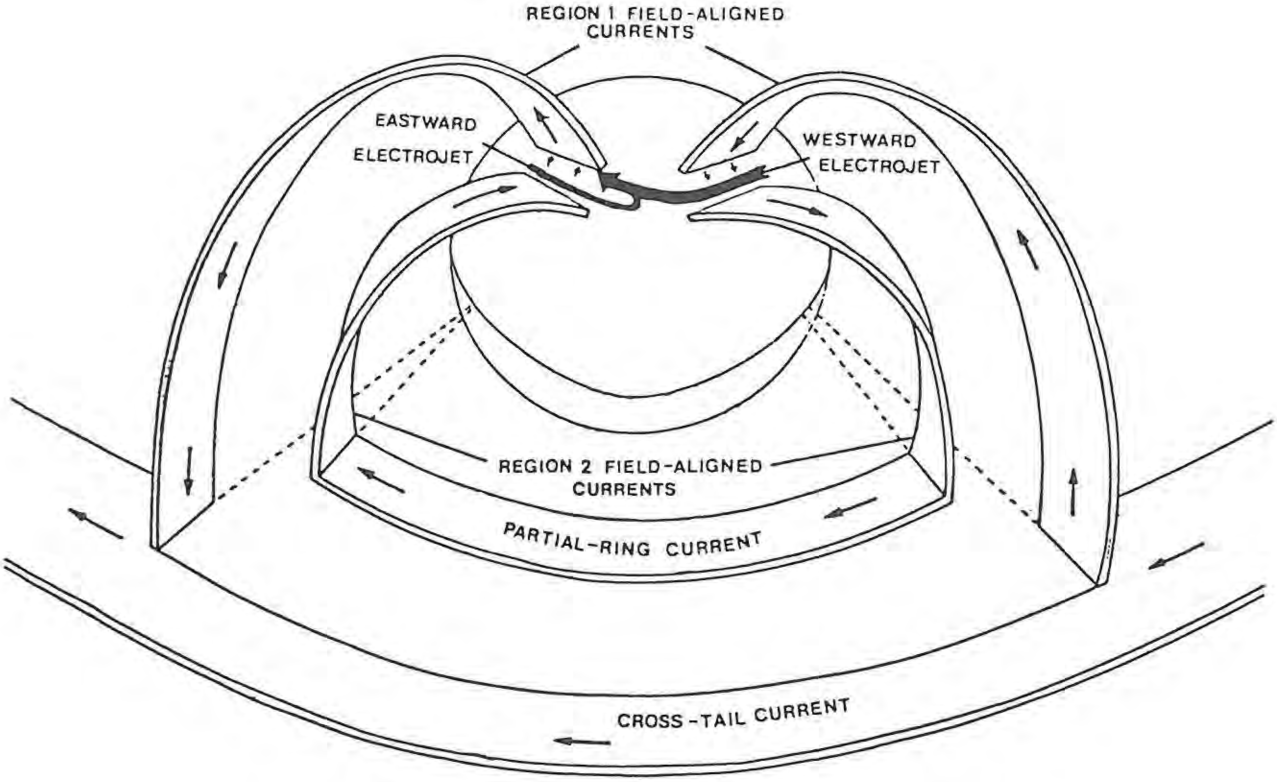

Figure B.7 Schematic diagram showing the relationship between the main magnetospheric, field-aligned, and ionospheric current systems which flow during a magnetospheric substorm (adapted from Sutcliffe et al., 1984).

$$U_T(t+\tau) \sim \varepsilon(t) \qquad (2.2)$$

where τ allows for the possibility of a small time delay. The magnetosphere outputs its energy in three ways, i.e. U_T has three components: U_R - the ring current energy injection rate, U_J - the joule heat production rate, and U_A - the auroral particle energy injection rate. Such a system, where the output power follows the input power, is called a 'directly driven' system. (Note: During substorms the magnetosphere sometimes also releases excess energy by forming plasmoids - islands of hot plasma trapped in a nest of looping field lines - which are ejected from the magnetotail following field line reconnection (cf. Hones, 1979a, 1979b, 1984). In contrast to the directly driven model, other workers have favoured a model in which energy is accumulated in the magnetosphere during a growth phase prior to the onset of the substorm. This energy is then explosively released into the ionosphere at substorm onset (cf. Davis, 1972; McPherron, 1970, 1972, 1979; McPherron *et al.*, 1973; Russell and McPherron, 1973). This constitutes what has become known as an 'unloading' system. The advent of these two opposing models has generated a great deal of discussion and argument (cf. Swift, 1980; Akasofu, 1983; Ahn *et al.*, 1984; Coronti, 1985; Akasofu, 1985a; Hill and Siscoe, 1985; Russell, 1985; Akasofu, 1985b; Akasofu *et al.*, 1985; Akasofu, 1986, 1987). The two models are shown schematically in Figure B.8.

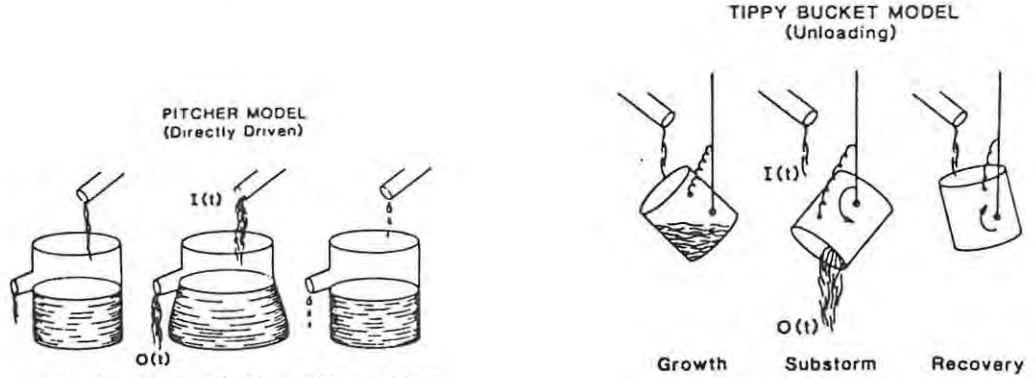

Fig. 1. Illustration of a directly driven "pitcher" model. The basic feature of the model is simply that time variations of the output rate are very similar to those of the input rate. The recovery phase results simply if the input rate is reduced.

Fig. 2. Illustration of the so-called "tippy bucket" model. The input energy is initially stored in the bucket. As the stored energy reaches a critical level (determined mainly by internal parameters, such as the amount of stored energy, a parameter equivalent to the spring constant, etc.), the stored energy is suddenly converted into substorm energy. This is basically an unloading process. The recovery phase results from the fact that the system relaxes as the stored energy is consumed.

Figure B.8 Schematic representation of the 'directly driven', and 'unloading' models of magnetospheric energy output (After Akasofu, 1985a).

In 1987 consensus was reached between several workers, amongst them Akasofu and McPherron, as to the fact that both the directly driven process and the unloading process make contributions to the energy input into the ionosphere at the expansive phase of a substorm, but that the directly driven process is dominant (Rostoker *et al.*, 1987). Other workers have found evidence in support of these conclusions, e.g. Sauvaud *et al.* (1987) and Ahn *et al.* (1989).

It is apparent that the ionospheric processes that take place during a substorm are fairly well understood. However, this is not the case with the magnetospheric processes. Kan (1990) has listed twelve signatures of magnetospheric substorms that have been identified by various studies. Six of these are ionospheric signatures, and they can be explained by a magnetosphere-ionosphere coupling (MIC) model (cf. Kan *et al.*, 1988). The remaining six signatures are magnetospheric and, as yet, cannot be explained by hard science. Kan (1990) expresses the need to develop a single self-consistent model of the plasma sheet that will explain the physics behind the magnetospheric signatures. Once this has been done, the next step will be the construction of a global substorm model that will include all twelve signatures. Despite the tremendous volume of substorm research that has been conducted in the last three decades, there is still no consensus view of the entire substorm process (Lui, 1991). Lui reviews six substorm models that are currently under consideration, and reiterates the need to integrate these to produce a synthesis model that will give a coherent explanation of substorm processes. Most of the recently developed substorm models are phenomenological ones, i.e. they attempt to explain the substorm characteristics that have been observed. Consequently, the continued accurate collection of substorm data on a global scale is important. This applies to ground-based photometric observations, even though their contribution to magnetospheric substorm research might be relatively small.

APPENDIX C

Determination of filter tilt angles from stepper-motor positions

The filters used in the Rhodes University photometer systems are tilted by means of cam-followers which are attached to the filter holders. Figure C.1 shows the geometry of the cam and cam-follower used to tilt a filter. The circular cam has a radius of R, and is mounted eccentrically on the axle of a stepper motor. The point of rotation of the cam is at P. The filter is tilted by a cam-follower of length L, which rests on the circumference of the cam. Let the distance between the axle and the point of contact of the cam-follower be r when the cam is in its rest position (i.e. when the filter is level). Thus the distance between the cam's axis of rotation and its centre is (R - r). The values of R, r and L can easily be measured.

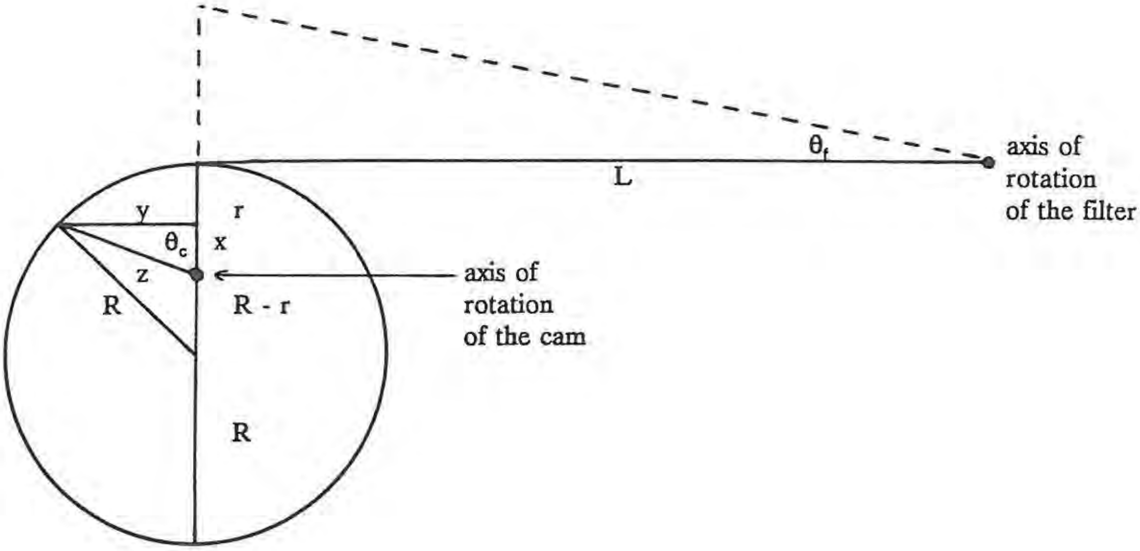

Figure C.1 The geometry of the filter tilting mechanism.

When the cam is rotated away from its rest position the distance between its axis of rotation (P) and the cam-follower changes, causing the filter to tilt. Let this distance be $z(\theta_c)$. It follows that for a given rotation angle θ_c of the cam from its rest position, the tilt angle of the filter will be given by

$$\theta_f = \arctan\left(\frac{z(\theta_c) - r}{L}\right) \qquad \text{(C.1)}$$

The only variable in this equation is z, which is a function of r, R and θ_c. In turn, θ_c, the angle of rotation, is a function of the number of motor steps taken from the rest position, and can easily be calculated (i.e. with 400 motor steps per cam revolution, $\theta_c = 0.9° \times$ step number). We need to find an equation for z in terms of the known parameters given above. This can be done in the following way:

From the two triangles in Figure C.1, we have

$$R^2 = (R - r + x)^2 + y^2 \tag{C.2}$$

and

$$z^2 = x^2 + y^2 \tag{C.3}$$

Expanding and re-arranging Equation C.2, and substituting for $(x^2 + y^2)$ from Equation C.3 gives

$$z^2 = 2Rr - 2Rx + 2rx - r^2 \tag{C.4}$$

We now use the fact that $x = z \cos \theta_c$, and substitute for x in Equation C.4:

$$z^2 = 2Rr - 2Rz\cos\theta_c - 2rz\cos\theta_c - r^2 \tag{C.5}$$

Re-arranging this equation gives

$$z^2 + 2z\cos\theta_c(R - r) = 2Rr - r^2 \tag{C.6}$$

By adding $\cos^2 \theta_c (R - r)^2$ to both sides, and factorizing the L.H.S, this equation becomes

$$\left(z + \cos\theta_c(R - r)\right)^2 = 2Rr - r^2 + \cos^2\theta_c(R - r)^2 \tag{C.7}$$

Substituting $(1 - \sin^2 \theta_c)$ for $\cos^2 \theta_c$ on the R.H.S. of this equation, and then simplifying it, yields

$$\left(z + \cos\theta_c(R - r)\right)^2 = R^2 - \sin^2\theta_c(R - r)^2 \tag{C.8}$$

Which, when re-arranging gives the following equation for z:

$$z = \sqrt{R^2 - \sin^2\theta_c(R - r)^2} - \cos\theta_c(R - r) \tag{C.9}$$

Finally, substituting for z from Equation C.9 into Equation C.1 gives the filter tilt angle in terms of the known quantities, R, r, l and θ_c:

$$\theta_f = \arctan\left(\frac{\sqrt{R^2 - \sin^2\theta_c(R - r)^2} - \cos\theta_c(R - r) - r}{L}\right) \tag{C.10}$$

In order to determine the values of R and r for a cam so that it will give a certain maximum filter tilt angle (for a given length of cam-follower), work backwards from Equation C.1: The filter will be at its most tilted when $\theta_c = 180°$. At this angle of cam rotation, Equation C.9 (or simple geometry) yields $z = (2R - r)$. Substituting this expression for z into Equation C.1 gives

$$(R - r) = \frac{L \tan\theta_f(\max)}{2} \tag{C.11}$$

where $\theta_f(\max)$ is the desired maximum filter tilt angle. From this equation, it can be seen that the maximum filter tilt angle is dependent only on the length of the cam-follower and the distance between the centre of the cam and its axle. Consequently, the radius of the cam does not have to be fixed. The cams constructed for the Rhodes University photometer systems were made for maximum filter tilt angles of either 10° or 15°. The length, L, of the cam-follower between the filter and the cam is 88 mm. The calculated values of (R - r), and the values of R and r that were used to construct the cams, are given in Table C.1.

Table C.1 Physical dimensions of the filter-tilt mechanisms used for maximum filter tilt angles of 10° and 15°.

Maximum filter tilt-angle (°)	l (mm)	R (mm)	r (mm)	R - r (mm)
10	88	21	13.2	7.8
15	88	25	13.2	11.8

Equation C.10 was used to calculate the filter tilt angles corresponding to filter positions between 0 and 200 at intervals of 5 steps. The tilt angles for step numbers $201 \leq N \leq 400$ are the same as those for step numbers (400 - N). Figure C.2 is a plot of filter tilt angle versus filter position for half rotations of both the 10° and 15° cams. This figure illustrates the non-linear change in tilt angle with filter position (number of motor steps).

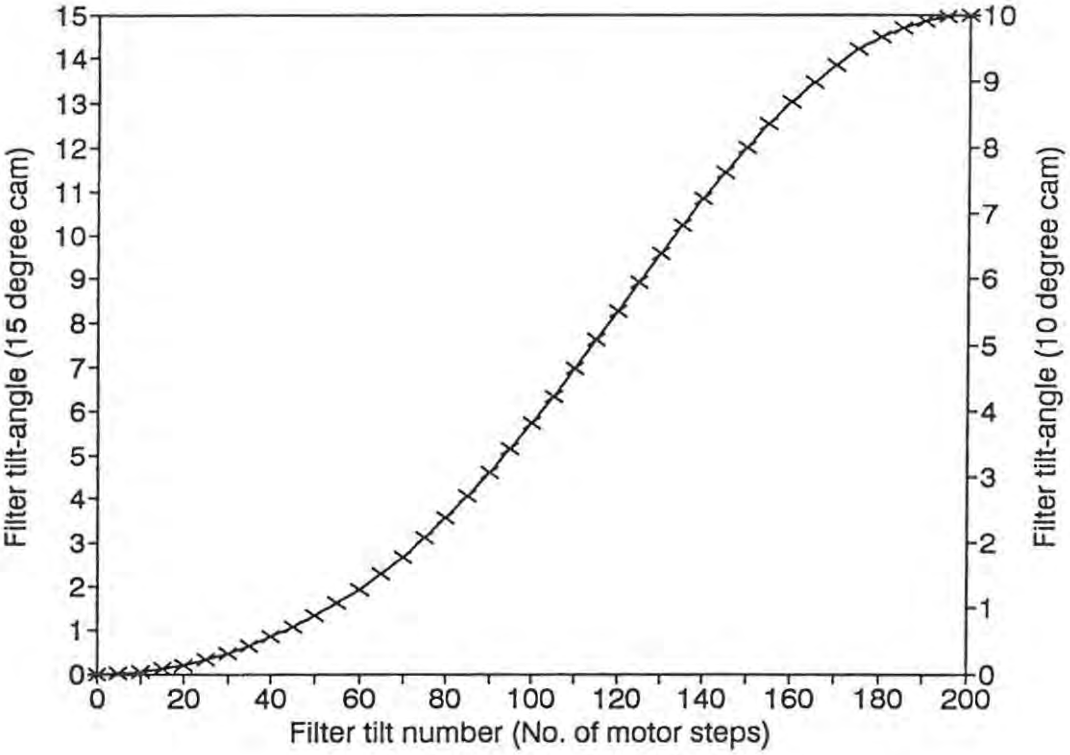

Figure C.2 Filter tilt-angle versus filter position for 10° and 15° cams.

APPENDIX D

Derivation of the equation relating surface brightness (B_λ) to spectral irradiance (E_λ)

A light source of uniform brightness can be obtained by illuminating a white screen with light from a lamp of known spectral irradiance E_λ. Given that the screen fills the field of view of a photometer, we then need to find the relationship between E_λ and the screen brightness, B_λ, measured by the photometer. Figure D.1 shows the spatial relationship between the lamp (L), the screen (S) and the photometer (P). Let the distance at which the spectral irradiance of the lamp was determined be d, and the distance between the lamp and the screen be D.

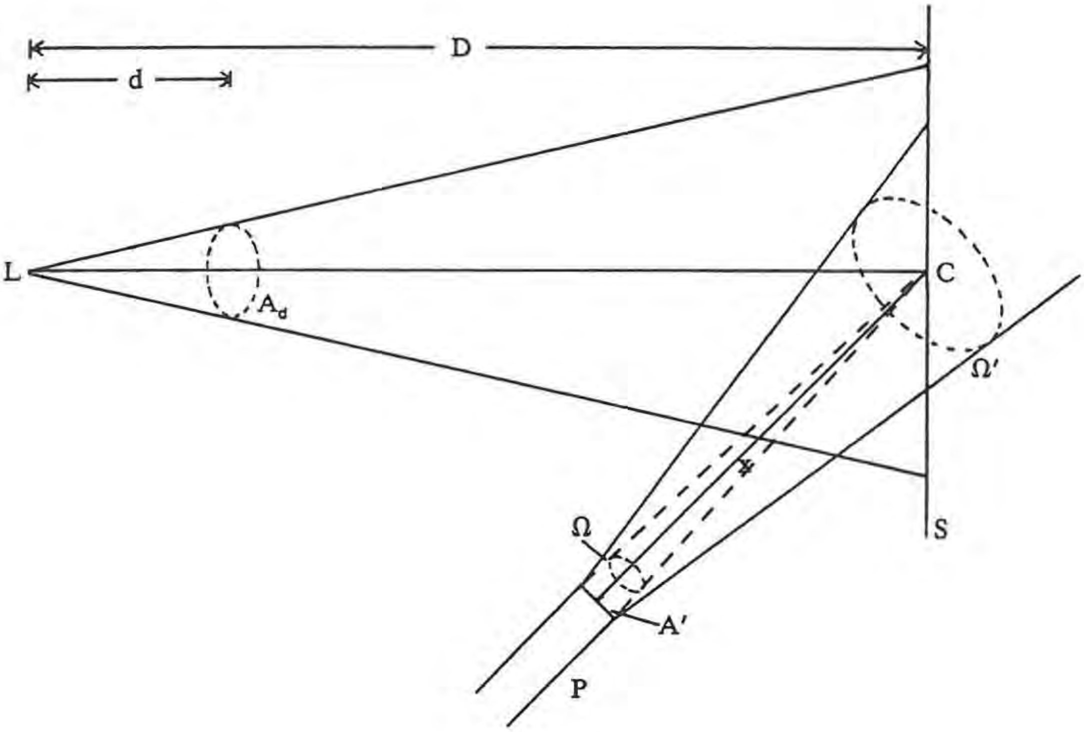

Figure D.1 Spatial geometry of the calibration apparatus used to measure the brightness of a screen illuminated by a standard lamp of known spectral irradiance.

We are given the spectral irradiance of the lamp in the direction of C, at distance d. Let this be $E_{\lambda,d}$ (in mW m^{-2} nm^{-1}), at wavelength λ (in nm). Clearly all the power that passes through an area A_d, at a distance d from the lamp, also reaches a distance D from the lamp, but is now spread over an area A_D ($= A_d D^2/d^2$).

Thus the spectral irradiance of the lamp at the screen (point C) is given by

$$E_{\lambda,D} = E_{\lambda,d} \frac{d^2}{D^2}$$

We would prefer to work in terms of numbers of photons rather than in terms of power. One photon of wavelength λ has an energy (in Joules) given by

$$U_\lambda = h\nu = \frac{h c}{\lambda}$$

where: h is Planck's Constant in J s,
ν is the frequency of the light,
c is the speed of light in m s , and
λ is the wavelength in m (not nm !).

It then follows that

$$1 \text{ mW} = 10^{-3} \text{ J s}^{-1}$$

$$= 10^{-3} \frac{\lambda}{h c} \text{ photons s}^{-1} \quad (\lambda \text{ in m})$$

$$= 10^{-12} \frac{\lambda}{h c} \text{ photons s}^{-1} \quad (\lambda \text{ in nm})$$

Consequently the spectral irradiance in terms of photon number is

$$E_{\lambda,D} = E_{\lambda,d} \frac{d^2}{D^2} \frac{10^{-12} \lambda}{h c} \text{ photons s}^{-1} \text{ m}^{-2} \text{ nm}^{-1}$$

$$\text{i.e.} \quad E_{\lambda,D} = E_{\lambda,d} \frac{d^2}{D^2} \frac{10^{-16} \lambda}{h c} \text{ photons s}^{-1} \text{ cm}^{-2} \text{ nm}^{-1}$$

This is the number of photons of wavelength λ ($\pm$ 0.5 nm) falling on 1 cm^2 of screen per second. If the reflectance of the screen at wavelength λ is ρ_λ, then the number of photons reflected from the cm^2 of screen per second is $\rho_\lambda E_{\lambda,D}$, i.e.

$$\rho_\lambda E_{\lambda,D} = \rho_\lambda E_{\lambda,d} \frac{d^2}{D^2} \frac{10^{-16}\lambda}{h c} \quad \text{photons s}^{-1} \text{ cm}^{-2} \text{ nm}^{-1}$$

The reflecting screen is assumed to be a Lambertian surface, i.e. the light scattered from the screen is radiated in all directions over the 2π steradians in front of the screen, with equal flux in all equal elements of solid angle. Figure D.2 shows an area dA of the screen, and an element on a hemisphere at a distance R from dA in the direction θ,ϕ.

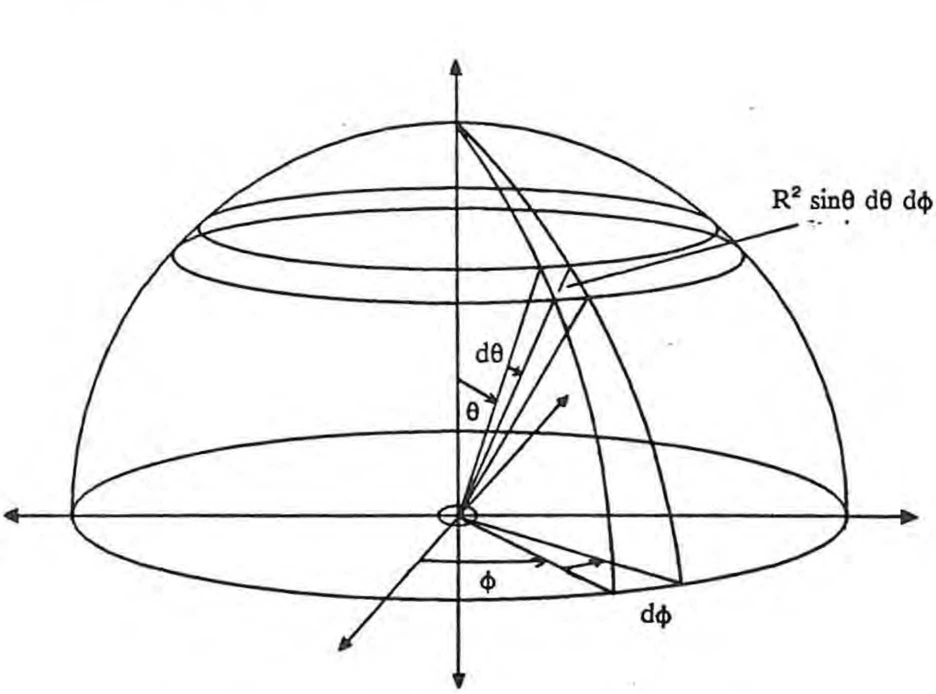

Figure D.2 Geometry needed for determining the total flux radiated by a surface element dA.

The area of this element is equal to $R^2 \sin\theta\ d\theta\ d\phi$. The solid angle $d\omega$ subtended by this element at dA is thus

$$d\omega = \sin\theta\ d\theta\ d\phi$$

Now the area dA of the screen is foreshortened when viewed at an angle θ to its normal, becoming dA $\cos\theta$ (this is the basis of Lambert's Cosine Law, which says that the brightness of a surface varies with $\cos\theta$, i.e. $B(\theta) = B(0)\cos\theta$). Thus the number of photons reflected from the area dA of the screen per second ($\rho_\lambda E_{\lambda,D}$ dA) is related to the spectral radiance L (the photon flux per solid angle) passing through the hemisphere by

$$\rho_\lambda \, E_{\lambda,D} \, dA = \int L \, dA \cos\theta \, d\omega$$

$$= L \, dA \int_0^{2\pi} \int_0^{\frac{\pi}{2}} \sin\theta \, \cos\theta \, d\theta \, d\phi$$

$$= L \, dA \, 2\pi \int_0^{\frac{\pi}{2}} \sin\theta \, \cos\theta \, d\theta$$

i.e. $$\rho_\lambda \, E_{\lambda,D} = L \, \pi$$

Hence L, the flux per steradian, in the direction θ,ϕ (as in any other direction) is

$$L = \frac{\rho_\lambda \, E_{\lambda,D}}{\pi}$$

i.e. $$L = \rho_\lambda \, E_{\lambda,d} \, \frac{d^2}{D^2} \, \frac{10^{-16} \, \lambda}{h \, c \, \pi} \qquad \text{photons s}^{-1} \text{ cm}^{-2} \text{ sr}^{-1} \text{ nm}^{-1}$$

The solid angle subtended at C by the photometer aperture A′ is

$$\Omega = \frac{A'}{x^2}$$

where x is the distance between the photometer aperture and the screen (A′ to C, as shown in Figure D.1). Thus the number of photons, from a unit area of the screen at C, entering the photometer per second is

$$\rho_\lambda \, E_{\lambda,d} \, \frac{d^2}{D^2} \, \frac{10^{-16} \, \lambda}{h \, c \, \pi} \, \frac{A'}{x^2} \qquad \text{photons s}^{-1} \text{ cm}^{-2} \text{ nm}^{-1}$$

This equation gives the number of photons originating from only a small area of the screen. We need to establish the total number of photons entering the photometer from the uniformly illuminated screen. If the photometer has a solid angle of view Ω', as shown in Figure D.1, then all the photons entering the photometer appear to come from an area $\Omega' x^2$, at distance x. Thus the total number of photons from the screen, counted by the photometer per second is

$$N_\lambda = \rho_\lambda E_{\lambda,d} \frac{d^2}{D^2} \frac{10^{-16} \lambda}{h c \pi} \frac{A'}{x^2} \Omega' x^2$$

$$\text{i.e.} \quad N_\lambda = \rho_\lambda E_{\lambda,d} \frac{d^2}{D^2} \frac{10^{-16} \lambda A' \Omega'}{h c \pi} \qquad \text{photons s}^{-1} \text{ nm}^{-1}$$

The surface brightness of a surface is defined as

$$B_\lambda = \frac{N_\lambda}{A' \Omega'}$$

$$\text{i.e.} \quad B_\lambda = \rho_\lambda E_{\lambda,d} \frac{d^2}{D^2} \frac{10^{-16} \lambda}{h c \pi} \qquad \text{photons s}^{-1} \text{ cm}^{-2} \text{ sr}^{-1} \text{ nm}^{-1}$$

Multiplying by a factor of $4\pi \times 10^{-6}$, to convert the units of this equation from photons s^{-1} cm^{-2} sr^{-1} to rayleighs gives

$$B_\lambda = \rho_\lambda E_{\lambda,d} \frac{d^2}{D^2} \frac{4 \times 10^{-22} \lambda}{h c} \qquad \text{R nm}^{-1}$$

Finally, substituting for h (= 6.62×10^{-34}), and c (= 3×10^8), we have the equation for the brightness B_λ of the screen, in terms of the spectral irradiance of the lamp used to illuminate it:

$$B_\lambda = \frac{2.01 \times 10^3 E_\lambda \rho_\lambda d^2}{D^2}$$

where: λ is the wavelength in nm,

E_λ (= $E_{\lambda,d}$) is the measured spectral irradiance of the standard lamp at wavelength λ and distance d, in mW m^{-2} nm^{-1},

ρ_λ is the reflectance of the screen at wavelength λ,

d is the distance at which the spectral irradiance of the lamp was measured, and

D is the distance between the lamp and the screen, for the current cross-calibration.

APPENDIX E

Coordinate systems and geomagnetic activity indices

There are any number of coordinate systems that can be used to uniquely specify the time and place of occurrence of a particular event. In addition to the familiar geographic spatial coordinates (latitude and longitude) and geographic time (i.e. UT or local time), there are a number of magnetically-based coordinate systems. Clearly the geomagnetic field, and any magnetic activity associated with it, has a major influence on many aeronomic processes. Consequently, it is more appropriate to use magnetic coordinates rather than geographic coordinates when working with auroral data. The best magnetic coordinate system to use depends on the subject of the study. This appendix describes some of the more important spatial and temporal magnetic coordinates that are used. In addition, descriptions are given of the geomagnetic indices that are used to characterize geomagnetic activity when studying auroral processes.

E.1 Geomagnetic coordinate systems

This section describes three spatial magnetic coordinate systems:

1/ Geomagnetic coordinates.
2/ Corrected geomagnetic coordinates.
3/ McIlwain's B-L coordinate system.

In addition to these three coordinate systems, the 'invariant latitude' coordinate, which is directly related to McIlwain's L parameter, is also discussed.

E.1.1 Geomagnetic coordinates

The geomagnetic coordinate system arises from a simple dipole approximation of the geomagnetic field. It is a spherical polar system which is fixed relative to the earth. The polar axis is inclined at 11.5° to the axis of rotation, intersecting the earth's surface at the geomagnetic north pole (geographic coordinates 78.5°N, 291.0°E) and south pole (geographic coordinates 78.5°S, 111.0°E). By definition, geomagnetic latitudes are negative south of the geomagnetic equator. Geomagnetic longitudes are measured eastward relative to the 0° geomagnetic meridian, which is defined by the American half of the great circle which passes through both the geographic and geomagnetic poles.

E.1.2 Corrected geomagnetic coordinates

A centred dipole is in fact a poor approximation of the geomagnetic field. A refinement of geomagnetic coordinates is the spherical polar system of corrected geomagnetic coordinates (Hakura, 1965). These coordinates are deduced from the International Geomagnetic Reference Field (IGRF) which is based on a spherical-harmonic model of the geomagnetic field. The IGRF is updated every five years (e.g. 1980, 1985, 1990...), and allows linear interpolation between adjacent models. As a comparison: In 1979 the geomagnetic coordinates for Sanae were lat. -63.86°, long. 44.94°; whereas the corrected geomagnetic coordinates were lat. -59.91°, long. 43.90°.

E.1.3 McIlwain's B-L coordinate system

The study of particles trapped in the geomagnetic field led McIlwain (1961) to introduce the L parameter, which is a function of I (the second adiabatic invariant) and B_m (the strength of the magnetic field at the mirror point, where particles spiralling down a field line are reflected back up the field line). L has the dimension of length and is specified in earth radii (R_e). In the case of a dipole field, L is the distance from the earth at which a field line crosses the equatorial plane. For $L < 5$, L varies by less than 1% along the field line (Hess, 1968), and thus can often be used to identify field lines even if they are not strictly dipolar.

Surfaces of constant L (L-shells) can be combined with surfaces of constant B (concentric, roughly ellipsoidal shells encircling the earth) to form a useful magnetic coordinate system for use in auroral studies. Note however, that the L parameter is frequently used by itself to characterize the location at which observations have been made, or data collected. A further point to be noted is the fact that for a given geographic position (latitude and longitude), L varies with altitude. This is shown in Appendix F, where L-values and invariant latitudes are derived for altitudes of 100 and 300 km in the vicinity of Sanae.

E.1.4 Invariant latitude

Another magnetic parameter, the invariant latitude Λ, is directly related to McIlwain's L parameter by

$$\Lambda = \cos^{-1}\sqrt{\frac{1}{L}} \qquad \text{(E.1)}$$

Invariant latitude is essentially the geomagnetic latitude from which a dipole-like field line would originate to intersect the geomagnetic equatorial plane at a distance of L earth radii. Being directly related to L-value, the invariant latitude of a particular geographic position also varies with altitude. Invariant latitude is perhaps the magnetic parameter most often used to characterize the position of auroral observations. Invariant longitude can be used together with invariant latitude to form a proper coordinate system (see e.g. Kilfoyle and Jacka, 1968). Note, however, that Vallance Jones (1974) warns that invariant longitude is not consistently defined, nor is a zero meridian consistently chosen. Although invariant latitude is often used, the author has seen little, if any, evidence of invariant longitude being used in auroral studies.

One advantage of using invariant latitude (or L-value) to characterize a station's position is that the station's conjugate point will, by definition, have the same coordinates.

E.2 Magnetic time coordinates

Owing to the difference between the location of the earth's geomagnetic and geographic axes, the geomagnetic local time of a station differs from its geographic local time. The magnetic local time of a station is the angle between the magnetic meridians through the station and through the Sun. Specific cases of magnetic local time are magnetic midnight, when the station's magnetic meridian is anti-sunward, and magnetic noon, when the sun is aligned with the station's magnetic meridian.

Magnetic local time (MLT) is derived by subtracting a station's magnetic declination (D) from its geographic local time (LT). For example, in the case of Sanae in 1979, which had a geographic longitude of 2.49°W and a declination of 17.93°

$$\begin{aligned} \mathrm{MLT} &= \mathrm{LT} - \mathrm{D} \\ &= \left(\mathrm{UT} - \frac{2.49}{15}\right) - \frac{17.93}{15} \\ \text{i.e.} \quad \mathrm{MLT} &= \mathrm{UT} - 1.36\,\mathrm{hr} \end{aligned}$$

Montbriand (1970) has developed a simple method of calculating corrected geomagnetic midnight (CGM) in terms of UT. This method takes into account the solar declination at different times of the year, by including a correction parameter α_c:

$$\mathrm{CGM} = \frac{360 - \Phi_c + \alpha_c}{15} \qquad \text{(D.2)}$$

where Φ_c is corrected geomagnetic longitude. Graphs of α_c versus Φ_c, for various values of solar declination, show that for the winter months at Sanae α_c varies between 63° (at June solstice) and 72° (at the equinoxes).

This gives a range in CGM values from 01:16 to 01:52 UT, respectively. Corrected geomagnetic local time is then given by (UT - CGM).

Evans (1972) defines invariant geomagnetic local time (INLT) which is calculated from invariant longitudes. A number of additional (minor) correction terms make Evans' equation for INLT highly accurate. Unfortunately the author has been unable to find an accurate value for Sanae's invariant longitude, and thus cannot use Evans' equation to calculate INLT values for Sanae.

E.3 Geomagnetic Indices

A number of numeric indices have been introduced to indicate the level of geomagnetic activity at a particular time, or for a period of time. Some indices are general (e.g. Kp, Ap), whilst others characterize a particular type of disturbance (e.g. the auroral electrojet indices (AE, AL, AU) and the ring current index, Dst). Detailed descriptions of the various geomagnetic indices are given by Lincoln (1967), Rostoker (1972) and Mayaud (1980). Menvielle and Berthelier (1991) give a review of the K-derived planetary indices (i.e the K- and a- indices), which is based on Mayaud's (1980) work. Brief descriptions of the more useful indices are given by Vallance Jones (1974) and Knecht and Shuman (1985). For convenience, a number of these indices are mentioned below.

E.3.1 General activity indices K, Kp, Km, Kn and Ks

The K index, for a given magnetic observatory, is an indication of the general level of geomagnetic disturbance at that station. It is defined for each three-hourly interval, as the largest range, R, of any of the X,Y, D or H components of the geomagnetic field. R is defined as the difference between the highest and lowest deviations from the regular daily variations of these components. K is a quasi-logarithmic representation of R, and can have integer values between 0 and 9. The mapping between K and R varies from station to station to allow for the different ranges in R experienced at the different stations (auroral stations have higher maximum R-values than mid-latitude stations).

Kp is a planetary index which is a worldwide index of the average level of geomagnetic activity. It is derived from the values of K at 12 stations between geomagnetic latitudes 48° and 63°, which were selected for a good longitudinal coverage. Kp ranges continuously between 0.0 and 9.0 in thirds of an integer. The symbols -, o and + are used, so that a value of Kp = 3.0 is represented by 3o, 3.33 by 3+, and 3.67 by 4- etc.

Sometimes ΣKp is used to indicate a daily index. ΣKp is the sum of the eight three-hourly Kp indices for a particular day. As Kp is logarithmic, averaging a day's Kp values to get a mean Kp is meaningless.

Although Kp is probably the most widely used of all of the geomagnetic indices, a newer index Km is supposed to represent an improvement on Kp. Whereas Kp is calculated only from K values in the northern (magnetic) hemisphere, Km is calculated from magnetic data from both hemispheres. It is, in fact, an average of two component indices, Kn and Ks, calculated for the northern and southern hemispheres respectively.

E.3.2 The ak, Ak, ap, Ap, am, Am and aa indices

These are linear indices, directly related to the various K indices mentioned above. The single station index ak, with values between 0 and 400, is derived from the station's K value, using a conversion table (see e.g. Table 4-4 of Knecht and Shuman, 1980). The planetary index ap also ranges between 0 and 400 and is derived directly from Kp. Table 4-3 of Knecht and Shuman (1980) gives the conversion between Kp and ap, for the 28 possible values of Kp.

In a similar way, the linear index am is related to Km. Note however that am is determined as the mean of the two hemispherical indices, an and as, which in turn are derived directly from the magnetic data. The values of Km, K_n and Ks are then determined from the values of am, an and as.

All of the linear indices that are described above, allow meaningful averages to be calculated, to give a daily index. Ak, Ap and Am are daily indexes defined as the average of the eight three-hourly ak, ap and am indices respectively.

The aa index (a for antipodal) is similar to the am index but is derived from data from only two stations situated at approximately antipodal locations in England and Australia. Data from these two stations are available as far back as 1868, thus providing an index that spans more than 120 years. The aa index is a good approximation of am (Knecht and Shuman, 1985).

Monthly tables of three-hourly Kp, Km, K, Ks values and daily Ap values are published in the Journal of Geophysics Research, and are readily obtainable. In addition, a number of aa-related parameters are given: N is the daily average aa value determined at the English observatory; S is the daily average aa value determined at the Australian observatory; and M are the half-daily aa averages (for the periods 00:00 to 12:00, and 12:00 to 24:00) for the observatories combined.

E.3.3 The auroral electrojet indices AE, AU, AL and Ao

The auroral electrojet index, AE, was first derived by Davis and Sugiura (1966) as a measure of global electrojet activity. Directly associated with the AE index are a number of other electrojet indices, namely AU, AL and Ao. All of these indices are derived from magnetograms recorded at 12 northern hemisphere auroral zone stations (originally only 7 stations were used). All of the stations are at magnetic latitudes between 60 and 70° and are selected to give a good longitudinal distribution. The auroral electrojet indices are obtained graphically by superimposing data from all of the stations: For each station, the deviation of the H component from its normal quiet-time value is plotted against universal time. The envelopes outlining the instantaneous maximum positive and negative excursions of the H components are drawn in. The height of the positive (or upper) envelope is then AU, whilst the height of the negative (or lower) envelope is AL. The total distance between the envelopes gives the AE index. A further index, Ao, is defined as the mean deviation of all the stations' H components, and is a curve midway between the AU and AL curves.

The auroral electrojet indices are so named because it is the electrojet currents which are responsible for the deviation of the H component from its quiet-time level. At a particular station, a positive H bay indicates an eastward auroral electrojet, whilst a negative bay indicates a westward electrojet.

Maclennan *et al.* (1991) have drawn up an electrojet index for the southern hemisphere, AE_s, which uses magnetic data from 22 Antarctic stations. They then compared values for this index with those of the standard AE index, derived from northern hemisphere stations. Good correlation was found between the northern and southern hemisphere indices.

E.3.4 Q and Qp indices

Q is an index based on the maximum deviation from a quiet-day curve of the more disturbed of the two horizontal components (X and Y). A number of observatories at geomagnetic latitudes above 58° are used to determine the associated planetary index, Qp, and so it is an indication of high-latitude magnetic activity. It is calculated every 15 minutes, and consequently has better temporal resolution than the K indices, but its availability is limited.

E.3.5 The ring current index Dst

A number of low geomagnetic latitude stations, again distributed in longitude, are used to derive the ring current index Dst (also referred to as the equatorial index). This index is the value of the horizontal disturbance component averaged over the contributing stations. It gives an hourly indication of low latitude activity. Dst was designed as a measure of the magnetospheric ring current that flows during magnetic storms. Consequently, to avoid the effects of electrojets, auroral and equatorial stations are not used in the determination of this index.

APPENDIX F

The determination of the L-values and invariant latitudes corresponding to the zenith angles used in a meridian scan

If the heights of the emission layers being observed by a meridian scan are known (or assumed), it is possible to derive the L-values or invariant latitudes of the emission layers, for each zenith angle used in the meridian scan.

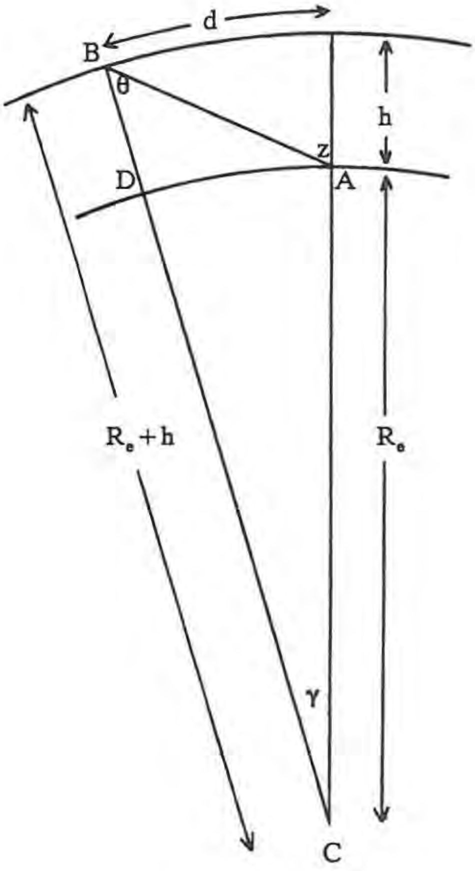

Figure F.1 The geometry of a photometric observation of an emission layer at altitude h, made with the photometer using a zenith angle z.

Figure F.1 shows the geometry that is involved when a photometer at point A, uses a zenith angle z to observe the airglow or auroral emissions that originate at a point B, which is at an altitude h above the point D. The process used to determine the L-value and the invariant latitude of the point B can be divided into a number of steps:

1/ Determine the great circle distance d between points A and D.

From Figure F.1, the distance d is the fraction of the earth's circumference corresponding to the angle γ, i.e.

$$d = \frac{\gamma}{360}(2\pi R_e) \tag{F.1}$$

where R_e is the radius of the earth (6370 km).

We now need to determine γ in terms of the zenith angle z. To do this we use the relationship

$$\gamma = z - \theta \tag{F.2}$$

and the Sine Law, applied to the triangle ABC:

$$\frac{R_e}{\sin\theta} = \frac{(R_e + h)}{\sin z} \tag{F.3}$$

Re-arranging Equation F.3 for θ, and substituting into Equation F.2 gives

$$\gamma = z - \arcsin\left(\left(\frac{R_e}{R_e + h}\right)\sin z\right) \tag{F.4}$$

Finally, substituting for γ in Equation F.1 gives d in terms of h and z:

$$d = \left(z - \arcsin\left(\left(\frac{R_e}{R_e + h}\right)\sin z\right)\right)\frac{2\pi R_e}{360} \tag{F.5}$$

2/ Determine the great circle course c between points A and D.

The photometers at Sanae are aligned to scan along the magnetic meridian. This means that one can use Sanae's magnetic declination (-17.93° in 1979) to determine the angle c of the meridian scan. The angle c used as the course in great circle calculations is, by definition, measured in a clockwise direction from geographic north.

Consequently, for the poleward section of the meridian scan:

$$c = 180° - 17.93° = 162.07°$$

and for the equatorward section of the meridian scan:

$$c = 360° - 17.93° = 342.07°.$$

3/ Determine the geographic coordinates of point D.

The standard great circle formulae can be used to calculate the geographic coordinates of point D, using the geographic coordinates of point A, the distance d and the course c. Normally the great circle formulae are equations for d and c, i.e.

$$d = 1.85 \text{ x } 60 \cos^{-1}\left(\sin L_1 \sin L_2 + \cos L_1 \cos L_2 \cos(\lambda_2 - \lambda_1)\right) \tag{F.6}$$

and

$$c = \cos^{-1}\left(\frac{\sin L_2 - \sin L_1 \cos\left(\frac{0.54d}{60}\right)}{\sin\left(\frac{0.54d}{60}\right) \cos L_1}\right) \tag{F.7}$$

where: L_1, and λ_1 are the latitude and longitude, respectively, of point A (i.e. Sanae),
L_2, and λ_2 are the latitude and longitude, respectively, of point D.

Note: Southern latitudes and eastern longitudes are negative.
d is in kilometres, i.e. the factor 1.85 in Equation F.6 converts nautical miles to kilometres, and the factor 0.54 in Equation F.7 converts kilometres to nautical miles.

Equations F.6 and F.7 can be re-arranged to give the following equations for the latitude and longitude of point D:

$$L_2 = \sin^{-1}\left(\sin\left(\frac{0.54d}{60}\right) \cos L_1 \cos c + \sin L_1 \cos\left(\frac{0.54d}{60}\right)\right) \tag{F.8}$$

and

$$\lambda_2 = \lambda_1 - \cos^{-1}\left(\frac{\cos\left(\frac{0.54d}{60}\right) - \sin L_1 \sin L_2}{\cos L_1 \cos L_2}\right) \qquad [0 < c < \pi]$$

(F.9)

or

$$\lambda_2 = \lambda_1 + \cos^{-1}\left(\frac{\cos\left(\frac{0.54d}{60}\right) - \sin L_1 \sin L_2}{\cos L_1 \cos L_2}\right) \qquad [\pi < c < 2\pi]$$

These formulae were used to calculate the geographic coordinates of all the locations of D, corresponding to the zenith angles used at Sanae in 1979, for altitudes of the emission layers of 100 and 300 km.

4/ Determine the L-value of point B.

A computer program, which uses the International Geomagnetic Reference Field (IGRF) model of the geomagnetic field, is used to determine the L-value of the point B, at a height h above the known geographic coordinates of point D. The Magnetic Observatory at Hermanus has a copy of this computer program. A table of the geographic coordinates, calculated in 3/ above, and relevant to Sanae in 1979, was supplied to Mr. Barry Pretorius of the Observatory. He kindly ran the program to calculate the L-values for heights of 100 and 300 km above these coordinates. The resulting L-values are tabulated, against zenith angle and altitude, in Table F.1.

5/ Determine the invariant latitude of point B.

Invariant latitude is related to L-value by the equation

$$\Lambda = \cos^{-1}\sqrt{\frac{1}{L}} \qquad \textbf{(F.10)}$$

This equation was used to calculate the invariant latitudes for all the locations of point B, again at altitudes of 100 and 300 km above D. The values obtained are given in Table F.1.

Table F.1 L-values and invariant latitudes for the zenith angles used at Sanae in 1979, assuming the altitudes of the emission layers to be 100 and 300 km.

Zenith angle (° North)	Altitude = 100 km		Altitude = 300 km	
	L-value (R_e)	Invariant latitude (°)	L-value (R_e)	Invariant latitude (°)
70	3.64	58.39	3.24	56.24
65	3.72	58.76	3.38	57.04
55	3.82	59.20	3.60	58.18
45	3.88	59.47	3.75	58.91
30	3.95	59.77	3.93	59.71
15	4.00	59.98	4.07	60.30
0	4.04	60.17	4.21	60.84
-15	4.09	60.35	4.36	61.38
-30	4.14	60.57	4.53	61.99
-45	4.21	60.84	4.80	62.83
-55	4.29	61.14	5.07	63.62
-65	4.43	61.62	5.54	64.87
-70	4.54	61.99	5.94	65.78

APPENDIX G

The determination of atmospheric correction factors for use with Sanae data

Section 4.3 shows that there are a number of models that can be used to determine the atmospheric correction factors that can be applied to photometric data, in order to yield the emission intensities of the airglow or the aurora at the emitting layer. Two methods, stemming from these models, were deemed suitable for application to the Sanae data:

1/ The Ashburn method (Ashburn, 1954), which corrects for atmospheric extinction, scattering, and ground reflections. This method is referred to as the A-method.

2/ A straightforward exponential correction method, which corrects only for the effects of atmospheric extinction, and does not cater for light scattered into the field of view, or for light reflected from the ground and then backscattered into the field of view. This method is referred to as the E-method.

The equations for both of these methods are given in Chapter 4, as Equation 4.31. They are repeated here for convenience:

$$\text{A-method:} \qquad C = \left(V\, e^{-\tau_{total} m} + e^{-\tau_{ozone}} (D + R)\right)^{-1} \tag{G.1}$$

and

$$\text{E-method:} \qquad C = \left(V\, e^{-\tau_{total} m}\right)^{-1} \tag{G.2}$$

Before these equations can be used to obtain values for C, a number of wavelength-dependent parameters need to be assigned values, viz. the extinction coefficients, τ_{total} and τ_{ozone}; the heights of the emission layers, h; and the albedo of the ground, r. The values used for these parameters are tabulated in Table 6.1 in Chapter 6. For convenience they are repeated in Table G.1.

The van Rhijn function, V, is given (Equation 4.23) in terms of the height of the emitting layer h, and the zenith angle z, by

$$V = \left(1 - \left(\frac{R_e}{(R_e + h)}\right)^2 \sin^2 z\right)^{-1/2} \tag{G.3}$$

where R_e is the radius of the Earth (taken as 6370 km).

Table G.1 Wavelength-dependent parameters needed for the determination of atmospheric correction factors. Note $\tau_{total} = (\tau + \tau_{ozone})$.

Emission wavelength (nm)	Extinction coefficient		Emission height h (km)	Ground albedo r
	τ_{total}	τ_{ozone}		
391.4	0.38	0.000	100	0.8
557.7	0.22	0.030	100	0.8
630.0	0.18	0.029	300	0.8

Values of V for 5° intervals of z, and various values of h, can be found in Table 12.1 of Chamberlain (1961). Values were extracted for the zenith angles used at Sanae, assuming emission heights of 100 km (for the 391.4 and 557.7 nm emissions) and 300 km (for the 630.0 nm emission). These values are tabulated in Table G.2. Also listed in this table are the values of the air mass, m, needed for the evaluation of the exponential terms in Equations G.1 and G.2. These were obtained from Table 16-2 of Valley (1965). By definition, the air mass values are given relative to an air mass of unity in the zenith (i.e. at z = 0°).

Table G.2 Values of the van Rhijn function for the zenith angles used at Sanae in 1979, for emission layers at 100 and 300 km. Values of the air mass for each zenith angle are also given.

Zenith angle z (degrees)	van Rhijn function V		Air mass m (relative to 1, at z = 0°)
	h = 100 km	h = 300 km	
0	1.00	1.00	1.00
15	1.03	1.03	1.04
30	1.15	1.14	1.15
45	1.39	1.36	1.41
55	1.69	1.61	1.74
65	2.22	2.00	2.36
70	2.63	2.27	2.90

Equation G.2 can now be used to compute E-method correction factor values, using the parameter values given in Tables G.1 and G.2. The correction factors obtained are given in Table G.3.

Table G.3 Atmospheric correction factors for Sanae, obtained using the E-method (i.e. the extinction-only model).

Zenith angle z (degrees)	Atmospheric correction factor C (using E-method)		
	λ = 391.4 nm	λ = 557.7 nm	λ = 630.0 nm
0	1.616	1.245	1.198
15	1.590	1.215	1.167
30	1.513	1.121	1.082
45	1.416	0.979	0.952
55	1.364	0.868	0.853
65	1.399	0.760	0.766
70	1.531	0.720	0.743

The determination of atmospheric correction factors using the A-method is less straightforward. Ashburn (1954) gives two integrals which can be solved to give the intensity of the scattered light components of the emission intensity, for any zenith angle z, emission height h, extinction coefficient τ and ground albedo r. However, in order to do this one needs access to a number of tables that he refers to. Unfortunately this author this been unable to locate copies of these tables. Consequently, the only way to obtain values for the A-method correction factors, is to interpolate values of D and R from the limited tables that Ashburn (1954) supplies. In his Table 1, Ashburn gives values for D and R for all combinations of the following parameter values:

Zenith angle z:	0°, 40°, 50°, 60°, 70°, 75°, 80° and 86.58°.
Emission height h:	100 km, 200 km, 300 km and ∞.
Extinction coefficient τ:	0.01, 0.05, 0.10, 0.15, 0.25 and 1.00.
Ground albedo r:	0.0, 0.25, 0.50 and 0.80.

Values of D can be extracted from those portions of Table 1 where the ground albedo = 0, and values of R from those portions where the ground albedo ≠ 0.

The author used the following two-stage process to interpolate values of D for the zenith angles used at Sanae, assuming the emission heights and total extinction coefficients as given in Table G.1:

1/ For heights of 100 and 300 km, the tabulated values for ground albedo = 0 were plotted against τ for all the zenith angles used by Ashburn. Smooth curves were fitted to each set of points. Values were then read off at the values of the assumed extinction coefficients (τ = 0.22 and 0.38 on the 100 km curves, and τ = 0.18 on the 300 km curves).

2/ The values of D obtained in stage 1 were then plotted against zenith angle, for each value of τ. Again smooth curves were fitted to each set of points. These curves were then used to give values of D at the required zenith angles (0, 15, 30, 45, 55, 65 and 70 degrees).

The same process was used to obtain values for R, except that the initial R values were taken from those portions of Ashburn's table applicable to a ground albedo of 0.80. The variations of D and R, with zenith angle and extinction coefficient, are shown in Figures G.1 and G.2 respectively. These graphs show that for a given zenith angle, both D and R increase with extinction coefficient. Furthermore, for a given extinction coefficient, the values of D and R both increase approximately exponentially with zenith angle. Once all the required D and R values had been obtained, Equation G.1 was used to compute the A-method correction factors. The resultant values of C are listed in Table G.4.

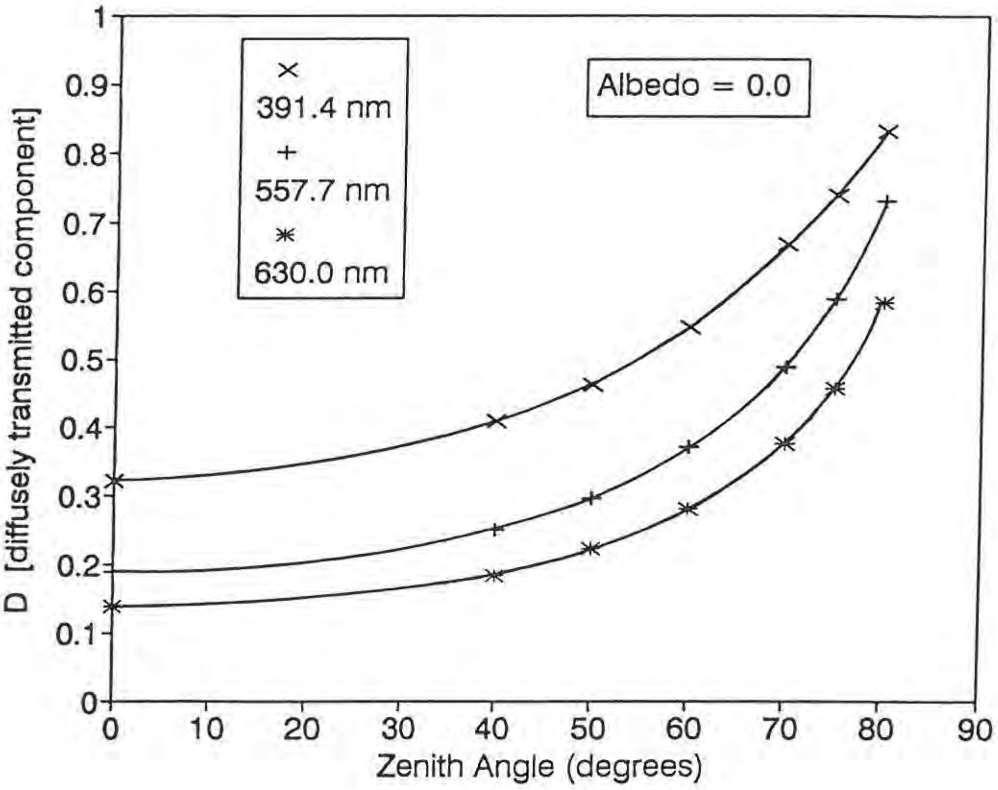

Figure G.1 The variation of D, the coefficient of the diffusely transmitted light, with zenith angle for the emissions observed at Sanae.

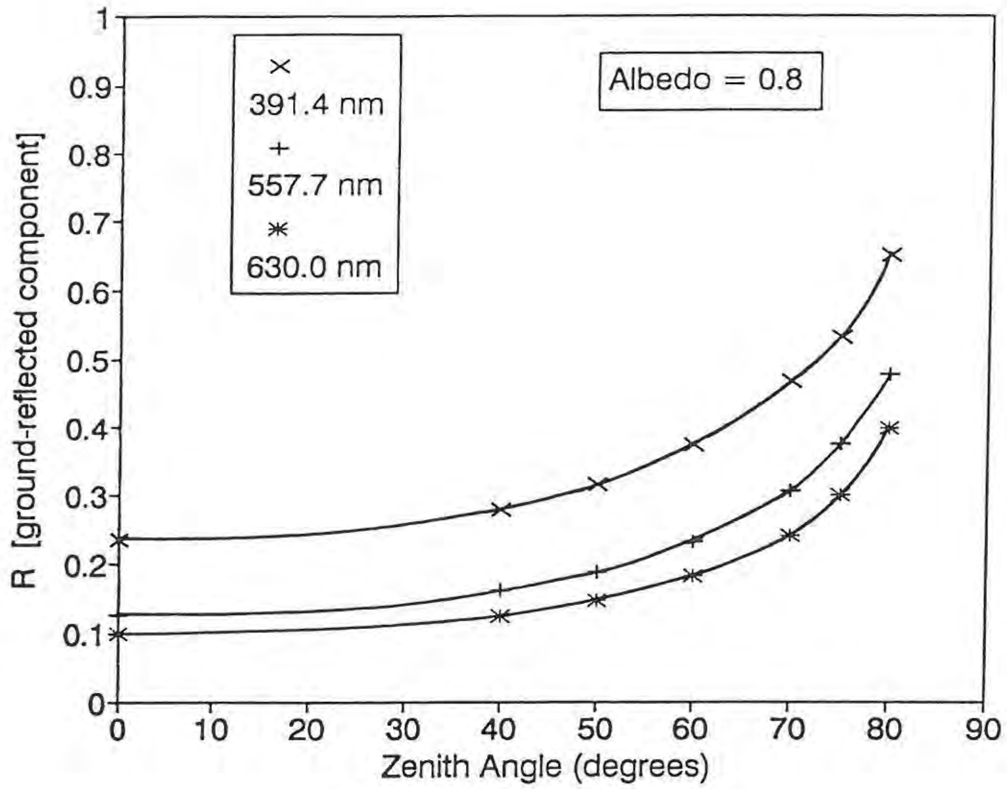

Figure G.2 The variation of R, the coefficient of the ground-reflected and backscattered light, with zenith angle for the emissions observed at Sanae.

Table G.4 Atmospheric correction factors for Sanae, obtained using the A-method (i.e. Ashburn's extinction and scattering model).

Zenith angle z (degrees)	Atmospheric correction factor C (using A-method)		
	λ = 391.4 nm	λ = 557.7 nm	λ = 630.0 nm
0	0.852	0.903	0.938
15	0.829	0.878	0.908
30	0.778	0.804	0.840
45	0.700	0.690	0.782
55	0.638	0.598	0.636
65	0.581	0.504	0.551
70	0.560	0.463	0.515

APPENDIX H

Results of the 1978 Sutherland cross-calibration of the Rhodes University low-brightness calibration sources, LBS #1 and LBS #2

Both of the Rhodes University variable-aperture low-brightness sources (LBS #1 and LBS #2) were cross-calibrated against the Hermanus ^{14}C-activated phosphor source at Sutherland in October 1978. The cross-calibration was conducted by R. Burnside of the NITR and D.K. Taylor of Rhodes University.

Before the actual cross-calibration, the ratio of the area of each aperture to the area of aperture #5 was determined for each source. This was done by comparing relative brightnesses (corrected for PMT dark-current) when different apertures were in place. The ratios are given in Table H.1.

Table H.1 Measured aperture area ratios for the Rhodes University LBS #1 and LBS #2 variable-aperture calibration sources.

Aperture number	Ratio of aperture's area to that of aperture #5	
	LBS #1	LBS #2
1	0.064 ± 0.002	0.070 ± 0.003
2	0.129 ± 0.004	0.146 ± 0.004
3	0.275 ± 0.011	0.223 ± 0.005
4	0.506 ± 0.009	0.487 ± 0.010
5	1.000	1.000
6	2.204 ± 0.027	2.022 ± 0.031
7	3.792 ± 0.036	3.890 ± 0.058
8	7.590 ± 0.036	7.726 ± 0.124

Then, during the cross-calibration, each LBS was calibrated against the ^{14}C source at 391.4, 486.1, 557.7 and 630.0 nm. Three different lamps were used with each LBS. Lamps 1, 2 and 3 were used with LBS #1, and Lamps 5, 6 and 7 were used with LBS #2. (Note: No mention is made in the cross-calibration records of a Lamp 4). Brightnesses obtained for LBS #1 and LBS #2 are given in Tables H.2 and H.3 respectively. Due to time limitations, brightness measurements were not made for every valid combination of source, lamp and aperture. Aperture 5 brightnesses were multiplied by the appropriate aperture area ratios (from Table H.1) to obtain the brightness values in brackets in Tables H.2 and H.3.

Table H.2 Brightnesses of LBS #1 determined at the Sutherland cross-calibration in September 1978, using the Hermanus ^{14}C source (previously owned by the NITR).

Lamp used in LBS	Aperture	Brightness (R nm^{-1})			
		391.4 nm	486.1 nm	557.7 nm	630.0 nm
Lamp #1	1	2.0	20.5	55.7	135
	2	3.9	42.4	113	272
	3	8.1	86.3	247	587
	4	15.6	165	443	1040
	5	30.9	325	880	1990
	6	69.5	709	1920	(4390)
	7	118	(1230)	(3340)	(7550)
	8	(235)	(2470)	(6680)	(15100)
Lamp #2	1	2.0	21.6	57.0	136
	2	3.9	44.3	115	275
	3	8.5	95.4	252	596
	4	15.5	174	456	1060
	5	31.2	342	904	2030
	6	68.8	744	1960	(4470)
	7	118	(1300)	(3430)	(7700)
	8	(237)	(2600)	(6860)	(15400)
Lamp #3	1	(2.1)	(22.7)	(58.5)	(135)
	2	(4.2)	(45.8)	(118)	(272)
	3	(8.9)	(97.6)	(251)	(580)
	4	(16.4)	(180)	(463)	(1070)
	5	32.5	355	914	2110
	6	(71.6)	(782)	(2010)	(4650)
	7	(123)	(1350)	(3470)	(8000)
	8	(247)	(2690)	(6940)	(16000)

Yoshida, S., G.H. Ludwig, and J.A. van Allen, Distribution of trapped radiation in the geomagnetic field, *J. Geophys. Res.*, **65**, 807, 1960.

Zeeman, P.B., and F.M. Hamm, *Airglow Data, SANAE 1967*, Merensky Institute for Physics, University of Stellenbosch, South Africa, 1967.

Zeeman, P.B., F.M. Hamm, and J.L. Steyn, *Airborne airglow measurements in and around the South Atlantic geomagnetic anomaly, October 1964*, Merensky Institute for Physics, University of Stellenbosch, South Africa, 1964.

Zeeman, P.B., F.M. Hamm, and J.L. Steyn, *Airborne airglow measurements in and around the South Atlantic geomagnetic anomaly, August 1966*, Merensky Institute for Physics, University of Stellenbosch, South Africa, 1966.

Zeeman, P.B., F.M. Hamm, and J.L. Steyn, *Airborne airglow measurements along the geomagnetic meridians through Cape Town and Walvis Bay, August 1969*, Merensky Institute for Physics, University of Stellenbosch, South Africa, 1969.

Zeeman, P.B., J.L. Steyn, and F.M. Hamm, *Airglow Data, SANAE 1968*, Merensky Institute for Physics, University of Stellenbosch, South Africa, 1968.

Zeeman, P.B., J.L. Steyn, and F.M. Hamm, *Airglow Data, SANAE 1969*, Merensky Institute for Physics, University of Stellenbosch, South Africa, 1969.

Zipf, E.C., The excitation of the $O(^1S)$ state by the dissociative recombination of O_2^+ ions: Electron temperature dependence, *Planet. Space Sci.*, **36**, 621, 1988.

Zipf, E.C., P.S. Espy, and C.F. Boyle, The excitation and collisional deactivation of metastable $N(^2P)$ atoms in auroras, *J. Geophys. Res.*, **85**, 687, 1980.

Table H.3 Brightnesses of LBS #2 determined at the Sutherland cross-calibration in September 1978, using the Hermanus ^{14}C source (previously owned by the NITR).

Lamp used in LBS	Aperture	Brightness (R nm^{-1})			
		391.4 nm	486.1 nm	557.7 nm	630.0 nm
Lamp #5	1	2.2	24.3	62.7	157
	2	4.3	51.5	134	327
	3	6.7	77.4	210	490
	4	14.4	169	450	1070
	5	30.3	349	934	2110
	6	61.7	697	1850	(4270)
	7	118	(1360)	(3630)	(8210)
	8	(234)	(2700)	(7220)	(16300)
Lamp #6	1	2.0	2.30	51.7	149
	2	4.1	47.6	128	307
	3	6.3	72.3	195	466
	4	14.1	160	428	1010
	5	28.9	326	884	2000
	6	58.8	652	1760	(4040)
	7	112	(1270)	(3440)	(7780)
	8	(223)	(2520)	(6830)	(15450)
Lamp #7	1	(2.2)	(23.6)	(62.5)	(146)
	2	(4.5)	(49.2)	(130)	(306)
	3	(6.9)	(75.2)	(199)	(466)
	4	(15.0)	(164)	(435)	(1020)
	5	30.8	337	893	2090
	6	(62.3)	(681)	(1810)	(4230)
	7	(120)	(1310)	(3470)	(8130)
	8	(238)	(2600)	(6900)	(16150)

REFERENCES

Abreu, V.J, and P.B. Hays, Parallax, and atmospheric scattering effects on the inversion of satellite auroral observations, *Appl. Opt.*, **20**, 2203, 1981.

Ahn, B.-H., Y. Kamide, and S.-I. Akasofu, Global ionospheric current distributions during substorms, *J. Geophys. Res.*, **89**, 1613, 1984.

Ahn, B.-H., H.W. Kroehl, Y. Kamide, D.J. Gorney, S.-I. Akasofu, and J.R. Kan, The auroral energy deposition over the polar ionosphere during substorms, *Planet. Space Sci.*, 37, 239, 1989.

Akasofu, S.-I., The development of the auroral substorm, *Planet. Space Sci.*, **12**, 273, 1964.

Akasofu, S.-I., The auroral oval and the internal structure of the magnetosphere, p. 267, in *Aurora and Airglow*, Ed. by B.M. McCormac, Reinhold Publishing Company, New York, 1967.

Akasofu, S.-I., *Polar and magnetospheric substorms*, D. Reidel, Dordrecht, Holland, 1968.

Akasofu, S.-I., A study of auroral displays photographed from the DMSP-2 satellite and from the Alaska meridian chain of stations, *Space Sci. Rev.*, **16**, 617, 1974.

Akasofu, S.-I., The solar wind - magnetosphere dynamo and the magnetospheric substorm, *Planet. Space Sci.*, **23**, 817, 1975a.

Akasofu, S.-I., The roles of the north-south component of the interplanetary magnetic field on large scale dynamics observed by the DMSP satellite, *Planet. Space Sci.*, **23**, 1349, 1975b.

Akasofu, S.-I., Recent progress in studies of DMSP auroral photographs, *Space Sci. Rev.*, **19**, 169, 1976.

Akasofu, S.-I., *Physics of magnetospheric substorms*, D. Reidel, Hingham, Mass., 1977.

Akasofu, S.-I., Recent progress in Antarctic auroral studies, *A.G.U. Ant. Res. Ser.*, **29**, 157, 1978.

Akasofu, S.-I., The solar wind-magnetosphere energy coupling and magnetospheric substorms, *Planet. Space Sci.*, **28**, 495, 1980.

Akasofu, S.-I., The aurora: An electrical discharge phenomenon surrounding the earth, *Rep. Prog. Phys.*, **44**, 1123, 1981a.

Akasofu, S.-I., Energy coupling between the solar wind and the magnetosphere, *Space Sci. Rev.*, **28**, 121, 1981b.

Akasofu, S.-I., Auroral arcs and auroral potential structure, in *Physics of Auroral arc formation*, Ed. by S.-I. Akasofu and J.R. Kan, AGU, Washington, D.C., 1981c.

Akasofu, S.-I., Energy flow and Dynamic coupling in the solar wind-magnetosphere-ionosphere system, *Radio Sci.*, **18**, 971, 1983a.

Akasofu, S.-I., The magnetospheric currents: an introduction, pp. 29-48, in *Magnetospheric Currents*, Ed. by T. Potemra, Geophysical Monograph 28, AGU, Washington, D.C., 1983b.

Akasofu, S.-I., Explosive magnetic reconnection: Puzzle to be solved as the energy supply process for magnetospheric substorms?, *Eos Trans. AGU*, **66**, 9, 1985a.

Akasofu, S.-I., Reply (to Hill and Siscoe (1985), and Russell (1985)), *Eos Trans. AGU*, **66**, 66, 581, 1985b.

Akasofu, S.-I., Some critical issues on magnetospheric substorms, *Planet. Space Sci.*, **34**, 563, 1986.

Akasofu, S.-I., Concluding remarks (Chapman Conference on magnetotail physics), pp. 429-433, in *Magnetotail physics*, Ed. by A.T.Y. Lui, John Hopkins University Press, Baltimore, 1987.

Akasofu, S.-I., and R.P. Lepping, Interplanetary magnetic field and magnetospheric substorms, *Planet. Space Sci.*, **25**, 895, 1977.

Akasofu, S.-I., C. Olmsted, E.J. Smith, B. Tsurutanti, R. Okida, and D.N. Baker, Solar wind variations and geomagnetic storms: A study of individual storms based on high time resolution ISEE 3 data, *J. Geophys. Res.*, **90**, 325, 1985.

Akasofu, S.-I., P.D. Perreault, F. Yasuhara, and C.-I. Meng, Auroral substorms and the interplanetary magnetic field, *J. Geophys. Res.*, **78**, 7490, 1973.

Allen, C.W., *Astrophysical Quantities*, 2nd Edition, Athlone Press, University of London, London, 1964.

Anderson, G.P., and H.S. Muench, Atmospheric Composition, Chapter 21, Section 21.1, pp. 21-1 to 21-14, in *Handbook of geophysics and the space environment*, Ed. by A.S. Jursa, Air Force Geophysics Laboratory, U.S.A.F., Cambridge, Mass., 1985.

Anderson, H.R., and R.R. Vondrak, Observations of Birkeland currents at auroral latitudes, *Rev. Geophys. Space Phys.*, **13**, 243, 1975.

Anger, C.D., Review of rocket auroral measurements, in *Aurora and Airglow*, Ed. by B.M. McCormac, Reinhold Publishing Company, New York, 1967.

Anger, C.D., T. Fancott, J. McNally, and H.S. Kerr, ISIS-II scanning auroral photometer, *Appl. Opt.*, **12**, 1753, 1973.

Anger, C.D., *et al.* (14 contributors), An ultraviolet auroral imager for the Viking spacecraft, *Geophys. Res. Lett.*, **14**, 387, 1987a.

Anger, C.D., *et al.* (21 contributors), Scientific results from the Viking ultraviolet imager: an introduction, *Geophys. Res. Lett.*, **14**, 383, 1987b.

Arnoldy, R.L., and P.B. Lewis, Jr., Correlation of ground-based and topside photometric observations with auroral electron spectra measurements at rocket altitudes, *J. Geophys. Res.*, **82**, 5563, 1977.

Ashburn, E.V., The effect of Rayleigh scattering and ground reflection upon the determination of the height of the night airglow, *J. Atmos. Terr. Phys.*, **5**, 83, 1954.

Axford, W.I., and C.O. Hines, A unifying theory of high latitude geophysical phenomena and geomagnetic storms, *Can. J. Phys.*, **39**, 1433, 1961.

Barth, C.A., The 5577-Angstrom airglow, *Science*, **134**, 1426, 1961.

Barth, C.A., Three-body reaction, *Ann. Geophys.*, **20**, 181, 1964.

Barth, C.A., and A.F. Hildebrandt, The 5577 Å airglow emission mechanism, *J. Geophys. Res.*, **66**, 985, 1961.

Bellew, W., and S. Silverman, General behaviour of 6300 Å [OI] at Sacramento Peak, New Mexico, *Planet. Space Sci.*, **14**, 407, 1966.

Bennett, R.T., Latitude dependence of 6300 Å (OI) twilight airglow enhancement, *J. Geophys. Res.*, **74**, 381, 1969.

Blacker, H.V., and M. Gadsden, On the calibration of airglow photometers, *Planet. Space Sci.*, **14**, 921, 1966.

Blifford, I.H., Factors influencing the performance of commercial interference filters, *Appl. Opt.*, **5**, 105, 1966.

Bond, F.R., and I.L. Thomas, The southern auroral oval, *Aust. J. Phys.*, **24**, 97, 1971.

Broadfoot, A.L., Resonance scattering by N_2^+, *Planet. Space Sci.*, **15**, 1801, 1967.

Burnside, R.G., J.W. Meriwether, Jr., and M.R. Torr, Contamination of ground-based measurements of OI (6300 Å) and NI (5200 Å) airglow by OH emissions, *Planet. Space Sci.*, **25**, 985, 1977.

Burnside, R.G., and C.A. Tepley, Airglow intensities observed in the southern and northern hemispheres, *Planet. Space Sci.*, **38**, 1161, 1990.

Chapman, S., History of aurora and airglow, pp. 15-26, in *Aurora and Airglow*, Ed. by B.M. McCormac, Reinhold Publishing Company, New York, 1967.

Chapman, S., and V.C.A. Ferraro, A new theory of magnetic storms, *Terr. Mag. Atmosph. Elect.*, **36**, 77, 1931.

Chamberlain, J.W., *Physics of the aurora and airglow*, Academic Press, New York, 1961.

Chamberlain, J.W., *Theory of planetary atmospheres: an introduction to their physics and chemistry*, 1st Edition, Academic Press, London, 1987.

Chamberlain, J.W., and D.M. Hunten, *Theory of planetary atmospheres: an introduction to their physics and chemistry*, 2nd Edition, Academic Press, London, 1987.

Chamberlain, M.T., and F. Jacka, Optical evidence for mid-latitude charged particle precipitation, *J. Atmos. Terr. Phys.*, **41**, 111, 1979.

Chandrasekhar, S., *Radiative transfer*, 2nd Edition, Dover Publications Inc., New York, 1960.

Chapman, S., Auroral Science, 1600 to 1965 - towards its golden age?, pp. 11-25, in *Atmospheric Emissions*, Ed. by B.M. McCormac and A. Omholt, Van Nostrand Reinhold, New York, 1969.

Christensen, A.B., L.R. Lyons, J.H. Hecht, G.G. Sivjee, R.R. Meier, and D.G. Strickland, Magnetic field-aligned electric field acceleration and the characteristics of the optical aurora, *J. Geophys. Res.*, **92**, 6163, 1987.

Clarke, J.B., *Internal morphology of pulsating aurora*, M.Sc. thesis, University of Natal, South Africa, 1985.

Cogger, L.L., and H.C. Carlson, An experiment to measure variations in nighttime E-region neutral concentration, *Radio Sci.*, **12**, 261, 1977.

Cogger, L.L., V.B. Wickwar, and H.C. Carlson, Combined airglow and incoherent scatter observations as a technique for studying neutral atmosphere variations, *Radio Sci.*, **9**, 205, 1974.

Cogger, L.L., R.D. Elphinstone, and J.S. Murphree, Temporal and latitudinal 5577 Å airglow variations, *Can. J. Phys.*, **59**, 1296, 1981.

Cogger, L.L., J.S Murphree, S. Ismail, and C.D. Anger, Characteristics of dayside 5577 Å and 3914 Å aurora, *Geophys. Res. Lett.*, **4**, 413, 1977.

Comfort, S.D.G., *The digital image processing of pulsating aurora*, M.Sc. thesis, University of Natal, South Africa, 1986.

Condron, T.P., and R.B. Toolin, Visibility, Chapter 14, Section 1 (Albedo), pp. 14-1 to 14-2, in *Handbook of Geophysics*, U.S.A.F., Cambridge Research Centre, Cambridge, Mass., 1960.

Coroniti, F.V., Explosive tail reconnection: The growth and expansive phases of magnetospheric substorms, *J. Geophys. Res.*, **90**, 7427, 1985.

Craven, J.D., and L.A. Frank, The temporal evolution of a small auroral substorm as viewed from high altitudes with Dynamics Explorer 1, *Geophys. Res. Lett.*, **12**, 465, 1985.

Craven, J.D., and L.A. Frank, Latitudinal motions of the aurora during substorms, *J. Geophys. Res.*, **92**, 4565, 1987.

Creutzberg, F., R.L. Gattinger, R.F. Harris, and A. Vallance Jones, Pulsating auroras in relation to proton and electron auroras, *Can. J. Phys.*, **59**, 1124, 1981.

Davidson, G.T., Expected spatial distribution of low-energy protons precipitated in the auroral zones, *J. Geophys. Res.*, **70**, 1061, 1965.

Davis, T.N., The application of image orthicon techniques to auroral observation, *Space Sci. Rev.*, **6**, 222, 1966.

Davis, T.N., Television observation of auroras, pp. 27-35, in *Atmospheric emissions*, Ed. by B.M. McCormac and A. Omholt, van Nostrand Reinhold, New York, 1969.

Davis, T.N., Auroral morphology, *Planet. Space Sci.*, **20**, 1369, 1972.

Davis, T.N., and L.L. Smith, Latitudinal and seasonal variations in the night airglow, *J. Geophys. Res.*, **70**, 1127, 1965.

Davis, T.N., and M. Sugiura, Auroral electrojet activity index AE and its universal time variations, *J. Geophys. Res.*, **71**, 785, 1966.

Davydov, V.S., L.S. Evlashin, M.V. Orlava, G.F. Tulinov, T.A. Khyviyuzova, and V.N. Khokhlov, OI and N_2^+ emissions in polar aurora during daylight hours, *Geomagn. & Aeron.*, **25**, 63, 1985.

Deehr, C.S., G.J. Romick, and G.G.Sivjee, Auroral morphology: A television image of solar and magnetospheric activity, pp. 259-266, in *Exploration of the polar upper atmosphere*, Ed. by C.S. Deehr and J.A. Holtet, D. Reidel, Dordrecht, Holland, 1981.

Deehr, C.S., J.D. Winningham, F. Yasuhara, and S.-I. Akasofu, Simultaneous observations of discreet and diffuse aurora by the Isis 2 satellite and airborne instruments, *J. Geophys. Res.*, **81**, 5527, 1976.

De Kock, S., F.M. Hamm, and P.B. Zeeman, *Airglow data, SANAE, Antarctica, 1973*, Report No. 75/S/1, Merensky Institute for Physics, University of Stellenbosch, South Africa, 1975.

Dick, K.A., G.G. Sivjee, and H.M. Crosswhite, Aircraft airglow intensity measurements: Variations in OH and OI (5577), *Planet. Space Sci.*, **18**, 887, 1970.

Donahue, T.M., T. Parkinson, E.C. Zipf, J.P. Doering, W.G. Fastie, and R.E. Miller, Excitation of the auroral green line by dissociative recombination of the molecular ion: Analysis of two rocket experiments, *Planet. Space Sci.*, **16**, 737, 1968.

Dore, I.S., Photometric observations of the aurora during the substorm of 27 July 1979, *S. Afr. J. Phys.*, 7, 24, 1984.

Dore, I.S., G.P. Evans, J.A. Gledhill, and R. Haggard, Preliminary ionospheric and airglow results of Project ISAAC, *Mem. Nat. Inst. Polar Res.*, Special Issue on the energetics and dynamics of the middle and the upper atmosphere at high southern latitudes, **38**, 146, 1985.

Duncan, C.N., and D.J. McEwen, Photometric studies of the post-noon dayside cleft region, *J. Geophys. Res.*, **84**, 6533, 1979.

Dungey, J.W., Interplanetary magnetic field and the auroral zones, *Phys. Rev. Lett.*, **6**, 47, 1961.

Eather, R.H., Auroral proton precipitation and hydrogen emissions, *Rev. Geophys.*, **5**, 207, 1967a.

Eather, R.H., Secondary processes in proton aurora, *J. Geophys. Res.*, **72**, 1481, 1967b.

Eather, R.H., Spectral intensity ratios in proton induced auroras, *J. Geophys. Res.*, **73**, 119, 1968.

Eather, R.H., Latitudinal distribution of auroral and airglow emissions: The 'soft' auroral zone, *J. Geophys. Res.*, **74**, 153, 1969a.

Eather, R.H., Latitudinal distribution of auroral and airglow emissions, pp. 233-239, in *Atmospheric emissions*, Ed. by B.M. McCormac and A. Omholt, van Nostrand Reinhold, New York, 1969b.

Eather, R.H., The auroral oval - a reevaluation, *Rev. Geophys. Space Phys.*, **11**, 155, 1973.

Eather, R.H., *Majestic Lights - the aurora in science, history and the arts*, AGU, Washington D.C., 1980.

Eather, R.H., Dayside auroral dynamics, *J. Geophys. Res.*, **89**, 1695, 1984.

Eather, R.H., Private communication, 1985a.

Eather, R.H., Polar cusp dynamics, *J. Geophys. Res.*, **90**, 1569, 1985b.

Eather, R.H., Results from Antarctic optical studies, *Rev. Geophys.*, **26**, 579, 1988.

Eather, R.H., and F. Jacka, Auroral hydrogen emission, *Aust. J. Phys.*, **19**, 241, 1966.

Eather, R.H., and S.B. Mende, Airborne observations of auroral precipitation patterns, *J. Geophys. Res.*, **76**, 1746, 1971a.

Eather, R.H., and S.B. Mende, Auroral precipitation patterns, pp. 255-266, in *The radiating atmosphere*, Ed. by B.M. McCormac, D. Reidel, Dordrecht, Holland, 1971b.

Eather, R.H., and S.B. Mende, Systematics in auroral energy spectra, *J. Geophys. Res.*, **77**, 660, 1972.

Eather, R.H., S.B. Mende, and R.J.R. Judge, Plasma injection at synchronous orbit and spatial and temporal auroral morphology, *J. Geophys. Res.*, **81**, 2805, 1976.

Eather, R.H., S.B. Mende, and E.J. Weber, Dayside aurora and relevance to substorm current systems and dayside merging, *J. Geophys. Res.*, **84**, 3339, 1979.

Eather, R.H., and B.J. O'Brien, Photometric observations in South America and their relation to trapped radiation, *J. Atmos. Terr. Phys.*, **30**, 1585, 1968.

Eather, R.H., and D.L. Reasoner, Spectrophotometry of faint light sources with a tilting-filter photometer, *Appl. Opt.*, **8**, 227, 1969.

Eather, R.H., and B.P. Sandford, The zone of hydrogen emission in the night sky, *Aust. J. Phys.*, **19**, 25, 1966.

Edgar, B.C., W.T. Miles, and A.E.S. Green, Energy deposition of protons in molecular nitrogen and applications to proton auroral phenomena, *J. Geophys. Res.*, **78**, 6595, 1973.

Engebretson, M.J., L.J. Cahill, R.L. Arnoldy, S.B. Mende, and T.J. Rosenberg, Correlated irregular magnetic pulsations and optical emissions observed at Siple Station, Antarctica, *J. Geophys. Res.*, **88**, 4841, 1983.

Evans, J.E., A geomagnetic time system, *Eos Trans. A.G.U.*, **53**, 1102, 1972.

Fastie, W.G., Ultraviolet measurements in planetary atmosphere, *Appl. Opt.*, **6**, 397, 1967.

Feldstein, Y.I., Some problems concerning the morphology of auroras and magnetic disturbances at high latitudes, *Geomagn. & Aeron.*, **3**, 183, 1963.

Feldstein, Y.I., Peculiarities in the auroral distribution and magnetic disturbance distribution in high latitudes caused by the asymmetrical form of the magnetosphere, *Planet. Space Sci.*, **14**, 121, 1966.

Feldstein, Y.I., and G.V. Starkov, Dynamics of auroral belt and polar geomagnetic disturbances, *Planet. Space Sci.*, **15**, 209, 1967.

Feldstein, Y.I., G.V. Starkov, and V.A. Zverev, Conjugacy of auroral oval, *Mem. Nat. Inst. Polar Res.*, **3**, 29, 1974.

Fenn, R.W., S.A. Clough, W.O. Gallery, R.E. Good, F.X. Kneizys, J.D. Mill, L.S. Rothman, E.P. Shettle, and F.E. Volz, Optical and infrared properties of the atmosphere, Chapter 18, Table 18-14, p. 18-68, in *Handbook of geophysics and the space environment*, Ed. by A.S. Jursa, Air Force Geophysics Laboratory, U.S.A.F., Cambridge, Mass., 1985.

Forsyth, R.J., and P.C. Wraight, A survey of research on nightglow variability, *Planet. Space Sci.*, **35**, 1449, 1987.

Frank, L.A., and K.L. Ackerson, Observations of charged particle precipitation into the auroral zone, *J. Geophys. Res.*, **76**, 3612, 1971.

Frank, L.A., and J.D. Craven, Imaging results from Dynamics Explorer 1, *Rev. Geophys.*, **26**, 249, 1988.

Frank, L.A., J.D. Craven, K.L. Ackerson, M.R. English, R.H. Eather, and R.L. Carovillano, Global auroral imaging instrumentation for the Dynamics Explorer Mission, *Space Sci. Instrum.*, **5**, 369, 1981.

Frank, L.A., J.D. Craven, and R.L. Rairden, Images of the Earth's aurora and geocorona from the Dynamics Explorer mission, *Space Res.*, **5**, 53, 1985.

Fukunishi, H., Dynamic relationship between proton and electron auroral substorms, *J. Geophys. Res.*, **80**, 553, 1975.

Fukuyama, K., Airglow variations and dynamics in the lower thermosphere and upper mesosphere - II. Seasonal and long term variations, *J. Atmos. Terr. Phys.*, **39**, 1, 1977.

Gadsden, M., The Aurora Australis, pp. 403-428, in *Antarctica*, Ed. by T. Hatherton, Praeger, New York, 1962.

Gadsden, M., and E. Marovich, The nightglow continuum, *J. Atmos. Terr. Phys.*, **35**, 1601, 1973.

Gast, P.R., Thermal radiation, Chapter 16, pp. 16-1 to 16-32, in *Handbook of Geophysics*, U.S.A.F., Cambridge Research Centre, Cambridge, Mass., 1960.

Gattinger, R.L., F.R. Harris, and A. Vallance Jones, The height, spectrum, and mechanism of Type-B red aurora and its bearing on the excitation of O(^{1}S) in aurora, *Planet. Space Sci.*, 33, 207, 1985.

Gattinger, R.L., and A. Vallance Jones, The intensity ratios of auroral emission features, *Ann. Geophys.*, **28**, 91, 1972.

Gattinger, R.L., A. Vallance Jones, J.H. Hecht, D.L. Strickland, and J. Kelly, Comparison of ground-based optical observations of N_2 Second Positive to N_2^+ First Negative emission ratios with electron precipitation energies inferred from the Sondre Stromfjord Radar, *J. Geophys. Res.*, **96**, 11341, 1991.

Gerdjikova, M.G., and G.G. Shepherd, Evaluation of auroral 5577-Å excitation processes using Intercosmos Bulgaria 1300 satellite measurements, *J. Geophys. Res.*, **92**, 3367, 1987.

Ginsburg, V.L., L.V. Kurnosova, V.I. Logachev, A.A. Razorenov, I.A. Sirotkin, and M.I. Fradlin, Investigation of charged particle intensity during the flights of the second and third space ships, *Planet. Space Sci.*, **9**, 845, 1962.

Gledhill, J.A., Aeronomic effects of the South Atlantic anomaly, *Rev. Geophys. Space Phys.*, 14, 173, 1976.

Gledhill, J.A., Electron precipitation during the magnetospheric substorm on 27 July 1979, *S. Afr. J. Phys.*, 7, 33, 1984.

Gledhill, J.A., I.S. Dore, C.K. Goertz, R. Haggard, W.J. Hughes, M.W.J. Scourfield, D.P. Smits, P.H. Stoker, P.R. Sutcliffe, P.A. Wakerley, and A.D.M. Walker, A magnetospheric substorm observed at Sanae, Antarctica, *J. Geophys. Res.*, **92**, 2461, 1987.

Gledhill, J.A., I.S. Dore, G.P. Evans, R. Haggard, M.A. Abdu, Y. Sahai, and A.J. Foppiano, Aeronomic effects of charged particle precipitation in the South Atlantic Anomaly: The Project Isaac Cruise, Unpublished report, 1988.

Gledhill, J.A., and R.A. Hoffman, Nighttime observations of 0.2- to 26-keV electrons in the South Atlantic anomaly made by Atmospheric Explorer C, *J. Geophys. Res.*, **86**, 6739, 1981.

Gledhill, J.A., and H.O. van Rooyen, The South Atlantic geomagnetic anomaly and the radiation belts, *Proc. 5th Internat. Symp. on Space Technol. and Sci.*, Tokyo, 1003, 1963.

Gorney, D.J., U.S. Progress in auroral research: 1983-1986, *Rev. Geophys.*, **25**, 555, 1987.

Greenspan, D.J., Synoptic description of the 6300 Å nightglow near 78°west longitude, *J. Atmos. Terr. Phys.*, **28**, 739, 1966.

Greenspan, J.A., and C.A. Stone, The longitudinal variation of night airglow intensity in the region of the South Atlantic magnetic anomaly, *J. Geophys. Res.*, **69**, 465, 1964.

Grum, F., and G.W. Luckey, Optical sphere paint and a working standard of reflectance, *Appl. Opt.*, 7, 2289, 1968.

Gussenhoven, M.S., D.A. Hardy, and N. Heinemann, Systematics of the equatorward diffuse auroral boundary, *J. Geophys. Res.*, **88**, 5692, 1983.

Guttman, A., Extinction coefficient measurements on clear atmospheres and thin cirrus clouds, *Appl. Opt.*, **7**, 2377, 1968.

Hakura, Y., Tables and maps of geomagnetic coordinates corrected by the Higher order spherical harmonic terms, *Rep. Ionos. Space Res. Japan*, **19**, 121, 1965.

Hamm, F.M., T. Monaci, J.L. Steyn, and P.B. Zeeman, 'n Outomatiese meridiaanfotometer vir luggloed- en aurorawaarnemings in Antarktika (An automatic meridian-photometer for airglow and auroral observations in Antarctica), *Tydskrif vir Natuurwetenskappe*, **13**, 147, 1973.

Hamm, F.M., C.U. Schulz, and P.B. Zeeman, *Airglow Data, SANAE, Antarctica, 1974*, Report No. 75/S/2, Merensky Institute of Physics, University of Stellenbosch, South Africa, 1975.

Hartz, T.R., and N.M. Brice, The general pattern of auroral particle precipitation, *Planet. Space Sci.*, **15**, 301, 1967.

Harrison, A.W., Recent observations of the auroral spectrum between 1.02μ and 1.13μ, *Can. J. Phys.*, **47**, 599, 1969.

Hayes, D.S., and D.W. Latham, A rediscussion of the atmospheric extinction and the absolute spectral energy distribution of Vega, *Astrophys. J.*, **197**, 593, 1975.

Hays, P.B., and C.D. Anger, Influence of ground scattering on satellite auroral observations, *Appl. Opt.*, **17**, 1898, 1978.

Hays, P.B., G.R. Carignan, B.C. Kennedy, G.G. Shepherd, and J.C.G. Walker, The visible airglow experiment on Atmospheric explorer, *Radio Sci.*, **8**, 369, 1973.

Helliwell, R.A., S.B. Mende, J.H. Doolittle, W.C. Armstrong, and D.L. Carpenter, Correlations between λ4278 optical emissions and VLF wave events observed at L $\sim$ 4 in the Antarctic, *J. Geophys. Res.*, **85**, 3376, 1980.

Henriksen, K., Absolute calibration of auroral photometers and ground-based measurements in the 3200-7500 Å spectral region, *Appl. Opt.*, **13**, 1196, 1974.

Hernandez, G., Contamination of the OI ($^3P_2$ - $^1D_2$) emission line by the (9-3) band of the OH $X^2\Pi$ in high resolution measurements of the night sky, *J. Geophys. Res.*, **79**, 1119, 1974.

Hernandez, G., Analytical description of a Fabry-Perot spectrometer, 7: TESS. a high-luminosity high-resolution twin-etalon scanning spectrometer, *Appl. Opt.*, **21**, 507, 1982a.

Hernandez, G., Vertical motions of the neutral thermosphere at mid-latitudes, *Geophys. Res. Lett.*, **9**, 555, 1982b.

Hernandez, G., and T.L. Killeen, Optical measurements of winds and kinetic temperatures in the upper atmosphere, *Space Res.*, **8**, 149, 1988.

Hernandez, G., and O.A. Mills, Feedback stabilized Fabry-Perot interferometer, *Appl. Opt.*, **12**, 126, 1973.

Hernandez, G., O.A. Mills, and J.L. Smith, TESS: A high-luminosity high-resolution twin-etalon scanning spectrometer, *Appl. Opt.*, **20**, 3687, 1981.

Hernandez, G., and R.G. Roble, Thermospheric dynamics investigations with very high resolution spectrometer, *Appl. Opt.*, **18**, 3376, 1979.

Hernandez, G., and R.G. Roble, The geomagnetic quiet nighttime thermospheric wind pattern over Fritz Peak Observatory during solar cycle minimum and maximum, *J. Geophys. Res.*, **89**, 327, 1984.

Hess, W.N., *The radiation belt and magnetosphere*, Blaisdell Publishing Company, Waltham, Mass., 1968.

Hill, T.W., and G.L. Siscoe, The other side of the substorm, *Eos Trans. AGU*, **66**, 577, 1985.

Hilliard, R.L., and G.G. Shepherd, Wide-angle Michelson Interferometer for measuring Doppler line widths, *J. Opt. Soc Am.*, **56**, 362, 1966a.

Hilliard, R.L., and G.G. Shepherd, Upper atmosphere temperatures from Doppler line widths. IV: A detailed study using the OI 5577 Å auroral and nightglow emission, *Planet. Space Sci.*, **14**, 383, 1966b.

Holzworth, R.H., and C.-I. Meng, Mathematical representation of the auroral oval, *Geophys. Res. Lett.*, **2**, 377, 1975.

Hones, E.W., Jr., Transient phenomena in the magnetotail and their relation to substorms, *Space Sci. Rev.*, **23**, 393, 1979a.

Hones, E.W., Jr., Plasma flow in the magnetotail and its implication for substorm theories, p. 545, in *Dynamics of the magnetosphere*, Ed. by S.-I. Akasofu, D. Reidel, Hingham, Mass., 1979b.

Hones, E.W., Jr. (Ed.), Plasma sheet behaviour during substorms, p. 178, in *Magnetic reconnection in space and laboratory*, Geophysical Monograph 30, AGU, Washington D.C., 1984.

Hopgood, P.A., *Measurements of [OI] 6300Å night-airglow from a mid-latitude station during solar minimum*, Ph.D. thesis, La Trobe University, Melbourne, Australia, 1976.

Hunten, D.M., E.G. Rawson, and J.K. Walker, Rapid measurements of N_2^+ rotational temperatures in aurora, *Can. J. Phys.*, **41**, 258, 1963.

Hunten, D.M., F.E. Roach, and J.W. Chamberlain, A photometric unit for the airglow and aurora, *J. Atmos. Terr. Phys.*, **8**, 345, 1956.

Huruhata, M., and J. Nakamura, Airglow observations on board the Soya, *Rep. Ionos. Res. Space Res. Jap.*, **11**, 35, 1957.

Iijima, T., and T.A. Potemra, Field-aligned currents in the dayside cusp observed by Triad, *J. Geophys. Res.*, **81**, 5971, 1976.

Iijima, T., and T.A. Potemra, Large-scale characteristics of field-aligned currents associated with substorms, *J. Geophys. Res.*, **83**, 599, 1978.

Jacka, F., Application of Fabry-Perot spectrometers for measurement of upper atmosphere temperatures and winds, *Middle Atmosphere Program Handbook* (ICSU-SCOSTEP), **13**, 19, 1984.

Johnson, R.G., R.E. Meyerott, and J.E. Evans, Coordinated satellite, ground-based and aircraft-based measurements on auroras, pp. 149-159, in *Aurora and Airglow*, Ed. by B.M. McCormac, Reinhold Publishing Company, New York, 1967.

Judge, R.J.R., Electron excitation and auroral emission parameters, *Planet. Space Sci.*, **20**, 2081, 1972.

Kamide, Y., The relationship between field-aligned currents and the auroral electrojets: A review, *Space Sci. Rev.*, 31, 127, 1982.

Kamide, Y., *Electrodynamic processes in the earth's ionosphere and magnetosphere*, Kyoto Sangyo University Press, Japan, 1988.

Kamide, Y., and S.-I. Akasofu, Latitudinal cross section of the auroral electrojet and its relation to the interplanetary magnetic field polarity, *J. Geophys. Res.*, **79**, 3755, 1974.

Kamide, Y., and S.-I. Akasofu, The auroral electrojet and global auroral features, *J. Geophys. Res.*, **80**, 3585, 1975.

Kan, J.R., Developing a global model of magnetospheric substorms, *Eos Trans. A.G.U.*, **71**, 1083, 1990.

Kan, J.R., R.L. Williams, and S.-I. Akasofu, A mechanism for the westward travelling surge during substorms, *J. Geophys. Res.*, **89**, 2211, 1984.

Kan, J.R., L. Zhu, and S.-I. Akasofu, A Theory of substorms: Onset and subsidence, *J. Geophys. Res.*, **93**, 5624, 1988.

Kasting, J.F., and P.B. Hays, A comparison between N_2^+ 4278 Å emission and electron flux in the auroral zone, *J. Geophys. Res.*, **82**, 3319, 1977.

Kilfoyle, B.P., and F. Jacka, Geomagnetic L coordinates, *Nature*, **220**, 773, 1968.

Killeen, T.L., Energetics and Dynamics of the Earth's Thermosphere, *Rev. Geophys.*, **25**, 433, 1987.

Killeen, T.L., and P.B. Hays, O(^{1}S) from dissociative recombination of O_2^+: Nonthermal line profile measurements from Dynamics Explorer, *J. Geophys. Res.*, **88**, 10163, 1983.

Knecht, D.J., and B.M. Shuman, The geomagnetic field, Chapter 4, pp. 4-1 to 4-37, in *The handbook of geophysics and the space environment*, Ed. by A.S. Jursa, Air Force Geophysics Laboratories, U.S.A.F., Cambridge, Mass., 1985.

Kok, C.J., Private communication (The calibration certificate for the two standard lamps calibrated by the NPRL of the CSIR, Pretoria, South Africa), 1984.

Krassovsky, V.I., N.N. Shevov, and V.I. Yarin, Atlas of the airglow spectrum 3000 - 12400 Å, *Planet. Space Sci.*, **9**, 883, 1962.

Kulkarni, P.V., A direct-calibrating type night airglow photometer, *Ann. Geophys.*, **25**, 747, 1969.

Lambert, S., *Corrections for geometric and atmospheric effects of Photometric observations of aurora*, Internal Research Report, Series V, No. 23, Magnetic Observatory of the CSIR, Hermanus, South Africa, 1980.

Lambert, S., and P.R. Sutcliffe, Photometric Observations of proton aurora at Sanae, *J. Atmos. Terr. Phys.*, **43**, 355, 1981.

Langford, A.O., V.M. Bierbaum, and S.R. Leone, Auroral implications of recent measurements on O(^{1}S) and O(^{1}D) formation on the reaction of N^+ with O_2, *Planet. Space Sci.*, **33**, 1225, 1985.

Lauche, H., Observations of the oxygen green line airglow during the winter anomaly campaign 1975/76, *J. Geophysics*, **44**, 35, 1977.

Lincoln, J.V., Geomagnetic Indices, pp. 67-100, in *Physics of geomagnetic phenomena*, Ed. by S. Matsushita and W.H. Campbell, Academic Press, New York, 1967.

Lui, A.T.Y., A synthesis of magnetospheric substorm models, *J. Geophys. Res.*, **96**, 1849, 1991.

Lui, A.T.Y., and C.D. Anger, A uniform belt of diffuse auroral emission seen by the Isis-2 scanning photometer, *Planet. Space Sci.*, **21**, 799, 1973.

Lui, A.T.Y., C.D. Anger, and S.-I. Akasofu, The equatorward boundary of the diffuse aurora and auroral substorms as seen by the Isis 2 auroral scanning photometer, *J. Geophys. Res.*, **80**, 3603, 1975a.

Lui, A.T.Y., C.D. Anger, D. Venkatesan, W. Sawchuk, and S.-I. Akasofu, The topology of the auroral oval as seen by the Isis 2 scanning auroral photometer, *J. Geophys. Res.*, **80**, 1795, 1975b.

Lui, A.T.Y., P. Perreault, S.-I. Akasofu, and C.D. Anger, The diffuse aurora, *Planet. Space Sci.*, **21**, 857, 1973.

Lummerzheim, D., M.H. Rees, and G.J. Romick, The application of spectroscopic studies of the aurora to the thermospheric neutral composition, *Planet. Space Sci.*, **38**, 67, 1990.

Lummerzheim, D., M.H. Rees, J.D. Craven, and L.A. Frank, Ionospheric conductances derived from DE-1 auroral images, *J. Atmos. Terr. Phys.*, **53**, 281, 1991.

Maclennan, C.G., L.J. Lanzerotti, S.-I. Akasofu, A.N. Zaitzev, P.J. Wilkinson, A. Wolfe, and V. Popov, Comparison of 'electrojet' indices from the northern and southern hemispheres, *J. Geophys. Res.*, **96**, 267, 1991.

Mahadevan, P., and F.E. Roach, Mechanism for the auroral emission of OI (6300Å), *Nature*, **220**, 150, 1968.

Markham, T.P., and R.E. Anctil, Airborne night airglow measurements in the South Atlantic magnetic anomaly, *J. Geophys. Res.*, **71**, 997, 1966.

Mayaud, P.N., *Derivation, meaning, and use of geomagnetic indices*, Geophysical Monograph 22, AGU, Washington D.C., 1980.

McDade, I.C., and E.J. Llewellyn, A comment on the proposed mechanisms for the excitation of $O(^1S)$ in the aurora, *Planet. Space Sci.*, **32**, 1195, 1984.

McDade, I.C., and E.J. Llewellyn, The excitation of $O(^1S)$ and O_2 bands in the nightglow: A brief review and preview, *Can. J. Phys.*, **64**, 1626, 1986.

McDade, I.C., D.P. Murtagh, R.G.H. Greer, P.H.G. Dickinson, G. Witt, J. Stegman, E.J. Llewellyn, L. Thomas, and D.B. Jenkins, Eton 2: Quenching parameters for the proposed precursors of $O_2(b^1\Sigma_u^+)$ and $O(^1S)$ in the terrestrial nightglow, *Planet. Space Sci.*, **34**, 789, 1986.

McEwen D.J., and C.N. Duncan, A campaign to study pulsating aurora, *Can. J. Phys.*, **59**, 1029, 1981.

McIlwain, C.E., Coordinates for mapping the distribution of magnetically trapped particles, *J. Geophys. Res.*, **66**, 3681, 1961.

McPherron, R.L., Growth phase of magnetospheric substorms, *J. Geophys. Res.*, **75**, 5592, 1970.

McPherron, R.L., Substorm related changes in the magnetotail: The growth phase, *Planet. Space Sci.*, **20**, 1521, 1972.

McPherron, R.L., Magnetospheric Substorms, *Rev. Geophys. Space Phys.*, **17**, 657, 1979.

McPherron, R.L., C.T. Russell, and M.P. Aubry, Satellite studies of magnetospheric substorms on August 15, 1968, 9, Phenomenological model for substorms, *J. Geophys. Res.*, **78**, 3131, 1973.

Meier, R.R., Thermospheric aurora and airglow, *Rev. Geophys.*, **25**, 471, 1987.

Mende, S.B., P.M. Banks, R. Nobles, O.K. Garriott, and J. Hoffman, Photographic observations of earth's airglow from space, *Geophys. Res. Lett.*, **10**, 1108, 1983a.

Mende, S.B., and R.H. Eather, Spectroscopic determination of the characteristics of precipitating auroral particles, *J. Geophys. Res.*, **80**, 3211, 1975.

Mende, S.B., and R.H. Eather, Monochromatic all-sky observations and auroral precipitation patterns, *J. Geophys. Res.*, **81**, 3771, 1976.

Mende, S.B., O.K. Garriott, and P.M. Banks, Observations of optical emissions on STS-4, *Geophys. Res. Lett.*, **10**, 122, 1983b.

Mende, S.B., R.H. Eather, M.H. Rees, R.R. Vondrak, and R.M. Robinson, Optical mapping of ionospheric conductance, *J. Geophys. Res.*, **89**, 1755, 1984.

Meng, C.-I., Electron precipitations and polar aurora, *Space Sci. Rev.*, **22**, 223, 1978.

Menvielle, M., and A Berthelier, The K-derived planetary indices: description and availability, *Rev. Geophys.*, **29**, 413, 1991.

Menzies, J., Private communication, (South African Astronomical Observatory), 1985.

Meriwether, J.W., Jr., Measurement of weak airglow emissions with a programmable scanning spectrometer, *Planet. Space Sci.*, **27**, 1221, 1979.

Meriwether, J.W., Jr., Observations of thermospheric dynamics at high latitudes from ground and space, *Radio Sci.*, **18**, 1035, 1983.

Meriwether, J.W., Jr., Ground-based measurements of mesosphere temperatures by optical means, *Middle Atmosphere Program Handbook* (ICSU-SCOSTEP), **13**, 1, 1984.

Meriwether, J.W., Jr., W.M. Benesch, and S.G. Tilford, Characteristics of a visual aurora following a solar flare, *Planet. Space Sci.*, **18**, 525, 1970.

Meriwether, J.W., Jr., and J.C. G. Walker, First negative band system on the night sky over Arecibo during geomagnetic storms, *J. Geophys. Res.*, **85**, 1279, 1980.

Montbriand, L.E., A simple method for calculating the local time of corrected geomagnetic midnight, *J. Geophys. Res.*, **75**, 5634, 1970.

Montbriand, L.E., The proton aurora and auroral substorm, pp. 366-373, in *The radiating atmosphere*, Ed. by B.M. McCormac, D. Reidel, Dordrecht, Holland, 1971.

Morton, G.A., Photon counting, *Appl. Opt.*, **7**, 1, 1968.

Nagata, T., T. Hirasawa, and M. Ayukawa, Auroral oval and polar substorms observed by a satellite and ground-based observations in Antarctica, in Proceedings of IAGA meeting on unmanned observatories in Antarctica, *Mem. Nat. Inst. Polar Res.*, **6**, 25, 1976.

Nakamura, J., Latitude effect of night airglow, *Rep. Ionos. Res. Space Res. Jap.*, **12**, 419, 1958.

Niciejewski, R.J., and P.A. Forsyth, Auroral influence on ionospheric electron content, *Can. J. Phys.*, **66**, 175, 1988.

Niciejewski, R.J., J.W. Meriwether, Jr., A. Vallance Jones, R.L. Gattinger, C.E. Valladares, V.B. Wickwar, and J. Kelly, Ground-based observations of O_2^+ 1N band enhancements relative to N_2^+ 1N band emission, *Planet. Space Sci.*, **37**, 131, 1989.

O'Brien, B.J., and H. Taylor, High-latitude geophysical studies with satellite INJUN-3, 4. Auroras and their excitation, *J. Geophys. Res.*, **69**, 45, 1964.

Omholt, A., *The optical aurora*, Springer-Verlag, Berlin, 1971.

Parkinson, T.D., and E.C. Zipf, Energy transfer from $N_2(A^3\Sigma_u^+)$ as a source of $O(^1S)$ in the aurora, *Planet. Space Sci.*, **18**, 895, 1970.

Paulson, K.V., H. Chang, and G.G. Shepherd, The evaluation of the time-varying parameters pertinent to the excitation of $O(^1S)$ in aurora, *Planet. Space Sci.*, **38**, 161, 1990.

Peterson, V.L., and W.R. Steiger, F-region nightglow emissions of atomic oxygen 2. Analysis of 6300 Å and electron density data, *J. Geophys. Res.*, **71**, 2267, 1966.

Perrault, P., and S.-I. Akasofu, A study of magnetic storms, *Geophys. J. R. Astro. Soc.*, **54**, 547, 1978.

Pike, C.P., and J.A. Whalen, Satellite observations of auroral substorms, *J. Geophys. Res.*, **79**, 985, 1974.

Pike, C.P., J.A. Whalen, and J. Buchau, A 12-hour case study of auroral phenomena in the midnight local time sector: F layer and 6300 Å measurements, *J. Geophys. Res.*, **82**, 3547, 1977.

Ranade, N., P.B. Choudhary, and A.D. Tillu, 5577 Å and 5893 Å emissions in the lower thermosphere and their dynamic coupling, *Phys. Scr.*, **37**, 496, 1988.

Reed, E.I., and J.E. Blamont, Some results concerning the principal airglow lines as measured from the OGO-II satellite, *Space Res.*, **7**, 337, 1966.

Reed, E.I., and S. Chandra, The global characteristics of atmospheric emissions in the lower thermosphere and their aeronomic implications, *J. Geophys. Res.*, **80**, 3053, 1975.

Rees, M.H., *Absolute photometry of the aurora*, Ph.D. thesis, University of Colorado, Boulder, Colorado, 1958.

Rees, M.H., Spectroscopic diagnostics of the formation of auroral arcs, pp. 50-55, in *The physics of auroral arc formation*, Ed. by S.-I. Akasofu and J.R. Kan, Geophysical monograph 25, AGU, Washington D.C., 1981.

Rees, M.H., On the interaction of auroral protons with the earth's atmosphere, *Planet. Space Sci.*, **30**, 463, 1982.

Rees, M.H., Auroral excitation and energy dissipation, pp. 753-780, in *Solar-terrestrial physics*, Ed. by R.L Carovillano and J.M. Forbes, D. Reidel, Dordrecht, Holland, 1983.

Rees, M.H., Excitation of $O(^1S)$ and emission of 5577 Å radiation in aurora, *Planet. Space Sci.*, **32**, 373, 1984a.

Rees, M.H., Reply to I.C. McDade and E.J. Llewellyn's comments on proposed mechanisms for the excitation of $O(^1S)$ in the aurora, *Planet. Space Sci.*, **32**, 1199, 1984b.

Rees, M.H., *Physics and chemistry of the upper atmosphere*, Cambridge University Press, Cambridge, 1989a.

Rees, M.H., Antarctic upper atmosphere investigations by optical methods, *Planet. Space Sci.*, **37**, 955, 1989b.

Rees, M.H., and V.J. Abreu, Auroral photometry from the Atmospheric Explorer satellite, *J. Geophys. Res.*, **89**, 317, 1984.

Rees, M.H., and P.C. Benedict, The auroral proton oval, *J. Geophys. Res.*, **75**, 4763, 1970.

Rees, M.H., and D. Luckey, Auroral electron energy derived from ratio of spectroscopic emissions 1. Model computations, *J. Geophys. Res.*, **79**, 5181, 1974.

Rees, M.H., and D. Lummerzheim, Characteristics of auroral electron precipitation derived from optical spectroscopy, *J. Geophys. Res.*, **94**, 6799, 1989.

Rees, M.H., D. Lummerzheim, R.G. Roble, J.D. Winningham, J.D. Craven, and L.A. Frank, Auroral energy deposition rate, characteristic electron energy, and ionospheric parameters derived from Dynamics Explorer 1 images, *J. Geophys. Res.*, **93**, 12841, 1988.

Rees, M.H., and R.G. Roble, Excitation of O(^{1}D) atoms in aurora and emission of the [OI] 6300-Å line, *Can. J. Phys.*, **64**, 1608, 1986.

Rees, M.H., R.G. Roble, J. Kopp, V.J. Abreu, L.H. Brace, H.C. Brinton, R.A. Heelis, R.A. Hoffman, D.C Kayser, and D. W. Rusch, The spatial-temporal ambiguity in auroral modelling, *J. Geophys. Res.*, **85**, 1235, 1980.

Rees, M.H., G.G. Sivjee, and K.A. Dick, Studies of molecular nitrogen bands from airborne auroral spectroscopy, *J. Geophys. Res.*, **81**, 6046, 1976.

Rees, M.H., A.I. Stewart, W.E. Sharp, P.B. Hays, R.A. Hoffman, L.H. Brace, J.P Doering, and W.K. Peterson, Coordinated rocket and satellite measurements of an auroral event, 1. Satellite observations and analysis, *J. Geophys. Res.*, **82**, 2250, 1977.

Richards, P.G., and D.G. Torr, Auroral modelling of the 3371 Å emission rate: Dependence on characteristic electron energy, *J. Geophys. Res.*, **95**, 11337, 1990.

Roach, F.E., Photometric observations of the airglow during the IQSY, *IQSY Instruction Manual No. 5, AIRGLOW*, CIG-ISQY Committee, London, 1963.

Roach, F.E., L.R. Megill, M.H. Rees, and E. Marovich, The height of the nightglow 5577, *J. Atmos. Terr. Phys.*, **12**, 171, 1958.

Roach, F.E., and A.B. Meinel, The height of the nightglow by the van Rhijn Method, *Astrophys. J.*, **122**, 530, 1955.

Roach, F.E., and L.L. Smith, The worldwide morphology of the atomic oxygen nightglows, pp. 29-39, in *Aurora and Airglow*, Ed. by B.M. McCormac, Reinhold Publishing Company, New York, 1967.

Robertson, G.T., *Airglow photometer observations and inter-relations between auroral activity and other upper atmosphere phenomena observed at Sanae, Antarctica, 1964*, M.Sc. thesis, University of Stellenbosch, South Africa, 1966.

Roederer, J.G., Geomagnetic field distortions and their effects on radiation belt particles, *Rev. Geophys. Space Phys.*, **10**, 599, 1972.

Rohrbaugh, R.P., B.A. Tinsley, H. Rassoul, Y. Sahai, N.R. Teixeira, R.G. Tull, D.R. Doss, A.L. Cochran, W.D. Cochran, and E.S. Barker, Observations of optical emissions from particle precipitation of energetic neutral atoms and ions from the ring current, *J. Geophys. Res.*, **88**, 6317, 1983.

Romick, G.J., and A.E. Belon, *The determination of the spatial distribution of auroral luminosity*, Final Report; NSF G15725, National Science Foundation, Washington D.C., 1964.

Romick, G.J., and A.E. Belon, The spatial variation of auroral luminosity - II. Determination of volume emission rate profiles, *Planet. Space Sci.*, **15**, 1695, 1967.

Rostoker, G., Geomagnetic Indices, *Rev. Geophys.*, **10**, 935, 1972.

Rostoker, G., A quantitative relationship between AE and Kp, *J. Geophys. Res.*, **96**, 5853, 1991.

Rostoker, G., S.-I. Akasofu, J. Foster, R.A. Greenwald, Y. Kamide, K. Kawasaki, A.T.Y. Lui, R.L. Mcpherron, and C.T. Russell, Magnetospheric Substorms - Definition and signatures, *J. Geophys. Res.*, **85**, 1663, 1980.

Rostoker, G., S.-I. Akasofu, W. Baumjohann, Y. Kamide, and R.L. McPherron, The role of direct input of energy from the solar wind and unloading of stored magnetotail energy in driving magnetospheric substorms, *Space Sci. Rev.*, **46**, 93, 1987.

Rusch, D.W., J.-C. Gerard, and W.E. Sharp, The reaction of N(^{2}D) with O_2 as a source of O(^{1}D) atoms in aurora, *Geophys. Res. Lett.*, **5**, 1043, 1978.

Russell, C.T., Explosive reconnection: Red herring or paradigm lost?, *Eos Trans. AGU*, **66**, 581, 1985.

Russell, C.T., and R.L. McPherron, The magnetotail and substorms, *Space Sci. Rev.*, **15**, 205, 1973.

Sahai, Y., J.A. Bittencourt, H. Takahashi, N.R. Teixeira, J.H.A. Sobral, B.A. Tinsley, and R.P. Rohrbaugh, Multispectral optical observations of ionospheric F-region storm effects at low latitude, *Planet. Space Sci.*, **36**, 371, 1988a.

Sahai, Y., H. Takahashi, J.A. Bittencourt, J.H.A. Sobral, and N.R. Teixeira, Solar cycle and seasonal variations of the low latitude OI 630 nm nightglow, *J. Atmos. Terr. Phys.*, **50**, 135, 1988b.

Sandford, B.P., The behaviour of night-sky 6300, 5577 and 3914 Å emissions at Scott Base, Antarctica, *J. Atmos. Terr. Phys.*, **21**, 182, 1961.

Sandford, B.P., Aurora and airglow intensity variations with time and magnetic activity at southern high latitudes, *J. Atmos. Terr. Phys.*, **26**, 749, 1964.

Sandford, B.P., Optical emissions in the polar cap, pp. 299-321, in *The polar ionosphere and magnetospheric processes*, Ed. by G. Skovli, Gordon and Breach Science Publishers, Inc., New York, 1970.

Saskind, D.E., and W.E. Sharp, A comparison of measurements of the oxygen nightglow and atomic oxygen in the lower thermosphere, *Planet. Space Sci.*, **39**, 627, 1991.

Sauvaud, J.A., J.P. Treilhou, A. Saint-Marc, J. Dandouras, H. Reme, A. Korth, G. Kremser, G.K. Parks, A.N. Zaitzev, V. Petrov, L. Lazutine, and R. Pellinen, Large scale response of the magnetosphere to a southward turning of the interplanetary magnetic field, *J. Geophys. Res.*, **92**, 2365, 1987.

Sawchuck, W., *Measurements of the intensity ratio I5577/I3914 in auroras using a scanning photometer*, Ph.D. thesis, University of Calgary, Canada, 1973.

Sawchuck, W., and C.D. Anger, A dual wavelength ground-based auroral scanner, *Planet. Space Sci.*, **20**, 1935, 1972.

Sawchuck, W., and C.D. Anger, Intensity ratio I(5577)/I(3914) in type B red aurora, *Planet. Space Sci.*, **24**, 893, 1976a.

Sawchuck, W., and C.D. Anger, Intensity ratio I(5577)/I(3914) in morning and evening pulsating aurora, *Planet. Space Sci.*, **24**, 896, 1976b.

Scourfield, M.W.J., *Fast temporal and spatial variations in pulsating auroras*, Ph.D. thesis, University of Calgary, Canada, 1970.

Scourfield, M.W.J., and N.R. Parsons, An image intensifier-vidicon system for auroral cinematography, *Planet. Space Sci.*, **17**, 75, 1969.

Scourfield, M.W.J., and N.R. Parsons, Television imaging of fast auroral waves, *Planet. Space Sci.*, **19**, 437, 1971.

Sharp, W.E., M.H. Rees, and A.I. Stewart, Coordinated rocket and satellite measurements of an auroral event, 2. The rocket observations and analysis, *J. Geophys. Res.*, **84**, 1977, 1979.

Sheehan, R.E., and R.L. Carovillano, Characteristics of the equatorward auroral boundary near midnight determined from DMSP images, *J. Geophys. Res.*, **83**, 4749, 1978.

Shemansky, D.E., and A.L. Broadfoot, Excitation of N_2 and N_2^+ systems by electrons. I: Absolute transition probabilities, *J. Quant. Spectrosc. Radiat. Transfer*, 11, 1385, 1971.

Shepherd, G.G., Optical remote sensing of the polar upper atmosphere, pp. 149-158, in *Exploration of the polar upper atmosphere*, Ed. by C.S. Deehr and J.A. Holtet, D. Reidel, Dordrecht, Holland, 1981.

Shepherd, G.G., and R.H. Eather, On the determination of auroral electron energies and fluxes from optical spectral measurements, *J. Geophys. Res.*, **81**, 1407, 1976.

Shepherd, G.G., T. Fancott, J. McNally, and H.S. Kerr, ISIS-II atomic oxygen red line photometer, *Appl. Opt.*, **12**, 1767, 1973.

Silverman, S.M., Night airglow phenomenology, *Space Sci. Rev.*, **11**, 341, 1970.

Siskind, D.E., and W.E. Sharp, A comparison of measurements of the oxygen nightglow and atomic oxygen in the lower thermosphere, *Planet. Space Sci.*, **39**, 627, 1991.

Slater, D.W., L.L. Smith, and E.W. Kleckner, Correlated observations of the equatorward diffuse auroral boundary, *J. Geophys. Res.*, **85**, 531, 1980.

Smith, F.L., and C. Smith, Numerical evaluation of Chapman's grazing incidence integral ch(x/χ), *J. Soc. Res.*, **77**, 3502, 1972.

Smith, L.L., and W.R. Steiger, Night airglow intensity variations in the [OI] 5577 Å, [OI] 6300 Å, and NaI 5890-5896 Å emission lines, *J. Geophys. Res.*, **73**, 2531, 1968.

Smith, R.W., D. Rees, and R.D. Stewart, Southern hemisphere thermospheric dynamics: A review, *Rev. Geophys.*, **26**, 591, 1988.

Solheim, B.H., and E.J. Llewellyn, An indirect mechanism for the production of O(^{1}S) in the aurora, *Planet. Space Sci.*, **27**, 473, 1979.

Solomon, S.C., Auroral excitation of the N_2 2PG (0,0) and VK (0,9) bands, *J. Geophys. Res.*, **94**, 17215, 1989.

Solomon, S.C., P.B. Hays, and V.J. Abreu, Tomographic inversion of satellite photometry, *Appl. Opt.*, **23**, 3409, 1984.

Solomon, S.C., P.B. Hays, and V.J. Abreu, The auroral 6300 Å emission: Observations and modeling, *J. Geophys. Res.*, **93**, 9867, 1988.

Spjeldvik, W.N., and P.L. Rothwell, The radiation belts, Chapter 5, p. 5.9, in *Handbook of geophysics and the space environment*, Ed. by A.S. Jursa, Air Force Geophysics Laboratory, U.S.A.F., Cambridge, Mass., 1985.

Srivastava, V., and V. Singh, Model calculations of $O(^1S)$ and $O(^1D)$ emissions under proton bombardment, *J. Geophys. Res.*, **93**, 5855, 1988.

Starkov, G.V., Analytical representation of the equatorward boundary of the auroral oval zone, *Geomagn. & Aeron.*, **9**, 614, 1969.

Steele, D.P., and D.J. McEwen, Electron auroral excitation efficiencies and intensity ratios, *J. Geophys. Res.*, **95**, 10321, 1990.

Stegman, J., and D.P. Murtagh, High resolution spectroscopy of oxygen u.v. airglow, *Planet. Space Sci.*, **36**, 927, 1988.

Steiger, W.R., Low latitude observations of airglow, pp. 419-433, in *Aurora and Airglow*, Ed. by B.M. McCormac, Reinhold Publishing Company, New York, 1967.

Stern, D.P., Electric currents and voltage drops along auroral field lines, *Space Sci. Rev.*, **34**, 317, 1983.

Steyn, J.L., *Emission of 6300 and 5577Å airglow lines of atomic oxygen in equatorial regions*, Ph.D. thesis, University of Stellenbosch, South Africa, 1973.

Steyn, J.L., P.B. Zeeman, and F.M. Hamm, Airglow enhancements near the equator, *Planet. Space Sci.*, **19**, 672, 1971a.

Steyn, J.L., P.B. Zeeman, and F.M. Hamm, *Airborne Airglow Observations, July 1971*, Merensky Institute for Physics, University of Stellenbosch, South Africa, 1971b.

Steyn, J.L., P.B. Zeeman, F.M. Hamm, C.U. Schulz, and M.M. Hallatt, *Airglow Data, SANAE, Antarctica, 1970*, Report No. 73/S/1, Merensky Institute for Physics, Stellenbosch University, South Africa, 1973.

Stott, I.P., and B.A. Thrush, Laboratory studies of the mechanism of the oxygen airglow, *Proc. R. Soc. Lond. A Series*, **424**, 1, 1989.

Strickland, D.J., R.R. Meier, J.H. Hecht, and A.B. Christensen, Deducing composition and incident electron spectra from ground-based auroral optical measurements: Theory and model results, *J. Geophys. Res.*, **94**, 13527, 1989.

Sutcliffe, P.R., and D.P. Smits, Proton aurora during the magnetospheric substorm of 27 July 1979, *S. Afr. J. Phys.*, **7**, 20, 1984.

Sutcliffe, P.R., D.P. Smits, A.D.M. Walker, W.J. Hughes, and C.K. Goertz, Magnetic signatures during the magnetospheric substorm of 27 July 1979, *S. Afr. J. Phys.*, **7**, 7, 1984.

Swider, W., The determination of the optical depth at large solar zenith distances, *Planet. Space Sci.*, **12**, 761, 1964.

Swift, D.W., Substorms and magnetospheric energy transfer processes, p. 327, in *Dynamics of the magnetosphere*, Ed. by S.-I. Akasofu, D. Reidel, Hingham, Mass., 1980.

Thuillier, G., J. Christophe, C. Dousset, and M. Fehrenbach, Auroral occurrence from 1963-1970 as observed at Dumont D'urville station, *Ann. Geophys. Ser. A.*, **4**, 247, 1986.

Tibbenham, M.I., M.W.J. Scourfield, and P.A. Wakerley, An improved television system for auroral cinematography at Sanae, Antarctica, *S. Afr. J. Phys.*, **7**, 69, 1984.

Tinsley, B.A., and R.G. Burnside, Precipitation of energetic neutral hydrogen atoms at Arecibo during a magnetic storm, *Geophys. Res. Lett.*, **8**, 87, 1981.

Tinsley, B.A., R.P. Rohrbaugh, Y. Sahai, and N.R. Teixeira, Energetic oxygen precipitation as a source of vibrationally excited N_2^+ in emissions observed at low latitudes, *Geophys. Res. Lett.*, **9**, 543, 1982.

Torr, D.G., and W.E. Sharp, The concentration of atomic oxygen in the auroral lower thermosphere, *Geophys. Res. Lett.*, **6**, 860, 1979.

Torr, D.G., M.R. Torr, J.C.G. Walker, and R.A. Hoffman, Particle precipitation in the South Atlantic geomagnetic anomaly, *Planet. Space Sci.*, **23**, 15, 1975.

Torr, M.R., Night-time enhancements in the 6300 Å line at Sanae and the relationship to the movement of the auroral oval, *Ann. Geophys.*, **27**, 201, 1971.

Torr, M.R., Private communication, 1985.

Torr, M.R., R.G. Burnside, P.B. Hays, A.I. Stewart, D.G. Torr, and J.C.G. Walker, Metastable ^2D atomic nitrogen in the mid-latitude nocturnal ionosphere, *J. Geophys. Res.*, **81**, 531, 1976a.

Torr, M.R., P.B. Hays, B.C. Kennedy, and D.G. Torr, Discussion of a significant photometer calibration error using extended standard sources, *Appl. Opt.*, **15**, 600, 1976b.

Torr, M.R., P.B. Hays, B.C. Kennedy, and J.C.G. Walker, Intercalibration of airglow observations with the *Atmosphere Explorer* satellite, *Planet. Space Sci.*, **25**, 173, 1977.

Torr, M.R., and D.G. Torr, Discussion of letter by Robert T. Bennett 'Latitude dependence of 6300 Å (OI) twilight airglow enhancement', *J. Geophys. Res.*, **74**, 5187, 1969.

Torr, M.R., and D.G. Torr, OI and N_2^+ emissions observed at Sanae, *S. Afr. J. Ant. Res.*, **1**, 24, 1971.

Torr, M.R., and D.G. Torr, The role of metastable species in the thermosphere, *Rev. Geophys. Space Phys.*, **20**, 91, 1982.

Torr, M.R., and D.G. Torr, Energetic oxygen in a mid-latitude aurora, *J. Geophys. Res.*, **89**, 5547, 1984.

Vallance Jones, A., Auroral spectroscopy, *Space Sci. Rev.*, **11**, 776, 1971.

Vallance Jones, A., *Aurora*, D. Reidel, Dordrecht, Holland, 1974.

Vallance Jones, A., Private communication, 1991.

Vallance Jones, A., F. Creutzberg, R.L. Gattinger, and F.R. Harris, Auroral studies with a chain of meridian scanning photometers, 1. Observations of proton and electron aurora in magnetospheric substorms, *J. Geophys. Res.*, **87**, 4489, 1982.

Vallance Jones, A., and R.L. Gattinger, TV morphology of some episodes of pulsating aurora, *Can. J. Phys.*, **59**, 1077, 1981.

Vallance Jones, A., R.L. Gattinger, F. Creutzberg, R.A. King, P. Prikryl, L.L. Cogger, D.J. McEwen, F.R. Harris, C.D. Anger, J.S. Murphree, and R.A. Koehler, A comparison of CANOPUS ground optical data with images from the Viking UV camera, *Geophys. Res. Lett.*, **14**, 391, 1987a.

Vallance Jones, A., R.L. Gattinger, P. Shih, J.W. Meriwether, Jr., V.B. Wickwar, and J. Kelly, Optical and radar characteristics of a short-lived event at high latitudes, *J. Geophys. Res.*, **92**, 4575, 1987b.

Vallance Jones, A., D.J. McEwen, and T. Oguti, TV all-sky observations of pulsating aurora, *Eos Trans. A.G.U.*, **61**, 341, 1980.

Valley, S.L. (Ed.), *Handbook of geophysics and space environment*, Air Force Geophysics Laboratory, U.S.A.F., Cambridge, Mass., 1965.

Van der Walt, A.J., P.H. Stoker, J.P. Maree, P.B. Zeeman, and F.M. Hamm, Airglow and enhanced penetrating electromagnetic radiation in the southern radiation anomaly, *Space Res.*, **6**, 189, 1966.

Venkatesan, D., and S.M. Krimigis, Probing the heliomagnetosphere, *Eos Trans. A.G.U.*, **71**, 1755, 1990.

Vernov, S.N., and A.E. Chudakov, Terrestrial corpuscular radiation and cosmic rays, *Space Res.*, **1**, 751, 1960.

Vondrak, R.R., and R.D. Sears, Comparison of incoherent scatter radar and photometric measurements of the energy distribution of auroral electrons, *J. Geophys. Res.*, **83**, 1665, 1978.

Wallace, L. and M.B. McElroy, The visual dayglow, *Planet. Space Sci.*, **14**, 677, 1966.

Whalen, J.A., The aurora - phenomenology, morphology, and occurrence, Chapter 12, pp. 12-1 to 12-19, in *Handbook of geophysics and the space environment*, Ed. by A.S. Jursa, Air Force Geophysics Laboratory, U.S.A.F., Cambridge, Mass., 1985.

Wickwar, V.B., L.L. Cogger, and H.C. Carlson, The 6300 Å O(^{1}D) airglow and dissociative recombination, *Planet. Space Sci.*, **22**, 709, 1974.

Wiens, R.H., and A. Vallance Jones, Studies of auroral hydrogen emissions in west-central Canada. III Proton and electron auroral ovals, *Can. J. Phys.*, **47**, 1493, 1969.

Wilkes, M.V., A table of Chapman's grazing incidence integral Ch (x,χ), *Proc. Phys. Soc.*, **B67**, 304, 1954.

Winningham, J.D., C.D. Anger, G.G. Shepherd, E.J. Weber, and R.A. Wagner, A case study of the aurora, high-latitude ionosphere, and particle precipitation during near-steady state conditions, *J. Geophys. Res.*, **83**, 5717, 1978.

Wolf, R.A., The quasi-static region of the magnetosphere, pp. 303-368, in *Solar-terrestrial physics*, Ed. by R.L. Carovillano and J.M. Forbes, D. Reidel, Dordrecht, Holland, 1983.

Wu, Q., T.J. Rosenberg, L.J. Lanzerotti, C.G. Maclennan, and A. Wolfe, Seasonal and diurnal variations of the latitude of the westward auroral electrojet in the nightside polar cap, *J. Geophys. Res.*, **96**, 1409, 1991.

Yoshida, S., G.H. Ludwig, and J.A. van Allen, Distribution of trapped radiation in the geomagnetic field, *J. Geophys. Res.*, **65**, 807, 1960.

Zeeman, P.B., and F.M. Hamm, *Airglow Data, SANAE 1967*, Merensky Institute for Physics, University of Stellenbosch, South Africa, 1967.

Zeeman, P.B., F.M. Hamm, and J.L. Steyn, *Airborne airglow measurements in and around the South Atlantic geomagnetic anomaly, October 1964*, Merensky Institute for Physics, University of Stellenbosch, South Africa, 1964.

Zeeman, P.B., F.M. Hamm, and J.L. Steyn, *Airborne airglow measurements in and around the South Atlantic geomagnetic anomaly, August 1966*, Merensky Institute for Physics, University of Stellenbosch, South Africa, 1966.

Zeeman, P.B., F.M. Hamm, and J.L. Steyn, *Airborne airglow measurements along the geomagnetic meridians through Cape Town and Walvis Bay, August 1969*, Merensky Institute for Physics, University of Stellenbosch, South Africa, 1969.

Zeeman, P.B., J.L. Steyn, and F.M. Hamm, *Airglow Data, SANAE 1968*, Merensky Institute for Physics, University of Stellenbosch, South Africa, 1968.

Zeeman, P.B., J.L. Steyn, and F.M. Hamm, *Airglow Data, SANAE 1969*, Merensky Institute for Physics, University of Stellenbosch, South Africa, 1969.

Zipf, E.C., The excitation of the $O(^1S)$ state by the dissociative recombination of O_2^+ ions: Electron temperature dependence, *Planet. Space Sci.*, **36**, 621, 1988.

Zipf, E.C., P.S. Espy, and C.F. Boyle, The excitation and collisional deactivation of metastable $N(^2P)$ atoms in auroras, *J. Geophys. Res.*, **85**, 687, 1980.